Electrodeposition of Co, Ni-based Alloys in Ionic Solutions and their Electrocatalytic Propert

Yuelin Xie

To cite this version:

Yuelin Xie. Electrodeposition of Co, Ni-based Alloys in Ionic Solutions and their Electrocatalytic Propert. Theoretical and/or physical chemistry. Sorbonne Université, 2023. English. NNT : 2023SORUS560 . tel-04800207

HAL Id: tel-04800207
https://theses.hal.science/tel-04800207v1

Sorbonne Université

Ecole doctorale ED388

Chimie-Physique et Chimie Analytique de Paris Centre

Laboratoire de Réactivité de Surface

Electrodeposition of Co, Ni-based Alloys in Ionic Solutions and their Electrocatalytic Properties

Par Yuelin XIE

Thèse de doctorat de Chimie Physique

Dirigée par Mireille TURMINE et Vincent VIVIER

Soutenance prévue le 23/11/2023

Devant un jury composé de :

Jean-Yves HIHN, Professeur, Université de Franche-Comté	Rapporteur
Loïc ASSAUD, MdC HDR, Université Paris-Saclay	Rapporteur
Benoit LESCOP, MdC HDR, Université de Bretagne Occidentale	Examinateur
Sophie CASSAIGNON, Professeur, Sorbonne Université	Présidente
Vincent VIVIER, Directeur de recherche, Sorbonne Université	Co-encadrant
Mireille TURMINE, MdC HDR, Sorbonne Université	Directrice de thèse

Acknowledgment

First, I deeply appreciate the members of the jury, Dr. Jean-Yves Hihn, Dr. Loïc Assaud, Dr. Benoit Lescop, Dr. Sophie Cassaignon, Dr. Mireille Turmine and Dr. Vincent Vivier, for agreeing to judge my work.

I wish to convey my deepest respect and heartfelt appreciation to my supervisor Dr. Mireille Turmine, and co- supervisor, Dr. Vincent Vivier. Their unwavering support and guidance were instrumental throughout every phase of this research journey. Over the course of the past three years, their support, kindness, and encouragement have been invaluable to me, and I wish to express my profound gratitude once again.

I would like to appreciate Dr. Hélène Pernot for her kindness and support in my daily academic working life in LRS (Laboratoire de Réactivité de Surface), Sorbonne Université. I extend my sincere gratitude to Mr. Antoine MICHE, Mr. David Montero, and Mr. Mohamed Selmane for their invaluable assistance in numerous material characterizations, and the dedicated efforts of all our colleagues at LRS, whose diligent work contributed significantly to the seamless execution of our scientific research.

I would like to thank the China Scholarship Council for providing me with financial support over the past three years.

I am very grateful to my colleagues and friends, Ekaterina, Duncan, Yaojun, Zhuoqun, Qinfan and Chengguan, for their help and companionship, in scientific research work and daily life, which makes life full of hope and pleasure. I am also grateful to my gaming friends, Zheng, Yunfan and Dawei for alleviating my weekend solitude.

Finally, I would like to thank my parents, my grandparents, my wife. Their support and expectations are one of the main motivations for me to complete the work in my thesis.

Yuelin Xie

解岳霖

Contents

Résumé en français

Le développement de diverses applications utilisant l’hydrogène en tant que vecteur énergétique ouvre des voies prometteuses pour l'avenir. L’hydrogène peut être produit de différentes manières, l’une d’entre elles est l’électrolyse de l’eau et plus particulièrement sa réduction qui conduit à la production d’hydrogène (connue sous le nom de Hydrogen Evolution Reaction, HER). Cette technique nécessite l’emploi d’électrocatalyseurs performants. À l'heure actuelle, les catalyseurs à base d'alliages ou de composés de métaux nobles se distinguent par leur rendement électrocatalytique exceptionnel dans le cadre de la production d'hydrogène. Cependant, leur coût élevé et leurs réserves limitées compliquent leur utilisation à grande échelle dans l'industrie. C'est pourquoi il est impératif de concevoir et de développer de nouveaux matériaux permettant de produire de l'hydrogène économiques et respectueux de l'environnement. Ces dernières années, de nouveaux matériaux, notamment les alliages à base de métaux de transition tels que le nickel (Ni) et le cobalt (Co), ont été proposés et ont démontré d'excellentes propriétés catalytiques. Cependant, réduire davantage les coûts de préparation tout en améliorant les performances catalytiques et en respectant l'environnement s'avère être un défi de taille. C'est pourquoi, dans cette étude, nous mettrons l'accent sur la préparation d'alliages par électrodépôt, une méthode économique, et nous explorerons les effets de la composition élémentaire, de la structure de phase et de la morphologie de surface sur les performances électrocatalytiques. Au cours du processus d'électrodéposition, nous employons des électrolytes non conventionnels, communément désignés sous l'appellation de liquides ioniques. Comparativement aux solutions aqueuses, ces liquides ioniques présentent une teneur en eau considérablement moindre. Cette particularité sert à réduire la formation d'oxydes de métaux de transition. Par ailleurs, les liquides ioniques se caractérisent par une fenêtre électrochimique élargie, ce qui élargit notre éventail d'options en termes d'éléments d'alliage. Cette diversification nous autorise à scruter l'influence de divers éléments sur les performances de l'évolution de l'hydrogène, offrant ainsi des perspectives précieuses. De plus, la surface spécifique de l'électrocatalyseur joue un rôle central dans l'incidence sur les performances de la génération d'hydrogène. Une méthode connue sous l'appellation de désalliage est employée pour éliminer sélectivement une fraction des éléments d'alliage, ce qui conduit à la formation d'une structure nanoporeuse. Cette modification accroît davantage la surface spécifique du matériau.

Nous avons mené avec succès l'électrodépôt d'alliages à base de Ni/Co dans des liquides ioniques ou des solvants eutectiques profonds (DES) en vue de préparer des électrocatalyseurs, puis nous les avons soumis à un traitement de surface par désalliage, fournissant ainsi de nouvelles informations sur le développement de matériaux pour la production d'hydrogène.

Dans les chapitres 1 et 2, nous avons approfondi les aspects bibliographiques et le contexte de cette recherche. Nous avons exposé de manière exhaustive les détails expérimentaux, couvrant les méthodes de caractérisation et de mesure de divers matériaux ainsi que leurs propriétés respectives. Notre présentation englobe une exploration approfondie du paysage actuel de l'énergie liée à l’hydrogène et de l'évolution de la réaction de formation d'hydrogène, complétée par des discussions sur les mécanismes électrochimiques et les techniques de mesure associées. De plus, nous avons fourni des informations sur l'utilisation des alliages dans le cadre de la réaction de formation d'hydrogène et avons clarifié le processus d'électrodépôt des alliages dans des liquides ioniques.

Dans le chapitre 3, nous avons étudié les paramètres influençant les propriétés des électrodépôts de nickel (Ni), cobalt (Co) et de différentes compositions d'alliages Ni-Co, en utilisant comme substrats des verres revêtus d’oxyde d’étain dopés au fluor (FTO) et les plaques de cuivre (Cu), dans l'éthylammonium nitrate (NEA), un liquide ionique protique. Nous avons pu ainsi électrodéposer dans le NEA, pour la première fois à notre connaissance, du cobalt pur amorphe, du nickel nanocristallin et des alliages Ni-Co nanocristallins ou amorphes sur des verres FTO, et ce, dans des conditions exemptes d'oxygène. L'impact de l'ajout du cobalt dans des alliages à base de nickel sur les performances en électrocatalyse de la réaction de réduction de l'hydrogène (HER) a été étudié en examinant à la fois des électrodépôts réalisés sur les verres FTO et sur les plaques de cuivre. Il est intéressant de noter qu’à composition équivalente, l'alliage amorphe présente une surtension cathodique plus faible pour la réduction de l’hydrogène et une cinétique de réaction plus rapide que l’alliage cristallin.

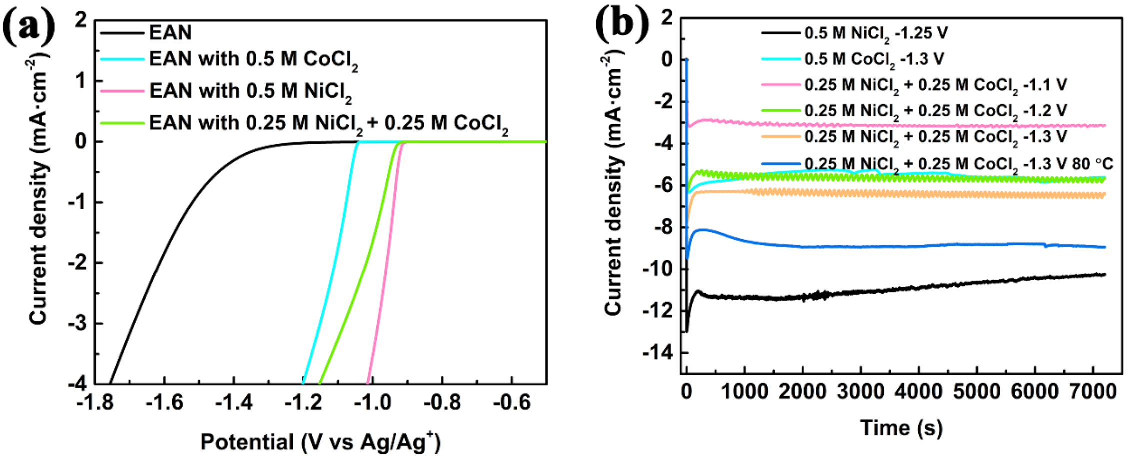

Figure 0.1 a) Courbes de voltampérométrie à balayage linéaire (v = 1 mV s^{-1}) du NEA avec différents ions sur du verre FTO à 60 °C réalisées en boîte à gants. b) Courbes de chronoampérométrie obtenues dans diverses conditions lors des électrodépôts.

Dans cette section, afin de modifier la composition de l'alliage en termes de rapport de Co/Ni, nous avons examiné l'effet de la température, du temps et du potentiel d'électrodépôt et de la teneur en ion Ni et Co dans le NEA lors d'électrodépôts sur du verre FTO. La Figure 0.1 présente les courbes voltampérométriques (LSV) ainsi que les chronoampérométries des quelques dépôts. Les structures des phases des différents électrodépôts ont été ensuite analysées par diffraction des rayons X (Figure 0.2).

Il est remarquable qu'en faisant varier le potentiel d'électrodépôt, tout en gardant les mêmes conditions de température, de temps de dépôt ou de composition de l'électrolyte, l'alliage peut être soit amorphe (potentiel le plus cathodique de -1,3 V/ref) ou nanocristallins pour les potentiels moins cathodiques. De plus, les observations au microscope électronique à balayage (MEB) ont confirmé que tous les échantillons préparés étaient des films denses.

L'épaisseur du film a été étudiée par microanalyse par dispersion d'énergie (EDS) et le MEB. En outre, grâce à l'EDS, nous avons exploré l'impact de divers paramètres d'électrodépôt sur la composition des dépôts, notamment le rapport Ni/Co. Les analyses cartographiques effectuées à l'aide de la spectroscopie de photoélectrons à rayons X (XPS) et de l'EDS ont toutes deux confirmé l'électrosynthèse de l'alliage, et non la présence d'amas individuels de nickel et de cobalt élémentaires indépendants, et ont révélé que les oxydes ne constituaient pas le composant principal.

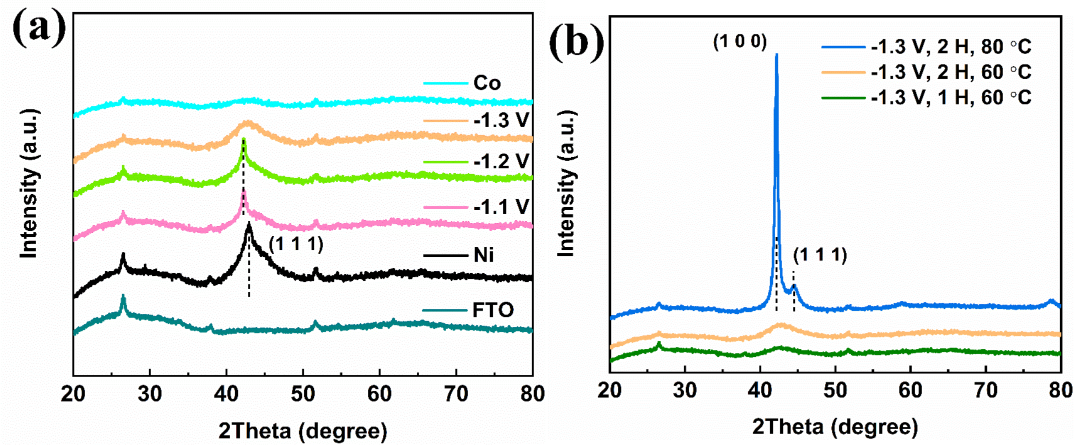

Figure 0.2 Modèles XRD de différents alliages électrodéposés.

Les alliages Ni-Co présentent des surtensions pour l'HER inférieures à celles du nickel et du cobalt purs. Il a été observé pour différents alliages cristallins Ni-Co que l'incorporation de Co réduit les surtensions de l'HER. Par comparaison avec les alliages cristallins conventionnels, la réduction des surtensions de l'HER des alliages amorphes peut s'expliquer par un effet synergique des atomes dans l'alliage, mais aussi l'énergie de surface élevée de l'état amorphe. Par conséquent, il est important d'étudier les propriétés électrocatalytiques d'alliages amorphes de différentes compositions. L'ajout de Co conduit généralement à une diminution de la pente de Tafel et à une augmentation de la vitesse de réaction pour la plupart des alliages Ni-Co.

Cependant, cette valeur n'est pas idéale pour la réaction de formation de l'hydrogène (HER) en raison de l'instabilité de la surface pendant la réaction. Lorsque l'électrode de travail est remplacée par une plaque de cuivre, on constate une nette amélioration de la stabilité du matériau éléctrocatalytique. Diverses caractérisations ont été effectuées sur différents matériaux électrodéposés, et ont montré des résultats similaires en termes de variation de la composition des matériaux. En ce qui concerne leurs performances électrocatalytiques, on observe que les alliages électrodéposés sur les plaques de cuivre conservent de bonnes performances catalytiques, même après dix cycles (Figure 0.3).

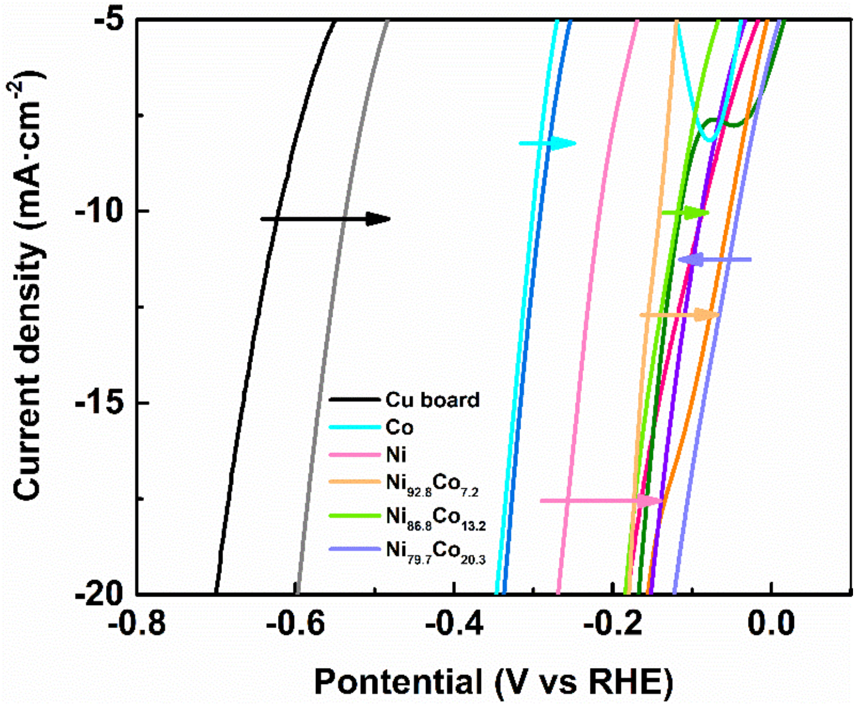

Figure 0.3 Courbes LSV (v= 10mV s^{-1}) sur des alliages Ni-Co de différents rapports atomiques après 10 cycles de réaction catalytique.

Nous avons également étudié l'électrodépôt du nickel dans des solvants eutectiques profonds (DES). Nous avons considéré deux DES. Le premier est l’éthaline, un mélange d’éthylène glycol et de chlorure de cholinium et le second est un DES hydrophobe à base de menthol. À la lumière des résultats et des discussions présentés dans le chapitre 3, on montre que l'incorporation du cobalt dans les alliages de nickel conduit à une amélioration significative de la formation électrocatalytique de l'hydrogène. Notamment, les alliages amorphes à base de nickel et de cobalt présentent des performances intéressantes dans ce contexte. Par conséquent, au vu des résultats encourageants obtenus pour les alliages nickel-cobalt, il est important d’envisager l'introduction d'autres éléments dans la matrice de l'alliage afin d’améliorer encore les performances électrocatalytiques de la réaction de formation d'hydrogène.

Ainsi, nous avons envisagé le zinc, cependant nos travaux sur cet élément demeurent relativement limités en comparaison avec ce qui précède. Il est impératif de minimiser la formation d'oxydes dans des solutions non aqueuses et de faire des alliages à base de nickel et de cobalt (Ni/Co) l'objet principal de l'étude. L'incorporation d'éléments métalliques légers, tels que le zinc, ainsi que la variation de la composition des électrolytes, constituent les principaux facteurs influençant la préparation et les propriétés électrocatalytiques pour l'électrolyse de l'eau (water splitting).

Dans le chapitre 4, nous avons principalement examiné l'électrodéposition du nickel dans le solvant eutectique profond éthaline, ce qui a conduit à la découverte que les performances électrocatalytiques de la mousse de cuivre peuvent être améliorées grâce à l'électrodéposition de Ni. Il est à noter que des dépôts presque purs de zinc, de nickel et de cobalt peuvent être obtenus par électrodéposition dans l'éthaline.

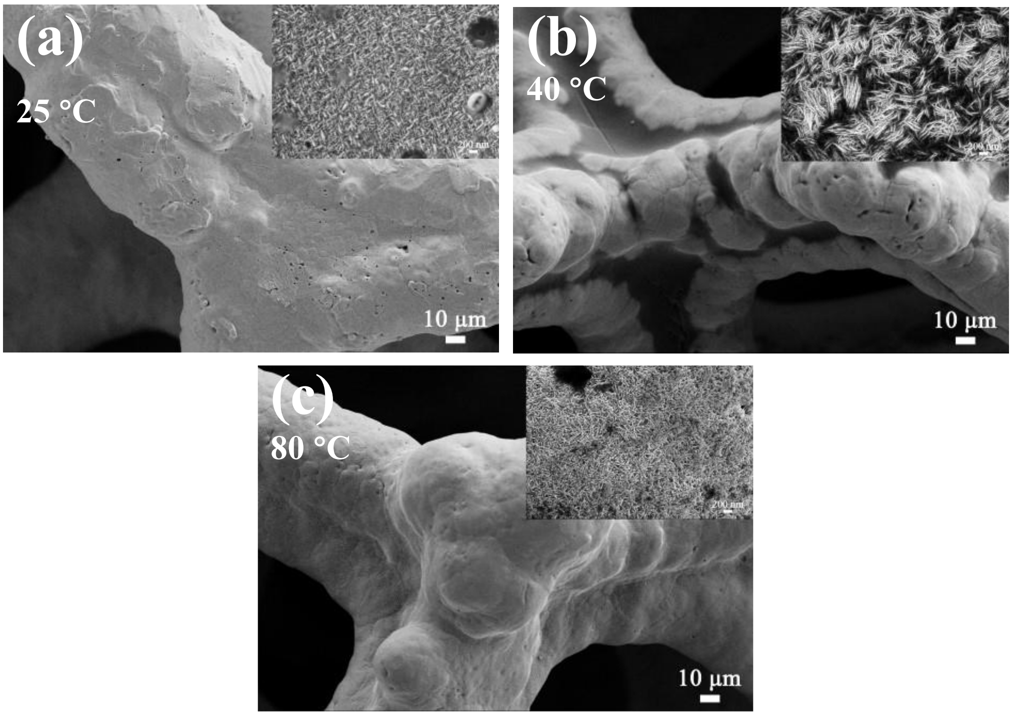

Figure 0.4 Morphologies SEM de la mousse de Cu à 25,40 et 80 °C.

Initialement, nous avons tenté l'électrodépôt sur une mousse de cuivre dans des DES à base d'éthaline et de menthol. Nous avons constaté que, même en prolongeant le temps dépôt à 15 heures, la quantité maximale de nickel déposée dans le DES à base de menthol demeure limitée à 40 °C. Par conséquent, nous en avons conclu que, bien que l'électrodépôt de nickel soit possible dans le DES à base de menthol, la quantité déposée demeure trop faible. Même sur la mousse de cuivre, caractérisée par sa surface spécifique élevée et son excellente conductivité, seulement 25,75 % (en atome) de nickel peuvent être obtenus après un processus d'électrodépôt de 15 heures, ce qui a été confirmé par des observations au microscope électronique à balayage. Par conséquent, nous avons abandonné l'étude des électrodépôts de matériaux catalytiques dans le DES à base de menthol.

À une température de 25 °C, un simple dépôt d'une demi-heure dans l'éthaline produit des structures cristallines en forme d'aiguilles à l'échelle nanométrique, en accord avec les résultats de la diffraction des rayons X. Lorsque la température augmente à 40 °C puis à 80 °C, la morphologie en forme d'aiguille devient plus prononcée et de plus grande dimension (Figure 0.4). Notamment, à 80 °C, ces structures en forme d'aiguilles se rejoignent pour former une topographie plus étendue. Cependant, on n'observe pas d'épaississement significatif du revêtement avec l'augmentation de la température, il faudrait donc trouver un autre paramètre, plus pertinent que la température, pour pallier cet inconvénient. Ainsi, une augmentation significative de l'épaisseur du revêtement de surface est observée lorsque le temps de dépôt est augmenté. Bien que des mesures numériques précises posent problèmes, la topographie de la surface présente des fissures dues à une épaisseur de dépôt excessive. Cela signifie que prolonger le temps de dépôt constitue une approche efficace pour améliorer à la fois le contenu et l'épaisseur des dépôts. Lors de l'évaluation de l'HER, il a été constaté que la mousse de cuivre recouverte de nickel présente des performances électrocatalytiques nettement meilleures, par rapport à la mousse de Cu seule.

Notre objectif principal est de préparer des alliages par électrodéposition qui contiennent du nickel ou du cobalt en tant qu'éléments principaux, auxquels s'ajoute du zinc en tant qu'élément secondaire. Cette approche nous permettra d'explorer l'impact de l'ajout de zinc sur les performances électrocatalytiques de ces alliages. Notre tâche suivante consiste à obtenir des alliages ayant des compositions variables en jouant sur divers paramètres expérimentaux, notamment la composition de l'électrolyte, le potentiel de dépôt, la durée de dépôt et la température. En ajustant systématiquement ces paramètres, notre objectif est de générer des alliages présentant des compositions différentes, ce qui facilitera une exploration complète de leurs propriétés électrocatalytiques.

Les alliages à base de zinc, de nickel et de leurs combinaisons peuvent être déposés sur des plaques de cuivre dans l'éthaline sous atmosphère ambiante. Il est également important de noter qu'il a été observé que l'ajout de zinc peut améliorer la réaction électrocatalytique de formation d'hydrogène des alliages à base de nickel. Cependant, il est essentiel de noter que l'excès de zinc peut avoir un impact négatif sur les performances catalytiques de ces alliages (Figure 0.5). Par conséquent, déterminer la composition d'alliage appropriée lors du processus de préparation des matériaux électrocatalytiques Ni-Zn revêt une importance cruciale pour atteindre des performances optimales.

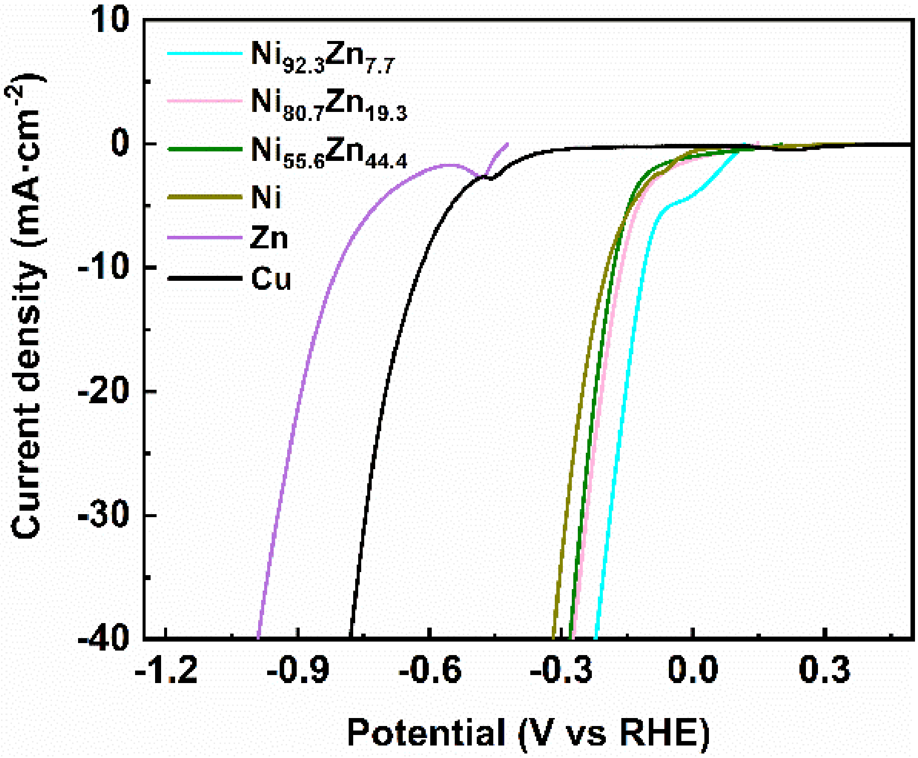

Figure 0.5 Courbes LSV des alliages Ni-Zn avec différents rapports atomiques.

Les résultats décrit dans le chapitre 4 ont révélé que l'ajout d'une petite quantité de zinc n'a pas d'effet négatif sur l'efficacité électrocatalytique de la réaction de formation d'hydrogène sur le nickel électrodéposé ; au contraire, cela a amélioré les performances globales. Ce chapitre est principalement consacré aux processus d'électrodépôt, de désalliage et des performances électrocatalytiques de la réaction de formation d'hydrogène sur les systèmes Zn-Ni/Co-Cu, Zn-Ni/Cu et Zn-Ni-Co/Cu, en utilisant différents solutions d'éthaline.

Nous avons également abordé une méthode d'électrodépôt en deux étapes pour la préparation d'alliages Zn-Ni-Cu-Co et le désalliage de ces derniers. Tout d'abord, le cobalt est électrodéposé sur la surface de la plaque de cuivre, ce qui permet d'obtenir des alliages Cu-Co après un traitement thermique. Ensuite, les alliages Zn-Ni sont électrodéposés sur la surface des alliages Cu-Co dans l'éthaline. Un deuxième traitement thermique conduit à la formation d'alliages Zn-Ni-Cu-Co. La préparation d'alliages poreux par désalliage de différents alliages à base de Zn-Ni a été ensuite examiné. Il est essentiel de noter que les alliages nanoporeux présentent des caractéristiques fascinantes en ce qui concerne leur morphologie, leur distribution élémentaire (Figure 0.6) et leurs performances dans le contexte de la réaction de formation d'hydrogène. En modifiant la solution de désalliage et les paramètres associés nous avons pu jouer, à la fois sur la morphologie et sur la distribution élémentaire au sein de ces alliages nanoporeux. Il a été observé que le zinc pouvait être éliminé plus facilement, permettant la formation de pores et de structures nanoporeuses, tandis que le cuivre sert de charpente dans les zones précédemment occupées par le zinc. Enfin, les propriétés de ces alliages sont discutées. De plus, le co-électrodépôt de trois éléments, à savoir le nickel, le zinc et le cobalt, a également été exploré et discuté dans ce chapitre.

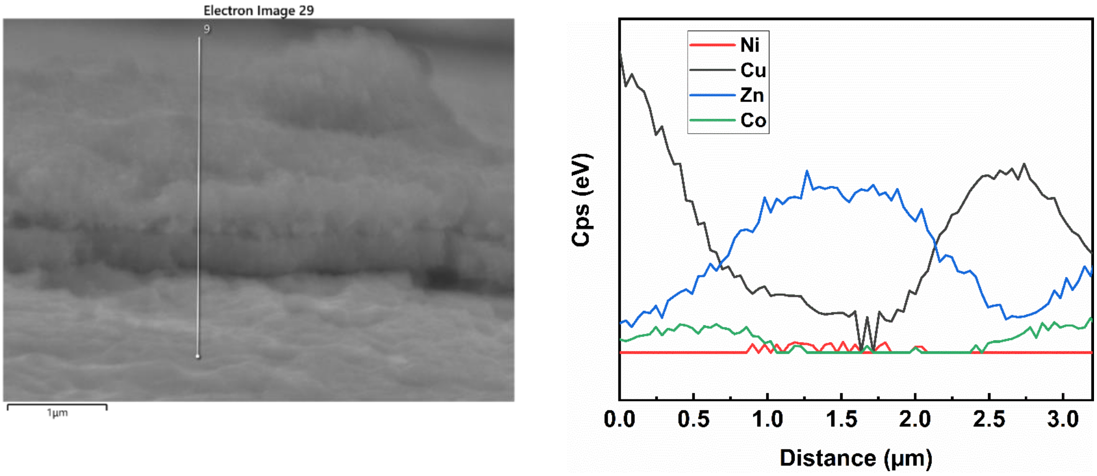

Figure 0.6 Les courbes de balayage des lignes SEM et EDS des alliages déposés en deux étapes.

Nous avons réussi à préparer des alliages nanoporeux Zn-Ni-Co-Cu en utilisant des techniques d'électrodépôt en une et deux étapes, suivies d'un traitement thermique et d'un désalliage subséquent. Comparativement aux alliages nanoporeux Zn-Ni-Cu dépourvus de cobalt, la variante Zn-Ni-Co-Cu présente une amélioration significative en termes de performances vis-à-vis de l’HER. L'obtention de ces performances requiert une minutieuse optimisation à la fois de la surface spécifique de l'alliage et de la répartition des éléments au sein du matériau.

Introduction

The use of fossil energy, one of the main contributors to carbon emissions and a major source of pollution, has become a hot topic of discussion in recent years. Predicted energy shortages and the resulting environmental challenges are forcing mankind to look for alternatives to fossil fuels.

Hydrogen is attracting increasing attention as a clean energy source, with high energy density and minimal emissions. It represents a promising, low-carbon energy carrier ready to supplant fossil fuels, particularly in the demanding industrial and transport sectors, where decarbonization is particularly difficult to implement. According to existing literature, there are three main methods for producing hydrogen: hydrogen production from (i) fossil fuels, (ii) gasification, and (iii) water splitting.

Water electrolysis under renewable resource conditions can practically eliminate carbon emissions, which is a significant difference compared to hydrogen production from fossil fuels (66 gCO_2 e/MJ) or gasification (55 gCO_2 e/MJ). Clearly, hydrogen production by electrolysis under ideal conditions has the distinct advantage of being environmentally friendly, with a low carbon footprint. Furthermore, water electrolysis offers many advantages, including the production of high-purity hydrogen, the simultaneous production of oxygen as a by-product, and simple installation.

Although the hydrogen evolution reaction (HER) by water electrolysis provides numerous advantages for hydrogen production applications, its industrial adoption remains relatively limited, especially behind the production of hydrogen from fossil fuels. One of the main obstacles to its widespread use is the choice of electrocatalytic materials. Precious metals have exceptional electrocatalytic properties; however, their high cost and limited abundance on earth limit their practical application in all industries. Consequently, the search for cost-effective alternatives involving transition metals and the improvement of electrocatalyst performance through alloying and adjustments of surface morphology has emerged as important and dynamic lines of research.

A wide range of techniques have been explored for synthesizing transition metal alloys used in electrocatalytic HER. Among these methods, electrodeposition stands out for its streamlined process, ease of implementation, and precise control, making it a versatile choice for large-scale applications. However, the hydrolysis of water during electrodeposition poses a problem. This can be effectively resolved by employing ionic liquids (ILs) as electrolytes, which are becoming increasingly popular due to their wide electrochemical window, high ionic conductivity, and user-friendly characteristics arising from their non-volatile and non-flammable nature. Surprisingly, research on the electrodeposition of alloys in ionic liquids remains relatively scarce. Consequently, combining the electrodeposition of alloy electrocatalysts with ionic liquids represents an attractive avenue to explore.

In this work, we address the following questions:

(1) Is it possible to prepare transition metal-based alloys by electrodeposition in ionic liquids?

(2) What kinds of alloys can be prepared by electrodeposition in ionic liquids?

(3) What is the impact of other elements (Co, Zn, Cu) on the HER properties of alloys?

(4) How can the HER properties of alloys be enhanced by surface modification (dealloying)?

Chapter 1 Bibliographic studies

1.1. Development of hydrogen energy

Since the end of the 20th century, environmental pollution and energy consumption have increased at an unexpected speed, leading to various problems for the earth and the human being. Through the information from Keeling Curve in Figure 1.1 [1], the quantity of CO_2 in the air increased rapidly from 330 ppm in 1974 to 419 ppm in 2021, further exacerbating the greenhouse effect, leading to a series of problems about environment and human socioeconomic issues. In order to reduce greenhouse gas emissions and unite people around the world to face climate change issues, many proposals have been recommended, such as the Paris Agreement signed by 194 parties. Reducing carbon emissions is a major objective of the Paris Agreement. The consumption of fossil energy, one of the main sources of carbon emissions, has been a hot topic in recent years. The foreseeable shortage of energy and the resulting environmental problems are pushing mankind to find an alternative to fossil fuels.

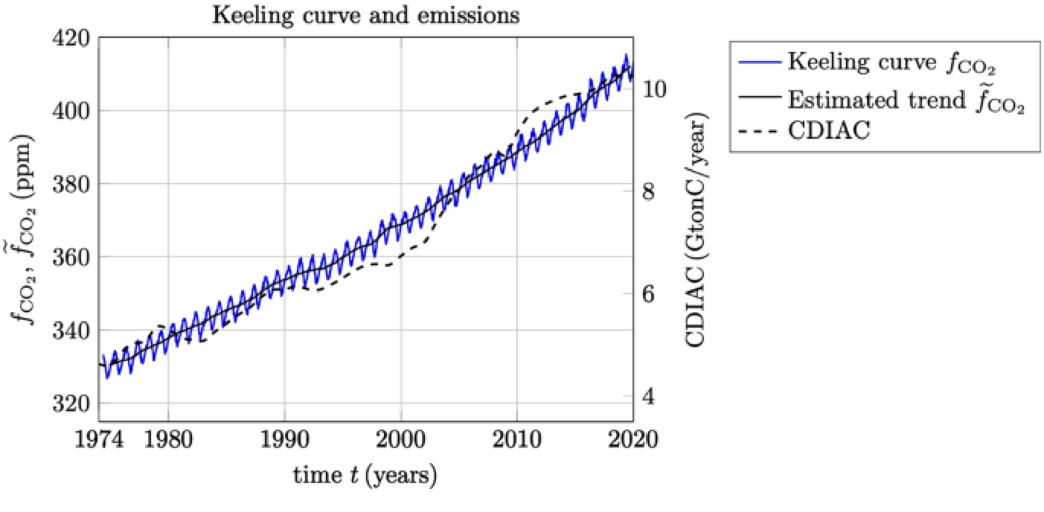

Figure 1.1 The Keeling curve and estimated trend in the amount of CO_2 in the atmosphere [1].

Hydrogen is attracting growing interest as a clean energy with high energy density and low emissions. As one of the simplest energy carriers, hydrogen (H_2) has been shown to have a high energy density, saving 4.92 eV of free energy on the chemical bonding [2]. Moreover, hydrogen can be prepared from recycled energy and stored in large quantities to be used in various domains in the future, as shown in Figure 1.2. To date, few hydrogen production methods have been studied and applied to actual production.

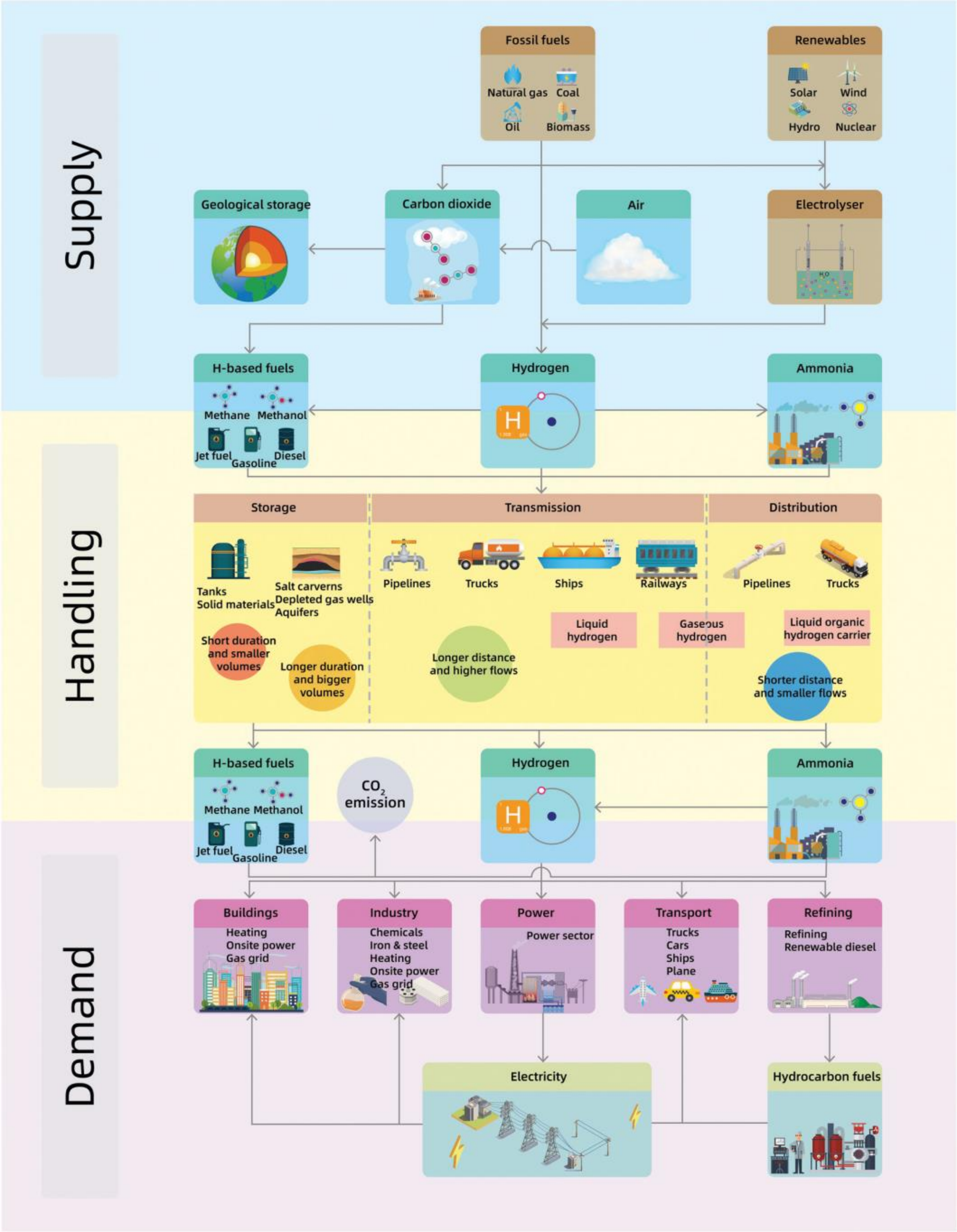

Figure 1.2 The path of hydrogen from generation to applications [3].

Figure 1.2 shows that hydrogen production can be divided in two categories according to resource type: fossil fuel and renewable resources. Based on the literature, there are currently three main methods of hydrogen production, (i) hydrogen production from fossil fuels, (ii) gasification hydrogen, and (iii) the hydrogen evolution reaction by water splitting. However, for the first two routes, the hydrogen generation is always accompanied by fossil fuel waste and

CO_2 production [4-6]. The related carbon generation value is shown in Table 1.1. Compared with other two routes, water electrolysis (water splitting: $2H_2O \rightarrow 2H_2 + O_2$) has many advantages, such as the production of high purity hydrogen, by-product oxygen, simple setup. Moreover, the latter technique gives the best results in terms of environmental protection. The electrocatalytic water splitting process, facilitated by renewable sources such as photovoltaic systems, hydropower, and wind power, demonstrates the conversion and storage of electrical energy into chemical energy. This reaction efficiently splits water into its constituent elements, hydrogen and oxygen. Then, thanks to appropriate storage and transport methods, the produced hydrogen serves as a vital raw material for hydrogen fuel cells. These fuel cells engage in a chemical reaction between hydrogen and oxygen, producing water in an environmentally-friendly way and converting chemical energy back into electrical energy. Building on the water cycle process, this sustainable approach enables the conversion and use of chemical and electrical energies while maintaining zero carbon emissions, thus illustrating the use of green energy. Therefore, water electrolysis has the potential to be the main route for the clean hydrogen production, but the development of electrocatalytic water splitting is required to improve this process.

Table 1.1 Carbon intensity for different hydrogen generations [7].

Method	Steam reforming of fossil fuels	Gasification	Electrolysis
Carbon intensity (gCO_2 e/MJ)	60 - 400	55 - 700	0 -150

1.2. Electrolysis of water

Water electrolysis, known as water splitting, is recognized as a highly promising approach for hydrogen production. The hydrogen resulting from water electrolysis possesses high purity, and the process itself is safe and straightforward. Extensive research on water electrolysis has been conducted for over two centuries since its first proposal by Paets van Troostwijil and Deiman in 1789 [8]. While hydrogen production from fossil fuels and industrial by-products has been extensively studied and implemented as a mature industrial system, concerns regarding energy waste and environmental pollution have become increasingly prominent. This is why, in recent years, particular attention has been paid to clean water splitting technologies. Water splitting reaction can be divided into two parts, hydrogen evolution reaction (HER) on the cathode and oxygen evolution reaction (OER) on the anode, as shown in Figure 1.3. Both reactions occur at the same time during the process.

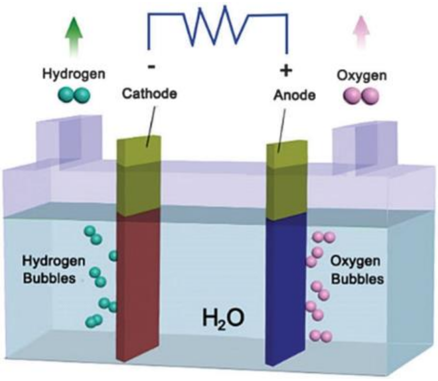

Figure 1.3 Scheme of water electrolysis [9].

Through the already studied scheme [10], in the context of hydrogen evolution reaction (HER) occurring in an acidic electrolyte, the reaction can be described by the Volmer reaction, wherein hydronium ions undergo discharge to produce hydrogen intermediates (H*) that can be adsorbed onto the electrode surface (Equation 1). On the other hand, in an alkaline electrolyte, water molecules serve as a source of protons for HER (Equation 2). Subsequently, the generation of molecular hydrogen follows two pathways, depending on the surface coverage of H* intermediates. When the coverage of H* is substantial, the Tafel step becomes the rate-limiting process, as two adjacent H* species combine to yield H_2 molecules (Equation 3). However, when the H* coverage is low, the dominant process is the Heyrovský reaction, which involves the simultaneous attraction of a single H* atom with an electron and a proton from the acidic medium (Equation 4), or with a water molecule in the alkaline media (Equation 5) [10].

Step 1 : $H_3O^+ + e^- + * \rightarrow H^* + H_2O$ (Volmer reaction) (acidic electrolyte) (Eq. 1)

$H_2O + e^- + * \rightarrow H^* + OH^-$ (Volmer reaction) (alkaline electrolyte) (Eq. 2)

Step 2 : $H^* + H^* \rightarrow H_2$ (Tafel reaction) (Eq. 3)

$H^* + H_3O^+ + e^- \rightarrow H_2 + H_2O$ (Heyrovský reaction) (acidic media) (Eq. 4)

$H^* + H_2O + e^- \rightarrow H_2 + OH^-$ (Heyrovský reaction) (alkaline media) (Eq. 5) where * represents the catalysts on the surface, H* is the absorbed hydrogen intermediate.

Electrochemical oxygen evolution reaction (OER) is a kinetic-limited process that encompasses four-electrode reactions, with the involvement of three surface-adsorbed intermediates, namely OOH*, O*, and OH*. In acidic electrolytes, the oxidation of water results in the production of oxygen and hydrogen ions, while in neutral and alkaline environments, the oxidation of hydroxyl ions leads to the formation of water and oxygen. Theoretical models put forth to explain these reactions and propose distinct mechanisms for the OER under both acidic and alkaline conditions, represented by Equations 6 - 9 and 10 - 13, respectively [10].

In acidic electrolyte,

$$H_2O + * \rightarrow HO* + H^+ + e^- \qquad \text{(Eq. 6)}$$

$$HO* \rightarrow O* + H^+ + e^- \qquad \text{(Eq. 7)}$$

$$H_2O + O* \rightarrow HOO* + H^+ + e^- \qquad \text{(Eq. 8)}$$

$$HOO* \rightarrow * + O_2 + H^+ + e^- \qquad \text{(Eq. 9)}$$

In alkaline electrolyte,

$$OH^- + * \rightarrow HO* + e^- \qquad \text{(Eq. 10)}$$

$$HO* + OH^- \rightarrow O* + H_2O + e^- \qquad \text{(Eq. 11)}$$

$$OH^- + O* \rightarrow HOO* + e^- \qquad \text{(Eq. 12)}$$

$$HOO* + OH^- \rightarrow * + O_2 + H_2O + e^- \qquad \text{(Eq. 13)}$$

where * represents the surface-active sites of the catalyst.

Since all the four steps during OER process are thermodynamically uphill processes, the potential-determining step in a reaction is the step with the highest energy barrier. In the case of the reaction, the thermochemical free energy for each step is determined to be 1.23 eV for an ideal catalyst [10]. However, practical studies conducted on various metal oxides have indicated that the difference in free energy between HOO* and HO* is approximately 3.2 ± 0.2 eV. In the context of research on the HER, the production of oxygen from the OER is often considered as a by-product. Additionally, different water splitting technologies may involve variations in electrode and electrolyzer structures.

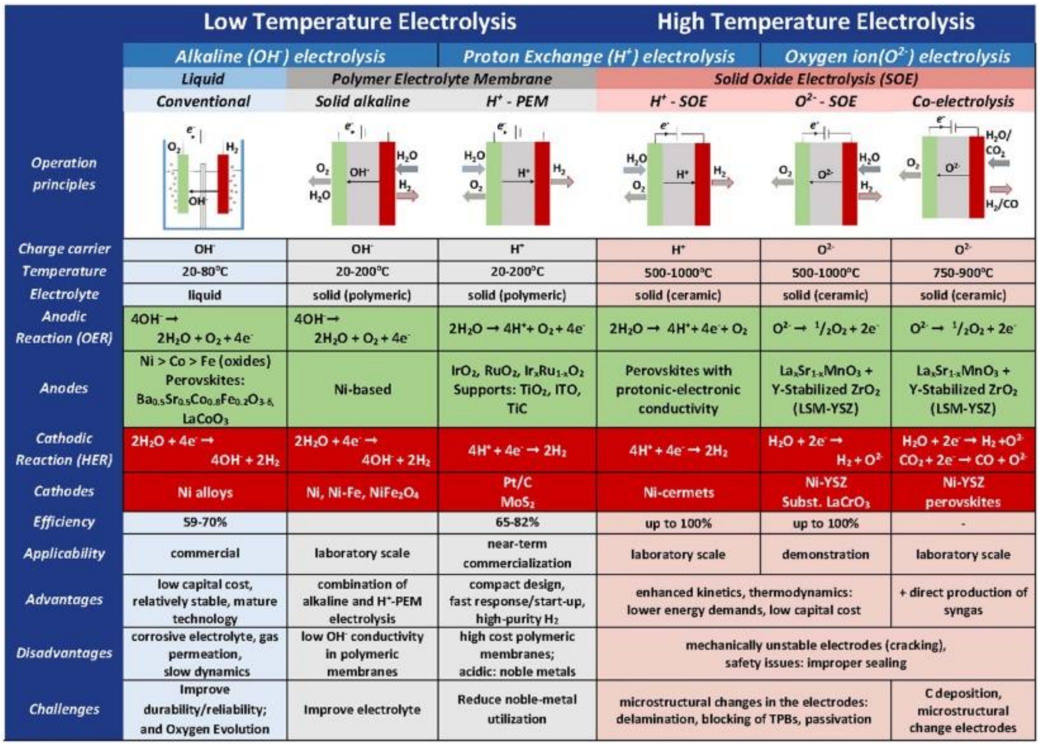

	Low Temperature Electrolysis			High Temperature Electrolysis		
	Alkaline (OH^-) electrolysis		Proton Exchange (H^+) electrolysis		Oxygen ion(O^{2-}) electrolysis	
	Liquid	Polymer Electrolyte Membrane		Solid Oxide Electrolysis (SOE)		
	Conventional	Solid alkaline	H^+ - PEM	H^+ - SOE	O^{2-} - SOE	Co-electrolysis
Operation principles	e^- O_2 H_2 OH^-	e^- O_2 H_2O OH^- H_2O H_2	e^- H_2O O_2 H^+ H_2	e^- H_2O O_2 H^+ H_2	e^- O_2 O^{2-} H_2O H_2	e^- O_2 O^{2-} H_2O/CO_2 H_2/CO
Charge carrier	OH^-	OH^-	H^+	H^+	O^{2-}	O^{2-}
Temperature	20-80°C	20-200°C	20-200°C	500-1000°C	500-1000°C	750-900°C
Electrolyte	liquid	solid (polymeric)	solid (polymeric)	solid (ceramic)	solid (ceramic)	solid (ceramic)
Anodic Reaction (OER)	$4OH^- \rightarrow 2H_2O + O_2 + 4e^-$	$4OH^- \rightarrow 2H_2O + O_2 + 4e^-$	$2H_2O \rightarrow 4H^+ + O_2 + 4e^-$	$2H_2O \rightarrow 4H^+ + 4e^- + O_2$	$O^{2-} \rightarrow {}^1/_2O_2 + 2e^-$	$O^{2-} \rightarrow {}^1/_2O_2 + 2e^-$
Anodes	Ni > Co > Fe (oxides) Perovskites: $Ba_{0.5}Sr_{0.5}Co_{0.8}Fe_{0.2}O_{3-\delta}$, $LaCoO_3$	Ni-based	IrO_2, RuO_2, $Ir_xRu_{1-x}O_2$ Supports: TiO_2, ITO, TiC	Perovskites with protonic-electronic conductivity	$La_xSr_{1-x}MnO_3$ + Y-Stabilized ZrO_2 (LSM-YSZ)	$La_xSr_{1-x}MnO_3$ + Y-Stabilized ZrO_2 (LSM-YSZ)
Cathodic Reaction (HER)	$2H_2O + 4e^- \rightarrow 4OH^- + 2H_2$	$2H_2O + 4e^- \rightarrow 4OH^- + 2H_2$	$4H^+ + 4e^- \rightarrow 2H_2$	$4H^+ + 4e^- \rightarrow 2H_2$	$H_2O + 2e^- \rightarrow H_2 + O^{2-}$	$H_2O + 2e^- \rightarrow H_2 + O^{2-}$ $CO_2 + 2e^- \rightarrow CO + O^{2-}$
Cathodes	Ni alloys	Ni, Ni-Fe, $NiFe_2O_4$	Pt/C MoS_2	Ni-cermets	Ni-YSZ Subst. $LaCrO_3$	Ni-YSZ perovskites
Efficiency	59-70%		65-82%	up to 100%	up to 100%	-
Applicability	commercial	laboratory scale	near-term commercialization	laboratory scale	demonstration	laboratory scale
Advantages	low capital cost, relatively stable, mature technology	combination of alkaline and H^+-PEM electrolysis	compact design, fast response/start-up, high-purity H_2	enhanced kinetics, thermodynamics: lower energy demands, low capital cost		+ direct production of syngas
Disadvantages	corrosive electrolyte, gas permeation, slow dynamics	low OH^- conductivity in polymeric membranes	high cost polymeric membranes; acidic: noble metals	mechanically unstable electrodes (cracking), safety issues: improper sealing		
Challenges	Improve durability/reliability; and Oxygen Evolution	Improve electrolyte	Reduce noble-metal utilization	microstructural changes in the electrodes: delamination, blocking of TPBs, passivation		C deposition, microstructural change electrodes

Figure 1.4 The classification of electrolysis of water [11].

Water electrolysis technology can be divided into three paths depending on electrolyte and temperature change. Except for alkaline water electrolysis, which has been extensively studied in recent years, polymer-electrolyte membrane (PEM) and solid oxide electrolyzers (SOE) are two other technologies that can be used in industrial applications.

Solid oxide electrolyzers (SOE) generally operate at temperatures above 500 °C, using steam as water source. Traditional SOE technology relies mainly on O^{2-} conductors, particularly yttria stabilized zirconia (YSZ). However, in recent years, several ceramic proton conductors have emerged for use in solid oxide fuel cells [11]. By contrast, alkaline and polymer electrolyzers operate at lower temperatures, typically below 100 °C, where water exists in a liquid state. Recent advances in fuel cell technology have focused on the development of polymeric membranes that can efficiently conduct protons at temperatures of up to 200 °C [11-13]. These innovations could also extend the operating temperature range of polymer electrolysis.

Each type of electrolysis possesses distinct advantages and disadvantages, as summarized in

Figure 1.4. Nonetheless, alkaline electrolysis is the most widely implemented commercial technology. The notable advantages of alkaline electrolysis include its cost-effectiveness, attributed to the use of non-noble electrodes, and its long-term stability. On the other hand, the acidic environment in polymer electrolyzers hampers the kinetics of redox reactions, necessitating the use of expensive noble metal catalysts and materials for bipolar plates.

1.3. Water electrolysis in alkaline electrolyte

In alkaline electrolyzers, the anode and cathode electrodes are immersed in the electrolyte, which is commonly potassium hydroxide. For the HER and OER, the electrode material is one of the keys for the water electrolysis. The performance of the electrode determines the cell voltage and energy consumption. According to the Volmer and Heyrovský reactions, proton adsorption and hydrogen desorption are two distinct processes. Thus, these kinetic activities and the general principles can be quantified by analyzing the free energy of hydrogen adsorption, ΔG_{H^*} [14]. Like Sabatier's principle, in the realm of heterogeneous catalysis and electrocatalysis, a widely accepted explanatory framework asserts that achieving optimal catalytic activity depends on a catalytic surface possessing intermediate binding energies (or adsorption free energies) for the reactive intermediates [14-17]. When the binding of intermediates is excessively weak, the surface encounters challenges in activating them. Conversely, if the binding is excessively strong, the intermediates will saturate all available surface sites, impeding the reaction process - thus, intermediate binding energies offer a favorable compromise between these extremes [18]. A lower value in hydrogen adsorption in HER of the metallic catalyst denotes a harder adsorption of proton in solution, whereas, a high value represents a harder desorption of hydrogen gas into the solution.

As shown in Figure 1.5, the plot of the variations of hydrogen adsorption free energy against the current density values has a volcano shape. Compared with other metals, the precious metals, such as Platinum (Pt), Palladium (Pd) are near the top of the "volcano", with a value close to 0 for ΔG_{H^*}. Moreover, Pt has been tested and proven as a HER electrocatalyst with high efficiency and high activity [19].

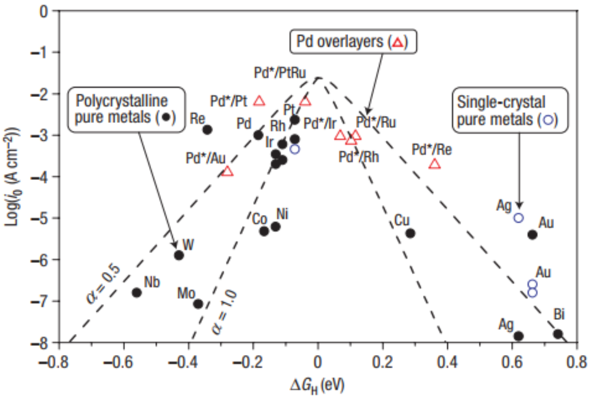

Figure 1.5 Volcano plot for the HER for various pure metals and metal overlayers [18].

1.3.1. Performance parameters of HER electrocatalysts

Despite the inherent challenges in directly characterizing the catalytic activity of various catalysts, it is possible to assess their overall electrochemical performance by utilizing pertinent parameters that reflect their electrocatalytic efficiency or activity. The evaluation of HER electrocatalyst materials typically revolves around several key indicators, including overpotential, Tafel slope, and electrochemically active surface area (ECSA).

1. Onset potential and overpotential

Normally, the onset potential is the overpotential at which significant current occurs. It can be marked from the current-potential curves. But it is still difficult to accurately determine the real onset potential value. One way for marking the onset potential is choosing the potential value corresponding to a current density of 0.5 to 1 mA·cm^{-2} [20]. Or using the intersection of the tangent from the non-Faradaic region and HER beginning part.

The overpotential for HER (HER potential) is another important parameter for the properties. Overpotential refers to the additional potential required, beyond the thermodynamic necessity, to drive the hydrogen evolution reaction at a specific current density. Comparatively, in order to quantitatively assess the performance of catalysts, the HER potential value at 10 mA·cm^{-2} is commonly employed as a significant reference point. These potential values can be determined via linear sweep voltammetry (LSV). Ideally, electrocatalysts exhibiting superior performance can achieve high current densities while maintaining low overpotentials.

2. Tafel slope

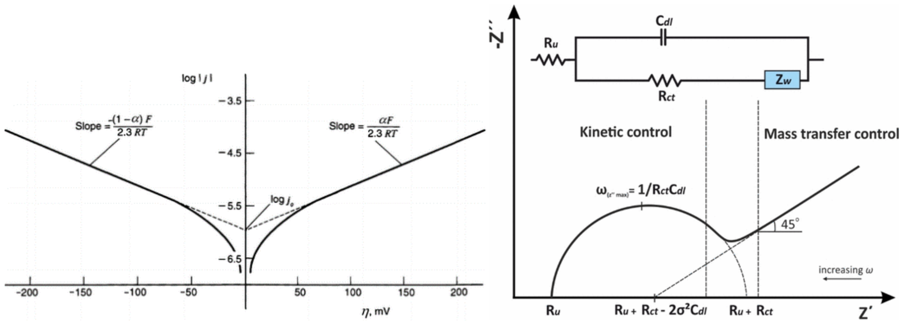

Figure 1.6 The Tafel slop schematic diagram (left) and electrochemical impedance spectroscopy (right) [21, 22].

Tafel slope is another important electrochemical kinetic parameter for reviewing the electrocatalytic properties. Normally it can be obtained using two different methods: conversion from polarization curves, and extraction from impedance data. Conversion from polarization curves is the most commonly employed approach to determine Tafel slope values. In this method, polarization curves are replotted as overpotential versus log (current density). However, due to the generation of substantial H_2 bubbles at high overpotentials, the log (current density) often deviates from a linear relationship within this potential range. Therefore, the Tafel slope is determined by fitting the linear portions at low overpotential to the Tafel equation (Eq 16), where η represents overpotential, j denotes the current density, and b signifies the Tafel slope. In the second method, Tafel slopes are calculated based on linear fitting plots of log (R_{ct}) versus overpotential. R_{ct} represents the charge transfer resistance in the equivalent circuit obtained from impedance spectroscopy. It corresponds to the resistance to the transfer of charge between the electrode surface and the electrolyte solution dur to a redox reaction at the interface. And the value of R_{ct} can be obtained after the experimental data fitting to the equivalent circuit model, as shown in Figure 1.6. This approach provides Tafel slopes that solely reflect the charge transfer kinetics of the electrode reaction. Regardless of the method used, it is crucial to ensure that the linearity of the investigated part of the fitting curve ortion reaches at least 99.9% for accurate data interpretation. For the cathodic and the anodic branches, the value of Tafel's slope can be calculated using the following equation (14-19) [20, 23].

$$j = j_0\left\{e^{[\frac{\alpha zF\eta}{RT}]} - e^{[-\frac{(1-\alpha)zF\eta}{RT}]}\right\} \qquad \text{Butler–Volmer equation (Eq. 14)}$$

$$\eta = \frac{2.303RT}{\alpha zF}\lg\frac{j_0}{[j]} - \frac{2.303RT}{\alpha zF}\lg\frac{j}{[j]} \qquad \text{Tafel equation (Eq. 15)}$$

$$\eta = b \lg j + a$$ Tafel equation (Eq. 16)

Where $b = \frac{-2.303RT}{\alpha zF}$, $a = \frac{2.303RT}{\alpha zF} j_0$, [j] is the value of current density, T is the absolute temperature (in K), R is the perfect gas constant (8.314 J $mol^{-1}K^{-1}$), z is the stoichiometric coefficient of electrons in the exchange reaction, F is the Faraday constant (96495 C mol^{-1}), $\alpha \approx 0.5$ is the symmetry coefficient [20, 24].

$$b = \frac{2.303RT}{\alpha F}$$ Volmer reaction (Eq. 17)

$$b = \frac{2.303RT}{(1+\alpha)F}$$ Heyrovský reaction (Eq. 18)

$$b = \frac{2.303RT}{2F}$$ Tafel reaction (Eq. 19)

3. Electrochemically active surface area (ECSA)

Brunauer-Emmett-Teller (BET) surface area analysis is one of the most popular ways for measuring the physical specific surface area of materials. However, it is not the first choice for bulk materials or the materials which are not very porous, due to its sensitivity. For the electrocatalysts, the ECSA of electrocatalyst can be determined by measuring the double layer capacitance (C_{dl}) at the solid-liquid interface using cyclic voltammetry (CV). CV experiments are conducted within a specific potential window devoid of Faradaic reaction processes [20, 25]. Various scan speeds (20 - 500 $mV \cdot s^{-1}$) are employed in CV experiments, typically with 5 - 10 consecutive data points selected. Optimal selection of the scan speed range ensured that the resulting CV curve maintained a rectangular shape. The relationship between the difference in current density and the scan speed at the intermediate overpotential within the applied potential range was plotted, and one-half of the slope value obtained from linear fitting represented the C_{dl} value, shown in Figure 1.7. A larger C_{dl} value indicates that the electrode material possessed a greater number of exposed surface reaction sites and higher current density, implying a larger ECSA. In addition, C_{dl} value can also be calculated through electrochemical impedance spectroscopy. Note that the double-layer capacitance measured by EIS is within 15% of that measured from the scan rate-dependent CVs [26]. Oxides on alloy catalysts can also interfere with ECSA measurements, which lead to uncertainties of up to ~700 % [27]. Therefore, the comparison of ECSA using C_{dl} measurement should be applied in the same system, such as the alloy catalyst system or the organic catalyst system.

In addition to the aforementioned catalyst activity parameters, stability is a crucial indicator for assessing the hydrogen evolution performance and determining the feasibility of electrocatalysts in practical applications. Two commonly used methods are employed to evaluate the long-term durability of catalysts. One method involves continuous electrolysis of water at a constant current density or constant potential for an extended period, with the subsequent recording of a chronopotential curve or chronoamperometry curve. A decrease in current density at a constant potential or an increase in overpotential at a constant current density (typically 10 mA·cm^{-2}) can unveil the catalyst's durability [20, 25]. Electrocatalysts exhibiting smaller changes in current density or overpotential demonstrate longer lifetimes and superior durability. Another method is the accelerated electrolysis test, which compares cyclic voltammetry (CV) curves or linear sweep voltammetry (LSV) curves before and after cycles electrocatalytic cycles. The onset overpotential and the change in overpotential at constant current density serves as indicators of the catalyst durability.

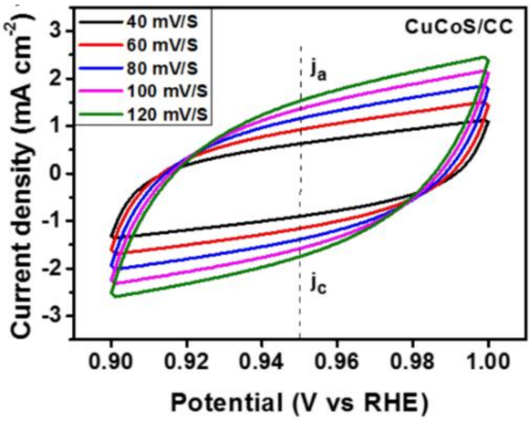

Figure 1.7 The scheme of calculation of C_{dl} through CV [28].

Finally, the value in Faradaic efficiency (FE) is another important parameter for the electrocatalytic properties, which describes the overall selectivity of an electrochemical process. This parameter is defined as the amount (in moles) of collected product relative to the amount that could be produced from the total charge passed, expressed as a fraction or a percentage [29]. Due to the complexity of electrode surface reactions, such as competitive reactions, corrosion processes, the FE value will not be calculated and analyzed in this thesis.

1.3.2. Noble metal-based electrocatalysts

Precious metals exhibit excellent properties in electrocatalysis. However, the high cost and the low quantity of these elements on earth limit their wide application in real life and industry. Therefore, there are several ways to improve catalysts using less noble metals such as Pt, and the main path can be divided into two directions.

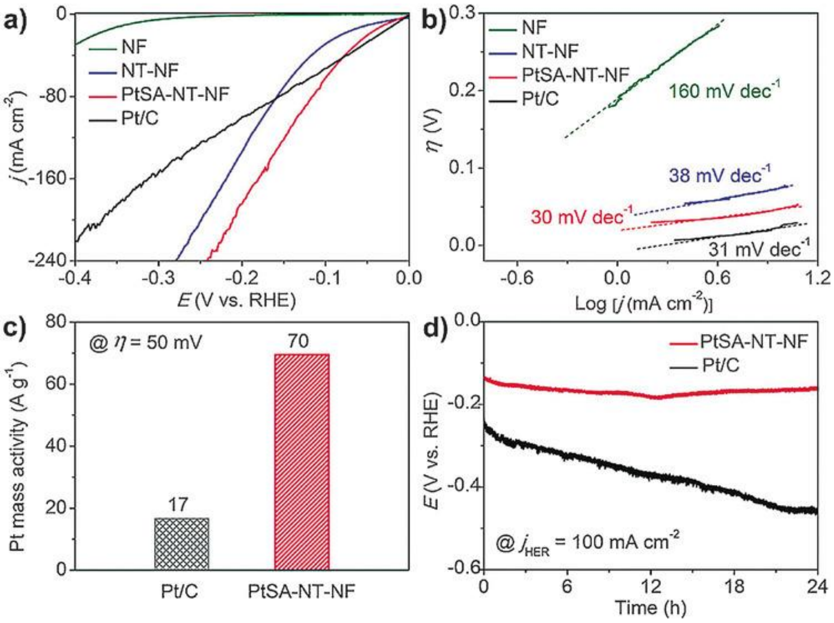

Figure 1.8 a) HER polarization curves of different prepared catalysts and Pt/C, at 5 mV s^{-1} in N_2-saturated 1 M PBS at 25 °C. b) Tafel plots of the polarization curves in (a). c) Pt mass activities of PtSA-NT-NF and Pt/C at η=50 mV. d) Chronoamperometric curves of PtSA-NT-NF and Pt/C at a constant j_{HER}=100 mA・cm^{-2}.

First direction is the change of the surface state, including the shape and the active point. Since only the atoms forming the surface or subsurface layers are the main electrocatalytic sites for the reaction, increasing the specific surface area and the number of active sites on the surface can improve the electrocatalysis. The use of Pt in HER can be increased from 9.5 to 26.0% by decreasing the size of Pt lateral length from 11.7 to 3.9 nm [30]. Low Pt content electrocatalysts (LPCEs), which can be loaded on different supports, have been more and more popular in these few years [31]. The Pt loaded on CoP-based nanotube (NT) arrays supported by a Ni foam (NF) (The electrocatalyst is termed as PtSA-NT-NF) shows an ultralow overpotential (η) of 24 mV for the HER current density (j_{HER}) of 10 mA·cm^{-2}, only 7 mV larger than that of commercial Pt/C [32], as shown in Figure 1.8a. Lasonen' group developed a pseudo-atomic-scale dispersion of Pt, i.e. individual atoms or subnanometer clusters, on the sidewalls of single-walled carbon nanotubes (SWNTs) by a facile electroplating deposition method, resulting in good HER catalytic performance in acidic conditions, compared to commercial Pt/C with similar platinum content [33].

Another direction is the addition of different elements in Pt-based materials for HER. The concentration of Pt can be decreased by alloying. Therefore, the alloying is one of the potential ways for development of Pt-based electrocatalysts. Moreover, the difference in size of various element atoms and Pt atom can result in synergistic effect with the deflection of electrons in the structure [34-37]. Based on d-band center theory, strong adsorption will be shown with the d-band center close to the Fermi energy level [38-40]. Transition metals, such as nickel (Ni), cobalt (Co), iron (Fe), can modify the electronic position of the Pt atom and its properties through alloying or compounds [41]. Yang et al. prepared Pt-Co alloy nanoparticles based on CNFs with a low Pt lowing content (ca. 5 wt%). It showed an overpotential of -63 mV, which is closed to that of commercial Pt/C (-57 mV) [42]. With different element additions, reaction surfaces and preparation ways of the alloys, the properties in HER can be modified. A novel hexapod-like ternary PtNiCo nanostructured alloy has been developed by Lee's group [43]. These Pt-based catalysts have demonstrated excellent electrocatalytic activity for HER in alkaline media.

Besides Pt, another precious metal, Pd, also has great properties in HER in alkaline solution. Jerkiewicz et al. have synthesized octahedral palladium nanoparticles (Pd-NPs) with an average tip to tip size of 7.8 nm [44]. Compared to bulk Pd or larger-sized Pd nanoparticles, these octahedral Pd-NPs exhibit superior hydrogen adsorption behavior due to their unique octahedral nanostructure and smaller size, offering potential in other energy applications, such as water splitting and novel batteries.

1.3.3. Non-noble metal-based electrocatalysts

Although precious metals have excellent properties for water splitting (HER and OER), their low natural reserves and high prices make their large-scale use unavoidable. The preparation of highly efficient electrocatalysts based on non-noble metals for HER and OER has therefore been a hot research topic of research in recent years.

The practical considerations involved in developing electrocatalysts for the three electrolysis technologies, shown in Figure 1.4, vary according to operating conditions. However, good electrocatalysts should generally exhibit the following key characteristics: high intrinsic catalytic activity, high specific surface area, high conductivity, excellent stability, and so forth.

One approach to reducing the cost of water electrolysis is to replace noble metal catalytic materials with non-noble metal alternatives. Electrode materials based on non-noble metals are generally more suitable for alkaline environments, although the rate of HER in alkaline media is often higher than in acidic media [45]. On the other hand, OER, involving multiple electron transfers, is a bottleneck in the water splitting process and tends to proceed at a slower rate, especially due to metal oxidation [45-47]. Therefore, we will discuss non-noble metal-based electrocatalysts applied to HER in alkaline solutions. Non-noble metals, such as iron, cobalt, nickel, manganese (Mn), copper (Cu), molybdenum (Mo), tungsten (W), and other elements, hold significant potential as electrocatalytic materials for HER owing to their abundant reserves, wide distribution, low cost, and favorable structural controllability.

There are a few different classifications of electrocatalysts based on non-noble metal, such as alloys, metal sulfide, metal phosphide metal, oxides/hydroxides, and so on. For instance, MoS_2 is one of the electrocatalysts for HER, that was studied very early. Hinnermann et al. designed and prepared MoS_2 nanoparticles supported on graphite with the criterion of the free energy of atomic hydrogen binding to the catalyst close to zero [48]. It has a moderate overpotential of 0.1 - 0.2 V in HER. The free energy also confirms the excellent properties of MoS_2, as shown in Figure 1.9. The structure and electron distribution of W_2S is close to that of MoS_2 and it has also been studied as HER electrocatalysts [49]. We can note that the various electrocatalysts are always designed based on the free energy. As discussed above, the addition of different elements in single metal through alloying is one of the potential ways for the electrocatalyst development. It has not been investigated as much as other compounds. Therefore, in the framework of this study, the main work is focus on alloys preparation and properties in HER.

For all kinds of typical alloys, the structures of alloys can be classified into solid solutions and intermetallic compounds [50, 51]. Through different atom size of two elements, the position of the atoms and the crystal structure, the solid solution alloys can be classified in the substitutional solid solution and interstitial solid solution. The elements mixing can be varied almost arbitrarily, and the solid solution has the same physical properties as the pure metal. In the intermetallic compounds, each element has a definite stoichiometry, such as AB, AB_2, A_3B. Unlike solid solutions, the different elements A and B are not randomly distributed in the alloys, but arranged in specific positions [50]. And the formed intermetallic compound has a different and ordered crystal structure from the original metal [50, 51]. The advantage of the intermetallic compound catalytic lies in the formation of covalent bonds or ionic bonds between heterogeneous elements, which can regulate the adsorption energy of reaction intermediate products, thereby enhancing the intrinsic catalytic activity [50, 51]. The different elements in the intermetallic compound have electron transfer due to their different electronegativity, optimizing their adsorption energy, so that they have better catalytic activity than single metals. And adjusting the electron structure of transition metal-based materials by using alloying, through the d-band center theory discussed in last part, is one of the approaches being considered. Through the volcano plot in Figure 1.5, the ΔG_{H*} of some transition metals, like Ni, Co, Cu, shows similar value to the noble metals [52]. By this value, the transition metal-based electrocatalysts are considered as alternative to replace these noble metals, especially for HER. However, these monometallic transition metal elements often exhibit inadequate catalytic activity due to the hydrogen adsorption energy being either excessively strong or weak. Consequently, enhancing the HER catalytic activity of these transition metal-based materials has emerged as a prominent research focus in this field. The alloying is one of the potential ways for development of transition metal-based electrocatalyst.

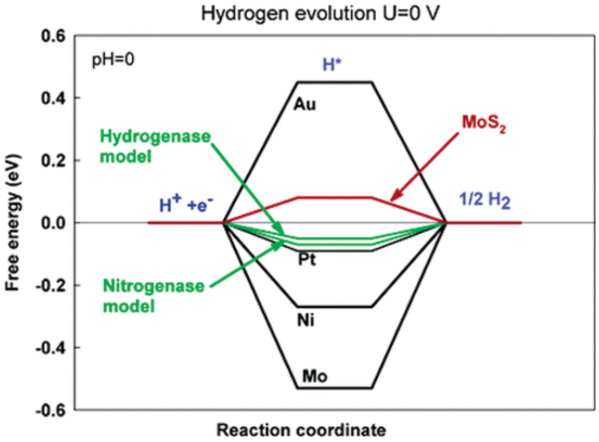

Figure 1.9 Free energy diagram for HER by MoS compound and typical other metals [53].

Since the first investigations of the HER mechanism on metallic Ni-Co in the 1960s, extensive research has been performed to develop the preparation and application of transition metal alloys [54, 55]. Different combinations of metal elements were investigated in previous works, such as Ni-Mo, Ni-Co, Ni-Al, Co-Mo, Co-Fe, and Fe-P and so on [56-66]. As shown in Table 1.2, we can find that the electrocatalytic properties by different element added Ni/Co/Fe-based alloys are different. For instance, Shetty et al. prepared Ni-Mo alloys through electrodeposition. By adjusting the electrodeposition current, the ratio of Ni and Mo can be changed, as shown in Figure 1.10. The overpotential of HER decreased with the addition of Mo [67].

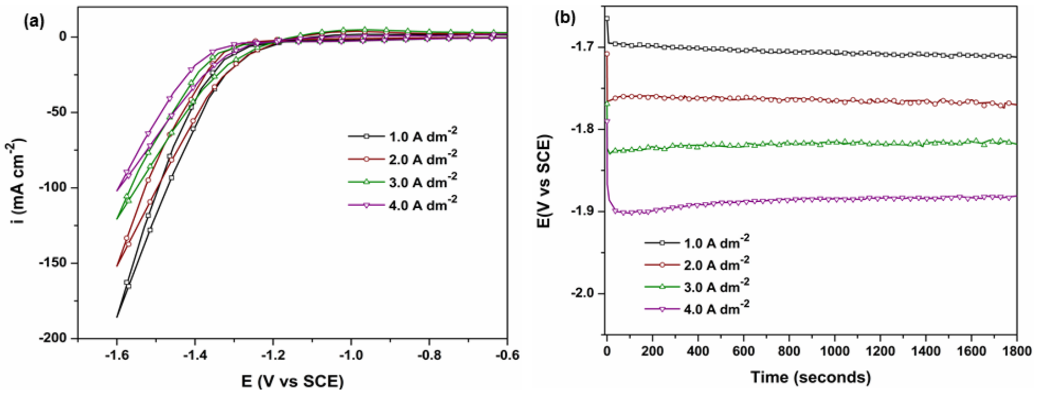

Figure 1.10 a) The cyclic voltammetry curves of different Ni-Mo alloys. b) The current-time curve during the alloy preparation [67].

In addition, to modify composition and morphology of transition metal-based alloys, adjusting the crystal structure is another way to improve HER performance. Amorphous alloys show characteristic in structural heterogeneities and high atomic diffusion rate resulting in great properties for chemical applications, especially in catalysis, due to their metastable structure and higher energy state [68-72]. Interestingly, electrodeposition is a possible route for the preparation of such alloys. For instance, Han et al.[73] prepared amorphous Ni-Mo alloy by pulse plating technique. They showed that the addition of 30 wt.% Mo, leads to a decrease in overpotential of 62 mV for a current density of -0.2 A·cm^{-2} at 80°C. Similarly, the amorphous Ni-Fe-Co-P alloy prepared by Bachvarov et al.[74] showed a decrease in overpotential of 89 mV when compared to the crystalline Ni-Fe-Co alloy. Although crystalline alloys generally do not perform as well as amorphous alloys, nanocrystalline alloys have been studied in recent years and show excellent properties for water splitting applications [75-78]. However, it remains to be determined whether amorphous or nanocrystalline alloys are the better choice.

Table 1.2 Electrocatalysis parameters in literature.

	Alloy	Solution	Overpotential (mV)
Ni-based	Ni-Mo [62]	KOH	-100
	Ni-Co [64]	NaOH	-86.7
	Ni-Co [63]	KOH	-168
	Ni-Cu [65]	KOH	-202
	Ni-Zn [66]	KOH	-138
Co-based	Co-Mo [59]	KOH	-120
	Co-W [79]	NaOH	-326
Fe-based	Fe-Ni [80]	KOH	-143

1.4. The preparation of electrocatalysts

Many methods have been considered to synthesize transition metal alloys for electrocatalytic HER, such as melting [81], sintering [82], pulsed layer deposition [83, 84], sol-gel [85], and electrodeposition [54, 86-91].

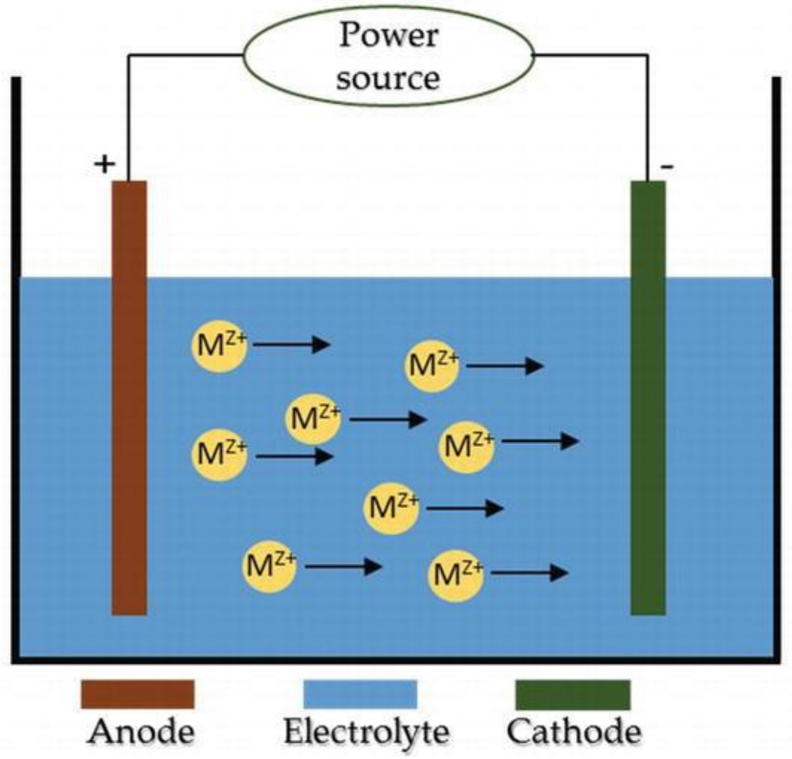

Figure 1.11 Schematic of an electrodeposition process [92].

Among these techniques, electrodeposition has the advantage of involving fewer steps, being easy to implement and control, making it a versatile method for large-scale applications. In an electrodeposition system, the key components are electrodes (consisting of an anode and a cathode), electrolyte, an electrolytic cell, and a power source, as shown in Figure 1.11. The electrolyte is a solution containing metal or alloy salts, which must be deposited on the cathode, which serves as a conductive substrate, during the electrolysis process. When a power source is connected to the electrode terminals of the, an electric current is established, causing a flow of electrons through the system. Consequently, the positively charged metal cations (designated by M^{Z+}) present in the electrolyte are attracted to the cathode surface by the electric field generated. These metal cations undergo reduction at the cathode and are then deposited there. The continuous deposition of metal on the cathode surface occurs through the reduction process, resulting in the formation of a uniform layer of metal. This deposition is the consequence of the electrochemical reduction of metal cations into metal atoms or clusters, which adhere to the cathode surface. During the electrodeposition process, the following chemical reactions take place at the cathode and anode [92]:

$$\text{Cathode: } M^{Z+} + Ze^{-} \rightarrow M \qquad \text{(Eq. 20)}$$

$$\text{Anode: } M \rightarrow M^{Z+} + Ze^{-} \qquad \text{(Eq. 21)}$$

In the electrodeposition process, two types of anodes can be utilized based on specific requirements: sacrificial anodes and permanent anodes. The sacrificial anode, as the name indicates, is a consumable anode made of the same metal deposited on the cathode. During the electrodeposition process, the sacrificial anode gradually dissolves, releasing metal ions into the electrolyte. Its primary purpose is to act as a source of metal ions for deposition. In contrast, the permanent anode, also known as an inert anode, is typically made of materials such as platinum or carbon. The role of the permanent anode is to ensure the uninterrupted flow of electrons within the system without undergoing significant changes [92]. As a result, when compared to the electrodeposition with the sacrificial anode, the permanent anode can relatively reduce the impact of precipitated anode ions on the composition and concentration of the electrolyte ions, further reducing the impact on the electrodeposition products. It should be emphasized that various factors, such as the composition of the electrolyte, the applied voltage or current, and the duration of electrolysis, can significantly impact the quality and properties of the deposited metal layer.

Until now, there have been a few research focused on the preparation of metal based electrocatalysts by electrodeposition. Ahn et al. [87] have prepared Ni dendrites by electrodeposition on glassy carbon for HER in alkaline electrolyte. The stability of HER was maintained without significant variation in overpotential for 2000 cycles. Nickel nanoparticles electrodeposited on a Ni substrate by Zhou et al. shows higher current density than regular Ni-modified substrate with the same overpotential [93]. Recently, nanostructured Ni-Co alloys with different morphologies were electrodeposited in water showing an improvement of the electrocatalytic activity [55, 76, 94-96]. However, the unavoidable presence of water in the electrodeposition electrolyte can lead to undesirable hydrolysis of water in electrolyte and creates unwanted compounds. The narrow potential window of the aqueous solutions and outgassing result in hydrogen embrittlement and a low coulombic efficiency, which are then the main problems in the preparation of HER electrocatalysts by electrochemistry.

1.5. Ionic liquids

1.5.1. ILs category

The problem of water hydrolysis during electrodeposition can be circumvented by using ionic liquids (ILs) electrolyte which are more and more used as electrolyte for electrodeposition due to their large electrochemical window, high ionic conductivity, and simplicity of handling thanks to their non-volatility and inflammability. Ionic liquid is a room temperature molten salt made up of an organic cation and organic or inorganic anion. Since the ethylammonium nitrate (EAN) synthesis in 1914 by Walden [97, 98], with a melting point of 12 °C, many other ionic liquids have been described and characterized. But it was only in the 1990s that the application of ILs attracted the attention of scientists. Numerous ILs with different anions, such as $[BF_4]^-$, $[PF_6]^-$, $[NO_3]^-$, $[NTf_2]^-$, $[OTf_3]^-$, have been synthesized and published as alkylimidazolium ILs [99-101]. Since the beginning of the 21st century, more and more new ILs have been created and studied.

Ionic Liquids are organic (or partly organic) salts that melt commonly below 100 °C, constituted entirely by charged species, usually an organic cation and an organic or inorganic anion [102]. ILs are known for their interesting properties, they show good selective solubility, low volatility, low melting point (normally lower than 100 ℃), good conductivity at room temperature, high thermal stability and wide potential windows in electrochemistry. ILs can be categorized in four main types through the cation difference, alkylammonium-, alkylimidazolium-, alkylphosphonium- and alkylpyridinium-based ILs, shown in Figure 1.12 [103]. The literature reports a growing number of ILs for different applications, depending on the nature of the anion and cation they contain. Through the application difference, the ILs can also be categorized as room-temperature ILs (RTILs, whose melting point is lower than 100 ℃, such as ethylammonium nitrate, 12 ℃), task-specific ILs (TSILs), poly ionic liquids (PILs), and supported IL membranes (SILMs) that include composites of ILs supported on metal–organic frameworks (MOFs) [104]. By the structure of cation, the ILs can also be categorized as protic ILs (PILs) and aprotic ILs (ILs). Protic ionic liquids, consisting of combinations of Brønsted acids and bases through a neutralization reaction, have exchangeable (labile) protons. It is the main difference with aprotic ILs.

$[NR_xH_{4-x}]^+$ $[PR_xH_{4-z}]^+$

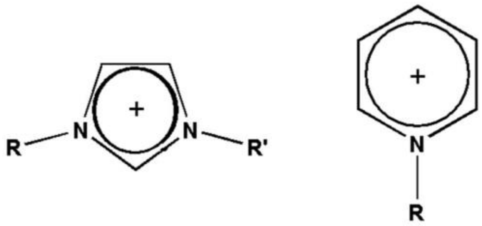

Figure 1.12 Alkylammonium, alkylphosphonium, dialkylimidazolium and N-alkylpyridinium cations [103].

1.5.2. Applications of ionic liquids

Because of their different structures and characteristics, ILs can be used in area variety of fields, as shown in Figure 1.13. In chemistry, and particularly in organic reactions, ILs are commonly used in C-C and C-O bonding reactions due to their high efficiency, recycle reaction and warm conditions. In addition, ILs are also useful as additives to improve the properties of different chemicals, such as lubricants, paints, shampoos and conditioners [105].

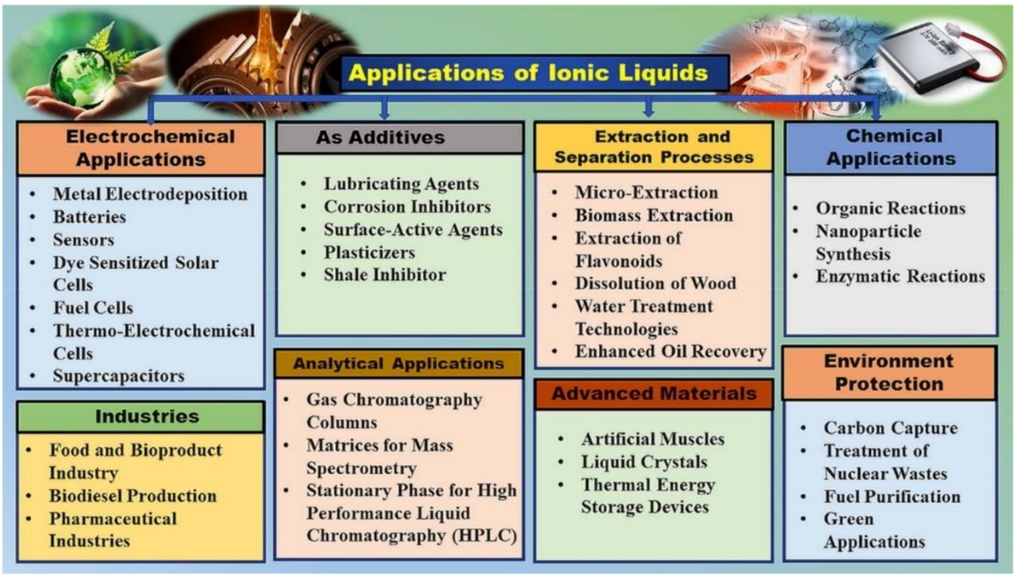

Figure 1.13 Applications of ionic liquids [105].

In these few years, the use ILs in electrochemistry has attracted considerable interest. Due to their wider potential window and lower volatility than aqueous solutions, they have been considered good candidates for electrochemical application. For batteries, ILs can act as an electrolyte with greater stability and longer life. Another important application for ILs in electrochemistry is electrodeposition. Many elements, including transition metals, can be electrodeposited in different ILs. Compared with electrodeposition in aqueous solutions, electrodeposition in ILs can reduce the presence of water and minimize the generation of oxide or other undesirable compounds. The automotive and aerospace industries attach great importance to the development of protective metal coatings due to their many advantages, including improved corrosion and wear resistance, as well as a smoother finish. To address environmental concerns, the use of ILs as solvents and supporting electrolytes in the electrodeposition of metals has received considerable attention [105].

Aluminum (Al) is one of the most studied electrodeposited metals in ILs. $AlCl_3$ based ILs can avoid the problem of electrodeposition in aqueous solutions, such as oxide layer growth on the surface, and it has been applied for a long time. Tang et al. deposited single Al on AZ91D magnesium (Mg) alloy from 1-ethyl-3-methylimidazolium chloride ([EMIM][Cl]) - $AlCl_3$ IL system [106]. Zhang et al. also prepared single Al from 1-butyl-3-methylimidazolium chloride ([BMIM][Cl]) - $AlCl_3$ IL system with the addition of nicotinamide, which can make the surface smooth [107]. Zinc (Zn) is another common electrodeposited metal in ILs. Deng et al. prepared protective Zn coatings on Mg alloys through N-butyl-N-methylpyrrolidinium dicyanamide ([BMP]DCA) [108]. Zn can also be prepared easily through deep eutectic solvent (DES), a new family of solvents often related to ILs. Usually, a DES is composed of a quaternary ammonium salts and a hydrogen bond donor [109]. Ethaline and reline are the most common DESs in electrodeposition. Ethaline is prepared by mixing choline chloride (ChCl) and ethylene glycol (EG) with a specific ratio. Reline is prepared from choline chloride and urea with a specific ratio. Bakkar et al. prepared smooth Zn layer on Mg substrate in different choline chloride and urea mixture [110]. The Zn deposited in ChCl/urea shows the best corrosion properties.

Except for the above light metal, the transition metals, like Fe, Ni, and Co also can be prepared by electrodeposition in ILs or DES. Moreover, nanocrystals can be electrodeposited from ILs more easily than in aqueous solutions [111]. Nanosize Co with different morphologies were prepared by Susan et al. in a hydrophilic IL, 1-ethyl-3-methylimidazolium ethylsulphate ([emim][$EtSO_4$]) [112]. Katayama's group prepared nanoparticles of Ni and Fe in a room-temperature ionic liquid, 1-butyl-1-methylpyrrolidinium bis(trifluoromethylsulfonyl)imide (BMPTFSI) containing $Ni(TFSI)_2$ or $Fe(TFSI)_2$, with a size from 1.9 nm to 4.6 nm [113].

Additionally, in earlier studies, although AILs have been more prevalent than PILs for electrodeposition applications, the latter have the advantage of easier synthesis. They also usually show lower viscosity and higher conductivity than AILs [114]. In recent years, the use of PILs in electrodeposition has been increasingly studied. As shown for instance in the case of zinc electrodeposition in 1-methylimidazolium trifluoromethylsulfonate ([MIm]TfO) [115], nickel electrodeposition in different PILs such as 2-methylimidazolium lactate ([Hmim][lactate]), 1-ethylimidazolium lactate ([Heim][lactate]), 1-butylimidazolium lactate ([Hbim][lactate]), 2-methylimidazolium glycolate ([Hmim][glycolate]), 1-ethylimidazolium glycolate ([Heim][glycolate]), 1-butylimidazolium glycolate ([Hbim][glycolate]) [116], and triethylammonium trifluoroacetate ([TEA][TFA]) [117]. However, most of these studies focus on single metal electrodeposition and further work is required to explore the capabilities of PILs as electrolytes for alloy deposition.

1.6. Nanoporous alloys electrocatalysts through dealloying

As discussed before, the specific surface area is one of the most important parameters for the electrocatalysts. The nanoporous alloys show high specific surface area due to the average distributed holes on the surface. Therefore, it shows properties as nano materials and strong potential in catalyst application.

The most common way for the preparation of nanoporous alloys is dealloying, including chemical dealloying and electrochemical dealloying. Selected elements may dissolve due to the potential difference of various elements, and the remain elements stay on surface and rebuild through diffusion. During the dealloying process, free atoms form a new structure on the surface by diffusion, which modifies the distribution of surface element and morphology[118, 119]. This reorganization of atoms is one of the reasons for the formation of the nanoporous structure. In chemical dealloying, the alloys are immersed in the liquid chemical, usually an acid or base. Selected elements dissolve according to different parameters, such as pH value, time, and temperature. Li et al. prepared nanoporous Ag by dealloying the precursor, amorphous Ag-Mg-Ga alloy, in HCl solution, as shown in Figure 1.14 [120]. First, the rapid dissolution of Mg and Ca atoms from the matrix into the HCl solution leads to the appearance of surface vacancies. Then, Ag atoms accumulate at the interface between matrix and solution, forming an Ag nanocluster, leading to a decrease in surface energy. Chen et al. prepared 3D nanoporous Cu-Ti alloys in two steps, dissolving Al in 6 M KOH and dissolving Ti in 0.05 M H_2SO_4, and they show a lower overpotential value for HER than that obtained with Pt/C [121].

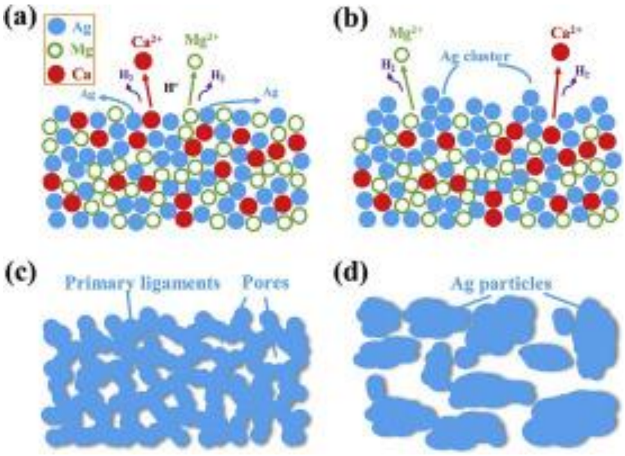

Figure 1.14 Preparation of nanoporous silver [120].

Compared with chemical dealloying, it is more precise to control the electrochemical dealloying process at given currents or potentials. The potentiostatic dealloying can control the dealloying potential easily. Chen et al. prepared nanoporous Co_2P in 0.5 M H_2SO_4 solution with a potential of 0.05 V for a controlled time of 5000 s [122]. The nanoporous Co_2P has a specific surface area of 40 m^2g^{-1}, shown an overpotential of -60 mV. The parameters of electrochemical dealloying can change the morphologies and electrocatalytic properties. Wang et al. prepared the $PtCu_3$ electrocatalysts by electrochemical dealloying by cyclic voltammetry for potential range from 0.05 V to 1.0 V in 5000 cycles at a rate of 1 V s^{-1} [123]. By increasing cycle times, the shape of nanoparticles changes from ball to cube, which is due to the rapid formation of Pt during the fast potential scan.

In recent years, the nanoporous alloys have been investigated with great interest as electrocatalysts for water splitting. However, it can be concluded from the literature that the morphologies and structure of nanoporous alloys can be adjusted by various parameters, such as time, temperature, matrix, alloy composition, potential in the electrochemical dealloying, of the dealloying process. A large number of studies have yet to be carried out.

1.7. Main works in this thesis

In light of the aforementioned, there is a need high-performance, low-cost electrocatalysts for water splitting. In this thesis, the main works focus on the preparation of Ni/Co-based alloys in ionic liquids and deep eutectic solvents, and the preparation of nanoporous Ni/Co alloys by dealloying, and their properties in electrocatalytic HER. The logical progression of the study is illustrated in Figure 1.15 and the work summaries are listed below.

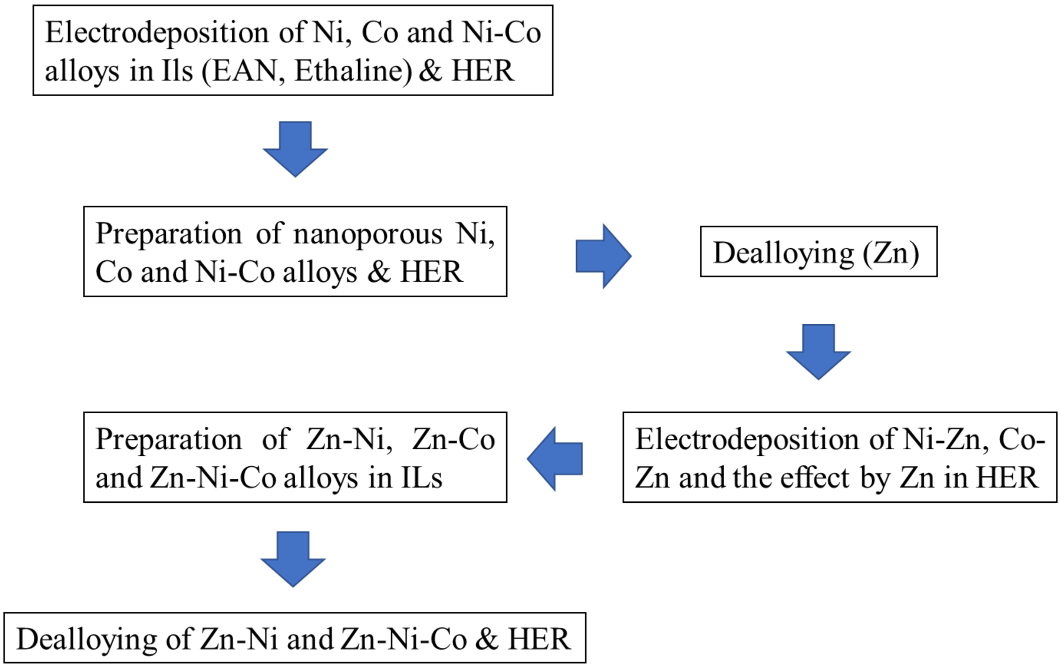

Figure 1.15 The study path of the work in this thesis.

(1) The Ni and Ni-Co alloys are prepared by electrodeposition in DES, ethaline and menthol-based DES, on Cu form. The effects of temperatures and time on the morphologies, compositions and the properties in HER have been studied.

(2) The electrodeposition of amorphous and nanocrystalline Ni-Co alloys in ethylammonium nitrate (EAN), a protic ionic liquid, is studied. The use of EAN in electrodeposition of Ni/Co-based materials is still scarce [124-126]. The electrochemical behavior of Co and Ni ions in EAN have first been studied by voltammetry. Amorphous and nanocrystalline Ni-Co alloy coatings on FTO glass and Cu foil with different thicknesses and Co contents have been prepared by electrodeposition and characterized using different techniques. These amorphous Ni-Co alloys were compared with the electrochemical behavior of nanocrystalline Ni-Co alloys.

(3) The electrodeposition of Ni-Zn and Co-Zn alloys in ethaline on Cu foil has been studied. The effect of the metal concentration, electrodeposition time, temperatures and potentials on the morphologies, content of alloys and properties of HER for water splitting have been studied.

(4) The preparations of Zn-Ni-Cu and Zn-Ni-Co-Cu alloys by electrodeposition in ethaline and EAN on Cu foil and heat treatment have been studied in this part. The nanoporous Ni/Cu-based alloys with different concentrations and morphologies have been prepared from chemical dealloying and electrochemical dealloying with different parameters, such as concentrations, potential and time of treatment. The properties of HER with different alloys after dealloying have been studied and discussed in this part.

Chapter 2 Methods and technologies

2.1. Synthesis of the ionic liquids

2.1.1. Synthesis of EAN

Ethylammonium nitrate (EAN) was prepared by mixing concentrated aqueous solutions of ethylamine and nitric acid with a molar ratio of 1:1. During this process, the nitric acid solution (68 wt.% in water) was added into ethylamine aqueous solution (70 wt.% in water) drop by drop under stirring at a controlled temperature (T = -10 °C) as shown on Figure 2.1. The purification of EAN was performed by lyophilization (Freeze Dryer -86 ℃, OPERON CO., LTD.) in order to get EAN with a low water content (below 100 ppm - vide infra).

The salts used for electrochemistry were dried by heating and lyophilization in order to reduce the amount of water in the electrolytes. Solutions of 0.5 M $NiCl_2$, 0.5 M $CoCl_2$, 0.25 M $NiCl_2$ + 0.25 M $CoCl_2$ and 0.375 M $CoCl_2$ + 0.125 M $NiCl_2$ in EAN were prepared by mixing the different compounds under stirring at 70 °C for 24 h after weighing.

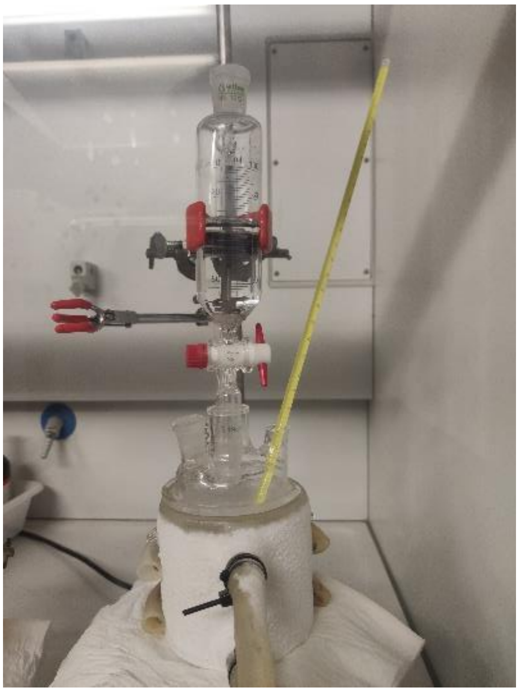

Figure 2.1 The synthesis of EAN.

2.1.2. Synthesis of DES

Ethaline was prepared by mixing choline chloride and ethylene glycol with a molar ratio of 1:2

by stirring the mixture at a temperature of 60 °C for 3 h to get homogeneous and transparent liquid. The solutions of ethaline with 0.5 M $ZnCl_2$, 0.2 M/0.5 M $NiCl_2$, 0.5 M $CoCl_2$, 0.2 M $NiCl_2$ + 0.3 M $CoCl_2$, 0.15 M $NiCl_2$ + 0.35 M $ZnCl_2$, 0.5 M $NiCl_2$ + 0.25 M $ZnCl_2$, 0.5 M $NiCl_2$ + 0.5 M $ZnCl_2$, 0.2 M $NiCl_2$ + 0.4 M $ZnCl_2$, 0.15 M $CoCl_2$ + 0.35 M $ZnCl_2$, 0.4 M $CoCl_2$ + 0.2 M $ZnCl_2$, 0.4 M $CoCl_2$ + 0.4 M $ZnCl_2$, 0.35 M $ZnCl_2$ + 0.15 M $NiCl_2$ + 0.02 M $CoCl_2$ were prepared by mixing the different salts and ethaline with stirring at 60 °C for 24 h.

The menthol-based DES was prepared by mixing menthol, ethanolamine and acetic acid with a molar ratio of 1:2:4, with a stirring at 80 °C for 30 min and then slowly cooled down until get a homogeneous transparent liquid [127]. The solution of menthol-based DES with 0.2 M $NiCl_2$ was prepared at 60 °C with stirring for 24 h.

2.2. Experiment methods

2.2.1. Electrochemical measurements

All electrochemical measurements were performed using a three-electrode cell, with a working electrode, counter and reference electrode, and a GAMRY REF600+ potentiostat with flowing argon and temperature controlled by a cryothermostat. Various electrochemical measurements were applied to the different parts.

(1) Open circuit potential (OCP) measurement

Open circuit potential is the potential measured between the working electrode (the metallic surface to be studied) and the environment, with respect to a reference electrode, which will be placed in the electrolyte close to the working electrode [128]. With a reversible electrode system, the OCP can be referred to as the equilibrium electrode potential. Otherwise, it can be called the rest potential, or the corrosion potential, depending on the system being studied [129]. It is helpful in corrosion study measurement and comparing the reducibility of different materials surface [130]. In this thesis, the OCP measurement was used to determine the onset potential of the electrochemical reactions.

(2) Cyclic voltammetry

Cyclic voltammetry (CV) is a powerful and popular electrochemical technique commonly employed to investigate the reduction and oxidation processes of electroactive species [131]. The CV curve shown in Figure 2.2H provides information on the relationship current and potential variations. The electrochemical reaction of ferrocenium ($[Fe(Cp)_2]^+$) (Cp = cyclopentadienyl), abbreviated as Fc^+, to ferrocene $[Fe(Cp)_2]$, abbreviated as Fc, is the most widely used to explain a redox reaction by CV. In the electrochemical process, the reaction is as follows,

$$Fc^+ + e^- \rightleftharpoons Fc \qquad \text{(Eq. 22)}$$

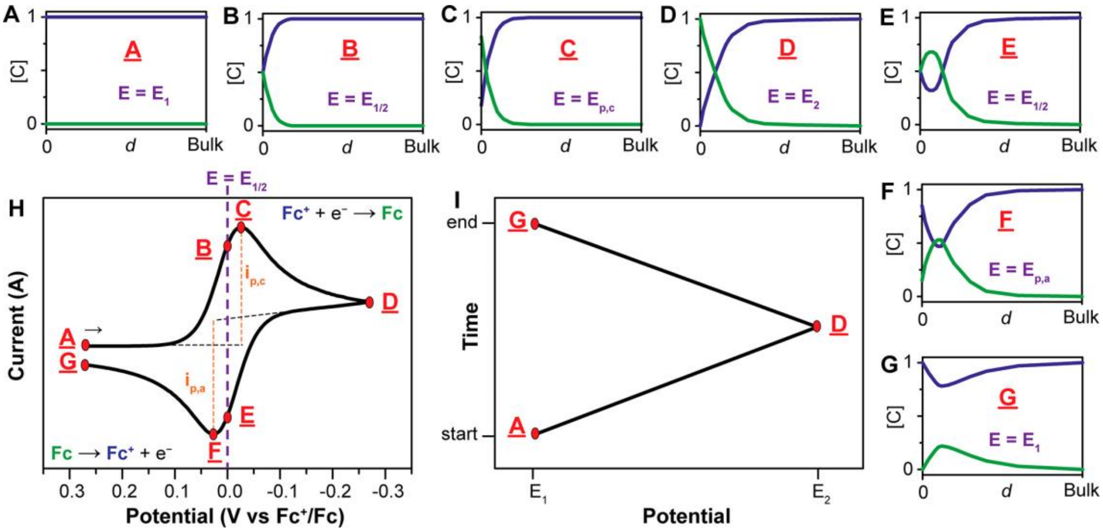

Figure 2.2 (A – G): The concentrations (in mM) of Fc^+ (purple) and Fc (green) change with their distance from the electrode (d) during the potential scan. (H) Voltammogram of the reversible redox reaction between 1 mM Fc^+ and Fc, at a scan rate of 100 mV · s^{-1}, with the applied potential shown in (I) [131].

The applied potential starts at E_1 and increases up to E_2. Variations in species concentrations as a function of distance from the electrode are shown in Figures 2.2A to 2.2D, which is known as the anodic trace (from a lower to a higher potential), obtained from this forward scan with a scan rate of 100 $mV{\cdot}s^{-1}$ ($\geq$ 20 $mV{\cdot}s^{-1}$). The oxidation reaction occurs during this forward scan. As shown in Figure 2.2I, the sweep direction is reversed after the potential E_2, from point D to G, and corresponds to the cathodic trace. The reduction reaction takes place during this sweep. The potential is linearly changing, as shown in Figure 2.2I, corresponding to the process illustrated in Figure 2.2H [131]. The exchange between Fc^+ and Fc is a reversible process, which is visualized by the two peaks. The potential E, standard potential (E_0) and oxidized/reduced (Ox/Red) analyte can be connected by Nernst equation during the electrochemical process according to Equation 23,

$$E = E^0 + \frac{RT}{nF}\ln\frac{(Ox)}{(Red)} = E^0 + 2.3026\frac{RT}{nF}\log_{10}\frac{(Ox)}{(Red)} \qquad \text{(Eq. 23)}$$

where F is the Faraday's constant (96495 C mol^{-1}), R is the universal (or perfect) gas constant (8.314 J K^{-1} mol^{-1}), n is the number of electrons and T is the temperature (in K). Using this equation, we can obtain the relationship between the ion concentration near the electrode and the potential value during the electrochemical reaction. The electrochemical reversibility refers to the electron transfer between the electrode and the analyte. If the reaction is not reversible, the electron transfer will not occur immediately. Therefore, a higher negative or positive potential is required to obtain the reduction or oxidation reaction, which means a higher value of the peak difference (ΔEp) [131]. Normally, we can also judge the reversibility of the reaction by checking whether the integral values of the two peaks are the same.

In this thesis, the electrochemical behavior of different ions in IL was obtained by cyclic voltammetry on a glassy carbon (GC) rotating-disk-electrode (RDE, Pine Research Instrumentation) with a surface area of 0.2 cm^2. A platinum grid was used as the counter electrode, and the reference electrode consisted of a double junction compartment, in which a silver wire was immersed in the first junction containing a saturated silver nitrate ($AgNO_3$) solution in IL with a sintered glass at the bottom. The second junction, containing pure IL, was separated from the first junction in order to prevent ion diffusion from the reference compartment to the studied electrolyte. All the cyclic voltammetry measurements of the solutes in ILs are started from the open circuit point, and scanned first to the cathodic domain, then to the anodic part.

(3) Linear sweep voltammetry (LSV)

In LSV, a linear potential variation is applied between the working electrode and the reference electrode, with a low scan rate (1 mV·s^{-1}). The current flowing between the working electrode and the counter-electrode is recorded and the current versus time (or potential) corresponds to the LSV curve. As shown in Figure 2.3, in the case of faradaic reaction, the current increases with the potential until a maximum value is reached, designated by i_p corresponding to the highest peak current. For reversible redox couple under dynamic state, the relationship between this peak current and the concentration of electroactive species is given by Equations 24 and 25 in CV curve (Randles-Sevcik equation) [132],

$$i_p = 0.4463\left[\frac{F^3}{RT}\right]^{1/2} n^{3/2} A D_o^{1/2} C_o^* v^{1/2} \qquad \text{(Eq. 24)}$$

At room temperature (25 °C), it can be written as

$$i_p = (2.69 \times 10^5) n^{3/2} A D_o^{1/2} C_o^* v^{1/2} \qquad \text{(Eq. 25)}$$

where A is the real working electrode area, D_0 is the diffusion coefficient of the electroactive species in the solution, ν is the scan rate, C_0 is the initial concentration of the analyte. The peak current of the electrode reaction is proportional to the concentration of the analyte for reversible redox couple.

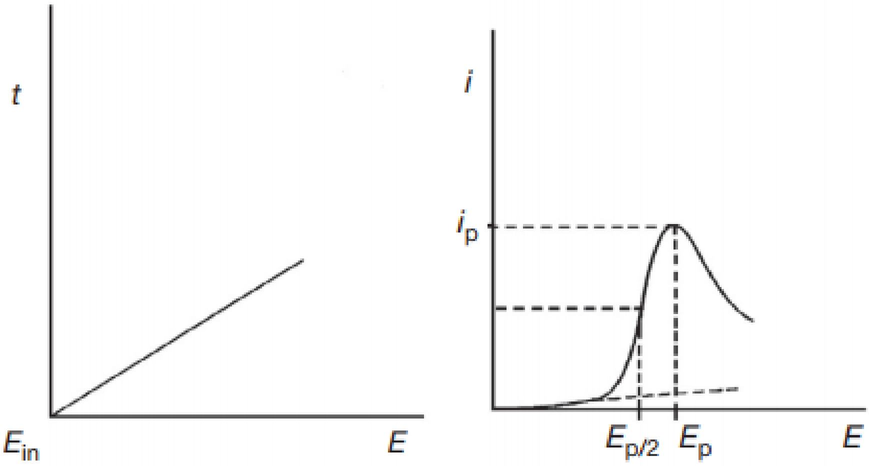

Figure 2.3 Potential variation with time (left) and current-potential curve in LSV (right) [132].

In LSV curve, the current reaches a maximum value by the change of potential, and then stabilizes with a low scan rate. It can show a stable line with a stationary state by RDE or microelectrodes. The relationship can be described by Levich or Koutecky-Levich equation (Equation 26 and 27), where ω is the angular velocity of the electrode rotation.

$$i = 0.62nFAD_0^{2/3}\omega^{1/2}v^{-1/6}C_o^0 \qquad \text{(Eq. 26)}$$

$$\frac{1}{i} = \frac{1}{i_k} + \frac{1}{0.62nFAD_0^{2/3}\omega^{1/2}v^{-1/6}C_o^*} \qquad \text{(Eq. 27)}$$

2.2.2. Electrodeposition

In this thesis, the alloys were prepared by electrodeposition using a chronoamperometric method. Chronoamperometry is a time-dependent technique, in which a potential is applied to the working electrode. The resulting electrode current fluctuates according to the diffusion of the analyte from the bulk solution to the sensor surface [133]. Consequently, this technique can be used to determine the current variation with time on the electrode controlled by the diffusion process. By integrating the area of the chronoamperometry curves, the amount of exchanged electrons and therefore the amount of alloy deposited can be obtained.

Electrodepositions of electrocatalytic materials were carried out on FTO glasses, Copper foams or Copper foils. Prior to use, the FTO glasses were washed in acetone, ethanol, and deionized water, for 15 minutes, respectively. Cu foams and Cu foils were washed in acetone and HNO_3, for 10 minutes, respectively. Cu foils were polished with 2400 grit sandpaper before electrodeposition to remove the oxide and obtain a smooth, clean surface.

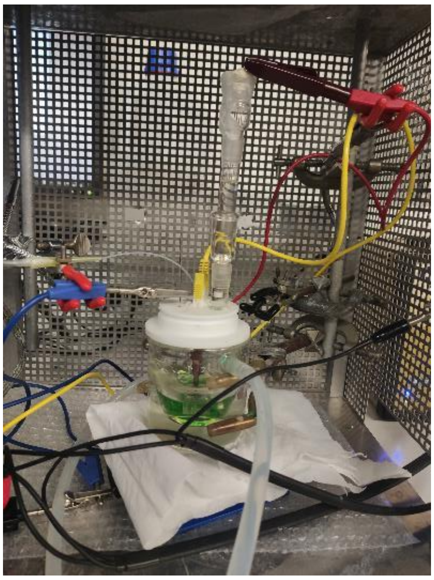

Figure 2.4 Electrodeposition setup used for ethaline.

A three-electrode electrochemical cell is used for electrodeposition, with a temperature controlled by a cryothermostat, as shown in Figure 2.4. A 15 mm diameter nickel ring, cobalt ring and zinc ring were used as a counter electrode in Ni ion-based, Co ion-based and Zn ion-based electrolyte, respectively. The area of FTO glass working electrode is 0.5 cm × 0.5 cm. The area of Cu foil and Cu form working electrode is 2 × 1.5 cm × 2 cm, and 2 × 1 cm × 0.5

cm, respectively. The reference electrode consisted of a double junction compartment as described in section 2.3.1. Before electrochemical deposition, argon was bubbled in the electrolyte for 15 minutes.

2.2.3. Physiochemical properties measurement

The water content in the freshly prepared solvent was titrated using a Karl–Fischer coulometer (C20, Mettler Toledo) in a glove-box (Concept GP, Jacomex).

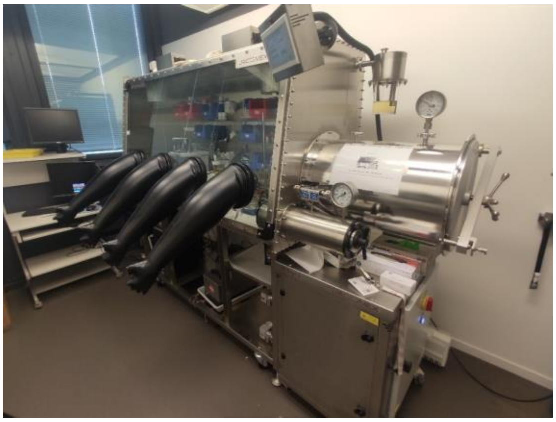

Figure 2.5 The glove box.

The chemical titration is as follows,

$$H_2O + SO_2 + I_2 + CH_3OH + 3\ RN \rightarrow [RNH]SO_4CH_3 + 2[RNH]I \qquad \text{(Eq. 28)}$$

$$I_2 = 2I^- - 2e \qquad \text{(Eq. 29)}$$

where RN is the pyridine content in the Karl Fisher reactant solution. This reaction is reversible. When the solution containing trace of water is added into the Karl Fisher electrolyte with I_2, I_2 starts to react with H_2O. Throughout the reaction, the electron exchange will be calculated from current variations until the end of the reaction.

The density and viscosity of the solutions were measured with a densimeter (DSA 5000M, Anton Paar) and a microviscosimeter (Lovis 2000M, Anton Paar), respectively. The conductivity and pH values of the solutions were measured with a conductimeter (CDM230, Radiometer Analytical) and a pH-meter (PHM250, Radiometer Analytical), respectively. Since we made only few measures (typically two or three different measures), error bars will not be shown in the data analysis.

Figure 2.6 The microviscosimeter (left) and densimeter (right).

2.2.4. Electrocatalysis measurement

A three-electrode cell was used for the electrocatalysis experiments. The electrocatalyst was used as working electrode, a platinum grid was used as counter electrode, the saturated calomel electrode (SCE) and Hg/HgO electrode were used as reference electrodes, respectively. The potential is converted to the reversible hydrogen electrode using Equations 30 and 31. The temperature of the electrolyte was maintained at 25 °C with a cryothermostatic bath. 1.0 M KOH solution was used as electrolyte. Argon was bubbled in the electrolyte 15 minutes before experiment and an Ar flux was maintained above the cell for all the duration of the measurement.

$$E\ (vs.\ \mathrm{RHE}) = E\ (vs.\ \mathrm{Hg/HgO}) + 0.0591\ \mathrm{pH} + 0.095 \qquad \text{(Eq. 30)}$$

$$E\ (vs.\ \mathrm{RHE}) = E\ (vs.\ \mathrm{SCE}) + 0.0591\ \mathrm{pH} + 0.2412 \qquad \text{(Eq. 31)}$$

As discussed in chapter 1.3.1, onset potential, overpotential, Tafel slope, effective active surface area (ECSA), stability are the main properties in electrocatalysis. electrochemical impedance measurements were performed for the stable electrocatalysts.

The onset potential is the overpotential indicated on the current-potential curves, corresponding to a current density of 1 mA·cm^{-2}. The overpotential for HER is defined for a current density of 10 mA·cm^{-2}, with a unit of mV or V. In order to note the value more clearly in LSV image, in this thesis, the overpotential for HER will be defined as HER potential, which has the same value as HER overpotential in the reaction, with the unit of mV/RHE. Tafel slopes are obtained by converting the polarization curves, which are plotted as overpotential versus the logarithm of the current density. Then the linear portions at low overpotential is fitted to the Tafel equation

($\eta = b \log(j) + a$), where η represents overpotential, j is the current density, and b corresponds to the Tafel slope. The effective active surface area (ECSA) of the samples was evaluated by measuring the interfacial capacitance (C^{σ}) using cyclic voltammetry with various scan rates (20 - 500 $mV \cdot s^{-1}$) [125]. The stability is determined by the overpotential through LSV after a few cycles of HER reactions. For the more stable electrocatalysts, the electrochemical impedance spectroscopy (EIS) is conducted to probe the HER kinetics under the operating conditions and the interface reactions at overpotential [20]. The charge transfer resistance (R_{ct}) is related to the interface charge-transfer process of the electrode and can be obtained from the Nyquist plot by the diameter of the semicircles in the high-frequency region [20]. The EIS is measured at frequency between 10^5 to 0.1 Hz.

2.3. Dealloying

In this thesis, two routes of dealloying are considered: chemical dealloying and electrochemical dealloying. For chemical dealloying, the solutions are 1 M KOH, 0.01 M HNO_3, EAN + 0.01 CH_3COOH (acetic acid), EAN + 0.025 M PTSA (para-toluenesulfonic acid). For electrochemical dealloying, the process was performed in 1 M KOH at various potential values. The temperature is changed from 25 to 40 °C. After the dealloying, all of the samples were washed by flowing ethanol.

2.4. Characterizations

Different characterizations are conducted to learn the structures and morphologies of the electrocatalyst in different scales.

X-ray diffraction (XRD) is a simple and direct way of learning about the grain structure of the materials. It uses the X-ray diffraction phenomenon in the crystal to obtain the X-ray signal or information characteristics after the diffraction in the crystal, and gets the diffraction pattern. Each crystal possesses a distinct atomic arrangement, resulting in a unique diffraction pattern that can be used for phase analysis. The distribution of diffraction lines within the pattern is influenced by the size, shape, and orientation of the crystal's unit cell. Furthermore, the intensity of the diffraction lines is determined by the types of atoms present and their respective positions within the unit cell. Bragg's law is the basic condition for X-ray diffraction in the crystal, as shown in Equation 32,

$$2d\sin\theta = n\lambda \tag{Eq. 32}$$

where θ is the incidence angle, d is the interplanar distance, n is the diffraction order, λ is the wavelength of the incident ray, and 2θ is the diffraction angle.

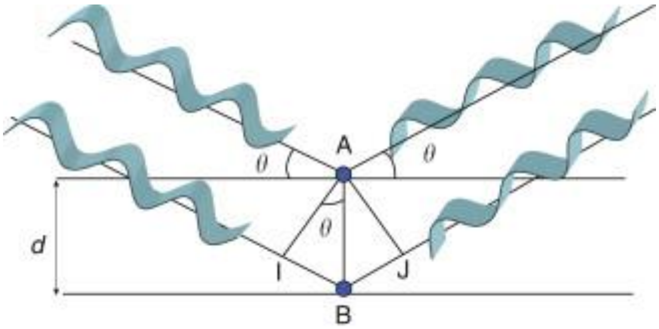

Figure 2.7 Bragg's law scheme [134].

The crystal structures of the electrodeposits were characterized by XRD, D8 ADVANCE BRUKER, with a scan rate of 3 degree·min^{-1} from 20° to 80° using the Cu Kα radiation. The Scherrer equation is applied to calculate the average grain size, which is presented in Equation 33,

$$\tau = \frac{K\lambda}{\beta\cos\theta} \tag{Eq. 33}$$

where τ is the average size of grains, K is the dimensionless shape factor, λ is the X-ray wavelength, β is the line broadening at half the maximum intensity (FWHM), θ is the incidence angle. For the electrocatalysts, the phases must first be examined and characterized, as the crystalline structure and nature of the phases (amorphous/crystalline) will have an impact on their HER performance.

Scanning electron microscopy is used for morphological characterization of materials. The scanning electron microscope (SEM) is based on the principle of using a finely focused high-energy electron beam to scan the sample, thereby obtaining a variety of physical information. By detecting, amplifying, and displaying this information, the SEM enables us to observe of surface topography of the sample under investigation. Morphology is determined by striking the material surface with an incident electron beam characterized by its energy, intensity, and spot diameter. Secondary electrons (SE) and backscattered electrons (BSE) are the main electrons tested after being reflected by the surface. BSE refer to incident electrons that undergo elastic scattering at angles greater than 90°. The ionization of sample atoms during the excitation of sample electrons results in the generation of secondary electrons. Besides the signals used for image formation, the interaction of an electron beam with a sample produce a variety of other signals, including the emission of characteristic X-rays, Auger electrons, and cathodoluminescence. [135]

Energy dispersive X-ray spectroscopy (EDS) is a technique for collecting and measuring the energy and intensity of X-rays emitted by a sample. The energy distribution of these X-rays provides information on the atomic characteristics of specific elements present in the sample. By analyzing the energy dispersive X-ray spectrum, the elemental composition of the sample can be determined. SEM and EDS are also important for characterizing electrocatalysts. The morphology of the material surface will affect the specific surface area and therefore make a difference in performance. By analyzing the distribution of elements, it is possible to establish a link between different combinations of elements and performance.

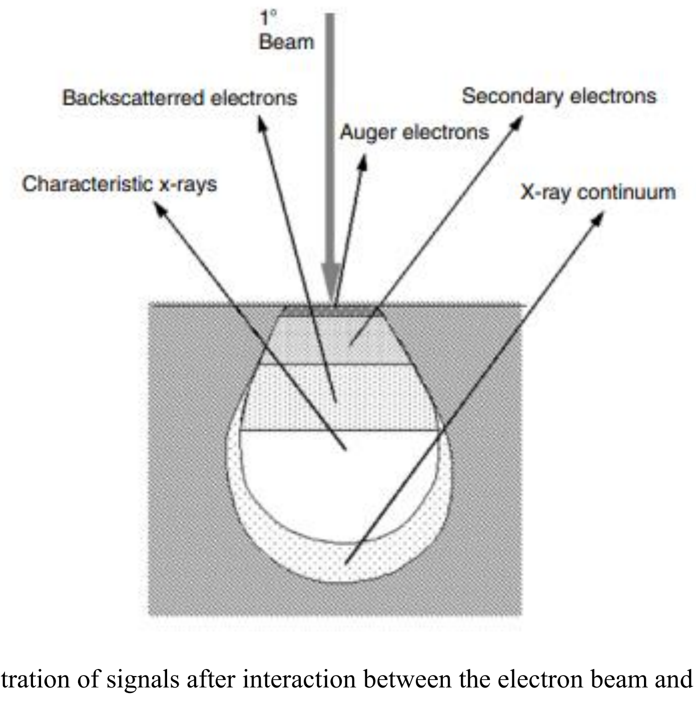

Figure 2.8 Illustration of signals after interaction between the electron beam and the surface [135].

The surface morphologies of pure Ni electrodeposit on Cu described in chapter 4 were obtained by SEM, ULTRA 55 ZEISS, equipped with energy-dispersive X-ray spectroscopy EDX Bruker QUANTAX. The morphologies of the others were observed by scanning electron microscopy (SU-70 HITACHI) with a potential of 5 kV and an energy dispersive X-ray spectroscopy with a potential of 15 kV (Ultim Max, Oxford Instruments), as shown in Figure 2.9.

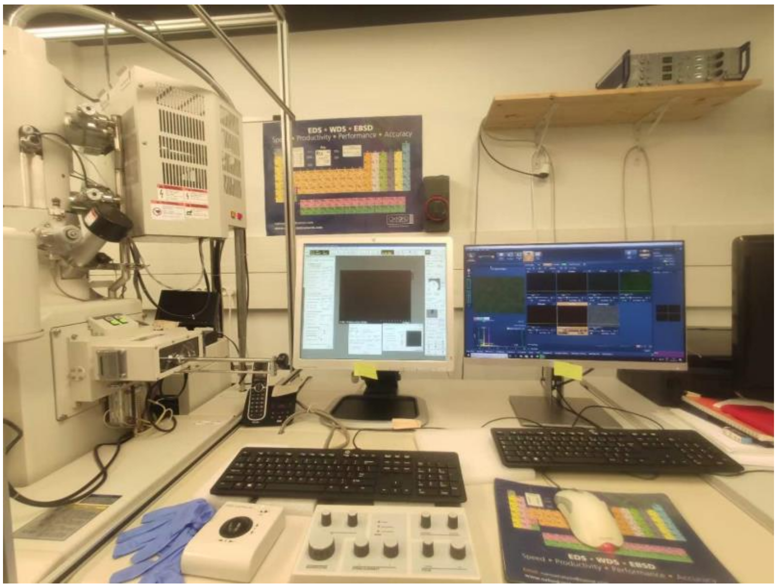

Figure 2.9 The working area of SEM.

The transmission electron microscope operates by projecting an accelerated and focused beam of electrons onto a thin sample. As the electrons interact with the atoms in the sample, they undergo scattering, resulting in a change in their direction. This direction change is translated into an angular scattering pattern. The scattered electrons are then collected and used to form an image of the sample's internal structure. Analysis of the scattering patterns provides information on the atomic arrangement, crystal structure, and other properties of the sample. The amount of electrons passing through the sample varies according to the thickness of different parts of the materials. As a result, different parts of the sample produce different images. Diffraction patterns in a transmission electron microscope (TEM) are created by adjusting magnetic lenses that control the trajectory of electrons passing through a sample crystal, forming a pattern of spots or rings on the detector. Studying the diffraction pattern and its associated symmetry provides information about the crystal structure and space group of the sample, enabling a comprehensive analysis of its atomic arrangement and crystallographic properties. In this thesis, TEM was used to assist in verifying the phase and grain size determined by XRD.

The grain size and structures of the alloys were determined by transmission electron microscope (TEM, JEM 2011, JEOL) with a potential of 200 kV. The alloys were scratched and separated on the Cu mesh using ethanol.

Raman spectroscopy is a technique based on the interaction between molecules and light. The information obtained in the Raman spectrum comes from the light scattering, which is different from infrared spectra, which are absorption spectra. Thanks to the different frequencies of photons scattered by the sample, we can obtain different bonding spectra between atoms and information on the vibrations of different groups in molecules. In this thesis, Raman spectroscopy was carried out on Kaiser Optical System, Raman Analyzer RXN1 microprobe equipped with a 785 nm laser diode.

X-ray Photoelectron Spectroscopy (XPS) is a technique used to measure the energy distribution of photoelectrons and Auger electrons emitted by the surface of a sample when it is irradiated with X-ray photons. In XPS, X-ray photons are generated in the source and interact directly with the atoms on the surface over 5 to 10 nm below the surface. Photoelectrons are then ejected from the atom. These photoelectrons are related to the types or chemical state of the atoms. By calculating the kinetic energies of photoelectrons, the binding energies of atoms can be obtained, which are the main parameters for studying the chemical state of atoms. The elemental composition of different electrocatalysts may be similar, but the valence state and bonding of each element may be different, which can have different effects on HER performance.

XPS analyses were performed using an Omicron Argus X-ray photoelectron spectrometer, equipped with a monochromated AlKα radiation source ($h\nu = 1486.6$ eV) and a 280 W electron beam power. The emission of photoelectrons from the sample was analyzed at a takeoff angle of 45° under ultra-high vacuum conditions ($\leq 10^{-9}$ mBar). Spectra were carried out with a 100eV pass energy for the survey scan and 20 eV pass energy for the different element regions. Element peak intensities were corrected by Scofield factors. The peak areas were determined after subtraction of a U 2 Tougaard background. The spectra were fitted using Casa XPS v.2.3.25 software (Casa Software Ltd, U.K.) and applying a Gaussian/Lorentzian ratio g/l equal to 70/30 for deconvolution. All XPS samples were transferred directly from the glove box to the XPS instrument after the sample has been prepared, and measured directly without Ar ion sputtering, in order to learn the real surface state.

Chapter 3 Electrodeposition of Ni-Co alloys in EAN and their properties with respect to HER

Through the bibliography in Chapter 1, we have shown that the effect of different elements in the alloys with respect to the HER still need more investigation. The combination of Ni and Co in HER performance is not clear yet. In addition, to our best of knowledge, there is no research about the electrodeposition of alloys in protic ionic liquid, such as the EAN. Only a few electrodepositions have been performed in EAN are results are summarized in Table 3.1. Most of them concern a single metal electrodeposition, whereas the others are metal oxide electrodeposition. Therefore, it is necessary and valuable to learn about the co-electrodeposition od bi-metallic material such as Ni and Co alloys in the neat protic ionic liquid, EAN.

Figure 3.1 Formula of EAN and the deposition of the Ni-Co alloy on FTO glass and Cu foil.

In this chapter, the study of the electrodeposition of Ni-Co alloys on FTO glasses (0.5 cm × 0.75 cm) and Cu foil (0.75 cm × 1.5 cm - on both sides of the sample) will be discussed. Amorphous and nanocrystalline Ni-Co alloys have been deposited in neat protic ionic liquid, EAN, varying different electrodeposition parameters: time, temperature, and electrode potential. All alloys electroplating were performed in the glove box to avoid oxygen contamination, but also to limit water ingress. The addition of Co in Ni-based alloys can promote the properties of HER. In addition, the amorphous alloys also show better properties for the HER than the crystalline Ni-Co alloys with similar concentration, thus providing a new route to prepared nanocrystalline and amorphous Ni-based alloys for HER electrocatalysis.

Table 3.1 Electrodeposition of various metals in EAN reported in the literature.

Deposit	Salt	Temperature	Method	Potential/Current
Co_xO_y [136]	$Co(NO_3)_2$	RT	Chronoamperometry	−0.95 V vs. $Fc^{0/+}$
MnO_x [137]	$Mn(CH_3COO)_2$	120 °C	Chronopotentiometry	200 $\mu A \cdot cm^{-2}$
Ag [114]	$AgNO_3$, AgBF	RT	Chronoamperometry	-0.2 V vs Ag/Ag^+
Ni [124]	$Ni(NO_3)_2$	-	Chronoamperometry	−4.5 V vs. $Fc^{0/+}$
Pd [138]	$PdCl_2$	RT	Chronoamperometry	-1.25 V vs Ag/Ag^+
Cu [139]	$CuCl_2$	RT	Chronoamperometry	0.03 V vs. $Fc^{0/+}$
MnO_x [140]	$Mn(ClO_4)_2 \cdot 6\,H_2O$	RT	Chronopotentiometry	200 $\mu A \cdot cm^{-2}$

3.1. Physicochemical properties of EAN electrolytes

In order to adjust the electrodeposition parameters, the physicochemical properties (viscosity, density, pH, and conductivity) of different electrolytes used in this chapter are presented in Table 0.1 as a function of temperature. For each solution with different ion concentrations, the density, the viscosity and the pH values decrease whereas the conductivity increases with increasing temperature, shown in Figure 3.2. Due to the slight swelling of the IL, the density decreases of EAN solutions at the same temperature. Similarly, the viscosity values of solution are increased with different levels. The viscosity of EAN containing 0.5 M $CoCl_2$ is 37.2 mPa·s at 25°C, which is a bit higher than that of the pure EAN, 36.4 mPa·s, but significantly lower than the viscosity of EAN containing $NiCl_2$ (55.0 mPa·s), shown in Figure 3.2b. The conductivity of all solutions increases with the addition of different salts. The conductivity of EAN containing 0.5 M $CoCl_2$ is very close to that of pure EAN over the whole temperature range and is higher than that of EAN containing $NiCl_2$ (Table 0.1, in the annexes). The pH of pure EAN at 25°C is 5.6, which is akin to the value in other work [141]. Indeed, the small amount of water (a few hundred ppm) after dissolving ions in the IL is due to the adsorbed water in the salts, which is difficult to remove. This little quantity of water will have little influence on the preparation of alloys during electroplating. We can see that the conductivity and the viscosity are higher when higher temperatures are used. Although the electrodeposition of Ni can be achieved at room temperature, in order to get a better deposition efficiency (*vide infra*), the electrodeposition temperature will be chosen above 60°C in this chapter.

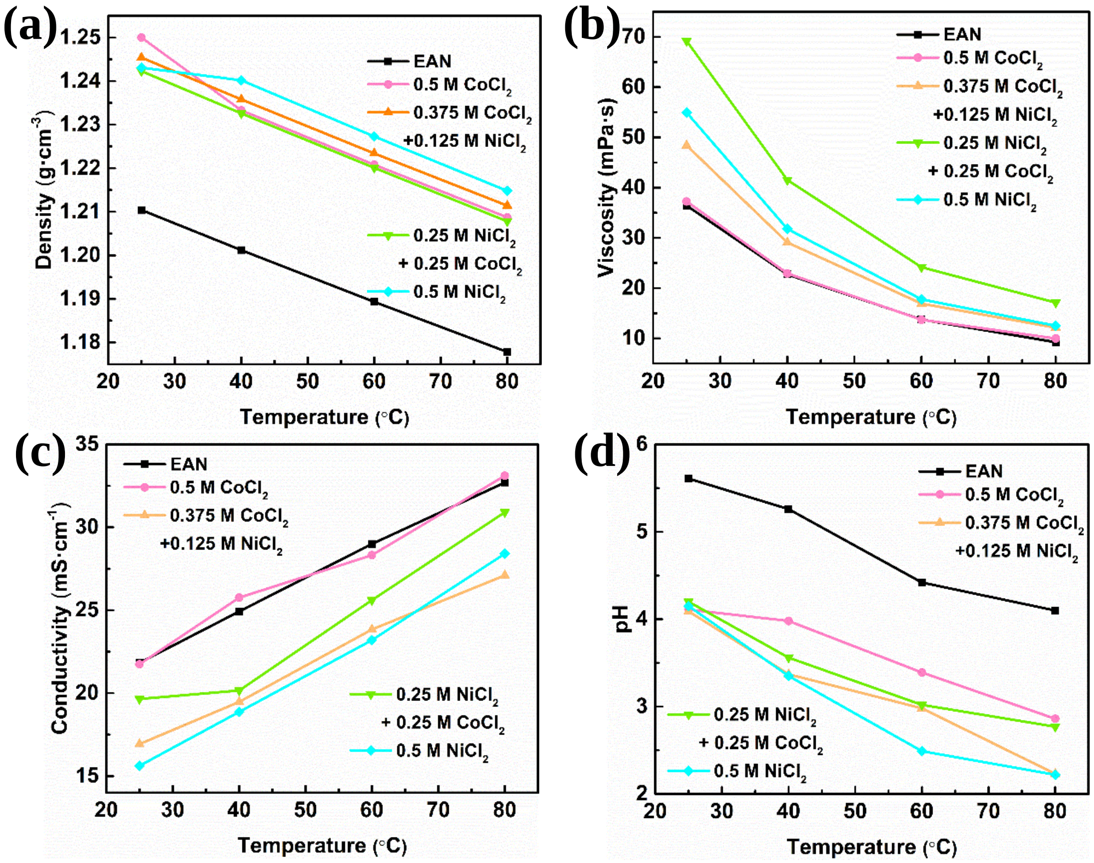

Figure 3.2 Evolution of density, viscosity, conductivity, and pH of EAN with different concentrations of cobalt and Ni salts as a function of the temperature. a) Density; b) Viscosity; c) Conductivity; d) pH.

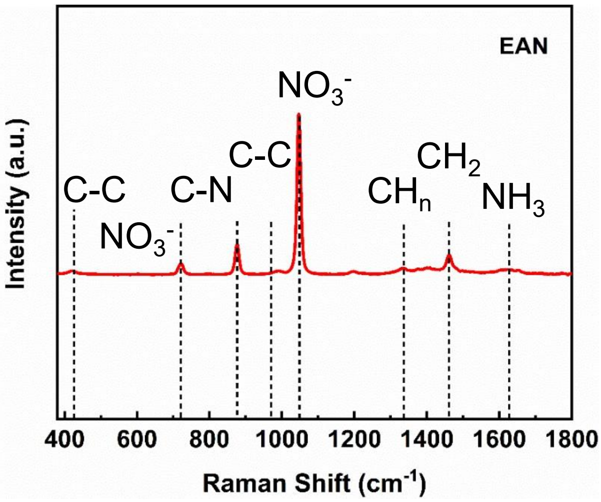

Figure 3.3 Raman spectrum of EAN solution.

Figure 3.3 shows the Raman spectrum of pure EAN. The peak at 420 cm^{-1} is ascribed to C-C bending motions, the peak at 718 cm^{-1} is ascribed to the bending of NO_3^-, and the two peaks at

873 cm^{-1} and 960 cm^{-1} are ascribed to the bending of C-N and C-C stretching, respectively. The most intense peak is at 1044 cm^{-1}, and is ascribed to the symmetric stretching of NO_3^-. The peak at 1200 cm^{-1} is assigned to the rocking motions of CH_n groups. The band at 1330 cm^{-1} derived from the CH_n scissoring motions and the peak at 1450 cm^{-1} are due to the CH_2 and CH_3 bending motions. The peak of 1610 cm^{-1} is referred to the NH_3 scissoring or the rocking motions [142]. Therefore, the EAN is prepared without other impurities bonding and with only a low content of water, which is lower than 100 ppm.

3.2. Electrochemical behaviors of EAN-based electrolyte

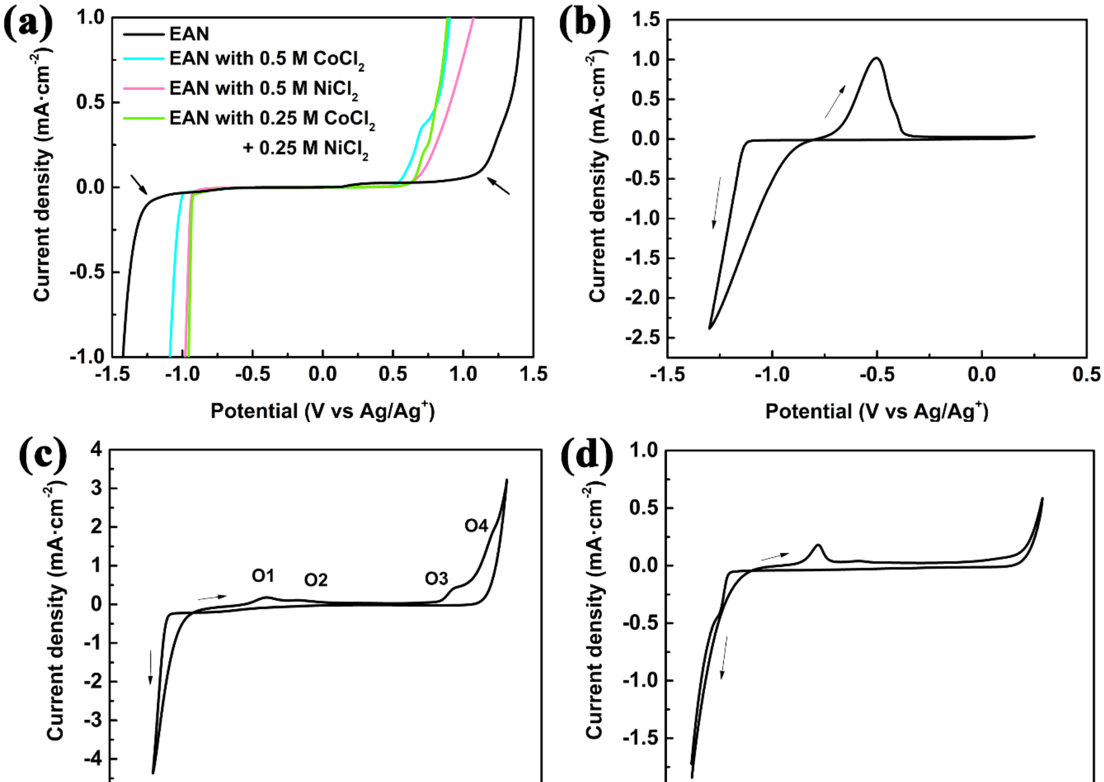

Figure 3.4 Electrochemical characterization of EAN with different ions on glassy carbon RDE at 60 ºC. a) Linear sweep voltammetry curves with or without additional ions performed at 1 mV·s^{-1} and 1000 rpm; and cyclic voltammetry curves, at 50 mV·s^{-1}, in EAN with b) 0.5 M $NiCl_2$, c) 0.5 M $CoCl_2$ and d) 0.25 M $NiCl_2$ + 0.25 M $CoCl_2$.

EAN is a hydrophilic IL, which means that the experiments performed in air atmosphere cannot avoid the participation of water and oxygen, although the water content of pure EAN is only 56 ppm. It is also necessary to study the electrochemical properties of these electrolytes used for electroplating before the preparation of the alloys.

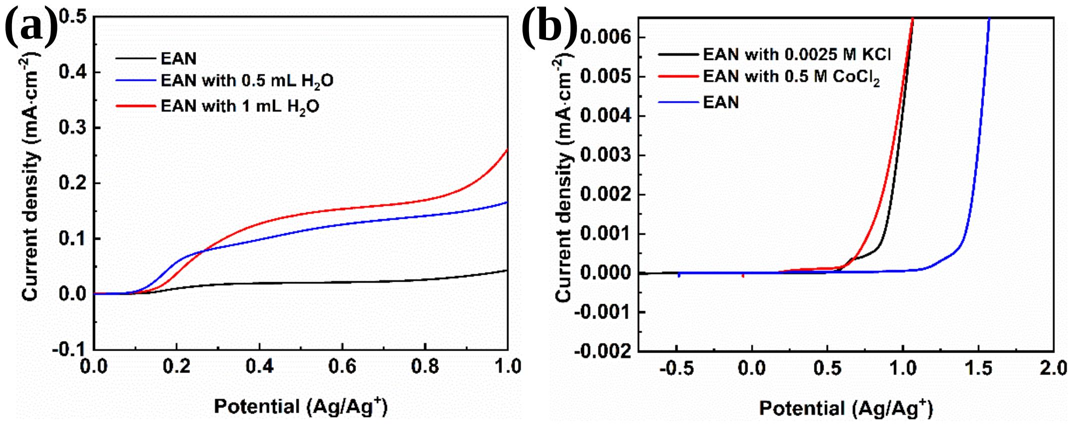

Figure 3.5 a) The LSV curves of glassy carbon in EAN with the addition of water. b) The LSV curves of glassy carbon in EAN with $CoCl_2$ or KCl.

Linear sweep voltammetry and cyclic voltammetry have been used to study the electrochemical characteristics of EAN solutions in this part. Figure 3.4a shows the LSV curves on a glassy carbon (GC) RDE at 1 mV·s^{-1} in pure EAN and for different ion concentrations. The electrochemical window of pure EAN obtained on GC electrode (Figure 3.4a) is about 2.31 V, which was obtained using a cut-off current density value of -0.01 mA·cm^{-2} for the reduction scan and 0.01 mA·cm^{-2} for the oxidation scan. Using these cut-off current densities, the lowest potential limit of the LSV curve in pure EAN is about -1.2 V/ Ag/Ag$^+$, which is due to the reduction of EAN, whereas on the anodic domain, the oxidation of EAN begin at about +1.11 V/Ag/Ag$^+$. A small current plateau is also observed on the anodic scan (starting at about 0.25 V/Ag/Ag$^+$), which was ascribed to the oxidation of a small amount of water present in the IL. This analysis is strengthened by the experiments performed by adjusting the water content, as shown in Figure 3.5a. When Co and Ni salts are added, a shift of the oxidation waves towards more cathodic values is observed. Figure 3.4a shows that the peak at 0.72 V/Ag/Ag$^+$ corresponds to the oxidation reaction of Co^{2+} to Co^{3+}, since it can be increased by increasing the Co^{2+} content. For the cathodic scan, the beginning of electroreduction reaction shifts to -0.94 V/Ag/Ag$^+$ and -1.01 V/Ag/Ag$^+$, corresponding to the reduction of Ni^{2+} to Ni and Co^{2+} to Co, respectively. On the other side, the potential window of salt-added solutions shifts to the left, which is due to the oxidation of Cl^-. As shown in Figure 3.5b, the same shift of the oxidation reaction occurs in EAN with KCl, which proves that the shift observed on the LSV curves is due to the oxidation of chloride ions.

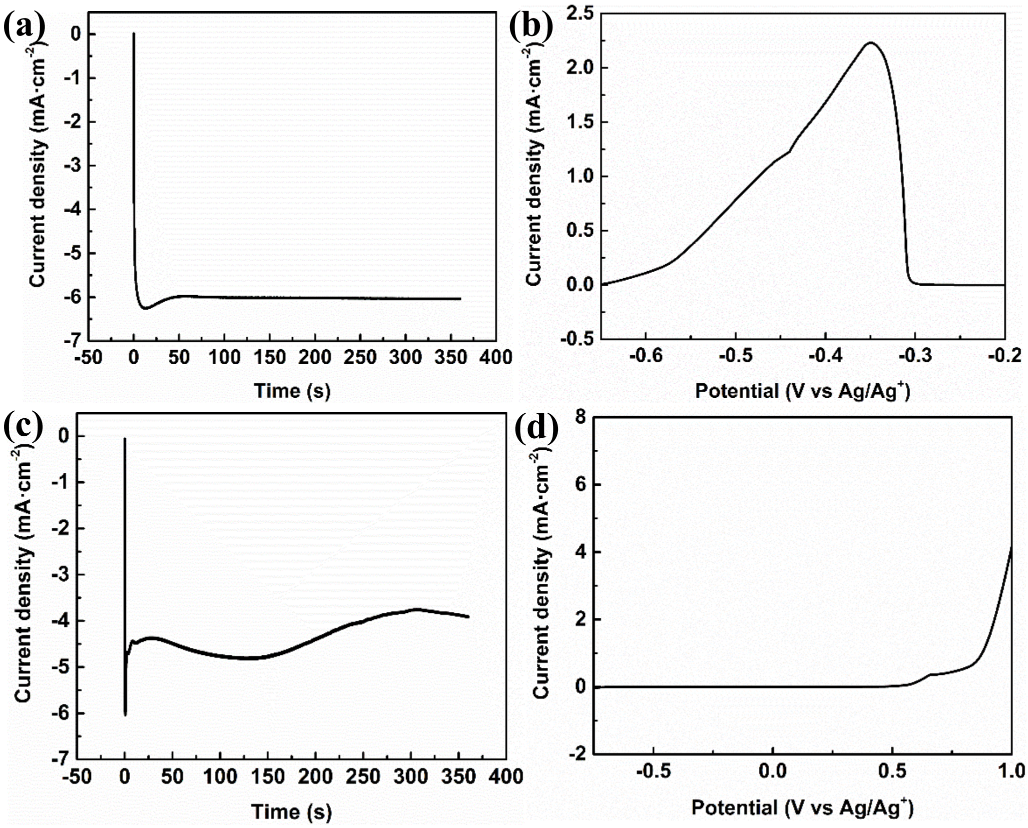

Figure 3.6 a) Chronoamperometry curve and oxidation LSV curve of Ni^{2+} and Co^{2+} on glassy carbon. a) Chronoamperometry curve of glassy carbon in EAN with 0.5 M $NiCl_2$. b) LSV curve of glassy carbon in EAN with 0.5 M $NiCl_2$. c) Chronoamperometry curve of glassy carbon in EAN with 0.5 M $CoCl_2$. d) LSV curve of glassy carbon in EAN with 0.5 M $CoCl_2$.

CV is used to study the reversibility of the electroplating for both metal on GC electrode in EAN solution. Although argon was bubbling during the reaction, oxidation of metal deposits, Ni and Co, was difficult to avoid (i.e., formation of a thin oxide film on the metal deposits). During the cathodic scan, the shape of the voltammogram is characteristic of a curve usually observed for a metal deposit (Figures 3.4 b-d) with a larger cathodic current during the backward swept, which results in a different curve than the cathodic scan current. During the anodic scan, Ni dissolves following two successive electron-exchange reactions ascribed to Ni to Ni^+ (at about -0.50 V/Ag/Ag^+) and Ni^+ to Ni^{2+} (at about -0.40 V/Ag/Ag^+). A similar oxidation process also occurred for the Co deposit [124]. The O1 and O2 peaks in Figure 3.4c are ascribed to the oxidation of Co to Co^+ (at -0.59 V/Ag/Ag^+) and Co^+ to Co^{2+} (at -0.42 V/Ag/Ag^+), respectively. An additional peak (O3) at about 0.5 V/Ag/Ag^+ is also observed and corresponds to the oxidation reaction of Co^{2+} to Co^{3+} [126]. At higher overpotentials, the peak O4 is ascribed to the oxidation of Cl^-, which was discussed in the previous paragraph, and previously identified with the help of blank experiment (Figure 3.5b), and also with the literature [143].

Due to the formation of a thin oxide film on the Ni and Co deposits, the reactivity of the electrode during the subsequent cycles is significantly altered, and it is hard to determine the current curve and peaks for reduction of cations during the cathode scan, rendering it impossible to independently compute the extent of charge transfer occurring in both the reduction and oxidation reactions by integrating the curve. Therefore, the determination of the reversibility of a redox reaction solely based on the cyclic voltammetry (CV) curve is inadequate. The use of complementary techniques and analyses are necessary to comprehensively assess the reversibility and charge transfer limitations of the redox reaction. This can be seen and analyzed quantitatively on the chronoamperograms presented in Figure 3.6. First, a short reduction reaction (electrodeposition) of Ni or Co was performed on the surface of GC for 6 min, and then, LSV was carried out for the oxidation of a grown film, with a scan rate of 0.5 $mV \cdot s^{-1}$. The charge obtained during the deposition step of the metal is very different from the charge obtained for the re-dissolution step. The charge exchanged during the electroplating by chronoamperometry can be calculated through Equation 34, where Q is the charge (in Coulomb), i the current, and t the time. During the short electrodeposition of Ni in Figure 3.6a, the electron charge is 0.433 C, which is significantly different from the value of 6.6×10^{-5} C, which is calculated through the LSV scan in the further oxidation part of the Ni deposition film.

$$Q(t) = \int_0^t i(t)dt \qquad \text{(Eq. 34)}$$

Similarly, the amount of the electric charge for the Co electrodeposition is 0.312 C whereas the value of electric charge during oxidation part is almost 0 C, which is thus described as a totally irreversible process.

To sum up, we can conclude that the electrochemistry of Co and Ni deposited on GC electrode in the air is not fully reversible, the oxide growth is the main issue for the electrodeposition in air, and the electroplating of Ni and Co alloys should be performed in an oxygen-free environment. Therefore, all of the electrocatalysts prepared in the following were electrodeposited in a glove box to avoid the presence of oxide and water in the atmosphere.

3.3. Electrodeposition of Ni-Co alloys in EAN on FTO glasses

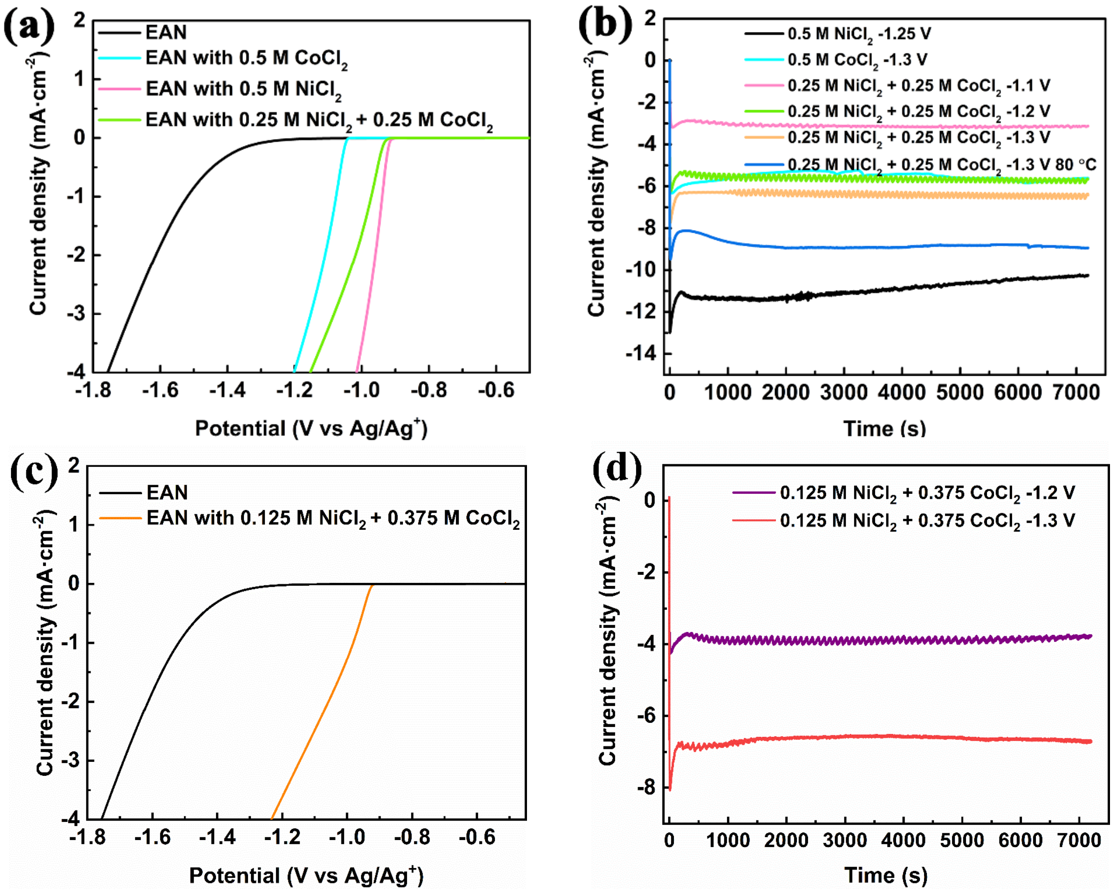

Figure 3.7 a, c) Linear sweep voltammetry curves of EAN with different ions on FTO glass at 60 ºC performed in a glove box. b, d) Comparison of different current-time curves obtained under various conditions during electrodeposition.

Before performing the electrodeposition step, it is necessary to study the electrochemical behavior of Ni^{2+} and Co^{2+} in the IL. Figure 3.7a shows the polarization curves of the EAN for different ion contents when experiments were performed on FTO glasses in a glove box. The reduction reaction of EAN on FTO glass starts at -1.31 V/Ag/Ag^+, whereas the reduction of Ni^{2+} starts at -0.91 V/Ag/Ag^+ and the reduction of Co^{2+} at -1.05 V/Ag/Ag^+. In principle, the electrodeposition potential should be chosen in the potential window of EAN, that is value larger than -1.31 V/Ag/Ag^+, in order to avoid the degradation reaction of the EAN. Therefore, the potential for Ni electrodeposition on FTO glass can be chosen between -0.91 V/Ag/Ag^+ and -1.3 V/Ag/Ag^+, whereas the Co electrodeposition can be performed between -1.05 V/Ag/Ag^+

and -1.3 V/Ag/Ag$^+$. The chronoamperometry curves of the electrodeposition process for different potentials, times, and temperatures are shown in Figures 3.7 b, d. Predictably, since the Faradaic efficiency is not 100% and the deposition efficiency is not 100% either, there must be an error in the conversion all current to deposition quantity. Under these conditions, with the same electrolytes and deposition substrates, and to facilitate comparison of the amount of the electrodeposition under different parameters, this error will be ignored.

Pure Ni and pure Co were prepared at high overpotential corresponding to electrode potentials of -1.25 V/Ag/Ag$^+$ and -1.3 V/Ag/Ag$^+$, respectively, whereas Ni-Co alloys were electrodeposited at different potentials in between (-1.1, -1.2, and -1.3 V/Ag/Ag$^+$). The two temperatures of 60 °Cand 80 °C were chosen for electrodeposition in order to achieve deposition in a short time and the duration for the electrodeposition was adjusted to 1 h and 2 h. In order to better describe the relationship between electrodeposition parameters, phase and composition of the metal deposits, another composition of the deposition bath was used (0.375 M $CoCl_2$ + 0.125 M $NiCl_2$) at different potentials, shown in Figures 3.7 c, d. The potentials of -1.2 V/Ag/Ag$^+$ and -1.3 V/Ag/Ag$^+$ have been applied for the electrodeposition for 2 hours.

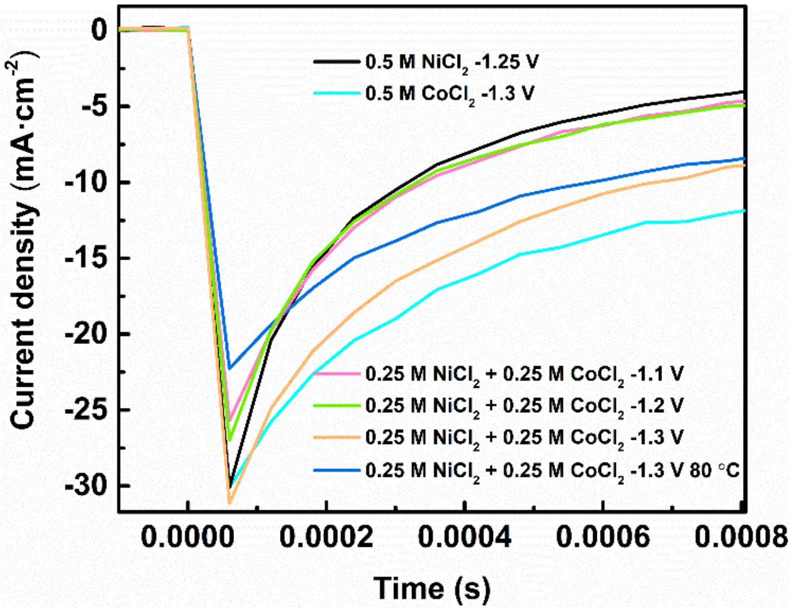

Figure 3.8 Evolution of the current transient for short periods of electrodeposition on FTO.

The shape of these curves is similar and the process of electrodeposition can be divided in three parts. For short time, the electric double layer is charged resulting in a sharp cathodic current transient as shown in Figure 3.8. Then, a second domain for current variations is observed forming a small bump on the curve which is attributed to the growth of the first crystallites. In a last step, the cathodic current stabilized to a constant value and the system reaches a quasi-steady state limited by the diffusion of species [144-146]. In many cases, nucleation process at the beginning of electrodeposition, in aqueous solutions, can be inferred from S-H modal and non-dimensional plot, separated as an instantaneous nucleation and a progressive nucleation [147, 148]. The deposition current reaches its maximum value for short time, from 1 s to 100 s. However, achieving this maximum current value in the electrochemical system under study requires a considerable time span ranging from tens to hundreds of seconds. This extended time can be attributed to the significantly higher viscosity of the ionic liquids compared to water, resulting in low diffusion coefficient. Moreover, it should be noted that the working electrode used differs from the conventional or widely employed electrode configurations. Consequently, the application of commonly utilized dimensionless formulae for the classification of nucleation mechanisms in ionic liquids is not applicable within the scope of this research, and thus, will not be addressed, nor discussed in this work.

Using the current density-time curves obtained by chronoamperometry, the charge and the amount of material electroplated can be calculated from Equations 34 and 35, as shown in Table 3.4,

$$Q(t) = nxF \qquad \text{(Eq. 35)}$$

where Q is the charge, n the number of electrons exchanged for the element, x the number of moles of materials, and F the Faraday's constant (96485.3 $C{\cdot}mol^{-1}$). After 2 h of electrodeposition, the number of moles of Ni and Co electroplated is 1.02×10^{-4} mol and 5.17×10^{-5} mol, respectively. It is also shown that with the same duration and temperature, but changing the potential from -1.1 V/Ag/Ag$^+$ to -1.2 V/Ag/Ag$^+$ and -1.3 V/Ag/Ag$^+$ leads to an increase of the electroplating, from 2.90×10^{-5} mol to 5.25×10^{-5} mol and 5.96×10^{-5} mol, respectively. Similarly, an increase of the electroplating duration or of the temperature also results in an increase of the amount of metal deposited, as shown in Table 0.2. For 1 h of electrodeposition, only 3.91×10^{-5} mol deposition is obtained, whereas this value reaches

8.21×10^{-5} mol when working at 80 °C.

3.4. Characterization of Ni-Co alloys in EAN on FTO glasses

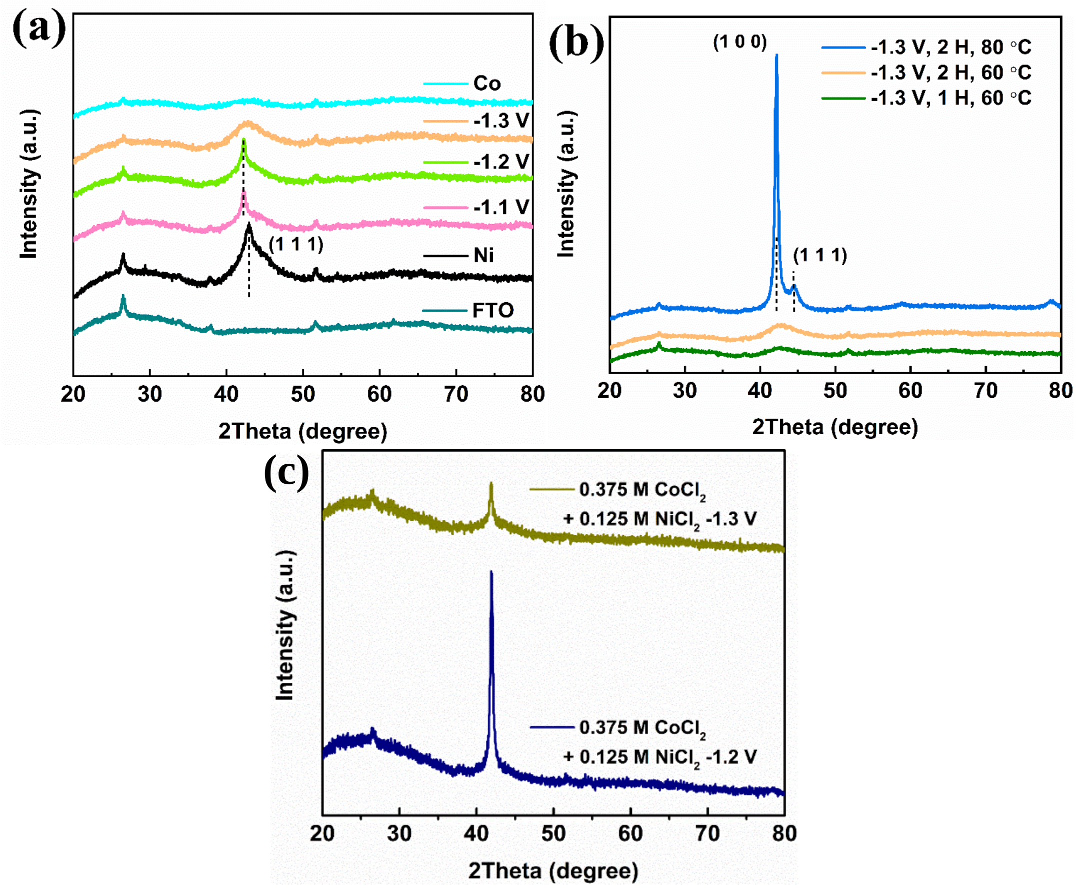

Figure 3.9 XRD patterns of different electrodeposited alloys. a) XRD spectra of pure Ni, pure Co and Ni-Co alloys prepared in EAN with 0.25 M $NiCl_2$ + 0.25 M $CoCl_2$ at different potentials on FTO. b) XRD spectra of Ni-Co alloys prepared in EAN with 0.25 M $NiCl_2$ + 0.25 M $CoCl_2$ at different temperatures and times on FTO. c) XRD spectra of Ni-Co alloys prepared in EAN with 0.125 M $NiCl_2$ + 0.375 M $CoCl_2$.

The XRD spectra obtained for various samples obtained by varying the experimental conditions are shown in Figure 3.9. It can be seen that there is no peak in the range of 40 degree to 50 degree in the spectrum curve of pure FTO glass. After the electrodeposition, there is a more or less well-defined peak in this range. The XRD spectrum presented in Figure 3.9a shows that the electrodeposited Ni has a short and wide peak, which corresponds to the (1 1 1) crystal plane and nanocrystalline structure. Moreover, all the electrodeposited Ni-Co alloys show a nanocrystalline structure as the electrodeposition potential increases from -1.1 to -1.2 V/Ag/Ag$^+$ in EAN with 0.25 M $NiCl_2$ + 0.25 M $CoCl_2$, and the (1 1 1) peak is shifted towards the lower angle compared with main initial peak, corresponding to the reduction of the lattice size due to the doping by Co atoms. When the potential reaches -1.3 V/Ag/Ag$^+$, the Ni-Co alloy structure prepared in EAN with 0.25 M $NiCl_2$ + 0.25 M $CoCl_2$ is similar to that of an amorphous alloy. More negative overpotentials result in smaller critical secondary particle sizes and the secondary particle formation energy decreases, while the secondary particle formation rate increases, meaning that the nucleation rate during electrodeposition increases faster than the nuclei growth rate. As a result, no crystal structure can be observed and an amorphous alloy is obtained [149]. Therefore, only amorphous phase can be tested in the deposition prepared with a higher potential, -1.3 V/Ag/Ag$^+$, in EAN with 0.25 M $NiCl_2$ + 0.25 M $CoCl_2$ at 60°C, both after 1 hour or 2 hours electrodeposition. However, the Ni-Co alloy prepared at the same potential for 2-hour deposit but at a higher temperature (80 °C) is crystallized. Amorphous Co was prepared by electrodeposition at a potential of -1.3 V/Ag/Ag$^+$, as shown in Figure 3.9a. A thin amorphous Co layer was obtained in the past, even by electrodeposition in the presence of thiourea [150]. Here, the presence of IL, and in particular the ethylammonium cation, can contribute to this phase. Figure 3.9 shows the XRD spectrum of a deposited material obtained using an electrolyte featuring a distinct composition (EAN with 0.125 M $NiCl_2$ + 0.375 M $CoCl_2$). Notably, the spectrum exhibits characteristic peaks that are characterized by a truncated and broadened nature, indicative of a nanocrystalline structure. Moreover, it is noteworthy that deposits prepared under a potential of -1.3 V exhibit shorter and broader (half width) characteristic peaks compared to those prepared under a potential of -1.2 V. This observation suggests a reduction in grain size, thereby implying the presence of smaller crystalline domains within the deposited material. Grain size will be discussed in the following section, using the Scherrer equation and TEM.

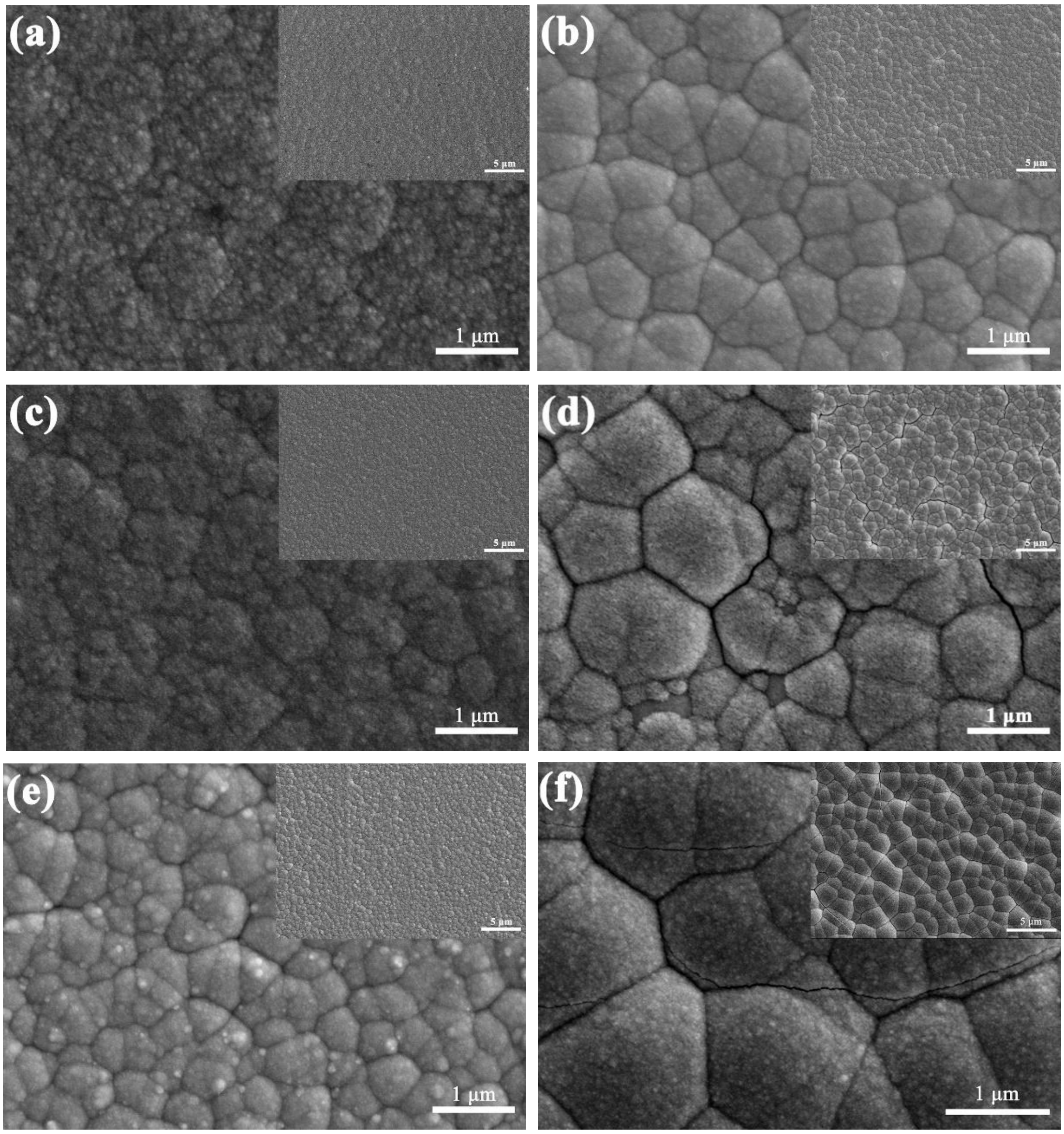

Figure 3.10 SEM morphologies of electrodeposited a) Ni, b) Co, and Ni-Co alloys prepared at c) -1.1 V/Ag/Ag$^+$, d) -1.2 V/Ag/Ag$^+$, e) -1.3 V/Ag/Ag$^+$ and f) -1.3 V/Ag/Ag$^+$ at 80 °C.

SEM is another important tool for the characterization of materials after the preparation. The morphologies of electrodeposited alloys are shown in Figure 3.10. The different electrodeposition potentials result in a rather similar smooth films on the surface. The surfaces consist of irregular secondary particles but the SEM does not allow us to observe nanocrystals and grain boundaries. The deposited nickel surface exhibits a relatively smooth morphology without apparent secondary particle structures (Figure 3.10a). In contrast, the deposited cobalt surface displays distinct secondary particles, which are attributed to the nucleation and subsequent growth processes (Figure 3.10b). Figures 3.10c-e illustrate that upon the introduction of cobalt into the electrolyte and with increasing electrodeposition potential, the secondary particles gradually become more marked, indicating a potential correlation with increasing cobalt content in the deposited material. Furthermore, the observations of the surface of the deposited materials at -1.3V/Ag/Ag$^+$ show the presence of not only secondary particles but also fine particles, suggesting the existence of structures whose morphology is at an early-stage and which have not undergone significant post-nucleation growth. Ni-Co alloys deposited at higher temperature, i.e., 80 °C, show bigger secondary particles and obvious cracks, which are ascribed to the expansion of the volume of the thick layer (Figure 3.10f).

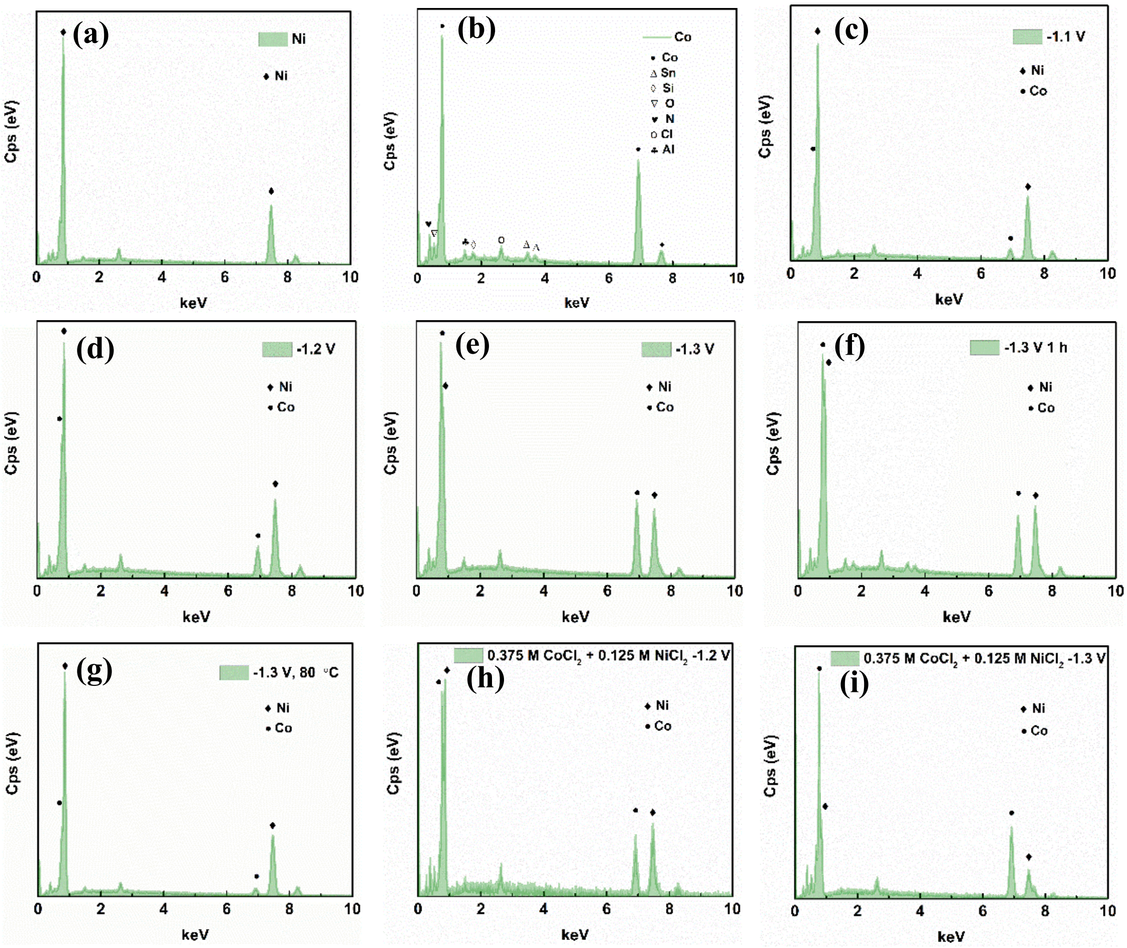

Figure 3.11 EDS analysis of the deposits under different conditions. a) 0.5 M $NiCl_2$, -1.25 V, 2h, 60°C. b) 0.5 M $CoCl_2$, -1.3 V, 2h, 60°C. c) 0.25 M $NiCl_2$ + 0.25 M $CoCl_2$, -1.1 V, 2h, 60°C. d) 0.25 M $NiCl_2$ + 0.25 M $CoCl_2$, -1.2 V, 2h, 60°C. e) 0.25 M $NiCl_2$ + 0.25 M $CoCl_2$, -1.3 V, 2h, 60°C. f) 0.25 M $NiCl_2$ + 0.25 M $CoCl_2$, -1.3 V, 1h, 60°C. g) 0.25 M $NiCl_2$ + 0.25 M $CoCl_2$, -1.3 V, 2h, 80°C. h) 0.375 M $CoCl_2$ + 0.125 M $NiCl_2$, -1.2 V, 2h, 60°C. i) 0.375 M $CoCl_2$ + 0.125 M $NiCl_2$, -1.3 V, 2h, 60°C.

Table 3.2 Element content of various electroplated alloys in EAN.

	Potential (V/Ag/Ag$^+$)	Time (h)	Temperature (°C)	Co (at%)	Ni (at%)	Composition
0.5 M $NiCl_2$	-1.25	2	60	0	100.00	C-Ni
0.5 M $CoCl_2$	-1.3	2	60	100.00	0	A-Co
0.25 M $CoCl_2$ + 0.25 M $NiCl_2$	-1.1	2	60	11.28	88.72	C-$Ni_{88.7}Co_{11.3}$
	-1.2	2	60	22.82	77.18	C-$Ni_{77.2}Co_{22.8}$
	-1.3	2	60	48.12	51.88	A-$Ni_{51.9}Co_{48.1}$
	-1.3	1	60	35.56	64.44	A-$Ni_{64.4}Co_{35.6}$
	-1.3	2	80	41.42	58.58	C-$Ni_{58.6}Co_{41.4}$
0.375 M $CoCl_2$ +0.125 M $NiCl_2$	-1.2	2	60	38.00	62.00	C-$Ni_{62.0}Co_{38.0}$
	-1.3	2	60	69.10	30.90	C-$Ni_{30.9}Co_{69.1}$

The elemental analysis performed by EDS is shown in Figure 3.11. The alloy composition can be tuned by changing the potential of the deposit, its duration and the temperature. Except for the peak of Ni and Co from the deposition, there are other elements illustrated in Figure 3.11b, for example. O comes from FTO glass, residual EAN the oxide developed on the surface when exposed to air during transfer. Sn, Si comes from FTO glass. N, Cl come from the residual EAN during the electrodeposition. Al comes from the workbench of SEM. For a given experimental conditions, namely at the same temperature (60°C), ion concentration (0.25 M $NiCl_2$ + 0.25 $CoCl_2$) and the duration of electrodeposition (2 hours), the Co content in the Ni-Co alloys gradually increases when the electrodeposition potential is shifted toward more cathodic values, from 11 at% to 23 at% and 48 at%, corresponding to a potential of -1.1, -1.2, and -1.3 V/Ag/Ag$^+$, respectively. Decreasing the electrodeposition time from 2 hours to 1 hour leads to a decrease of the Co content from 48 at% to 36 at%. When the temperature was increased up to 80°C, although the amount of deposition on the surface was obviously increased due to kinetic enhancement of the electrochemical reaction, the content of cobalt has decreases by 41 at%. Under identical electrodeposition potentials, an increase in the cobalt concentration in the electrolyte leads to a corresponding increase in cobalt in the electroplated material. In EAN with 0.125 M $NiCl_2$ + 0.375 M $CoCl_2$, the cobalt content for a deposit performed at a potential of -1.2 V/ Ag/Ag$^+$ is 38 at%, thus showing a higher Co content when compared to the deposit obtained in EAN with 0.25 M $NiCl_2$ + 0.25 M $CoCl_2$ (namely, 23 at%). At a potential of -1.3 V/

Ag/Ag$^+$, the cobalt content was 69 at%, which is significantly higher than the content obtained for the other electrolyte compositions. Table 3.2 summarizes the different alloys prepared according to the experimental conditions. Moreover, the mapping of the surfaces and of the cross sections of the sample by EDS clearly indicate that the distribution of Ni and Co elements is uniform. An example of these results is presented in Figure 3.12 for Ni-Co alloy prepared at -1.3 V/Ag/Ag$^+$. Under the resolution limit of the instrument, it can be seen that the distribution of each element is average on the surface and we cannot see any aggregated elements on these images. With the help of TEM in Figure 3.14, we can see that the size of most grains in the nanocrystalline alloy is about 13 nm. It can be considered that there is not a large amount of pure Ni or pure Co at the observable size. This indicates that the electroplated samples are made of mixture of Ni and Co, but not single Ni nor single Co crystal or particles. Therefore, from since analysis, we can conclude that the electroplated material are homogeneous alloys.

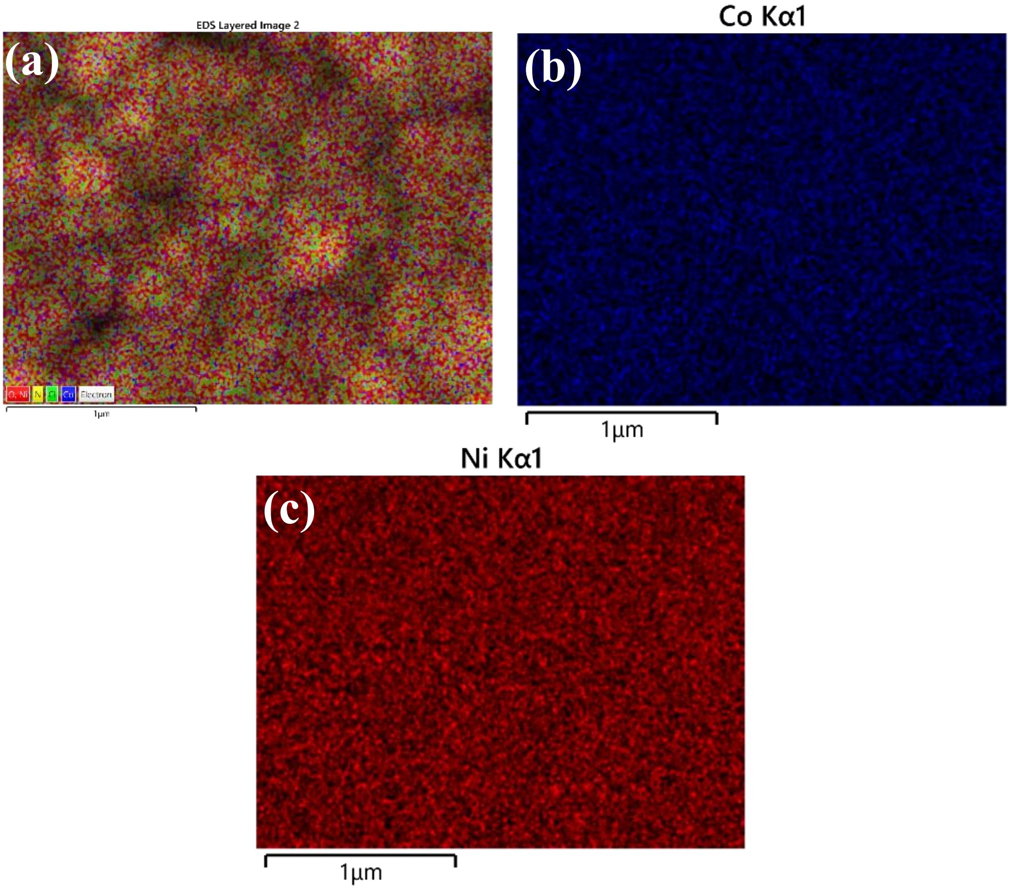

Figure 3.12 EDS mapping images of Ni-Co alloy prepared at -1.3 V/Ag/Ag$^+$. a) Full scan of the elements. b) Co distribution. c) Ni distribution.

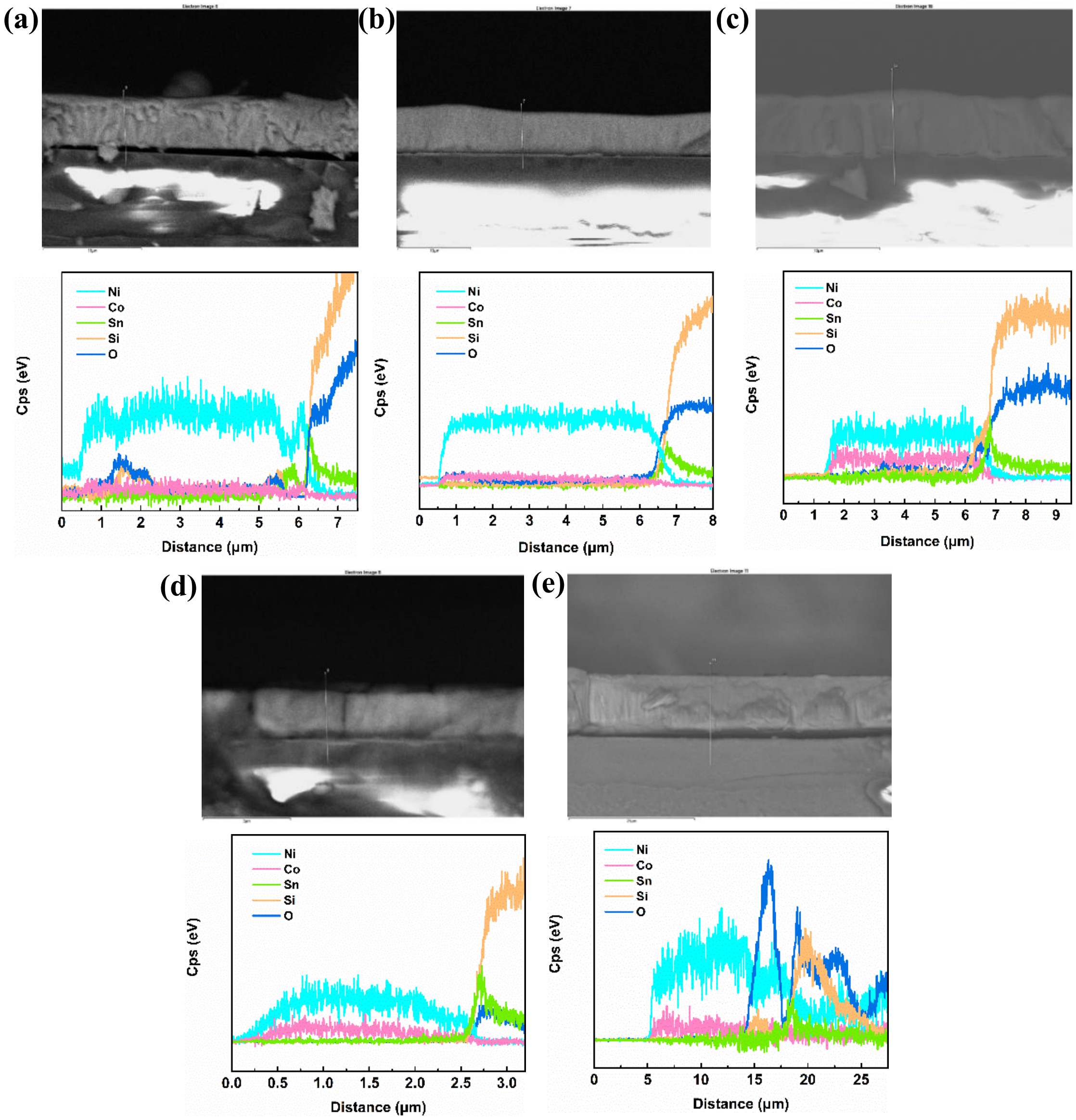

Figure 3.13 SEM morphology of the cross-section and EDS line scan of the electroplated samples obtained in various conditions. a) 0.25 M $NiCl_2$ + 0.25 M $CoCl_2$, -1.1 V, 2h, 60 ˚C. b) 0.25 M $NiCl_2$ + 0.25 M $CoCl_2$, -1.2 V, 2h, 60 ˚C. c) 0.25 M $NiCl_2$ + 0.25 M $CoCl_2$, -1.3 V, 2h, 60 ˚C. d) 0.25 M $NiCl_2$ + 0.25 M $CoCl_2$, -1.3 V, 1h, 60 ˚C. e) 0.25 M $NiCl_2$ + 0.25 M $CoCl_2$, -1.3 V, 2h, 80 ˚C.

The thickness of the different deposits can be obtained from the analysis of the cross section of each sample by EDS and SEM (Figure 3.13). The average thickness of Ni-Co alloys slightly depends on the electrodeposition potential, varying from 5.1, 7.5, and 6.2 µm for potentials of -1.1, -1.2 and -1.3 V/Ag/Ag^+, respectively. All the samples were washed with an ethanol flow in the same way and duration. Therefore, the error due to the peeling of the top surface during the cleaning process can be neglected for the comparison of the sample. As expected, the thickness of the deposit is proportional to the duration of the electrodeposition, 2.1 µm for 1 h electrodeposition, while an increase in temperature also results in an increase of the thickness, 15.2 μm for an electroplating at 80 °C.

Using the Scherrer equation (Eq. 32), the evaluation of crystalline domain size of the different alloys can be performed and is reported in Table 3.3. From the grain sizes of Ni-Co depositions prepared at different potentials in EAN with 0.25 M $NiCl_2$ + 0.25 M $CoCl_2$, we can see that the higher potential can result in a smaller grain size (-1.1 V/Ag/Ag$^+$, 14.8 nm > -1.2 V/Ag/Ag$^+$, 12.0 nm), or even amorphous phase (-1.3 V/ Ag/Ag$^+$). In addition, the Co content increases with the electrodeposition potential. The amorphous Ni-Co alloy, A-$Ni_{51.9}Co_{48.1}$, is formed at a higher potential, -1.3 V/Ag/Ag$^+$, with a higher cobalt content. Therefore, the formation of amorphous alloys may be due to high cobalt content or high electrodeposition potential (in absolute value).

Table 3.3 Phase and grain size of the different electroplated materials.

	Potential (V/Ag/Ag$^+$)	Time (h)	Temperature (°C)	State	Grain size (nm)
0.5 M $NiCl_2$	-1.25	2	60	Crystal	16.1
0.5 M $CoCl_2$	-1.3	2	60	Amorphous	-
0.25 M $CoCl_2$ + 0.25 M $NiCl_2$	-1.1	2	60	Crystal	14.8
	-1.2	2	60	Crystal	12.0
	-1.3	2	60	Amorphous	-
	-1.3	1	60	Amorphous	-
	-1.3	2	80	Crystal	20.5
0.375 M $CoCl_2$ +0.125 M $NiCl_2$	-1.2	2	60	Crystal	29.0
	-1.3	2	60	Crystal	22.2

For the alloys prepared by electrodeposition from another electrolyte concentration, the change in grain size with the potential also follows the same rules with a decrease of the grain size when the applied potential varies from -1.2 to -1.3 V/Ag/Ag$^+$. In the solution with an adjusted ionic ratio of 0.375 M $CoCl_2$ + 0.125 M $NiCl_2$, and with the same potential, temperature and time, the deposited Ni-Co alloys show a larger Co content than that in EAN with 0.25 M $NiCl_2$ + 0.25 M $CoCl_2$. The XRD spectra obtained for the electroplated materials in EAN containing 0.125 M $NiCl_2$ + 0.375 M $CoCl_2$ are presented in Figure 3.9c, d. It can be seen that, although the cobalt content is increased, the alloys electroplated in EAN with 0.375 M $CoCl_2$ + 0.125 M

$NiCl_2$ are all in crystalline state. The deposit at -1.2 V/Ag/Ag$^+$ (C-$Ni_{62.0}Co_{38.0}$) is crystallized and shows a similar atomic ratio to the sample which was prepared at -1.3 V/Ag/Ag$^+$ in EAN with 0.25 M $NiCl_2$ + 0.25 M $CoCl_2$. This indicates that the formation of amorphous alloy is not linked to the Co content of the alloy, but to the potential applied during the electrodeposition of the material. It can also be seen that the alloy with a higher Co content prepared at -1.3 V/Ag/Ag$^+$, C-$Ni_{30.9}Co_{69.1}$, shows a nanocrystalline structure but its peak is not as sharp as C-$Ni_{62.0}Co_{38.0}$, which was prepared at a lower potential, and shows smaller grain size (22.2 nm).

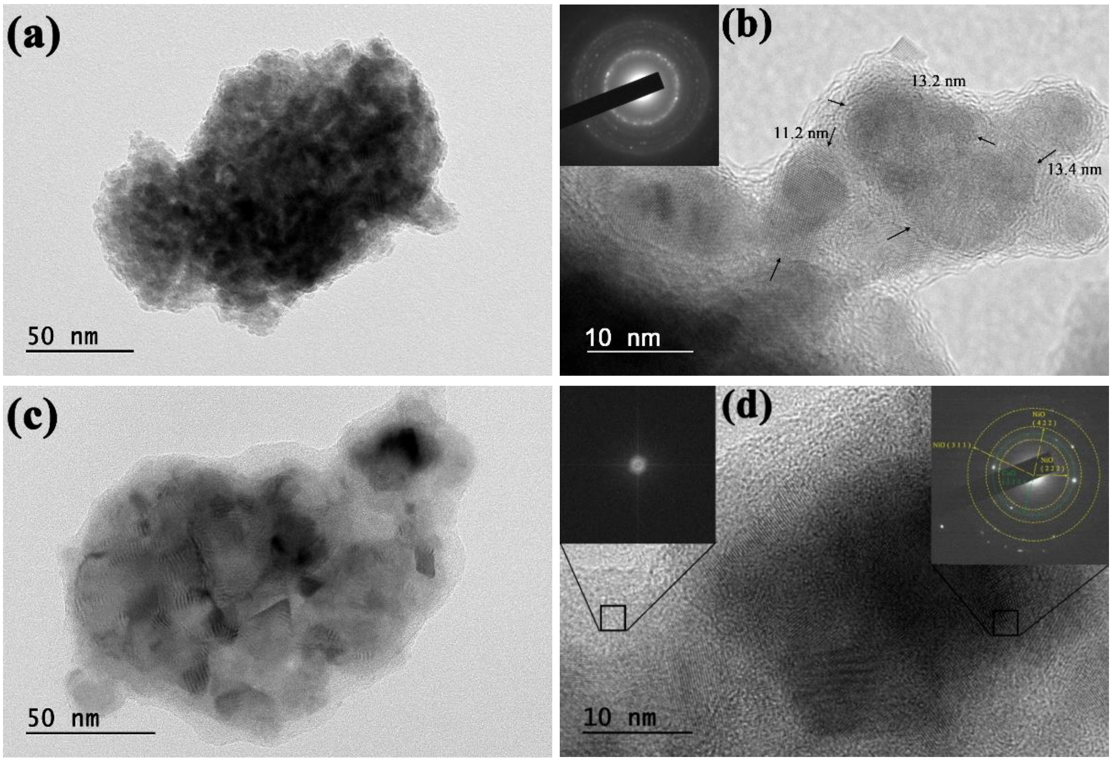

Figure 3.14 TEM images of different electroplated alloys. a, b) C-$Ni_{88.7}Co_{11.3}$ c,d) A-$Ni_{64.4}Co_{35.6}$.

The average grain size decreases from 14.8 to 12.0 nm when the potential shifts towards more cathodic values, until obtaining an amorphous alloy at the potential of -1.3 V/Ag/Ag$^+$. TEM analysis reveals that the collected particulate samples are made up of multiple nanocrystals, as shown by their distinct morphology. Notably, the size of the nanocrystals can be easily discerned by examining the comparatively thinner edge regions, which provide a clear indication of their dimensions in Figure 3.14b. The grain size of C-$Ni_{88.7}Co_{11.3}$ is around 13 nm. This value is similar to that calculated with the Scherrer equation (Table 3.3), showing that the grain size calculated with Eq. (32) may correspond to the actual grain size. The crystallographic nature of the nanocrystalline deposit was examined through electron diffraction analysis, revealing a polycrystalline crystal structure. The grains of the amorphous alloy A-$Ni_{51.9}Co_{48.1}$ could be the cobalt oxide and nickel oxide, which could be formed in the air during the preparation period of TEM measurements, as shown by electron diffraction in Figure 3.14d. In addition to the presence of randomly distributed oxide crystals, electron diffraction analysis at various locations provided valuable information, unveiling the presence of an amorphous structure in A-$Ni_{51.9}Co_{48.1}$.

XPS analysis was further used to characterize the surface state of different deposits prepared at different potentials. The binding energy measured by XPS for several compounds of interest is given in Table 0.4. As shown in Figure 3.15, for deposit performed in Ni-containing electrolytes, a mixture of Ni(0) (852.8 eV), Ni(II) from NiO and $Ni(OH)_2$ (855.5 eV, 855.6 eV) is obtained. NiO and $Ni(OH)_2$ originate from the oxidation during sample transfer, which also makes the main peak shifting towards higher energy. The oxide can also be identified from TEM in Figure 3.14b and d. The energy of electrons used for performing XPS analysis is such that the detector can only sense the signal from 10 first nanometers below the surface of the deposit, showing that the oxide film thickness is either smaller than 10 nm or the oxide film does not completely cover the surface. Similarly, for deposits performed from Co-containing electrolytes, a mixture of Co(0) (778.2 eV), Co(II) from CoO and $Co(OH)_2$ (780.6 eV) is also observed. For the Ni-Co alloys, in addition to the oxides and hydroxides, the main peak observed for Ni 2p and Co 2p (for the alloy prepared at -1.1 V/Ag/Ag^+) corresponds to the binding energy of Ni-Co (852.7 eV for Ni 2p and 778.5 eV for Co 2p), showing that the predominant bond in the crystallized Ni-Co alloy is the Ni-Co bond rather than elemental Ni and elemental Co contained in the amorphous Ni-Co alloy shown in Figures 3.15e and f. These results are in agreement with XRD analysis and TEM measurements, and confirm our preliminary analysis on the formation of a homogeneous alloys from the SEM/EDX experiments.

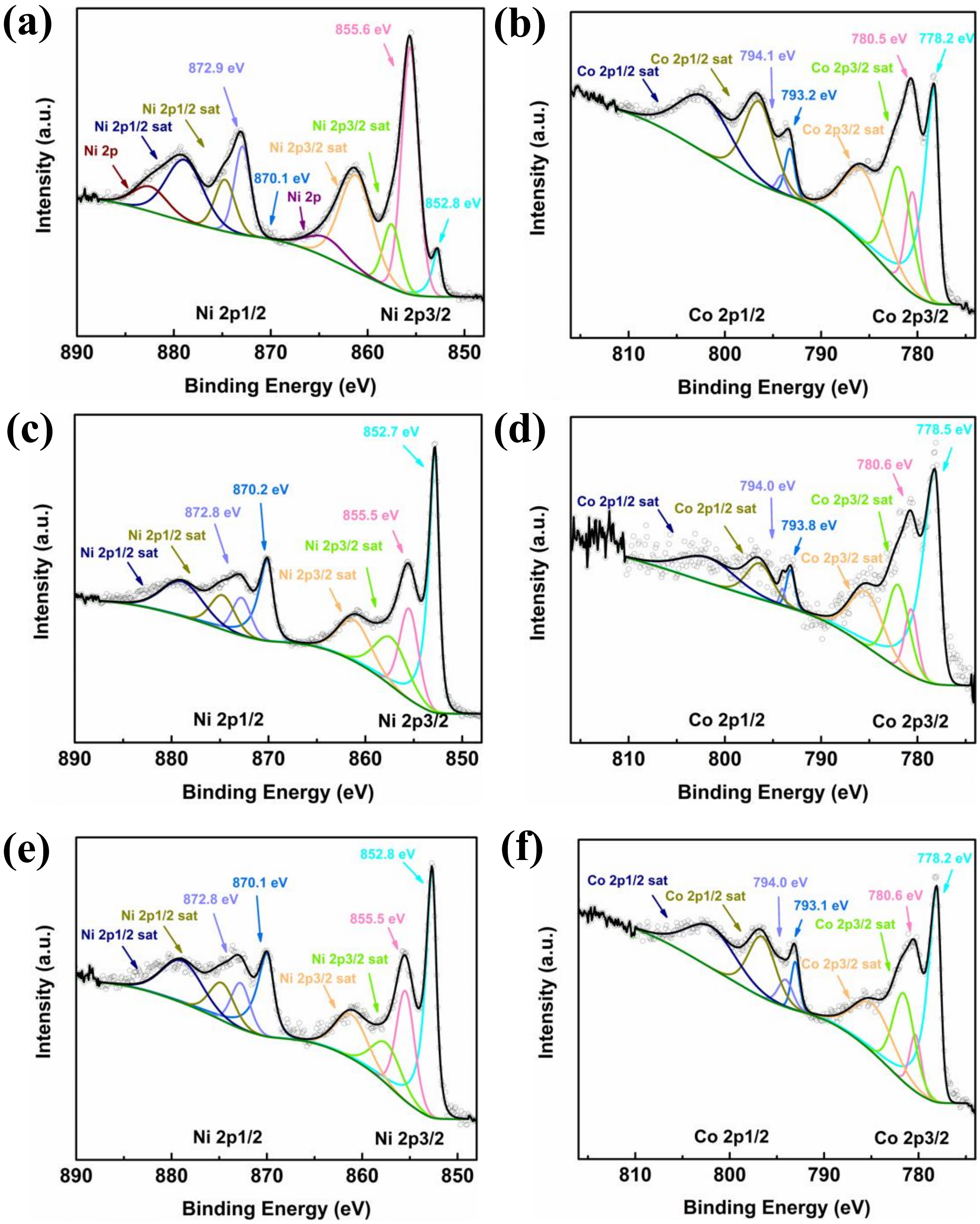

Figure 3.15 XPS spectra of different electrodeposited alloys. a) Ni 2p of deposited Ni, b) Co 2p of deposited Co, c) Ni 2p and d) Co 2p of deposited Ni-Co alloys prepared at -1.1 V/Ag/Ag+, e) Ni 2p and f) Co 2p of deposited Ni-Co alloys prepared at -1.3 V/Ag/Ag+.

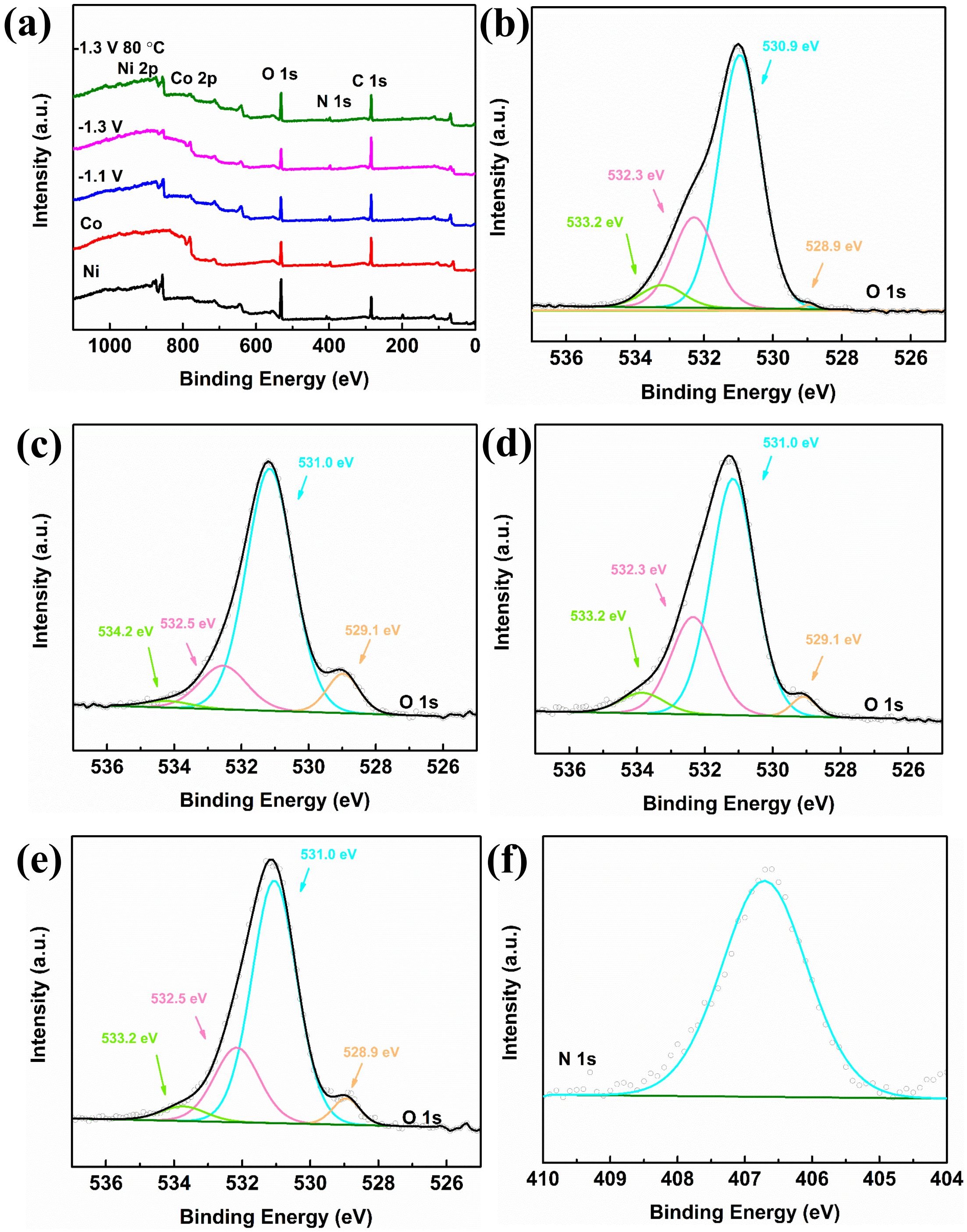

Figure 3.16 XPS spectra of different deposits. a) The full range of XPS spectrum. b) O1s of Ni. c) O1s of Co. d) O1s of deposited Ni-Co alloy with -1.1 V vs Ag/Ag$^+$. e) O1s of deposited Ni-Co alloy with -1.3 V vs Ag/Ag$^+$, f) N 1s of Ni.

From the analysis of the results presented in Figure 3.16a, the survey spectrum, the peaks ascribed to C, N and O can be deeply discussed. Combined with the main peaks of Ni and Co, we can obtain more information to characterize the element state. For each deposit, the binding energy of the O chemical bond can be primarily SnO (529.0 eV), which comes from FTO glass. In addition, the surface oxides and hydroxides of Ni, Co, and Ni-Co alloy were analyzed, yielding binding energy values of 528.9/532.3 for Ni-O bond and 529.1/532.5 for Co-O bond, respectively. Additionally, nitrate anions remain in the deposit due to the combination of NO_3^- with the alloys at the electrode surface during the electrodeposition process, which can also be observed in the EDS analysis presented in Figure 3.11 [151-154]. The element content can be also calculated by integrating the surface of XPS peaks. However, the surface depth detected by XPS is around 5-10 nm. We are more interested in the overall distribution of the catalyst elements obtained by EDS. Consequently, we will not discuss the element content calculated by XPS.

3.5. Electrocatalytic HER of Ni-Co alloys on FTO glasses

The electrocatalytic properties of these materials have been investigated towards the hydrogen evolution reaction (HER) by linear sweep voltammetry and cyclic voltammetry, in 1 M KOH aqueous solution (Figure 3.17). The ECSA (effective active surface area) was evaluated from the determination of the interfacial capacitance (C^{σ}) at different scan rates (Figure 3.18). The variation of the current density as a function of the scan rate for different alloys compositions is shown in Figure 3.17a. From the slope of these curves, the interfacial capacitance varies from 1.1 $mF.cm^{-2}$ for pure cobalt to 0.12 $mF.cm^{-2}$ for the alloys (determined from CV curves, shown in Figure 3.18). Compared with pure C-Ni, Ni-Co alloys show higher ECSA values (Table 3.4). The capacitance value of the crystalline C-$Ni_{30.9}Co_{69.1}$ is 0.47 $mF{\cdot}cm^{-2}$, which is almost 4 times higher than pure Ni. However, the capacitance values for the different Ni-Co alloys are lower than those of amorphous Co. Such large values may not be ascribed to the double layer capacitance (which is usually in the range of a about 10-50 $\mu F\ cm^{-2}$), but rather to the formation of a thin oxide film on the alloy when immersed in KOH solution, the thickness of which may depend on the initial alloy composition.

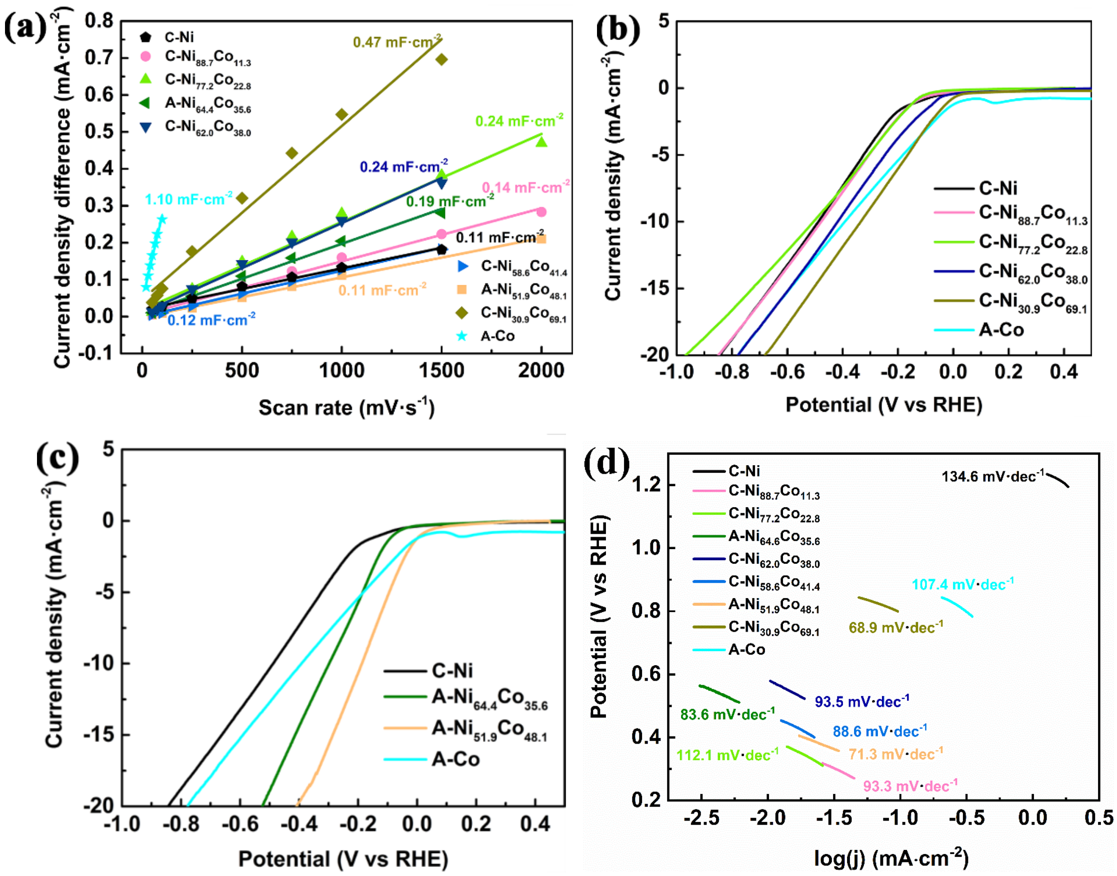

Figure 3.17 Electrocatalytic properties of the materials towards the HER for different Ni-Co alloys: a) C^{σ} of different Ni-Co alloys, b) LSV curves of Ni-Co alloys with different atomic ratio at a scan rate of 20 mV/s, c) LSV curves of crystalline Ni-Co alloy and amorphous Ni-Co alloy at a scan rate of 20 mV/s, d) Tafel slopes for different alloys for the HER.

The HER potential is delimited by the potential value for which the current density reaches -10 mA·cm^{-2}. It can be seen from Figure 3.17b that Ni-Co alloys show lower potentials for the HER when compared with the pure Ni and Co materials. With the addition of Co, the HER potential of the various crystalline Ni-Co alloys (still evaluated at -10 mA·cm^{-2}) decreases from -0.49 V/RHE to -0.48 V/RHE, -0.42 V/RHE and -0.34 V/RHE, corresponding to a Co content of 0 at%, 11 at%, 38 at% and 69 at%, respectively. For amorphous A-Ni$_{64.4}$Co$_{35.6}$ and A-Ni$_{51.9}$Co$_{48.1}$, the HER potential is -0.30 V/RHE and -0.19 V/RHE, which is lower than HER potentials of C-Ni and A-Co (Figure 3.17c). Comparing the alloys with similar atomic ratio, amorphous A-Ni$_{51.9}$Co$_{48.1}$ shows lower potential for HER and lower onset potential (-0.19 V/RHE and 0 V/RHE) than crystalline C-Ni$_{58.6}$Co$_{41.4}$ (-0.46 V/RHE and -0.17 V/RHE). Compared to the ordinary crystalline alloys, the lower HER potential of amorphous alloys is due to the synergistic effect of the alloy elements, the high surface energy of amorphous state and the active center density of amorphous alloys. The amorphous A-$Ni_{51.9}Co_{48.1}$ alloy also shows better value for the HER than other works in the literature with the same conditions, like -0.31 V/RHE for Ni-Co nanocomposite and -0.223 V/RHE for nanoporous alloy np-NiFeMoP [155, 156]. It is also lower that than -0.213 V/RHE for Ni-Co alloys with similar element ratio reported in another work [157]. Moreover, the amorphous alloys also show improved reaction rate, determined from a lower Tafel slope than for the crystalline alloys: 83.6 $mV \cdot dec^{-1}$, and 71.3 $mV \cdot dec^{-1}$, for A-$Ni_{64.4}Co_{35.6}$ and A-$Ni_{51.9}Co_{48.1}$, respectively. With the addition of Co, most of Ni-Co alloys show lower Tafel slope and higher reaction rate, with a value between 93.5 $mV \cdot dec^{-1}$ 68.9 $mV \cdot dec^{-1}$, compared to pure Ni and Co (134.6 $mV \cdot dec^{-1}$ and 107.4 $mV \cdot dec^{-1}$, respectively).

However, it is not an ideal value for the HER because of the unstable surface during the reaction. It has been observed that the electrocatalysis is always accompanied by structural rearrangement, possible mineral dissolution, oxidative damage, and physical stress from the gas evolution which render the catalyst physically unstable [158]. Indeed, after electrocatalytic testing, the surface is very damaged and part of the material has detached from the conductive substrate, as shown in Figure 3.19. Therefore, it is necessary to find a way to improve the lifetime of Ni-Co-based catalysts prepared by electroplating process.

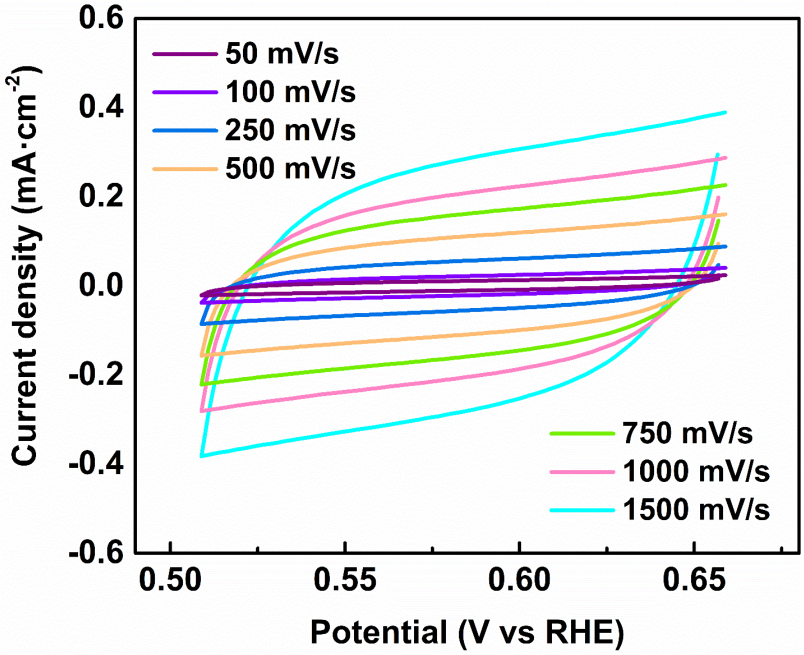

Figure 3.18 CV curves performed at different scan rate for C-$Ni_{58.6}Co_{41.4}$ in 1 M KOH solution.

Table 3.4 Properties of Ni-Co alloys in 1 M KOH solution towards the HER.

	C^{σ} ($mF \cdot cm^{-2}$)	OCP (V/RHE)	Onset potential (V vs RHE)	HER potential (V vs RHE)	Tafel slope ($mV \cdot dec^{-1}$)
C-Ni	0.11	0.45	-0.16	-0.49	134.6
C-$Ni_{88.7}Co_{11.3}$	0.14	0.56	-0.13	-0.48	93.3
C-$Ni_{77.2}Co_{22.8}$	0.24	0.57	-0.12	-0.51	112.1
A-$Ni_{64.4}Co_{35.6}$	0.11	0.62	-0.08	-0.3	83.6
C-$Ni_{62.0}Co_{38.0}$	0.19	0.61	-0.08	-0.42	93.5
C-$Ni_{58.6}Co_{41.4}$	0.12	0.58	-0.17	-0.46	88.6
A-$Ni_{51.9}Co_{48.1}$	0.24	0.64	0	-0.19	71.3
C-$Ni_{30.9}Co_{69.1}$	0.47	0.91	-0.01	-0.34	68.9
A-Co	1.1	0.91	0 I	-0.4	107.4

Figure 3.19 Photos of electrode before (left) and after (right) electrocatalytic testing.

3.6. Electrodeposition of Ni-Co alloys on Cu foils

In order to know if the stability of the deposit can be improved by using different substrates, the Ni-Co alloys were prepared on Cu foil with the similar experimental procedure. Before studying the electroplating, the electrochemical response of Cu foil in the same EAN solutions was obtained from LSV (Figure 3.20a). The polarization curves of the EAN with different ion contents were performed on Cu foil in a glove box. The reduction reaction of EAN on Cu starts at the potential of -1.11 V/Ag/Ag^+, whereas the reduction of Ni^{2+} is observed at -0.90 V/Ag/Ag^+, and the reduction of Co^{2+} at -0.98 V/Ag/Ag^+. Therefore, the potential for Ni electrodeposition on Cu foil can be chosen between -0.90 V/Ag/Ag^+ and -1.11 V/Ag/Ag^+, whereas the Co electrodeposition can be performed between -0.98 V/Ag/Ag^+ and -1.11 V/Ag/Ag^+. The chronoamperometry curves for the electroplating at different potentials, times, and temperatures are shown in Figure 3.20a.

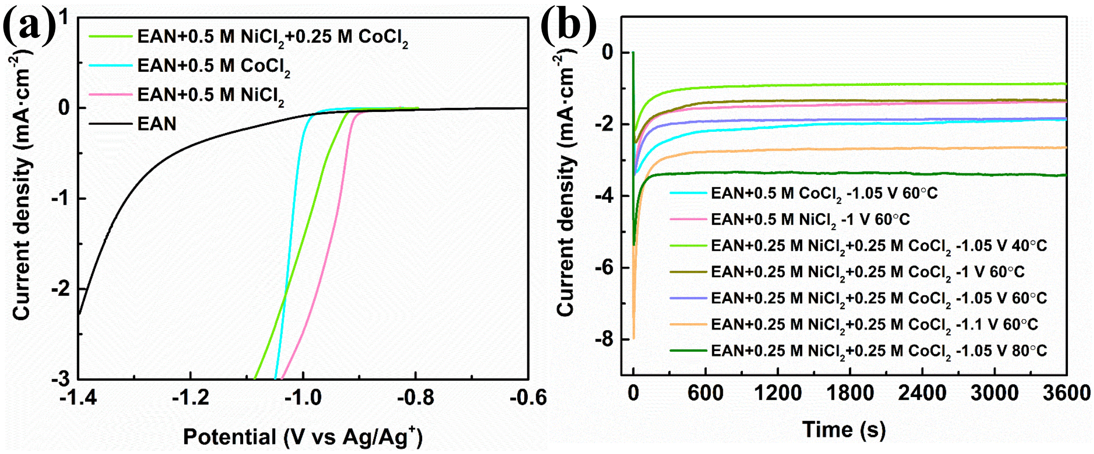

Figure 3.20 a) Linear sweep voltammetry curves of EAN with different ions on Cu foils at 60 ºC performed in glove box. b) Comparison of different current-time curves obtained under various conditions during electrodeposition.

On Cu foil, pure Ni and pure Co were prepared at -1.0 V/Ag/Ag$^+$ and -1.05 V/Ag/Ag$^+$, respectively, whereas Ni-Co alloys were electrodeposited at different potentials (-1.0, -1.05, and -1.1 V/Ag/Ag$^+$). The temperature 40°C, 60 °C, and 80 °C were chosen for electrodeposition in order to get deposition in short time and the duration for the electroplating was adjusted as 0.5 h, 1 h and 2 h. From the chronoamperometry curves, the amount of charge and material deposited were calculated (Table 3.5) using Eq.34 and 35.

For a one-hour electrodeposition, a total amount of 6.32×10^{-5} mol of Ni and 8.72×10^{-5} mol Co is obtained. As expected, when the electrodeposition time and temperature remain constant, increasing the electrodeposition overpotential leads to increase the amount of the material deposited. Specifically, the deposition quantities increase from 5.87×10^{-5} mol to 8.03×10^{-5} mol and 1.17×10^{-4} mol as the electrode potential is adjusted from -1.0 V/Ag/Ag$^+$ to -1.05 V/Ag/Ag$^+$ and -1.1 V/Ag/Ag$^+$, respectively. Similarly, increasing the electrodeposition time and temperature results in an increase in the deposition, as presented in Table 3.5. For a -1.05 V/Ag/Ag$^+$ electrodeposition duration of Ni-Co alloys, the amount of deposited material increases from 3.85×10^{-5} mol to 8.03×10^{-5} mol and 1.60×10^{-4} mol when the time is varied from 0.5 h to 1 h and 2 h, respectively. The amount of deposited material increases from 3.97×10^{-5}

mol to 8.03×10^{-5} mol and 1.43×10^{-4} mol when the temperature is varied from 40 °C to 60 °C and 80 °C, respectively.

Table 3.5 Charge and electrodeposition quantity of each sample on Cu foil.

	Potential (V/Ag/Ag$^+$)	Time (h)	Temperature (°C)	Exchanged charge (C)	Electrodeposition quantity (mol)
0.5 M $NiCl_2$	-1.0	1	60	12.19	6.32×10^{-5}
0.5 M $CoCl_2$	-1.05	1	60	16.82	8.72×10^{-5}
0.25 M $CoCl_2$ + 0.25 M $NiCl_2$	-1.0	1	60	11.33	5.87×10^{-5}
	-1.05	1	60	15.49	8.03×10^{-5}
	-1.1	1	60	22.50	1.17×10^{-4}
	-1.05	0.5	60	7.43	3.85×10^{-5}
	-1.05	2	60	30.83	1.60×10^{-4}
	-1.05	1	40	7.67	3.97×10^{-5}
	-1.05	1	80	27.50	1.43×10^{-4}

3.7. Characterizations of Ni-Co alloys on Cu foils

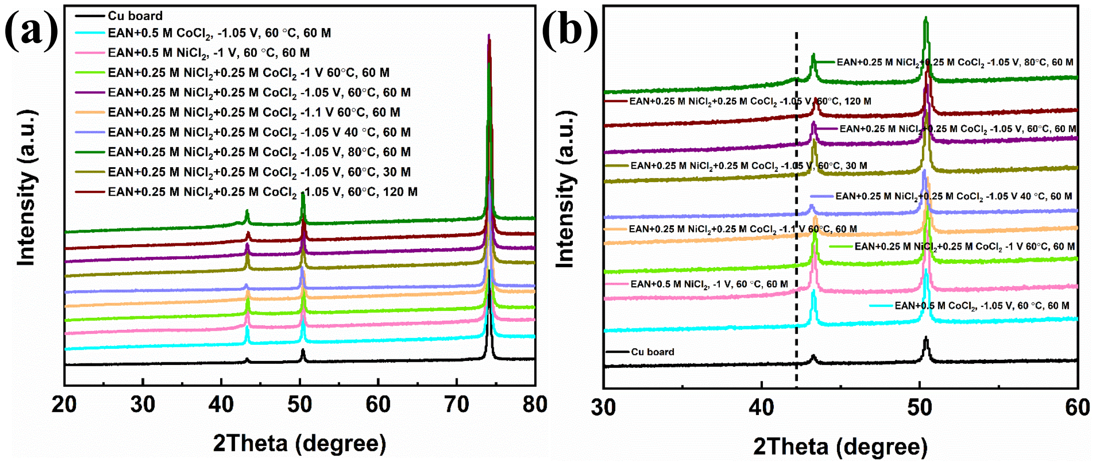

Figure 3.21 XRD patterns of different electrodeposited alloys on Cu foils. a) Full range. b) Partial zoom area.

The X-ray diffraction spectra, presented in Figure 3.21, show distinct features. The XRD spectrum of the pure copper foil shows three peaks within the range of 20 degrees to 80 degrees. These peaks correspond to the diffraction signals corresponding to the crystal planes of Cu (1 1 1), (2 0 0), and (2 2 0). In comparison to FTO glass, the electroplated alloy on copper shows additional peaks. Nonetheless, owing to the crystalline nature of the Cu substrate, the X-ray diffraction spectrum displays pronounced diffraction peaks, thereby obscuring a significant portion of the distinctive peaks associated with the deposited alloy. After electroplating with various parameters, slight alterations are observed in the diffraction patterns of Ni-Co alloys compared to that of pure Cu. By magnifying the XRD patterns of the alloys, presented in Figure 3.21b, a discernible amorphous peak between 41 degrees and 43 degrees is observed for the deposit performed in ethylammonium nitrate with a concentration of 0.5 M $NiCl_2$ (-1.0 V/Ag/Ag^+), 0.25 M $NiCl_2$ + 0.25 M $CoCl_2$ (1.05 V/Ag/Ag^+, 80 °C, 1 h). Consequently, XRD analysis reveals the absence of crystal peaks and structures in each alloy, which allows us to deduce that the alloys prepared on Cu foils are amorphous alloys. The morphologies of electrodeposited alloys are shown in Figure 3.22 and Figure 3.23. The different electrodeposition potentials result in smooth film on the surface, similar as that obtained on FTO glasses. The surface analysis reveals that the secondary particles present on the surface of the deposited nickel (Figure 3.22a) are more prominent compared to those observed on the deposited cobalt (Figure 3.22b). Additionally, as shown in Figures 3.22c-e, it is evident that lower electroplating potential does not contribute to a smoother surface in the case of nickel-based deposits (Figure 3.22e). However, when increasing the deposition potential, the secondary particle structure on the surface gradually decreases until a flat region is attained, as illustrated in Figure 3.22c, which corresponds to a deposition potential of -1.1V/Ag/Ag^+. Altogether, replacing the fluorine-doped tin oxide (FTO) glass working electrode (substrate) with a copper plate results in negligible morphological changes. Both substrates show a predominantly flat surface morphology in the long range, while displaying small-scale roughness, primarily attributable to the presence of secondary particle structures.

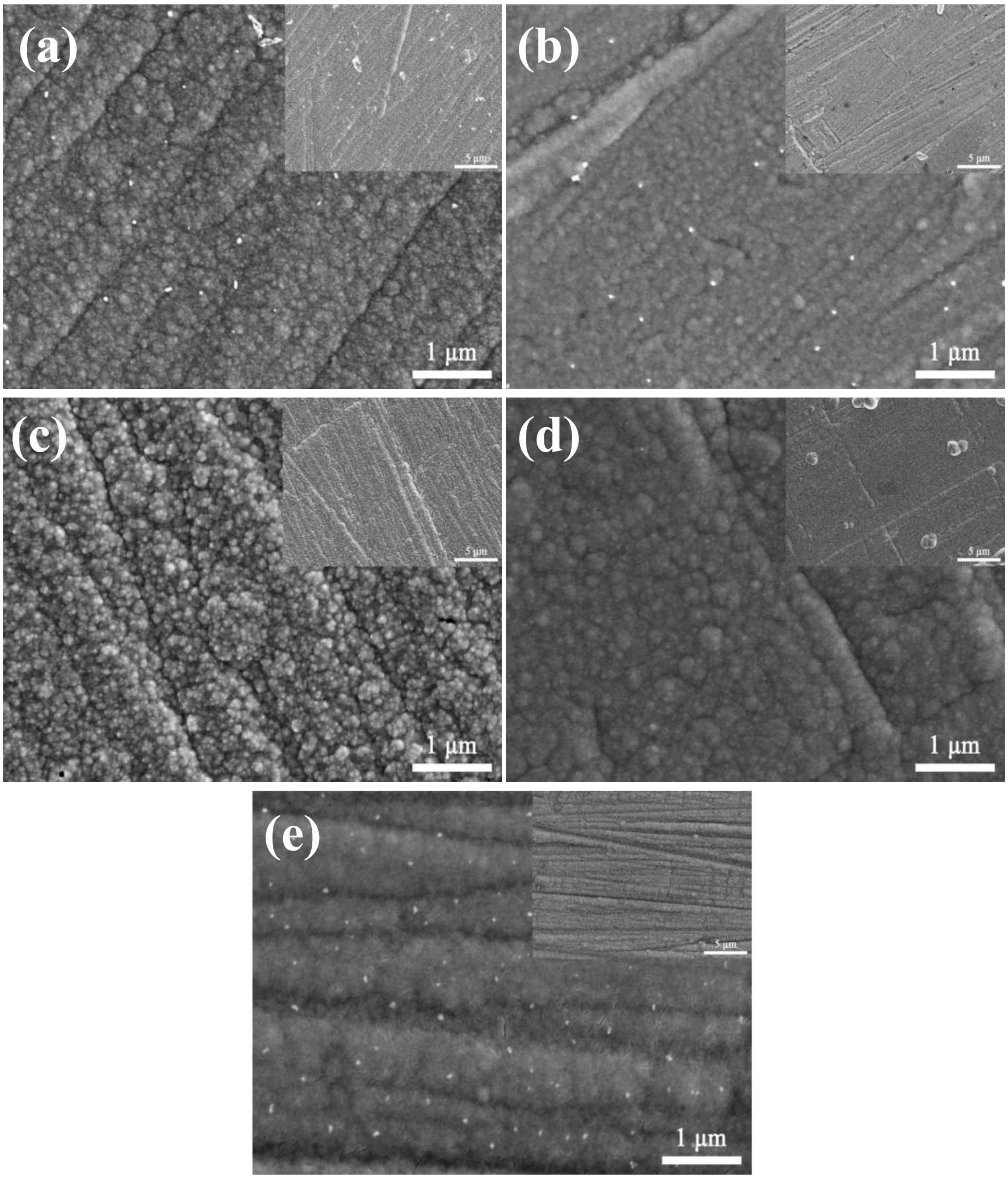

Figure 3.22 SEM images of various alloys electroplated on Cu foil. a) Ni, b) Co, and Ni-Co alloys prepared at c) -1.0 V/Ag/Ag$^+$, d) -1.05 V/Ag/Ag$^+$, e) -1.1 V/Ag/Ag$^+$ at 80 ℃.

The morphologies of electrodeposited Ni-Co alloys prepared in different time and temperature are presented in Figure 3.23. Similar to the other samples, the surface of the electroplated samples as a function of the deposition time and temperature retains a planar configuration characterized by the presence of secondary particles. Changing the deposition time to either 0.5 hours (Figure 3.23a) or 2 hours (Figure 3.23b) has no discernible effect on the morphology of the surface. Similarly, reducing the deposition temperature from 60 °C to 40 °C does not induce any changes in the deposit morphology (Figure 3.23c). However, heating the sediments to a uniform temperature of 80 °C significantly reduces the structure of surface secondary particles, resulting in a much smoother short-range morphology (Figure 3.23d).

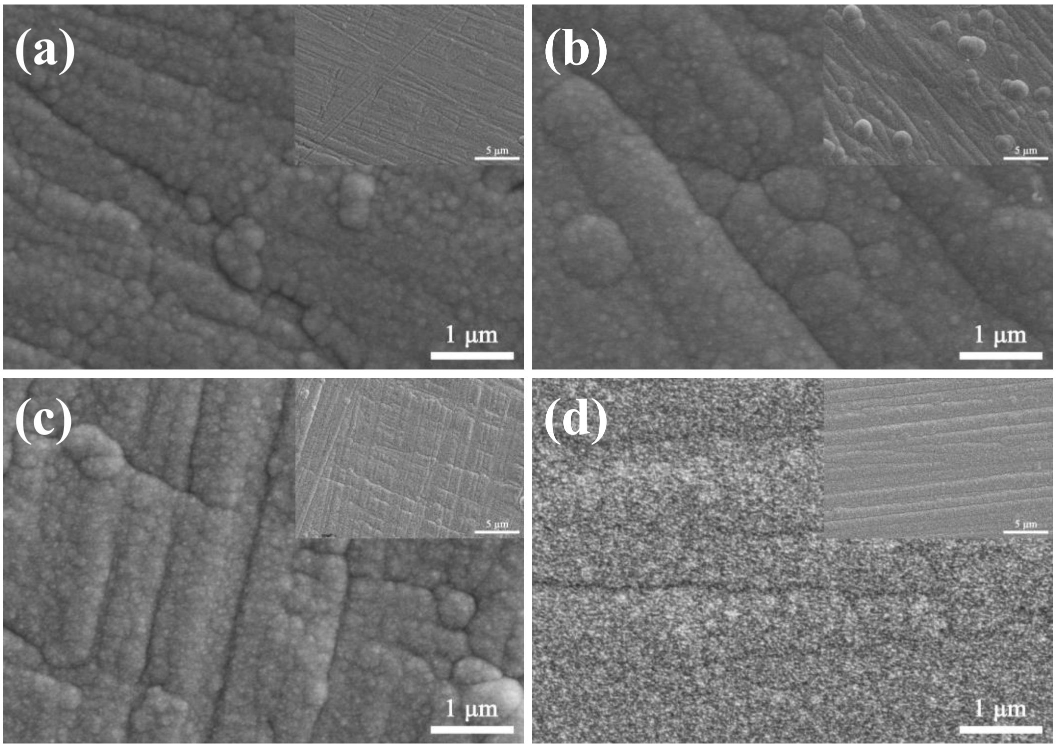

Figure 3.23 SEM morphologies of Ni-Co electrodeposition on Cu foil. Ni-Co alloys prepared at a) -1.05 V/Ag/Ag$^+$,0.5 h, 60 ˚C, b) -1.05 V/Ag/Ag$^+$, 2 h, 60 ˚C, c) -1.05 V/Ag/Ag$^+$,1 h, 40 ˚C, d)-1.05 V/Ag/Ag$^+$,1 h, 80 ˚C.

Due to its ductile nature, copper undergoes deformation prior to fracture. Therefore, unlike FTO glasses which can be broken directly and whose deposit thickness can be analyzed by EDS, direct fracture of copper cannot be used for thickness measurement. Therefore, in this study, SEM is employed as a direct means to observe and analyze the thickness of the deposits, bypassing the need for destructive fracture analysis. From the dimensional measurements of the edge breaks, some information about the deposited film thickness can be derived, as shown in Figure 3.24. The average thickness of the deposited nickel and cobalt is about 1.1 μm and 397.6 nm, respectively. With similar deposition time and temperature, the thickness of Ni-Co alloys prepared using different potentials, namely -1.0 V/Ag/Ag$^+$, -1.05 V/Ag/Ag$^+$, and -1.1 V/Ag/Ag$^+$ increases from 177.8 nm to 1.0 μm and 1.35 μm, respectively. It is generally observed that higher temperatures and longer deposition times lead to thicker deposits. In practical terms, the average thickness of Ni-Co alloys prepared at -1.05 V/Ag/Ag$^+$ can be increased from 490.0

nm to 1.0 μm and 1.6 μm when the deposition times are 0.5 h, 1 h, and 1.5 h, respectively. Similarly, the average thickness of Ni-Co alloys varies from 540.0 nm, 1.0 μm, and 1.2 μm when the temperature is raised from 40 °C, 60 °C, and 80 °C, respectively. The use of higher potentials and temperatures increases electrochemical kinetic energy and improves the electrodeposition process, resulting in greater deposit growth on the surface.

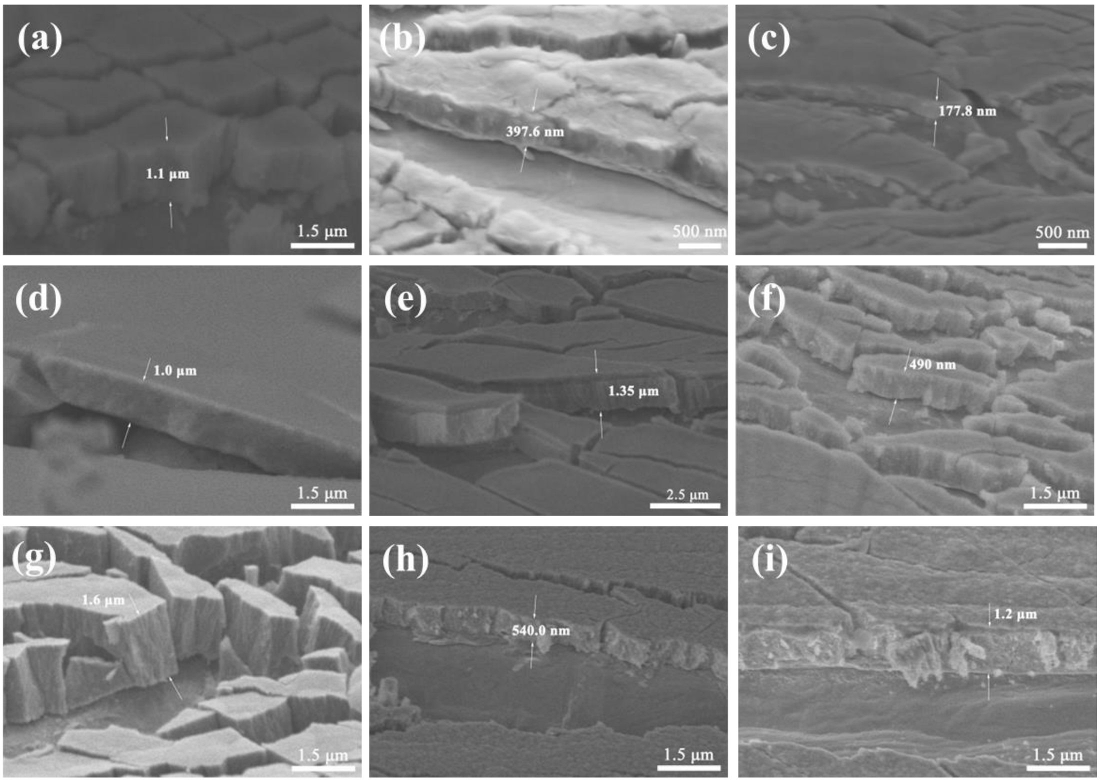

Figure 3.24 SEM morphology of Ni-Co electroplated on Cu foil. a) Ni deposition. b) Co deposition. Ni-Co alloys prepared at c) -1.0 V/Ag/Ag$^+$,1 h, 60 ˚C, d) -1.05 V/Ag/Ag$^+$, 1 h, 60 ˚C, e) -1.1 V/Ag/Ag$^+$,1 h, 60 ˚C, f)-1.05 V/Ag/Ag$^+$,0.5 h, 60 ˚C, g)-1.05 V/Ag/Ag$^+$,2 h, 60 ˚C, h) -1.05 V/Ag/Ag$^+$,1 h, 40 ˚C, i)-1.05 V/Ag/Ag$^+$,1 h, 80 ˚C.

The element concentration of different deposition from EDS is shown in Figure 3.25. The alloy composition on Cu foil can be tuned by changing the deposition potential, duration, and temperature, akin to the process on FTO glasses. As discussed in the context of electrodeposition on FTO glass, elements such as aluminum and chlorine originate from the workbench and the residual ethylammonium nitrate present in the electrodeposition process. Furthermore, an additional peak corresponding to copper is observed in the EDS spectrum, originating from the substrate. However, the EDS spectrum of the Ni-Co alloy prepared at a potential of -1.1 V/Ag/Ag$^+$ shows a noticeable oxygen peak (Figure 3.25e). It can be attributed to the reduction reaction of EAN due to the potential being too close to the limit of the EAN potential window. Nevertheless, the oxygen content in the other deposits remains below 10 at%, which can be due to the formation of a natural oxide film upon exposure to air atmosphere. Consequently, the presence of oxygen can be disregarded for the analysis of alloy composition.

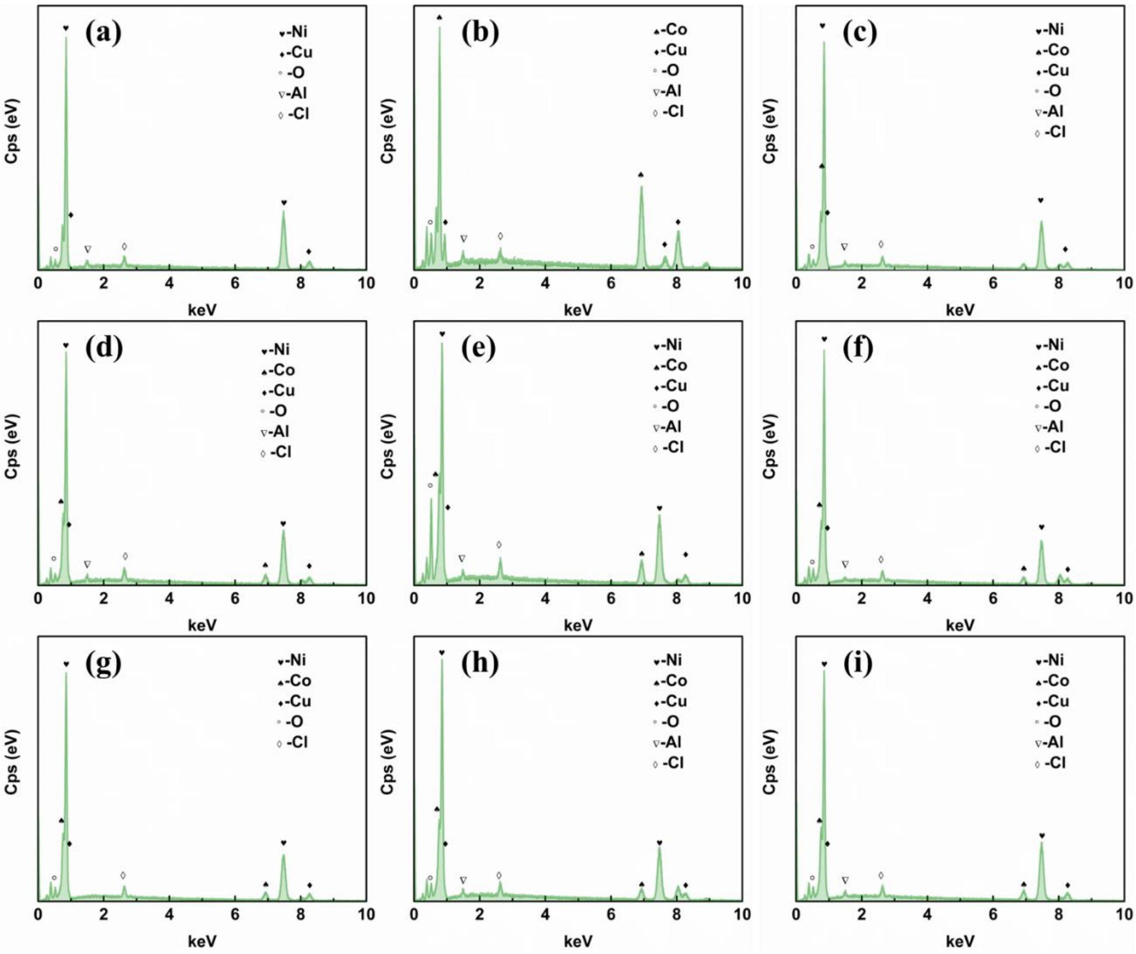

Figure 3.25 EDS spectra of electrodeposition on Cu foil. a) Ni deposition. b) Co deposition. Ni-Co alloys prepared at c) -1.0 V/Ag/Ag$^+$,1 h, 60 °C, d) -1.05 V/Ag/Ag$^+$, 1 h, 60 °C, e) -1.1 V/Ag/Ag$^+$,1 h, 60 °C, f) -1.05 V/Ag/Ag$^+$,0.5 h, 60 °C, g) -1.05 V/Ag/Ag$^+$,2 h, 60 °C, h) -1.05 V/Ag/Ag$^+$,1 h, 40 °C, i) -1.05 V/Ag/Ag$^+$,1 h, 80 °C.

Under a set of specific experimental conditions, including a temperature of 60 ℃, ion concentration of 0.25 M $NiCl_2$ + 0.25 M $CoCl_2$, and an electrodeposition duration of 1 hour, the cobalt content in the Ni-Co alloys gradually increases with a shift towards more cathodic potentials. The Co content ranges from 7.2 at% at -1.0 V/Ag/Ag$^+$, 10.9 at% at -1.05 V/Ag/Ag$^+$, and 20.3 at% at -1.1 V/Ag/Ag$^+$. Surprisingly, the concentration of Co does not show significant variation when the electrodeposition time and temperature are changed, remaining at about

10 at%. Hence, in the electrodeposition process of Ni-Co alloys in ethylammonium nitrate as electrolyte, the deposition time and temperature show an influence on the quantity of electrodeposition, whereas the electrodeposition potential affects both the quantity of electrodeposition and the elemental ratio. Table 3.6 provides a summary of the different alloys prepared on Cu foils based and the respective experimental conditions.

Table 3.6 Elements content of different electrodeposited alloys in EAN on Cu foil.

	Potential (V/Ag/Ag$^+$)	Time (h)	Temperature (°C)	Co (at%)	Ni (at%)	Composition
0.5 M $NiCl_2$	-1.0	1	60	0	100.00	C-Ni
0.5 M $CoCl_2$	-1.05	1	60	100.00	0	A-Co
0.25 M $CoCl_2$ + 0.25 M $NiCl_2$	-1.0	1	60	7.2	92.8	$Ni_{92.8}Co_{7.2}$
	-1.05	1	60	10.9	89.1	$Ni_{89.1}Co_{10.9}$
	-1.1	1	60	20.3	79.7	$Ni_{79.7}Co_{20.3}$
	-1.05	0.5	60	10.1	89.9	$Ni_{89.9}Co_{10.1}$
	-1.05	2	60	10.2	88.8	$Ni_{88.8}Co_{10.2}$
	-1.05	1	40	13.2	86.8	$Ni_{86.8}Co_{13.2}$
	-1.05	1	80	10.9	89.1	$Ni_{89.1}Co_{10.9}$

3.8. Electrocatalytic HER of Ni-Co alloys on Cu foils

The electrocatalytic characteristics of Ni-Co alloys on Cu foil have been studied for the HER using linear sweep voltammetry and cyclic voltammetry in a 1 M KOH aqueous solution, as illustrated in Figure 3.26. The electrocatalytic measurements were performed following the same procedure than the one used for FTO glass electrocatalysis analysis. Since many alloy compositions on the Cu plate are similar, we only select three alloys ($Ni_{92.8}Co_{7.2}$, $Ni_{86.8}Co_{13.2}$, $Ni_{79.7}Co_{20.3}$) with large compositional differences to evaluate the performance of the electrocatalytic hydrogen evolution reaction.

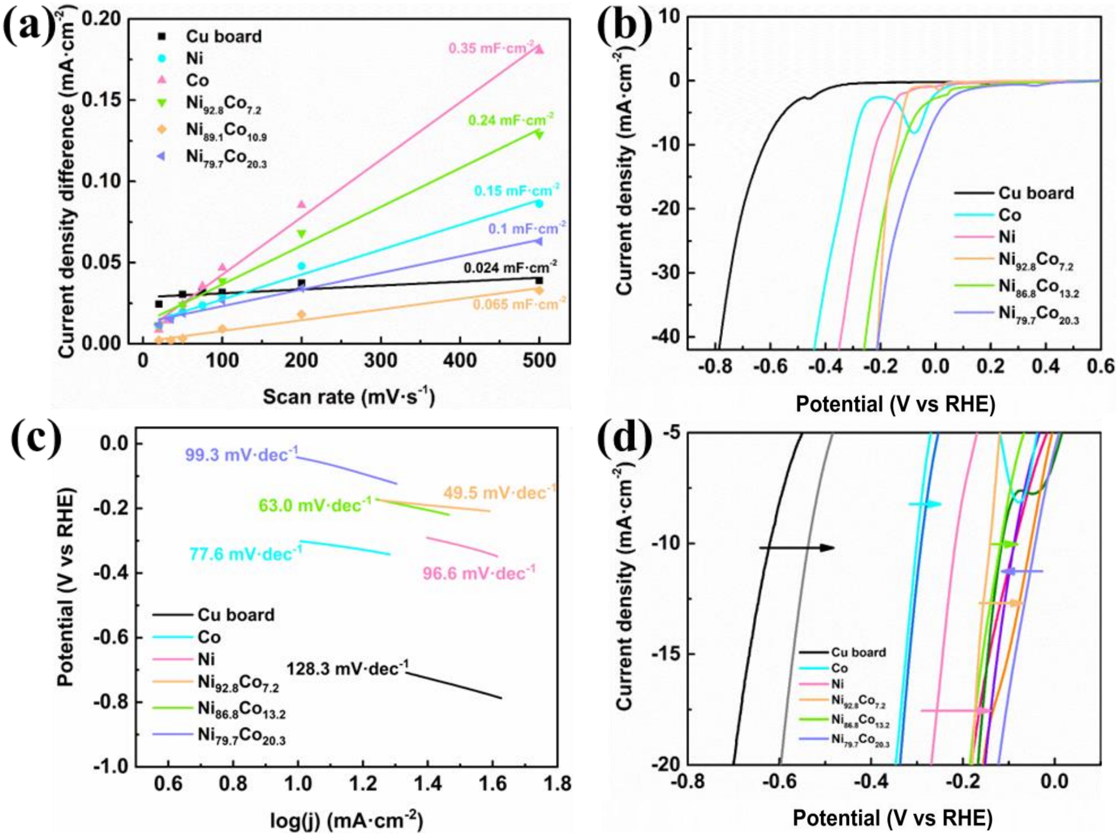

Figure 3.26 Electrochemical properties of the materials towards the HER for different Ni-Co alloys on Cu foil: a) C^{σ} of different Ni-Co alloys, b) LSV curves of Ni-Co alloys with different atomic ratio at a scan rate of 10 mV・s^{-1}, c) Tafel slopes for different alloys for the HER, d) LSV curves of Ni-Co alloys with different atomic ratio after 10 cycles at 10 mV・s^{-1}.

From the slope of the curves in Figure 3.26a, the interfacial capacitance varies from 0.024 mF·cm^{-2} (Cu foil) to 0.35 mF·cm^{-2} (deposited Co). After the electrodeposition process, a substantial increase in the interfacial capacitance of the surface, compared with pure Cu foil, reaching 0.24 mF·cm^{-2} for $Ni_{92.8}Co_{7.2}$. Consequently, the electroplating process resulted in a significant increase of the ECSA on the surface (from 10 to 150 times), indicating higher specific surface area values and therefore an increased number of available catalytic sites. As presented in Figure 3.26b, the electrocatalytic performance of Ni-Co alloys demonstrates lower potentials for the HER when compared to pure Ni and Co. The incorporation of Co into the Ni-Co alloys results in a noticeable reduction in the HER potential at a given current density (-10 mA·cm^{-2}), with values decreasing from -0.22 V/RHE for pure Ni to -0.14 V/RHE, -0.12 V/RHE, and -0.04 V/RHE for Ni-Co alloys containing 7.2 at%, 13.2 at%, and 20.3 at% of Co, respectively.

Table 3.7 Properties of Ni-Co alloys in 1 M KOH solution towards the HER.

.	Cu foil	Ni	$Ni_{92.8}Co_{7.2}$	$Ni_{86.8}Co_{13.2}$	$Ni_{79.7}Co_{20.3}$	Co
C^{σ} (mF·cm^{-2})	0.024	0.15	0.24	0.044	0.1	0.35
Onset potential (V vs RHE)	-0.37	0.04	-0.06	0.09	0.17	-0.04
HER potential (V vs RHE)	-0.62	-0.22	-0.14	-0.12	-0.04	-0.31
Tafel slope (mV·dec^{-1})	128.3	96.6	49.5	63	99.3	77.6
HER potential after 10 cycles (V vs RHE)	-0.54	-0.09	-0.05	-0.11	-0.09	-0.29

In the case of pure Ni, the Tafel slope is 96.6 mV·dec^{-1}. However, the addition of cobalt in the alloy leads to a decreased Tafel slope rate, reaching 49.5 mV·dec^{-1}, showing an enhancement of the reaction kinetics. This observation confirms that the addition of cobalt effectively improves the electrocatalytic performance of the Ni-Co alloy for the HER, similarly to the performance obtained for the Ni-Co alloys on FTO glass substrates. By replacing the substrate from FTO glass with a Cu foil, a notable enhancement in the stability of the Ni-Co alloy was observed. After 10 CV cycles of HER performance testing, no discernible surface damage can be seen on the alloy. The corresponding LSV curves obtained after the cycling experiments is presented in Figure 3.27d.

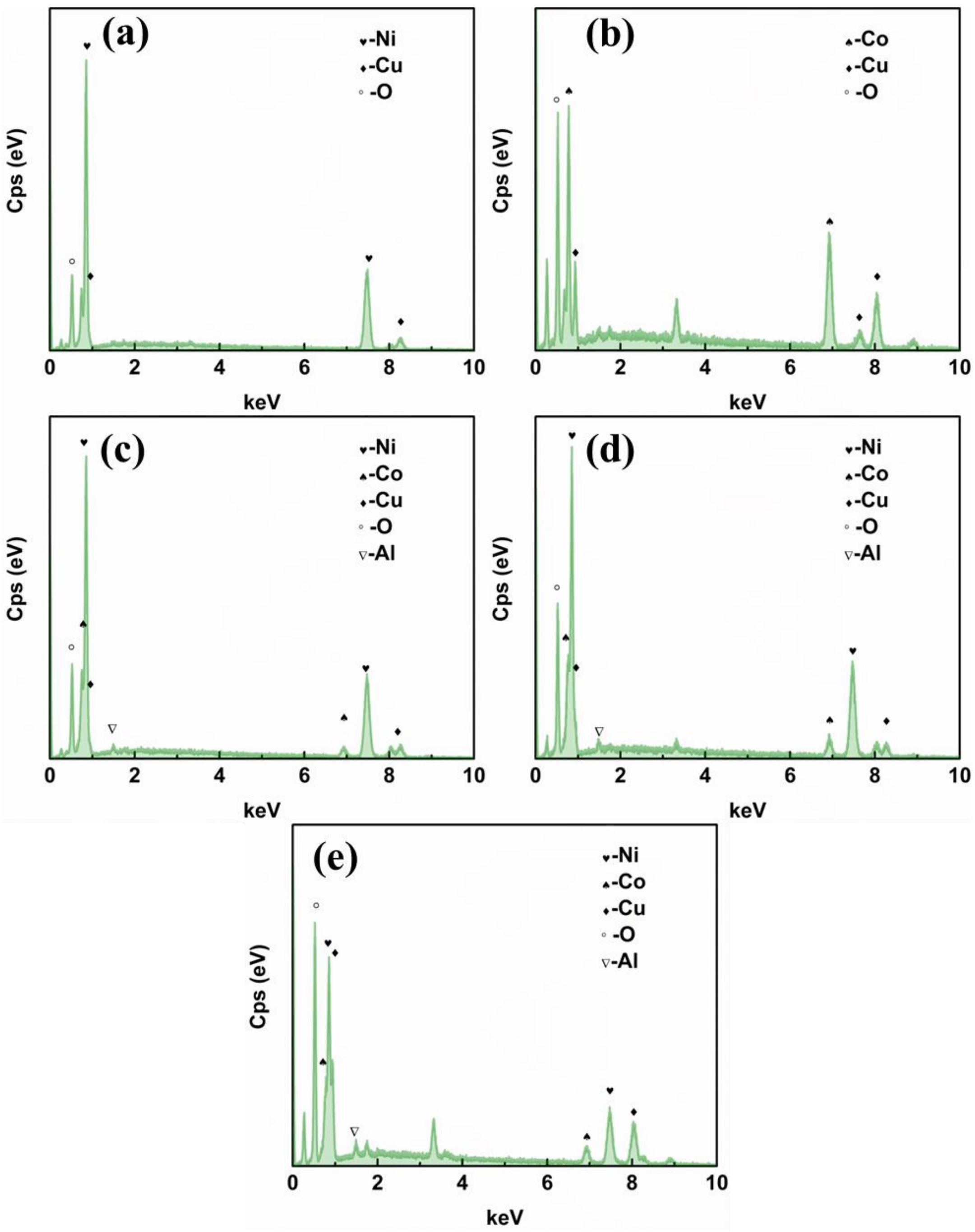

Figure 3.27 EDS spectrums of electrodeposition on Cu foil after 10 cycles HER. a) Ni, b) Co, c) $Ni_{92.8}Co_{7.2}$, d) $Ni_{86.8}Co_{13.2}$, e) $Ni_{79.7}Co_{20.3}$.

It can be seen that the Ni-Co alloy demonstrates a similar or even a decreased HER potential after 10 cycles, indicating its robust stability. For instance, in the case of $Ni_{86.8}Co_{13.2}$, the HER potential reduced from -0.12 to -0.11 V/RHE after the 10 cycles. Examination of the LSV curves before and after the reaction reveals the presence of a reduction peak corresponding to the oxide film in the initial curve, as exemplified by the Co curve in Figure 3.26b. As shown in

Figure 3.27, the EDS data after 10 cycles reaction revealed a high oxygen content on the surface of the sample after the reaction. This is an oxide produced in contact with water after several electrochemical reactions. Although the oxide film formation is facilitated upon contact with water in the absence of reaction, multiple cycles allow reduction reactions prior to HER, as shown in Figure 3.26d. The Co reduction peak of shows a decrease in amplitude (indicated by the blue curve). Consequently, during cycling, the oxide film is consumed by the reduction reaction, exposing the bare alloy surface to the electrolyte.

3.9. Conclusion

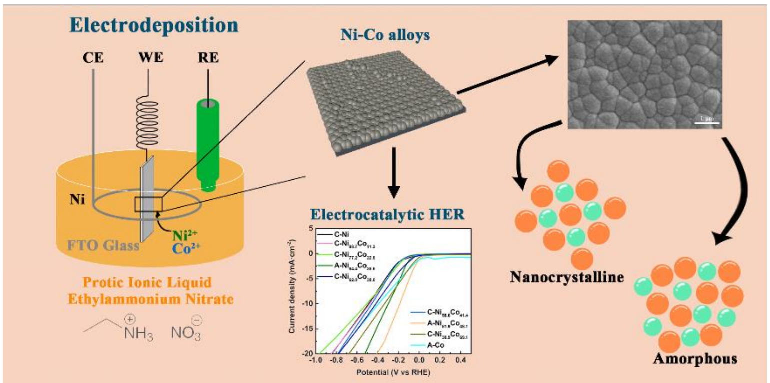

In this work, the electrodeposition of pure Ni, pure Co, and Ni-Co alloys of various compositions on different substrate (FTO glasses and Cu foils) in EAN, a protic ionic liquid, and their properties for HER have been studied. The deposit of Co and Ni as the pure metal on glassy carbon in EAN in the air atmosphere is not a reversible process since it leads to the formation of oxides. Nevertheless, we have succeeded in preparing, for the first time in EAN, pure amorphous Co, nanocrystalline Ni and nanocrystalline/amorphous Ni-Co alloys by electrodeposition on FTO glass in an oxygen-free environment. These electroplated compounds, Ni, Co and Ni-Co alloys were used as electrocatalysts for HER. The beneficial effect of the Co addition on the HER to Ni-based alloys was studied on both FTO glasses and Cu foils, and it was shown that the best performance as catalyst was obtained with the amorphous alloy, A-$Ni_{51.9}Co_{48.1}$. The amorphous state of the alloy exhibits a lower HER potential and faster reaction rate than crystalline alloys with the similar atomic ratio. The stability of Ni-Co alloys electrodeposition can be improved by changing the substrate from FTO glass to Cu foil, with stable surface and HER potential value after 10 cycles (reaching high current density). This study demonstrates that a protic ionic liquid such as EAN is a candidate for the electrodeposition of Ni-based materials and it paves the way for the preparation of Ni/Co-based electrocatalysts by electrodeposition in EAN, providing an interesting route for tuning the composition of alloys by electrodeposition.

Chapter 4 Electrodeposition of Ni/Co-based alloys in DES

From the bibliography review presented in Chapter 1, it was shown that the effect of different elements in the alloy composition on the properties for the HER is requiring a deeper investigation. In the recent years, the alloying of materials has been chosen as an efficient way for improving catalysis properties of the water splitting. In light of the Chapter 3, the incorporation of cobalt into nickel alloys shows significant improvement for the electrocatalytic hydrogen evolution reaction. Remarkably, amorphous alloys composed of nickel and cobalt exhibit promising performance in this regard. Hence, considering the properties of nickel-cobalt alloys, it seems of interest to further investigate the impact of introducing additional elements into the alloy matrix with the objective to increase the performance of the electrocatalytic hydrogen evolution performance. Moreover, from a fundamental point of view, the ability of electroplating alloys made of two or more element is of great interest.

Among various elements, the influence of some light metal (Al, Mg, Zn, et al.) has been studied by other groups [1, 159, 160]. To date, extensive literature has explored the role of Al on the electrocatalytic hydrogen evolution performance of transition metal-based materials [159, 161, 162]. In comparison, investigations concerning the influence of Zn remain restricted. Our search yielded only a solitary relevant document pertaining to this topic. Nady et al. prepared Zn-Ni nanocrystalline alloys by electrodeposition on Cu foil in aqueous solutions, which shows better properties than pure Ni and Zn. However, they didn’t provide any information about the content of oxygen on the alloy surface, and the elemental analysis showed that Zn was the main element in this alloy. We cannot get more information about the effect by Zn in Ni-based alloys.

In the work presented in this chapter, we investigate the possibility to prepare the Ni/Co-based alloys from ILs or DES solvents. In particular, we are interested on the role played by the ILs and DES on the electroplating of alloys, which are different solvents from traditional aqueous solutions. Moreover, the addition of alloyed light metal elements (e.g., Zn) in the alloys and the physicochemical properties of electrolytes will be deeply investigated.

Compared with pure ILs, the preparation of DES is easier and the electrodeposition of Ni in DES has already been studied by some other groups [163, 164]. Ethaline and Menthol-DES shown in Figure 4.1, which are novel DESs, were chosen as the electrolyte for the preliminary experiments [127]. The first question to answer is to study the possibility to prepared Ni in these DESs. Based on the discourse presented in chapter 3, it was observed that the Ni- based alloy film deposited on FTO glass exhibits a lack of stability and a diminished electrocatalytic performance potential when compared to Ni-based alloys deposited on copper foil. Consequently, for the investigations conducted in this chapter, copper shall be employed as the foundational material. Notably, copper foam, distinguished by its elevated specific surface area relative to copper foil, emerges as a better candidate for the substrate. Since it facilitates a greater specific surface area for the deposited material - a highly desirable attribute for electrocatalytic applications. As an initial step, the deposition of nickel shall be performed on the copper foam substrate.

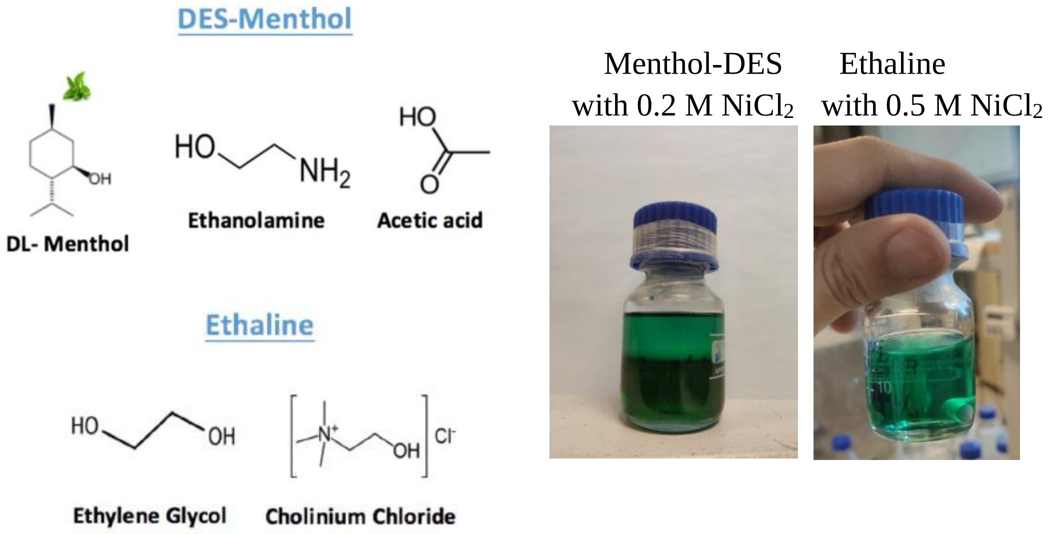

Figure 4.1 Chemical compositions of DES-Menthol and ethaline; and the electrolyte with $NiCl_2$ [127].

4.1. Electrodeposition of Ni on Cu foam in DES

From Figure 4.1, a separation phenomenon becomes apparent in menthol-DES, particularly following the introduction of nickel salt ($NiCl_2$). We thus deduce that it arises from the phase separation phenomenon triggered by the distinct solubility of $NiCl_2$ within the individual components of the DES. As a result, in order to improve ion diffusion and promote a more homogeneous mixing throughout the electrodeposition process, we implemented magnetic stirring during the electrodeposition in menthol-DES. In chapter 3, we found that Cu foil is more suitable for the electrodeposition (high stability) than FTO glasses. Therefore, Cu foam or foil will be used as the substrate for electrodeposition. Cu foam is a new multifunctional material with a large number of connected and unconnected holes uniformly distributed in the copper matrix. All Cu-based matrix were cleaned with acetone and 0.1 M HNO_3, respectively, to remove surface oxide. After solution cleaning, the Cu foils were polished as described in Chapter 2,.

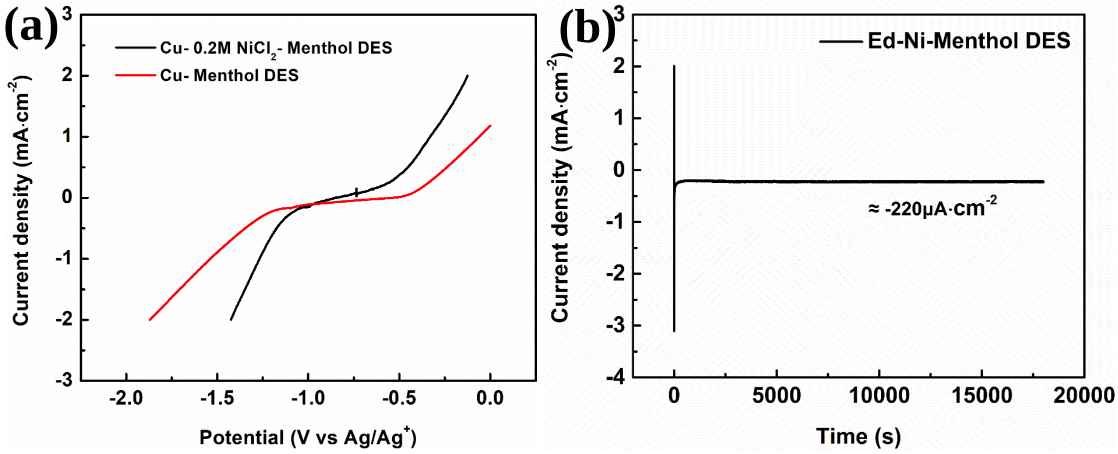

Figure 4.2 a) Linear sweep voltammetry of Cu foam in Menthol-DES with and without $NiCl_2$ (0.2 M); b) Chronoamperometry for the Cu electroplating in menthol-DES at 40 ℃ for 5 h.

For a better understanding of the electroplating process, it is important to determine the potential for the reduction reaction of Ni^{2+} in Menthol-DES. The polarization curves of Menthol-DES with a concentration of 0.2 M $NiCl_2$ were recorded during experiments conducted on Cu foam in air atmosphere (Figure 4.2a). The reduction reaction of Menthol-DES on Cu foam starts at a potential of -1.09 V/Ag/Ag^+, while the reduction of Ni^{2+} begins at -1.0 V/Ag/Ag^+. Considering the challenges associated with accurately determining the real surface area of foamed copper, we employed the geometric area (2 × 1 cm × 0.5 cm) when calculating the working area of the foamed copper. Moreover, to ensure clarity and minimize any potential ambiguity, we selected a potential of -1.05 V/Ag/Ag^+ and a temperature of 40 ℃ for the nickel electrodeposition process. From Figure 4.2b, we can see that the current density during the electrodeposition is rather low, about -220 μA·cm^{-2}. Therefore, long deposition times (5 hours and 15 hours) were used for the electroplating with such a low current density. The amount of electric charge can be calculated using Equation (35). For 5 h electrodeposition, one can obtain 2.59 C which were consumed, corresponding to 1.34×10^{-5} mol of Ni deposited on the Cu foam. These results are summarized in Table 4.1.

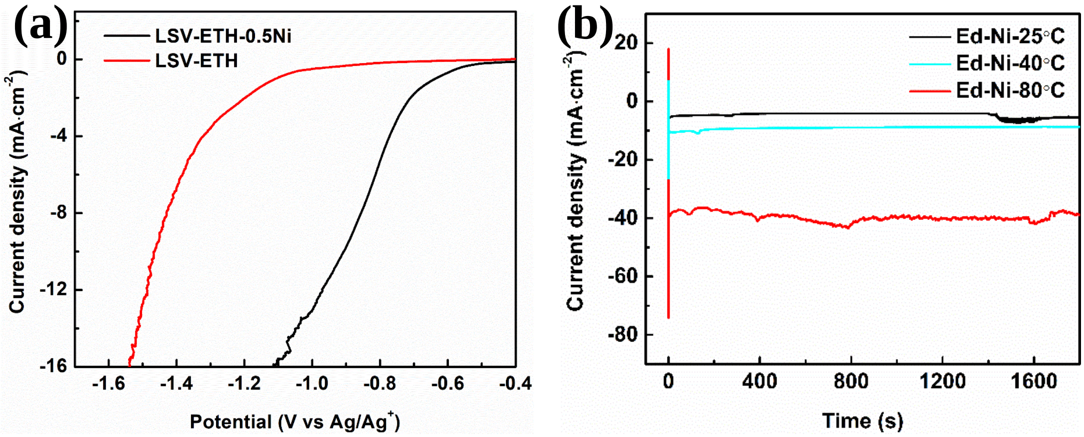

Figure 4.3 a) Linear sweep voltammetry curve of a Cu foam in ethaline with 0.5 M NiCl$_2$; b) Chronoamperometry curve of the electrodeposition in ethaline + 0.5 M NiCl$_2$ at different temperatures.

In addition, we explored the process of nickel electrodeposition in ethaline. The LSV curve presented in Figure 4.3a shows that the potential window of ethaline is limited to -1.01 V/Ag/Ag^{+} on the reduction domain. However, with the introduction of Ni^{2+}, the electrochemical window undergoes a rightward shift to -0.58 V/Ag/Ag^{+}, corresponding to the beginning of the reduction reaction of Ni^{2+}. This shift clearly indicates that the reduction of nickel can take place within the electrochemical window of ethaline. Consequently, we used -1.0 V as the deposition potential for nickel. As part of the electrodeposition process, temperature is a parameter that has been varied between 25 °C, 40 °C, and 80 °C. The current-time curves are shown in Figure 4.3b. It can be seen that the current value increases with temperature, reaching -40 mA·cm^{-2} for deposition at 80 °C. Additionally, the deposition time has been also been investigated (0.5 hours, 1 h, 5 hours, and 15 hours). As expected, it was shown that higher temperatures and longer deposition times lead to an increase of the amount of Ni electroplated. For instance, the deposition quantity increases from 5.19×10^{-5} mol, 1.02×10^{-4} mol, and 4.44×10^{-4} mol when the temperature increases from 25 °C, 40 °C, and 80 °C, respectively. Similarly, using a constant temperature and deposition potential, the deposition quantity shows a nearly proportional variation with the deposition time, varying from 2.41×10^{-4} mol, 8.87×10^{-4} mol, and 3.07×10^{-3} mol for electroplating durations of 1 hour, 5 hours, and 15 hours, respectively (Table 4.1).

Table 4.1 Charge and amount of Ni electroplated as a function of various parameter.

	Potential (V/Ag/Ag$^+$)	Time (h)	Temperature (℃)	Electron charge (C)	Electroplated Ni (mol)
Menthol-DES + 0.2 M $NiCl_2$	-1.05	5	40	2.59	1.34×10^{-5}
	-1.05	15	40	7.56	3.92×10^{-5}
Ethaline + 0.5 M $NiCl_2$	-1.0	0.5	25	10.0	5.19×10^{-5}
	-1.0	0.5	40	19.60	1.02×10^{-4}
	-1.0	0.5	80	85.61	4.44×10^{-4}
	-1.0	1	40	46.48	2.41×10^{-4}
	-1.0	5	40	171.00	8.87×10^{-4}
	-1.0	15	40	591.50	3.07×10^{-3}

4.2. Characterization of Ni alloys

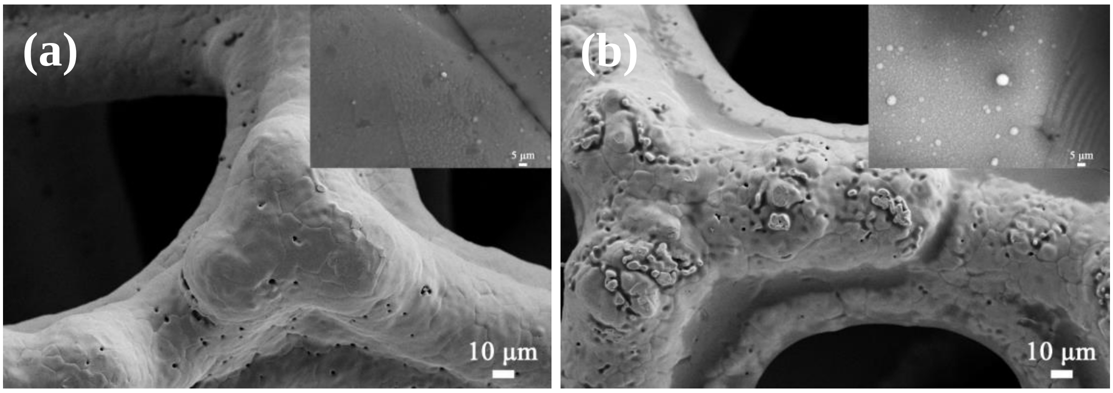

Figure 4.4 Morphologies electroplated Ni on Cu foam at 40℃ from Menthol-DES for 5 h (a) and 15 h (b).

The discussion in the previous sections has shown that the maximum amount of nickel deposition in Menthol-DES is low, so even if long deposition times are used, a large amount of deposition cannot be achieved. This can be verified by SEM observation presented in Figure 4.4. The results indicate that even after 5 hours of electrodeposition, the surface of the copper foam remains relatively smooth. However, closer examination reveals fine crystalline structures on the surface, although their growth is uneven, with significant areas devoid of deposits, as shown in Figure 4.4a. When increasing the deposition time up to 15 hours, a noticeable increase in sediment structures becomes apparent on the surface of the copper foam. A closer examination of the surface shows a greater density of crystal particles, which are more clearly visible when zoomed in, as shown in Figure 4.4b.

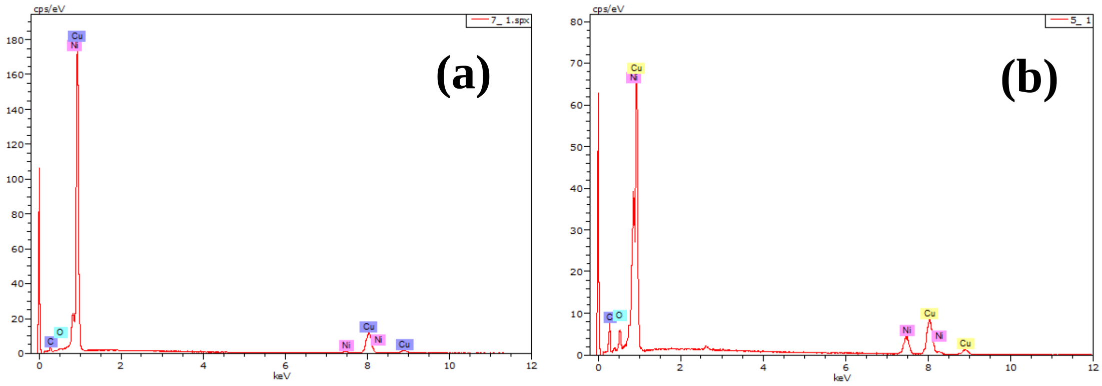

Figure 4.5 EDS analysis of electrodeposited Ni on Cu foam at 40℃ from Menthol- DES for 5 h (a) and 15 h (b).

However, EDS analysis illustrates that the amount of sediment obtained was not as expected. Figure 4.5a shows that no distinct nickel signal peak can be detected on the surface for five-hour deposition, with only a prominent copper peak from the substrate being observed. After 5 h deposition, we obtain only 4.5 at% Ni, which is very low and most of the elements are Cu from Cu foam (Table 4.2). After 15 h deposition, Figure 4.5b shows more intense Ni peaks than the one observed for the sample electroplated for 5 h. However, the Ni content is still lower that the Cu content (25.75 at%). The conclusion is that although nickel electrodeposition can be achieved in Menthol-DES, the deposition efficiency remains remarkably low. Even on the copper foam, which has a high specific surface area and an excellent conductivity, only 25.75

at% of nickel can be obtained after a 15-hour electrodeposition procedure. We have therefore chosen not to use Menthol-DES for these metal deposits.

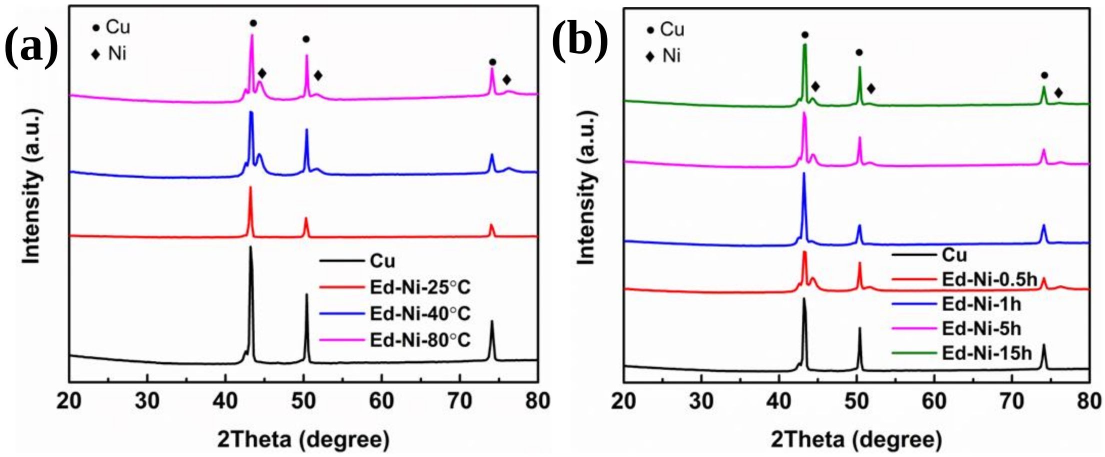

Figure 4.6 XRD patterns of different electrodeposited alloys. a) XRD spectra of deposited Ni in ethaline with 0.5 M $NiCl_2$ at different temperatures on Cu foam. b) XRD spectra of Ni prepared in ethaline with 0.5 M $NiCl_2$ with different times on Cu foam.

From the discussion in the previous parts, we deduced that the amount of nickel deposited in ethaline is significantly larger than the amount deposited from a Menthol-DES electrolyte. Despite the non-smooth surface of the copper foam, X-ray diffraction (XRD) can still be performed, showing distinct diffraction peaks characteristic of pure nickel crystals, as shown in Figure 4.6. As the temperature increases, the intensity of the nickel peak becomes more intense (Figure 4.6a). Furthermore, regardless of the change in the deposition time, the presence of the nickel peak can always be observed. Moreover, the half-peak width of nickel suggests that the deposited nickel possesses a nanocrystalline structure.

SEM analysis shows distinct electroplated layers formed on the foamed Cu surface. Figure 4.7 provides an overview of the samples obtained for various experimental conditions. At 25 °C, a half-hour deposition in ethaline shows needle-like crystal structures with nanoscale dimensions, which is in agreement with the XRD analysis. As the temperature increases up to 80 °C, the needle-like morphology is becoming better defined and increases in size. For instance, at 80 °C, the needle-like structures connect together, forming a more extensive topography with a branched structure.

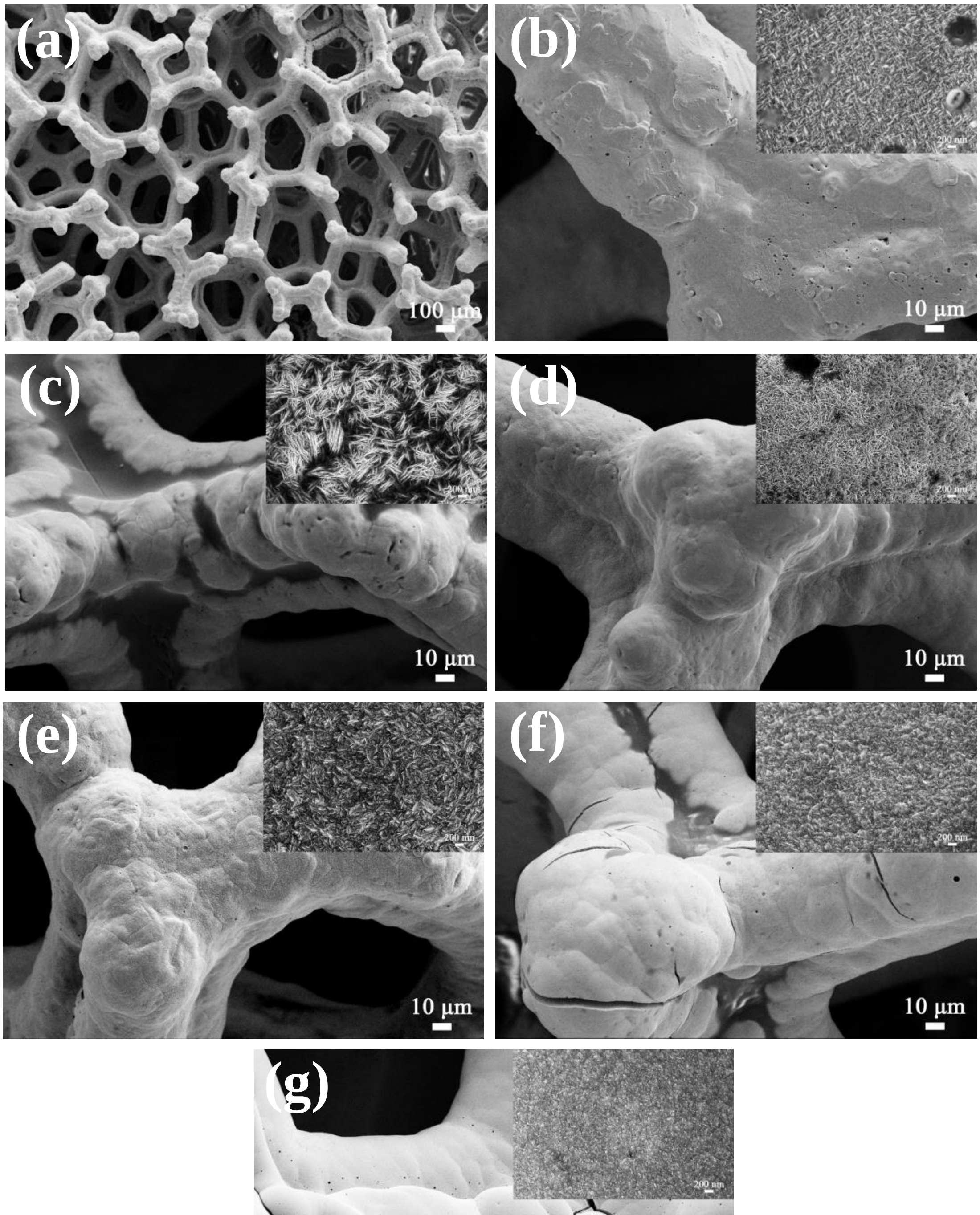

Figure 4.7 SEM images of a) Cu foam, and electrodeposited Ni on Cu foam in ethaline with 0.5 M $NiCl_2$ as a function of the temperature: b) 25 ℃, c) 40 ℃, d) 80 ℃ and as a function of time: e) 1 h, f) 5 h and g) 15 h.

However, no significant thickening of the coating is observed with increasing temperature, requiring further study. Furthermore, alongside the persisting needle-like structure, the surface coating demonstrates significant thickening with an increase of the deposition time. While precise numerical measurements are challenging, the topography of the surface exhibits cracks as a result of excessive deposit thickness. This indicates that increasing the deposition time is an effective approach to enhance both the content and thickness of the sediment.

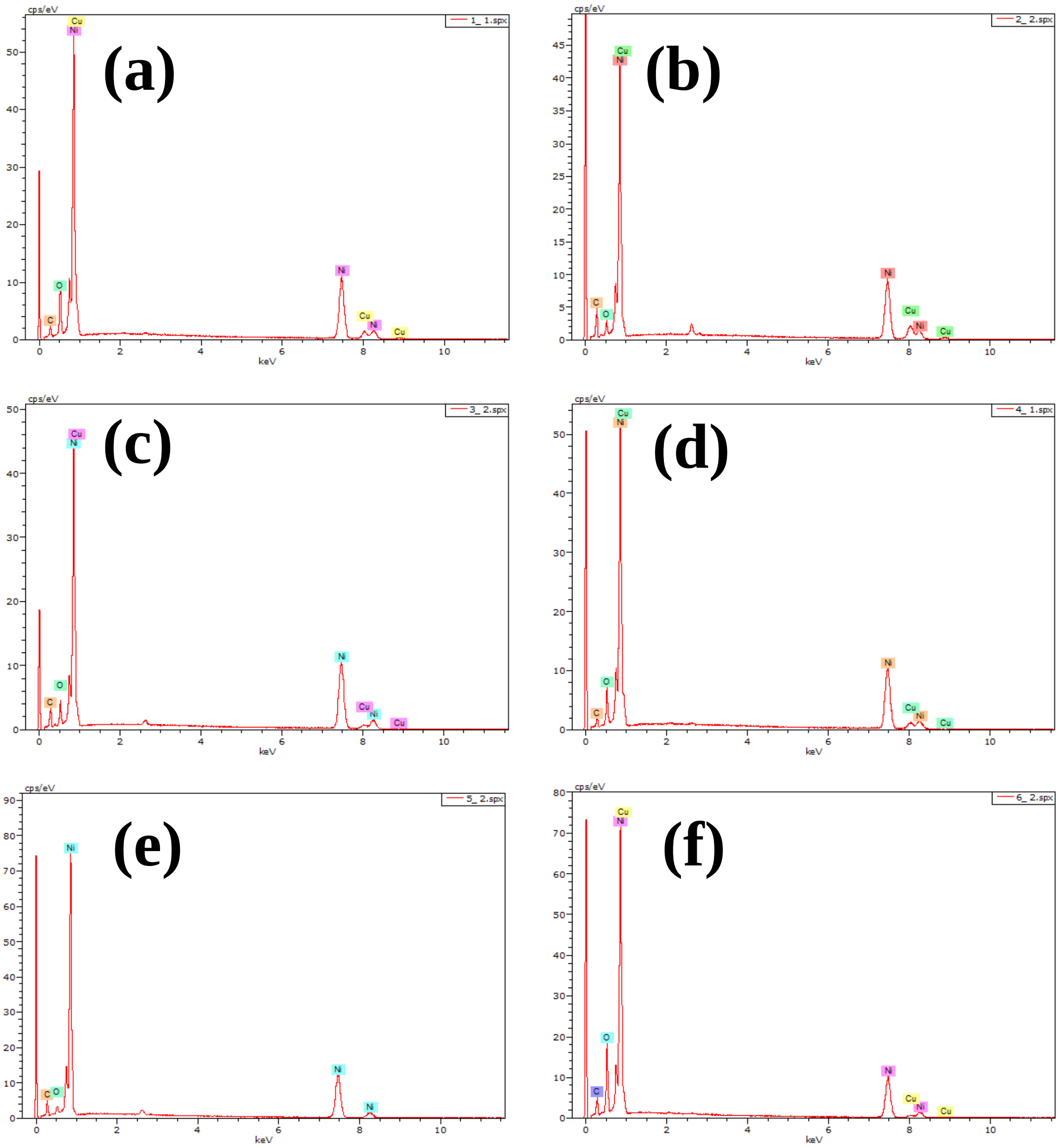

Figure 4.8 EDS analysis of electrodeposited Ni on Cu foam in ethaline with 0.5 M $NiCl_2$ at various temperatures of a) 25 ℃, b) 40 ℃, c) 80 ℃ and for different deposition times d) 1 h, e) 5 h and f) 15 h.

From EDS analysis, the elemental content of the electroplated material in ethaline can be obtained, enabling to deduce the quantity and thickness of deposits. For the same deposition duration and potential (Table 4.2), an increase in temperature results in a gradual decrease of

Cu from 13.29 at% at 25 °C to 11.51 at% at 40 °C, and 6.94 at% at 80 °C. Additionally, EDS analysis shows that as the deposition time increases, the thickness of the surface film also increases. For a deposition time of 5 hours, no copper can be detected, thus indicating that it has been effectively covered by a thick layer of nickel. However, it is noteworthy that even after a 15-hour deposition step, a signal of about 3.72 at% Cu can still be obtained by EDX analysis. This is likely due to the partial substrate exposure resulting from the fine cracks observed in the SEM images which can also lead to some material removal.

Table 4.2 Elemental analysis (by EDS) of electrodeposited Ni in different conditions.

	Potential (V/Ag/Ag$^+$)	Time (h)	Temperature (°C)	Cu (at%)	Ni (at%)
Menthol-DES + 0.5 M $NiCl_2$	-1.05	5	40	95.49	4.51
	-1.05	15	40	74.25	25.75
Ethaline + 0.5 M $NiCl_2$	-1.0	0.5	25	13.29	86.71
	-1.0	0.5	40	11.51	88.49
	-1.0	0.5	80	6.94	93.06
	-1.0	1	40	10.74	89.21
	-1.0	5	40	0	100.00
	-1.0	15	40	3.72	96.28

4.3. Electrocatalytic properties of Ni on Cu foam in HER

The electrocatalytic properties of electroplated Ni on Cu foam have been extensively investigated for the HER using linear sweep voltammetry and cyclic voltammetry in a 1 M KOH aqueous solution, as illustrated in Figures 4.9a & b. The electrocatalytic measurements were performed following the same experimental procedure used for studying the electrochemical response of the Ni-Co alloys on FTO glass. We only focus on the overpotentials (HER potentials) and Tafel slope of the deposited Ni in this part to review the HER properties.

As shown in Figures 4.9a & b, it can be seen that the HER potential decreases from -0.47 V/RHE for a copper foam to -0.16 V/RHE -0.18 V/RHE and -0.14 V/RHE, corresponding to materials prepared at 25 ℃, 40 ℃ and 80 ℃, respectively. It indicates that the reaction occurs more easily with a coating of Ni. Concerning the effect of the electrodeposition time, it can be seen that the HER potential decreases from -0.47 V/RHE to -0.18 V/RHE, -0.11 V/RHE, -0.02 V/RHE, and -0.06 V/RHE, corresponding to the materials prepared in 0.5 h, 1 h, 5 h and 15 h, respectively.

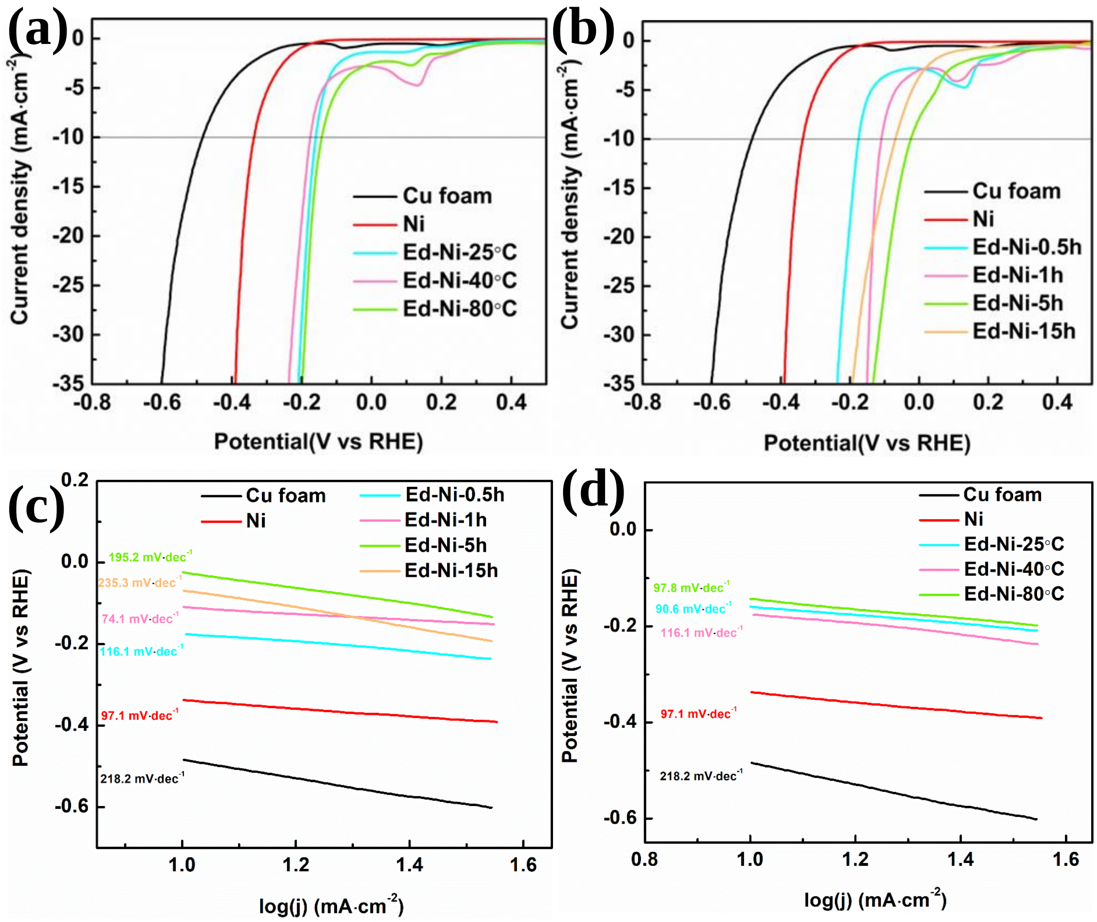

Figure 4.9 Polarization curves (a, b) and Tafel plots (c, d) for the HER observed for the electrodeposited Ni for different times or for different temperatures in alkaline solution.

In the case of pure Ni electrode, the Tafel slope is about 97.1 mV·dec^{-1}. However, the coating of Ni on Cu foam leads to a decreased Tafel slope, reaching 74.1 mV·dec^{-1}, corresponding to an increase of the reaction kinetics. Compared with pure Cu foam, the Tafel slope value for each electroplated Ni is always much lower than 218.2 mV·dec^{-1}.

Based on these results, the choice of materials was naturally directed towards nickel-based alloys electroplated on copper to study the electrocatalytic reaction of hydrogen evolution on these metals. However, it should be noted that sample characterization on Cu foam presents significant challenges, despite its high specific surface area and catalytic performance. In order to achieve as complete an understanding as possible of electrodeposition on copper surfaces, our subsequent experiments will therefore focus primarily on characterizing Cu plates.

Table 4.3 Properties of the different materials for the HER in basic solution.

Sample	**HER Potential (V vs RHE)**	**Tafel slope (mV·dec^{-1})**
Ni foil	-0.34	97.1
Cu foam	-0.48	216.2
25 °C/0.5 h	-0.16	90.6
40 °C/0.5 h	-0.18	116.1
80 °C/0.5 h	-0.14	97.8
40 °C/1 h	-0.11	74.1
40 °C/5 h	-0.02	195.2
40 °C/15 h	-0.07	-235.3

4.4. Physicochemical properties of ethaline solutions

Since the effect of Zn in Ni/Co-based alloys for HER reaction is still not clear, and the literature on the topic is poor (only a few papers have been published on Zn and Ni electrodeposition in ethaline)[165, 166], these alloys have been synthesized and characterized. Based on the study of the previous section, we believe that ethaline will be a suitable electrolyte solvent for electrodeposition. We now need to measure its physicochemical properties.

Table 0.4 (in the annex section) provides an overview of the physicochemical properties of various electrolytes used in this chapter, including viscosity, density, pH, and conductivity, as a function of temperature. For each electrolyte solution with different ion concentrations, the density, viscosity, and pH decrease, while conductivity increases when increasing the temperature, as shown in Figure 4.10. However, it is noteworthy that the addition of $CoCl_2$, $NiCl_2$, and $ZnCl_2$ to ethaline leads to a slight increase in density, possibly attributed to the slight swelling of ethaline at the same temperature.

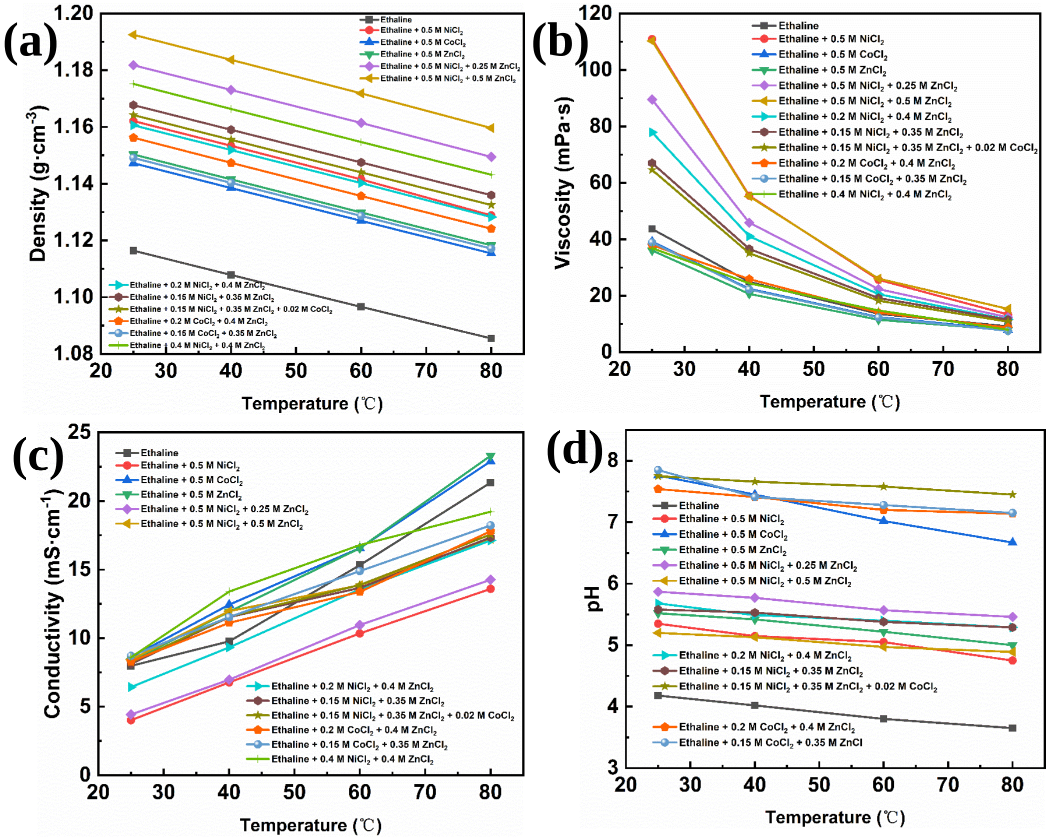

Figure 4.10 Evolution of the density (a), viscosity (b), conductivity (c), and pH (c) of ethaline electrolyte for different concentrations as a function of the temperature.

Moreover, an increase in the temperature results in a decrease in the viscosity of the solutions. For instance, the addition of $NiCl_2$ to ethaline significantly increases the viscosity of the solution, warranting special attention. For instance, the viscosity value of ethaline solution increases from 43.7 mPa·s to 110.9 mPa·s for a 0.5 M $NiCl_2$ addition. For other solutions in which $NiCl_2$ was added, they also show a higher viscosity than that of pure ethaline. Therefore, the electrodeposition in ethaline with $NiCl_2$ need higher temperature in order to improve diffusion of ions. Conversely, the addition of $ZnCl_2$ and $CoCl_2$ slightly reduces the viscosity of ethaline. The viscosity of ethaline with 0.5 M $CoCl_2$ and 0.5 M $ZnCl_2$ is 39.17 mPa·s and 36.05 mPa·s.

The solutions prepared with a mixture of $ZnCl_2$ and $CoCl_2$ also show a lower value in viscosity: 38.0 mPa·s, 38.9 mPa·s and 36.9 mPa·s, for ethaline containing 0.2 M $CoCl_2$ and 0.4 M $ZnCl_2$, 0.15 M $CoCl_2$ and 0.35 M $ZnCl_2$, and 0.4 M $CoCl_2$ and 0.4 M $ZnCl_2$, respectively. The conductivity of all these electrolytes increases with the addition of different salts. The conductivities of all ethaline solutions are similar, close to the value of pure ethaline, 7.97 $mS\cdot cm^{-1}$, except for ethaline with 0.5 $NiCl_2$ and with 0.5 $NiCl_2$ + 0.25 $ZnCl_2$, which shows a conductivity of 4.02 $mS\cdot cm^{-1}$ and 4.43 $mS\cdot cm^{-1}$, respectively. The pH of pure ethaline at 25 ℃ is 4.18. Except the solutions containing 0.5 M $CoCl_2$, metallic-salt containing ethaline solutions show higher pH when compared to pure ethaline. The specific pH measurements for $CoCl_2$ solutions are not available. The reaction of Co^{2+} and water in ethaline solution will produce H^+ and CoO, and the reaction of CoO and water will further produce more H^+, which leads to a decrease in pH value. [167] It is obvious that conductivity is significantly higher and viscosity significantly lower at elevated temperatures. Although Ni electrodeposition can be carried out at room temperature, greater deposition efficiency can be achieved by selecting an electrodeposition temperature above 60°C, as described later in this chapter.

4.5. Electrodeposition Ni/Co-Zn in ethaline

Prior to study the co-deposition of Ni and Co on a copper substrate, it is necessary to assess the ability for each individual element to be electroplated. Figure 4.11a illustrates that the addition of 0.5 M $NiCl_2$ or 0.5 M $CoCl_2$ to ethaline causes a noticeable shift in its electrochemical window towards more positive potentials. On pure copper plate electrodes, the cathodic scan of ethaline typically shows a reduction wave at -1.15 V/Ag/Ag^+, corresponding to the current density of -0.01 $mA\cdot cm^{-2}$, the left end of potential window of ethaline. However, the addition of 0.5 M $NiCl_2$ shifts the electrochemical window of ethaline to -0.81 V/Ag/Ag^+, while the addition of 0.5 M $CoCl_2$ shifts it to -0.92 V/Ag/Ag^+. This is ascribed by the metal deposit corresponding to the reduction reaction of Ni^{2+} and Co^{2+} that can occur within the electrochemical window of ethaline on a copper substrate, without the reaction of ethaline. For the reduction reaction of Zn^{2+}, it necessitates a position slightly beyond the electrochemical window of the solution. The electrochemical window value of ethaline with 0.5 M $ZnCl_2$ is -

1.16 V/Ag/Ag$^+$, with a distinct reduction reaction peak observed in the range from -1.16 V/Ag/Ag$^+$ to -1.94 V/Ag/Ag$^+$, corresponding to the reduction of Zn^{2+}. It means that between the potential range of -1.16 V/Ag/Ag$^+$ to -1.94 V/Ag/Ag$^+$, Zn can be deposited on the Cu, accompanied by the reduction reaction of a small part of ethaline. Consequently, the electrodeposition of pure Ni and pure Co can be performed in ethaline without any reaction involving the solvent reaction/degradation, while the electrodeposition of Zn can only be carried out slightly beyond the electrochemical window of ethaline, such as at -1.25 V/Ag/Ag$^+$. The chronoamperograms illustrating the electrodeposition of pure nickel, pure cobalt, and pure zinc are presented in Figure 4.11c. For the electrodeposition of zinc, a duration of 2 hours was used (for an easiest comparison, only the first hour displayed on this figure). Due to the sluggish diffusion process, the nucleation interval is considerably extended, exceeding 200 seconds. As a result, fitting analysis of the traditional nucleation mechanism, similarly to what was presented in Chapter 3, was not applied to this system. Calculation based on the data shows that 3.76×10^{-5} mol of zinc have been electrodeposited after 2 hours, disregarding the electron consumption during the reduction reaction of a small amount of ethaline. In contrast, after 1 hour of electrodeposition, 6.18×10^{-5} mol of nickel and 8.54×10^{-5} mol of cobalt were obtained.

Our objective is to prepare an alloy comprising nickel or cobalt as the primary elements and zinc as the secondary element by electrodeposition. This will enable us to investigate the impact of zinc addition on the electrocatalytic performance of the alloy. Consequently, our subsequent task involves obtaining various alloys with varying different parameters, including electrolyte composition, deposition potential, deposition time, and temperature. Figure 4.11b shows the LSV curves of ethaline containing various metallic salts (0.5 M $NiCl_2$ + 0.25 M $ZnCl_2$, 0.4 M $CoCl_2$ + 0.2 M $ZnCl_2$, 0.35 M $ZnCl_2$ + 0.15 M $NiCl_2$). In the polarization curve of ethaline with 0.35 M $ZnCl_2$ + 0.15 M $NiCl_2$, in addition to the reduction peak of nickel between -0.7 V/Ag/Ag$^+$ and -0.9 V/Ag/Ag$^+$, a reduction peak corresponding to Zn between -1.25 V and 1.35 V/Ag/Ag$^+$ can be observed. The chronoamperograms of partial alloys co-electrodeposition are shown in Figure 4.11d.

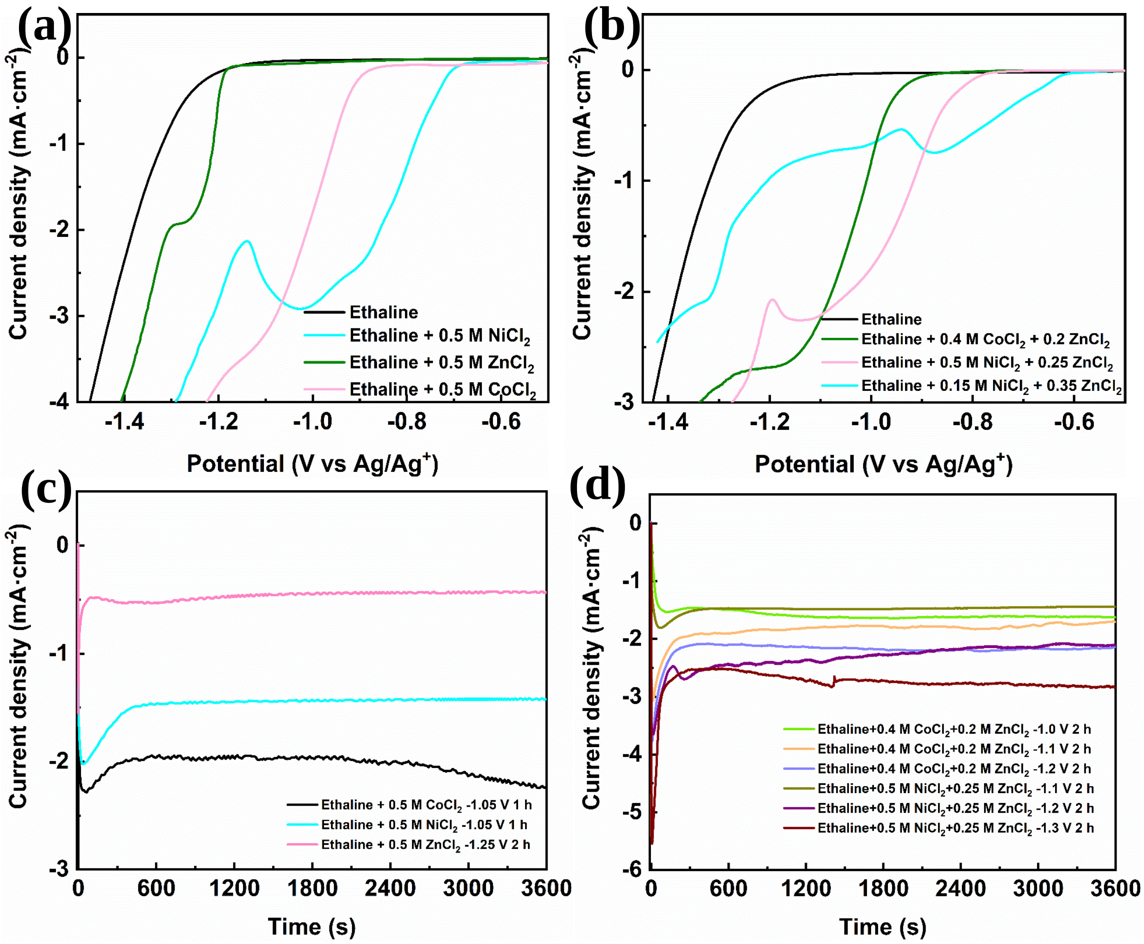

Figure 4.11 a, b) Linear sweep voltammetry curves of ethaline with different ions on Cu foil at 40 ºC performed in glove box. b, d) Comparison of different chronoamperograms obtained under various conditions during Ni/Co-based alloys electrodeposition.

The charge exchange and the amount material deposited for the various experimental conditions are summarized in Table 4.4. To investigate the co-deposition reaction of Ni and Co in ethaline, a solution containing 0.2 M $NiCl_2$ and 0.3 M $CoCl_2$ was used. A consistent trend was observed: with the same deposition time and temperature, decreasing the electrodeposition potential from -0.9 V/Ag/Ag$^+$ to -1.0 V/Ag/Ag$^+$ and -1.1 V/Ag/Ag$^+$ resulted in a significant increase in the quantity of material deposited, from 3.16×10^{-5} mol to 4.80×10^{-5} mol and 7.94×10^{-5} mol, respectively. Moreover, the addition of $ZnCl_2$ further enhanced the amount of electroplated material (with identical deposition potential, time, and temperature conditions). For instance, in the case of ethaline containing 0.5 M $NiCl_2$ and 0.5 M $ZnCl_2$, for an electrodeposition potential of -1.1 V/Ag/Ag$^+$, a deposition time of 2 hours, and a deposition temperature of 40 °C, a larger deposition amount was obtained compared to ethaline with 0.5 M $NiCl_2$ and 0.25 M $ZnCl_2$.

Table 4.4 Charge exchanged and evaluation of the amount of Ni/Co-Zn deposited on the Cu substrate.

ETHALINE +	Potential (V/Ag/Ag^+)	Time (h)	Temperature (°C)	Electron charge (C)	Electrodeposition quantity (mol)
0.5 M $ZnCl_2$	-1.25	2	40	7.25	3.76×10^{-5}
0.5 M $NiCl_2$	-1.05	1	40	11.93	6.18×10^{-5}
0.5 M $CoCl_2$	-1.1	1	40	16.48	8.54×10^{-5}
0.2 M $NiCl_2$ + 0.3 M $CoCl_2$	-0.9	1	40	6.09	3.16×10^{-5}
	-1.0	1	40	9.27	4.80×10^{-5}
	-1.1	1	40	15.32	7.94×10^{-5}
0.15 M $NiCl_2$ + 0.35 M $ZnCl_2$	-1.3	1	40	5.204	2.70×10^{-5}
	-1.3	2	40	11.45	5.93×10^{-5}
	-1.3	6	40	20.79	1.08×10^{-4}
	-1.35	1	40	7.94	4.11×10^{-5}
	-1.3	3.5	60	33.09	1.71×10^{-4}
0.5 M $NiCl_2$ + 0.25 M $ZnCl_2$	-1.1	2	40	23.66	1.23×10^{-4}
	-1.2	2	40	35.77	1.85×10^{-4}
	-1.3	2	40	46.86	2.43×10^{-4}
0.5 M $NiCl_2$ + 0.5 M $ZnCl_2$	-1.1	2	40	75.84	3.93×10^{-4}
	-1.2	2	40	128.20	6.64×10^{-4}
	-1.3	2	40	142.60	7.39×10^{-4}
0.2 M $NiCl_2$ + 0.4 M $ZnCl_2$	-1.2	2	40	13.56	7.03×10^{-5}
0.15 M $CoCl_2$ + 0.35 M $ZnCl_2$	-1.25	1	40	7.40	3.83×10^{-5}
	-1.3	1	40	8.31	4.31×10^{-5}
	-1.3	3.5	60	54.18	2.81×10^{-4}
0.4 M $CoCl_2$ + 0.2 M $ZnCl_2$	-1.0	2	40	25.56	1.32×10^{-4}
	-1.1	2	40	27.84	1.44×10^{-4}
	-1.2	2	40	35.25	1.83×10^{-4}
0.4 M $CoCl_2$ + 0.4 M $ZnCl_2$	-1.1	2	40	140.6	7.29×10^{-4}
	-1.2	2	40	141.3	7.32×10^{-4}
	-1.3	2	40	151.0	7.83×10^{-4}

4.6. Characterization of Ni/Co-Zn alloys

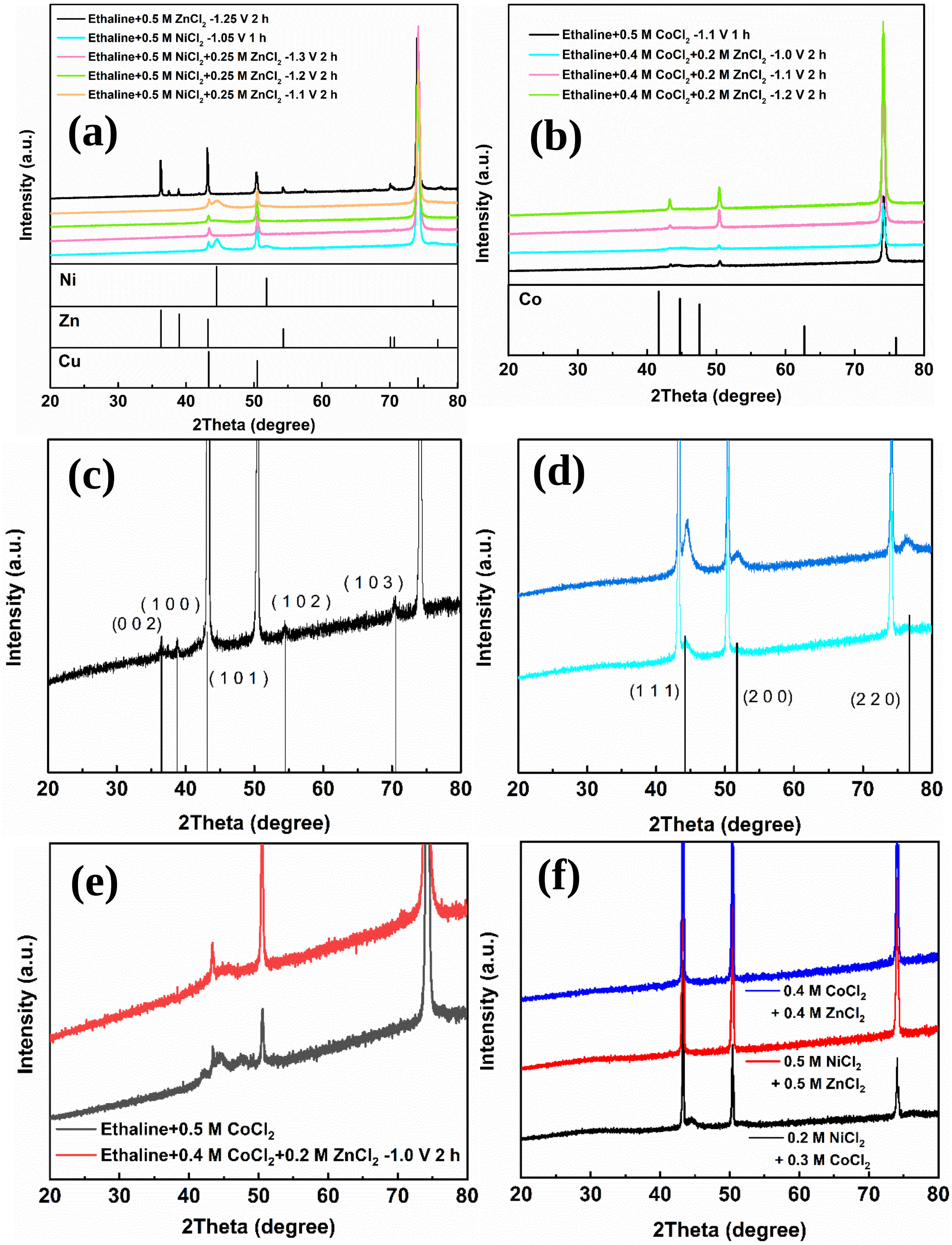

Figure 4.12 XRD patterns of different electrodeposited alloys. a) Ni and Ni-Zn deposits prepared in ethaline with 0.5 M $NiCl_2$ + 0.25 M $ZnCl_2$, b) pure Co and Co-Zn alloys prepared in ethaline with 0.4 M $CoCl_2$ + 0.2 M $ZnCl_2$, partial XRD of Zn (c), Ni and Ni-Zn deposit (d), and Co and Co-Zn deposit (e), f) XRD of other deposits on Cu foil.

Figure 4.12 shows the XRD patterns corresponding to the alloys prepared with the experimental conditions corresponding to results presented in Figure 4.11c and 4.11d. A deposition potential of -1.05 V/Ag/Ag$^+$ and a deposition time of 1 hour are sufficient to obtain detectable Zn signals in the XRD patterns. The enlarged XRD plot, presented in Figure 4.12c, shows characteristic peaks attributed to Zn. It is worth mentioning that the tiny peaks between the (0 0 2) and (1 0 0) crystal planes may arise from a small amount of ZnO on the surface. Moreover, the electrodeposited pure nickel exhibits a nanocrystalline structure, with an average grain size of approximately 60 nm, calculated using the half-width of the main peak. The crystal structure of Ni-Zn deposits, prepared in ethaline with 0.5 M $NiCl_2$ + 0.25 M $ZnCl_2$, also shows a tendency towards nanocrystalline grain, particularly for the samples obtained at a potential of -1.1 V/Ag/Ag$^+$. A closer inspection of Figure 4.12d (the lower curve), diffraction peaks corresponding to the three crystal planes (1 1 1), (2 0 0), and (2 2 0) of elemental nickel can be observed. However, no distinctive peak ascribed to Zn is observed, suggesting that the amount of Zn present is relatively low, and it is likely solid-dissolved within the nickel crystals or exists in amorphous state.

The XRD patterns of electroplated Co and Co-Zn prepared in ethaline with 0.4 M $CoCl_2$ + 0.2 M $ZnCl_2$ are shown in Figure 4.12b. The pure Cu peaks are virtually the only signal obtained in the Co-based deposits. A very weak peak characteristic of cobalt is observed only for pure Co electrodeposition, as shown in Figure 4.12e. Furthermore, the Co-Zn alloy prepared at a deposition potential of -1.0 V/Ag/Ag$^+$ shows an amorphous structure (Figure 4.12e). XRD diagrams of other deposits are shown in Figure 4.12f. It is evident that the majority of the XRD spectra of the sample show mainly characteristic peaks corresponding to the Cu substrate, and that it is difficult to observe clear signals from the deposited material. The limited amount of deposition is a major contributor to the lack of discernible information in the XRD patterns.

Figure 4.13 shows the SEM images of various deposits, including nickel, zinc, nickel-cobalt deposits prepared in ethaline with 0.2 M $NiCl_2$ + 0.3 M $CoCl_2$, and nickel-zinc deposits prepared in ethaline with 0.5 M $NiCl_2$ + 0.25 M $ZnCl_2$. The surface of pure nickel appears smooth, devoid of prominent features. Pure zinc, on the other hand, has a surface composed of coarse particles of approximately 1 micron in size, resulting in a highly irregular surface topography.

The morphologies of Ni-Zn deposits prepared in ethaline with 0.5 M $NiCl_2$ + 0.25 M $ZnCl_2$ are presented in Figure 4.13c-e. For a deposition potential of -1.1 V/Ag/Ag^+, the surface of Ni-Zn deposits shows dense needle-like grains, reminiscent of the Ni deposited on Cu foam discussed in the previous section. However, with a decrease of the deposition potential to -1.2 V/Ag/Ag^+, needle-like features gradually diminish, and the surface tends to be composed of larger secondary particles. Finally, for a potential of -1.3 V/Ag/Ag^+, the surface becomes flat, with no perceptible features or irregularities. The morphologies of Ni-Co deposits prepared in ethaline with 0.2 M $NiCl_2$ + 0.3 M $CoCl_2$ are presented in Figure 4.13f-h. Similarly, for a deposition potential of -0.9 V/Ag/Ag^+, Ni-Co deposit has a rough and cluster-like surface. As the deposition potential is decreased to -1.0 V/Ag/Ag^+, the surface morphology turns to a needle-like grain morphology. This needle-like crystal structure remains present even at a lower potential (-1.1 V/Ag/Ag^+).

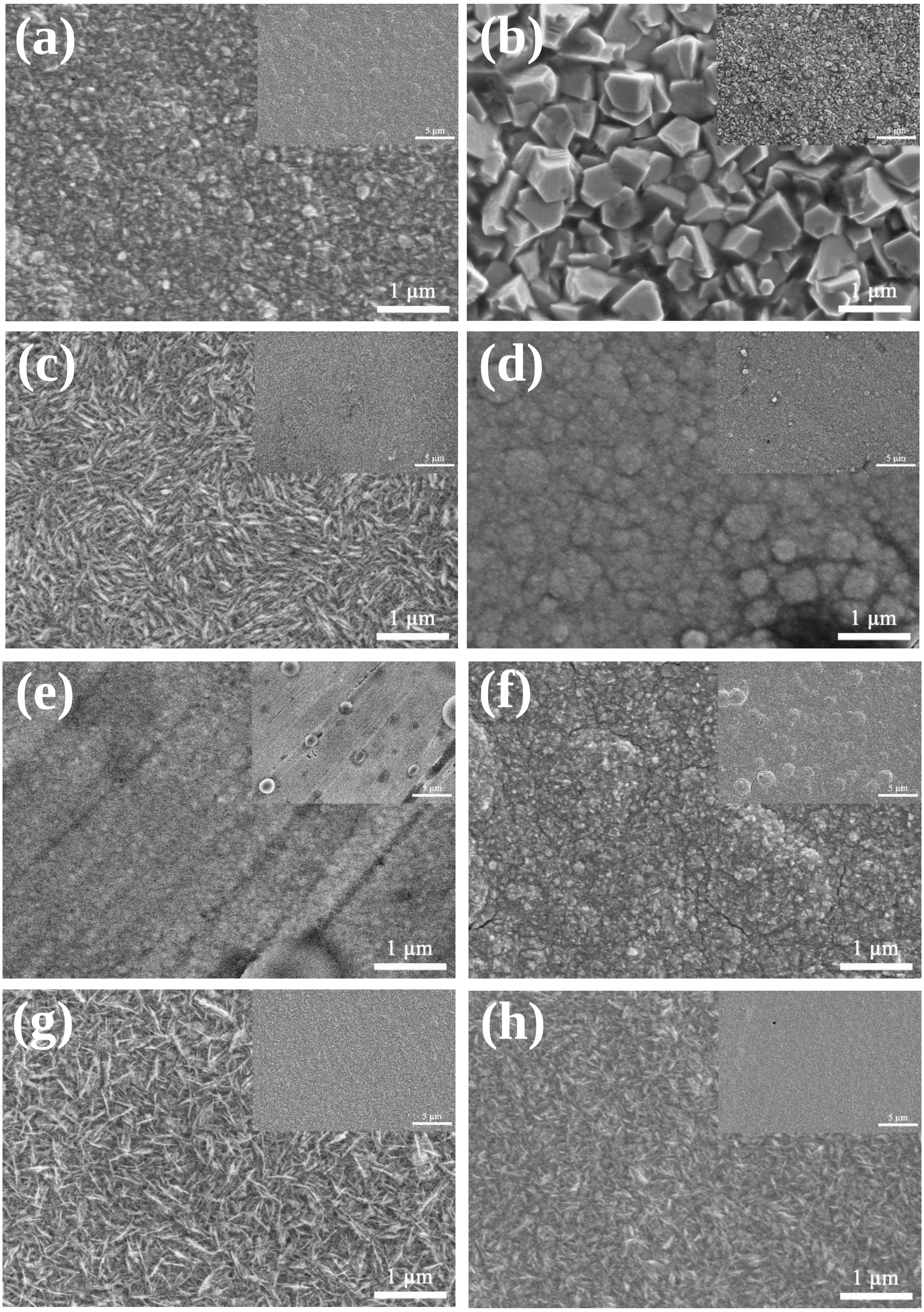

Figure 4.13 SEM morphologies of deposited Ni (a), Zn (b), Ni-Zn deposits prepared in ethaline with 0.5 M $NiCl_2$ + 0.25 M $ZnCl_2$ with a potential of -1.1 V/Ag/Ag^+ (c), -1.2 V/Ag/Ag^+ (d), -1.3 V/Ag/Ag^+ (e), Ni-Co deposits prepared in ethaline with 0.2 M $NiCl_2$ + 0.3 M $CoCl_2$.with a potential of -0.9 V/Ag/Ag^+ (f), -1.0V/Ag/Ag^+ (g) and -1.1 V/Ag/Ag^+ (h).

It is evident that deposits of nickel and nickel-based products tend to form rough surfaces characterized by a clustered composition and needle-like grain structure under appropriate deposition potentials. Such a surface morphology should have a beneficial impact on catalytic reactions by increasing the specific surface area of the deposits.

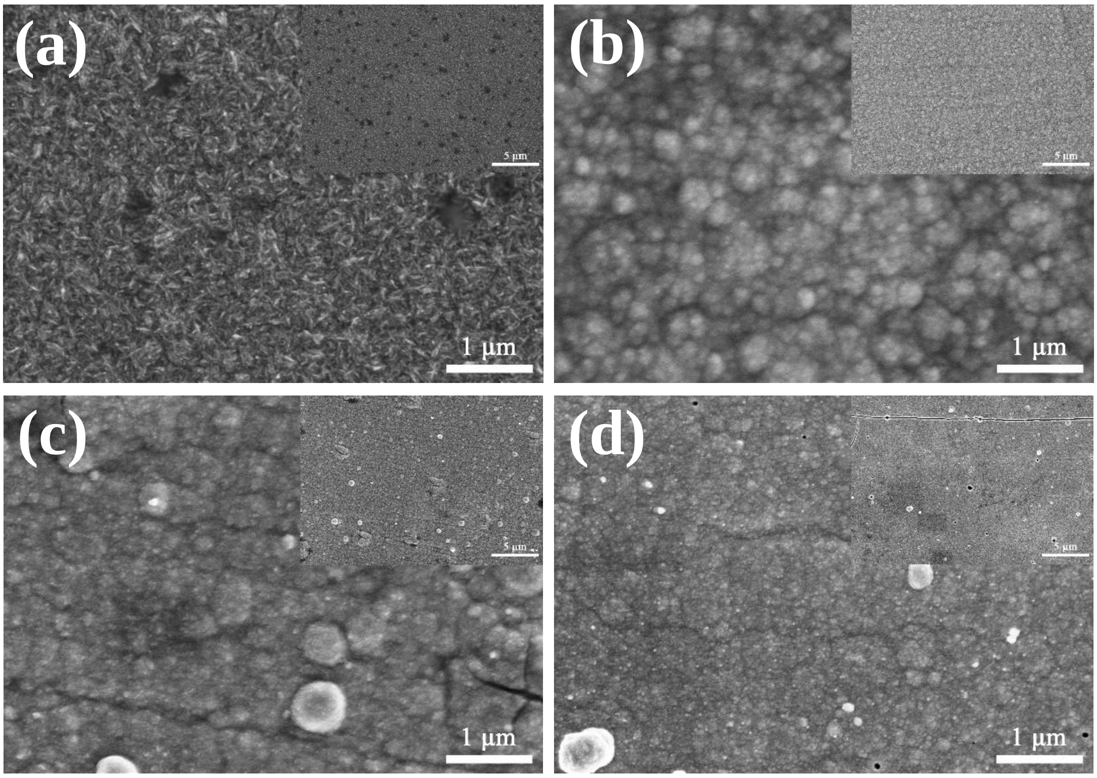

Figure 4.14 SEM morphologies of deposited Co (a), Co-Zn deposits prepared in ethaline with 0.4 M $NiCl_2$ + 0.2 M $ZnCl_2$ with a potential of -1.0 V/Ag/Ag^+ (b), -1.1 V/Ag/Ag^+ (c), and -1.2 V/Ag/Ag^+ (d).

The surface morphology of electroplated Co is presented in Figure 4.14, showing the presence of a similar fine needle-like structure to that observed for the electroplated Ni and Ni-Zn. When $ZnCl_2$ is added to the electrolyte, the surface morphology of Co-Zn deposits deposited at different potentials in ethaline with 0.4 M $NiCl_2$ + 0.2 M $ZnCl_2$ exhibits similarities, characterized by a secondary particle structure. With a decrease of the deposition potential from -1.0 V/Ag/Ag^+ to -1.1 V/Ag/Ag^+ and then to -1.2 V/Ag/Ag^+, the secondary particle structure on the surface becomes progressively denser. Finally, for the lower potentials, the surface morphology tends to become relatively smooth, as presented in Figure 4.14d.

EDS analysis allows the elemental content on the surface of the deposits in ethaline to be obtained, providing insights into the quantity and thickness of the deposits. The elements of interest in EDS analysis include Ni, Zn, Co, Cu, and O. The small peak observed adjacent to the Cl peak corresponds to Al, originating from the SEM bench, and will be disregarded in the data analysis. Figure 4.15a-c shows that nearly pure Ni, Co, and Zn deposits can be obtained, with oxygen contents of only 3.6 at%, 7.7 at%, and 9.6 at%, shown in Table 4.5, respectively. There is no significant presence of Cu on the surfaces of Zn and Co deposits, while Ni deposit shows a 2.2 at% Cu content.

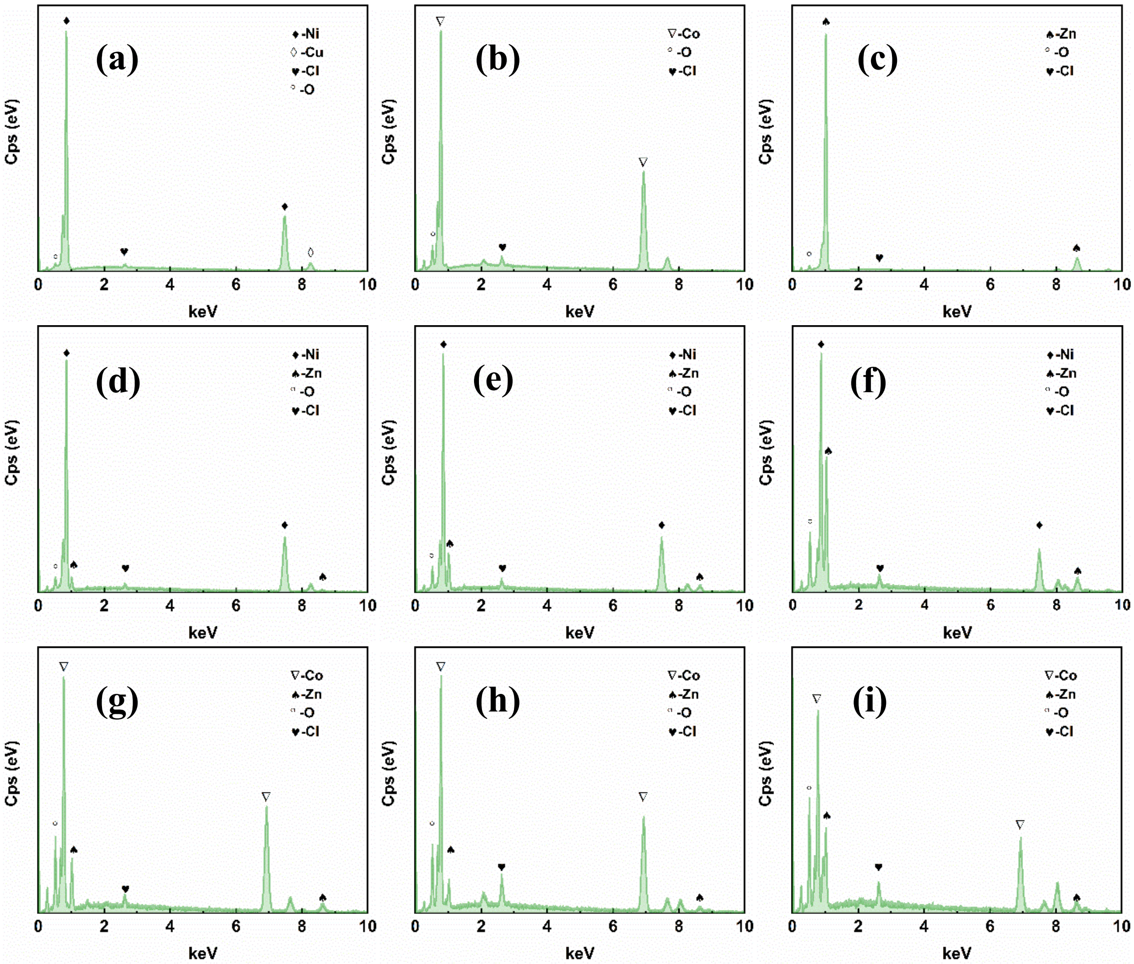

Figure 4.15 The EDS curves of electrodeposited Ni (a), Co (b), Zn (c), Ni-Zn deposits prepared in ethaline with 0.5 M NiCl$_2$ + 0.25 M ZnCl$_2$ at a potential of -1.1 V/Ag/Ag$^+$ (d), -1.2 V/Ag/Ag$^+$ (e), -1.3 V/Ag/Ag$^+$ (f), Co-Zn deposits prepared in ethaline with 0.4 M NiCl$_2$ + 0.2 M ZnCl$_2$ at a potential of -1.0 V/Ag/Ag$^+$ (g), -1.1 V/Ag/Ag$^+$ (h), and -1.2 V/Ag/Ag$^+$ (i).

The aim of adjusting deposition potential, electrolyte concentration ratio, temperature, and duration of the electroplating is to tune the composition of the deposits. Moreover, for all of the deposits, our goal is also to minimize the oxygen content, but also the copper content, thus indicating that a sufficient thickness of the coating, with deposition mainly in the form of metal alloys rather than oxides. For the Ni-Co co-deposition experiments in ethaline with 0.2 M NiCl$_2$

+ 0.3 M $CoCl_2$, we showed that it is possible to adjust the electroplating potential so as to obtain Ni-Co alloys with different compositions, together with a low oxygen and copper contents, (less than 10 at%). For the electrodeposition performed in ethaline containing 0.15 M $NiCl_2$ + 0.35 M $ZnCl_2$, we observed that at a negative electrodeposition potential (-1.3 V/Ag/Ag^+), more Zn than Ni was obtained. Although Ni content (41.9 at%) is larger than Zn (5.8 at%), by increasing the deposition time up to 6 hours, the large Cu content (36.6 at%) suggests inadequate film thickness or density. Indeed, during the electrodeposition process, a large number of bubbles are generated under a high overpotential for a long period of time, hindering nucleation and growth. For the electrodeposition in ethaline containing 0.5 M $NiCl_2$ + 0.5 M $ZnCl_2$, although the Cu and O contents are relatively low (less than 10 at%), adjusting the electrodeposition potential does not result in a significant difference in the Ni-to-Zn ratio. However, by decreasing the concentration of the zinc salt in ethaline (0.5 M $NiCl_2$ + 0.25 M $ZnCl_2$ containing electrolyte), alloys with different Ni and Zn ratios can be obtained, with the Zn content increasing progressively from 7.3 at% to 8.1 at% and 32.7 at% as the deposition potential decreases from -1.1 V/Ag/Ag^+ to -1.2 V/Ag/Ag^+, and finally to -1.3 V/Ag/Ag^+. Furthermore, the copper content is extremely low, and even the oxygen content at the surface of the alloy deposited at potentials -1.1 V/Ag/Ag^+ and -1.2 V/Ag/Ag^+ tends to zero. The formation of oxides at lower deposition potentials seems inevitable, which is also observed in subsequent Co-Zn electrodeposition. This is attributed to water electrolysis occurring beyond the electrochemical window during alloy deposition. Although they are permanently protected by argon, the large amount of oxygen generated in the electrolyte can still oxidize the deposits. For Co-Zn deposits, we observed that regardless the deposition conditions, a substantial quantity of oxides still remains at the surface of the electroplated material. Comparing these different results, we conclude that samples deposited in ethaline containing 0.4 M $CoCl_2$ + 0.2 M $ZnCl_2$ show notable variations in element ratios, with sufficient thickness characterized by low copper content (below 2 at%). In this section, the highest Zn content in a Nickel alloy is 74.6 at%. We did not increase the solubility further, as this content was sufficient to observe the effect of Zn.

Table 4.5 Elemental analysis of electroplated Ni/Co-Zn in different conditions.

ETHALINE +	Parameters	Ni (at%)	Co (at%)	Zn (at%)	Cu (at%)	O (at%)
0.5 M $ZnCl_2$	-1.25 V, 40 °C, 60 min	-	-	90.4	0	9.6
0.5 M $NiCl_2$	-1.05 V, 40 °C, 60 min	94.2	-	-	2.2	3.6
0.5 M $CoCl_2$	-1.1 V, 40°C, 60 min	-	92.3	-	0	7.7
0.2 M $NiCl_2$ + 0.3 M $CoCl_2$	-0.9 V, 40 °C, 60 min	59.9	31.8	-	3.1	5.1
	-1.0 V, 40 °C, 60 min	47.6	42.6	-	2.4	7.3
	-1.1 V, 40 °C, 60 min	36.2	59.7	-	0	4.1
0.15 M $NiCl_2$ + 0.35 M $ZnCl_2$	-1.3 V, 40 °C, 60 min	16.7	-	24.1	56.0	3.2
	-1.3 V, 40 °C, 120 min	7.7	-	49.9	36.6	1.6
	-1.3 V, 40 °C, 360 min	41.9	-	5.8	41.3	5.9
	-1.35 V, 40 °C, 60 min	3.1	-	13.0	80.6	3.3
	-1.3 V, 60 °C, 210 min	20.9	-	74.6	2.0	2.5
0.5 M $NiCl_2$ + 0.25 M $ZnCl_2$	-1.1 V, 40 °C, 120 min	85.2	-	7.3	0	7.6
	-1.2 V, 40 °C, 120 min	87.6	-	8.1	0	4.3
	-1.3 V, 40 °C, 120 min	36.1	-	32.7	8.5	22.8
0.5 M $NiCl_2$ + 0.5 M $ZnCl_2$	-1.1 V, 40 °C, 120 min	74.7	-	10.2	7.4	6.9
	-1.2 V, 40 °C, 120 min	75.3	-	11.0	8.6	5.1
	-1.3 V, 40 °C, 120 min	78.8	-	11.5	3.0	6.8
0.2 M $NiCl_2$ + 0.4 M $ZnCl_2$	-1.2 V, 40 °C, 120 min	8.8	-	8.1	75.9	7.1
0.15 M $CoCl_2$ + 0.35 M $ZnCl_2$	-1.25 V, 40 °C, 60 min	-	13.4	16.5	48.8	21.3
	-1.3 V, 40 °C, 60 min	-	8.9	4.7	70.7	15.7
	-1.3 V, 60 °C, 210 min	-	39.9	40.2	0	19.9
0.4 M $CoCl_2$ + 0.2 M $ZnCl_2$	-1.0 V, 40 °C, 120 min	-	75.8	12.0	0	12.2
	-1.1 V, 40 °C, 120 min	-	55.6	20.1	1.7	22.6
	-1.2 V, 40 °C, 120 min	-	48.7	25.8	1.2	24.4
0.4 M $CoCl_2$ + 0.4 M $ZnCl_2$	-1.1 V, 40 °C, 120 min	-	72.3	10.9	0	16.8
	-1.2 V, 40 °C, 120 min	-	71.4	8.5	2.3	17.7
	-1.3 V, 40 °C, 120 min	-	49.3	17.1	5.9	27.6

Therefore, for further studies of the electrocatalytic performance of the alloys, particularly with regard to the hydrogen evolution reaction (HER), we selected the Ni-Zn alloys prepared in ethaline containing 0.5 M $NiCl_2$ + 0.25 M $ZnCl_2$, hereinafter referred to as $Ni_{92.3}Zn_{7.7}$,

$Ni_{80.7}Zn_{19.3}$, $Ni_{55.6}Zn_{44.4}$, and Co-Zn alloys prepared in ethaline containing 0.4 M $CoCl_2$ + 0.2 M $ZnCl_2$, hereinafter referred to as $Co_{86.3}Zn_{16.7}$, $Co_{73.4}Zn_{26.6}$, $Co_{65.4}Zn_{34.4}$.

4.7. Electrocatalytic properties of Ni/Co-Zn alloys in HER

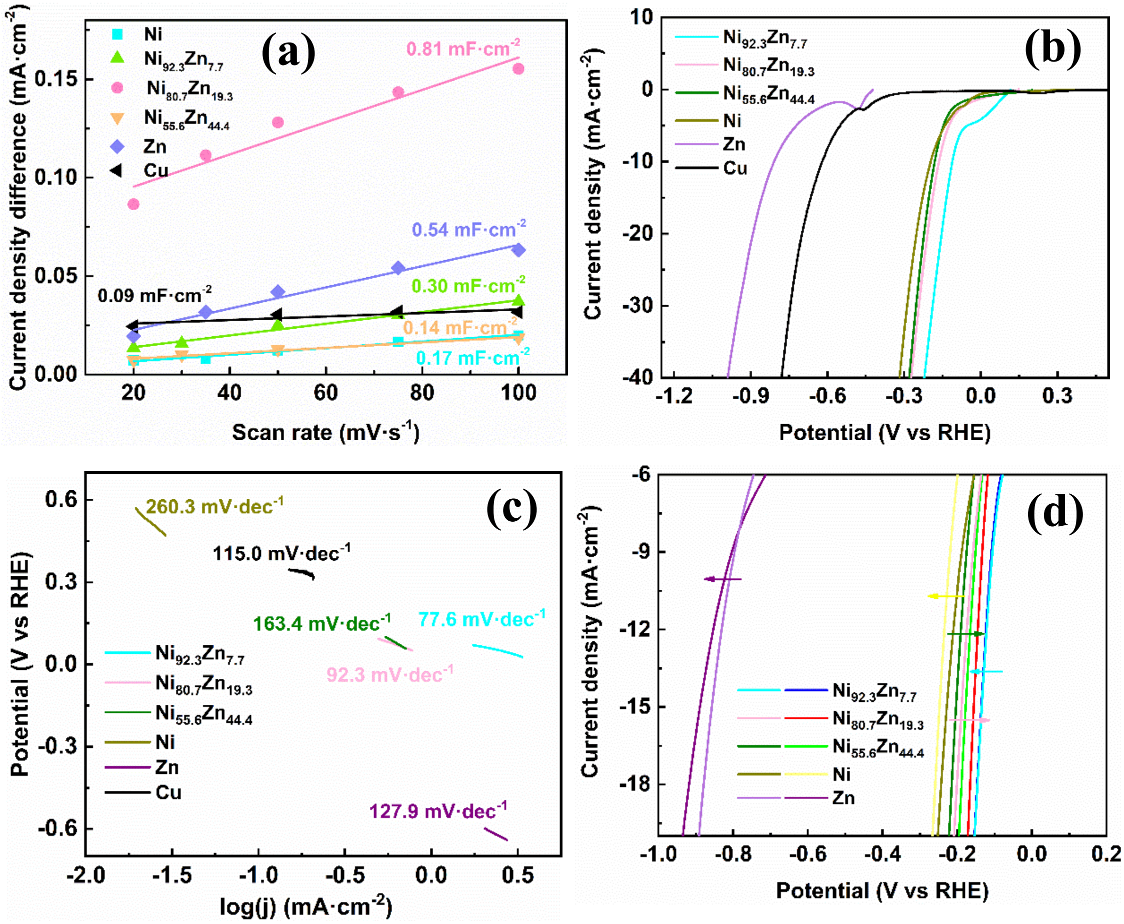

Figure 4.16 Electrochemical behavior of various alloys towards the HER for different Ni-Zn contents: a) C^{σ} of different Ni-Zn alloys, b) LSV curves of Ni-Zn alloys with different atomic ratio at a scan rate of 10 $mV{\cdot}s^{-1}$, c) Tafel slopes for different alloys for the HER, d) LSV curves of Ni-Zn alloys with different atomic ratio after 10 cycles catalytic reaction at a scan rate of 10 $mV{\cdot}s^{-1}$.

The electrocatalytic characteristics of Ni-Zn alloys electroplated on a Cu substrate have been deeply investigated for the HER using linear sweep voltammetry and cyclic voltammetry in a 1 M KOH aqueous solution, as illustrated in Figure 4.16 and Table 4.6. The electrochemical measurements were performed using the same experimental procedure to the one used when working on FTO substrate. We only select three alloys, $Ni_{92.3}Zn_{7.7}$, $Ni_{80.7}Zn_{19.3}$, $Ni_{55.6}Zn_{44.4}$, to evaluate the performance of the hydrogen evolution reaction.

The ECSA was determined by evaluating the interfacial capacitance (C^{σ}), as illustrated in Figure 4.16a. The pure Cu substrate shows an interfacial capacitance of 0.09 mF·cm^{-2}. Upon electrodeposition, a significant increase in the interfacial capacitance was observed on the surface, reaching 0.54 mF·cm^{-2} for Zn deposits and even 0.81 mF·cm^{-2} for Zn alloys, suggesting more surface-active sites.

Table 4.6 Properties of Ni-Co alloys in 1 M KOH solution towards the HER.

	Cu foil	Ni	Zn	$Ni_{92.3}Zn_{7.7}$	$Ni_{80.7}Zn_{19.3}$	$Ni_{55.6}Zn_{44.4}$
C^{σ}(mF·cm^{-2})	0.09	0.17	0.54	0.30	0.81	0.14
OCP (V/RHE)	0.71	0.72	-0.42	0.12	0.15	0.20
Onset potential (V/RHE)	-0.37	-0.03	-0.44	0.08	0.03	0.003
HER potential (V/RHE)	-0.62	-0.20	-0.81	-0.11	-0.16	-0.18
Tafel slope (mV·dec^{-1})	115.0	260.3	127.9	77.6	92.3	163.4
HER potential after 10 cycles (V/RHE)	-	-0.22	-0.82	-0.12	-0.14	-0.15

Figure 4.16b presents the electrocatalytic performance of Ni-Zn alloys, demonstrating lower HER potential compared to pure Ni and Zn. The alloying and incorporation of Zn into the Ni-based alloys led to a significant reduction in HER potential at a current density of -10 mA·cm^{-2}, which decreases from -0.20 V/RHE for pure Ni to -0.11 V/RHE, -0.16 V/RHE, and -0.18 V/RHE for Ni-Zn alloys containing 7.7 at%, 19.3 at%, and 44.4 at% Zn, respectively.

In the case of pure Ni, the Tafel slope was 260.3 mV·dec^{-1}. However, by adding Zn to the Ni-Zn alloy, the Tafel slope rate was reduced to 77.6 mV·dec^{-1}, indicating an improvement in reaction kinetics. This result confirms that the addition of zinc effectively enhances the electrocatalytic performance of the alloy. The electrocatalytic properties of Ni-Zn alloys are improved for the lowest content in zinc (among the 3 tested materials). The optimal ratio of elements needs to be carefully determined to achieve the desired performance characteristics (but this aspect has not been dealt with in this work).

The LSV curves obtained after cycling experiments are presented in Figure 4.16d. The Ni-Zn alloys show a constant or even lower HER potential after 10 cycles, indicating good stability. For example, in the case of $Ni_{80.7}Zn_{19.3}$, the HER potential reduced from -0.16 to -0.14 V/RHE after the 10 cycle HER. This is ascribed to the dissolution of the surface oxide film during the HER, allowing the bare alloy to be exposed to the electrolyte. A clear reduction peak attributed to the surface oxide can be observed in the first cycle of the reduction reaction for the $Ni_{92.3}Zn_{7.7}$ alloy. After 10 cycles, this peak has disappeared, indicating the consumption of most of the oxides, only a thin passive oxide layer remains.

During the HER performance evaluation of Co-Zn alloys, it was observed that the intense reduction peak produced by the oxide of cobalt or zinc has a significant impact on the HER performance evaluation (Figure 4.17). This was also confirmed with the EDS analysis that the quantity of oxide in the Co-Zn alloy is larger. Due to the interference caused by the oxide peaks, the accurate determination of overpotential at 10 $mA \cdot cm^{-2}$ is not very precise. However, by comparing the overpotential at 30 $mA \cdot cm^{-2}$, the addition of a small amount of Zn reduces the overpotential, while larger Zn contents lead to poorer hydrogen evolution performance.

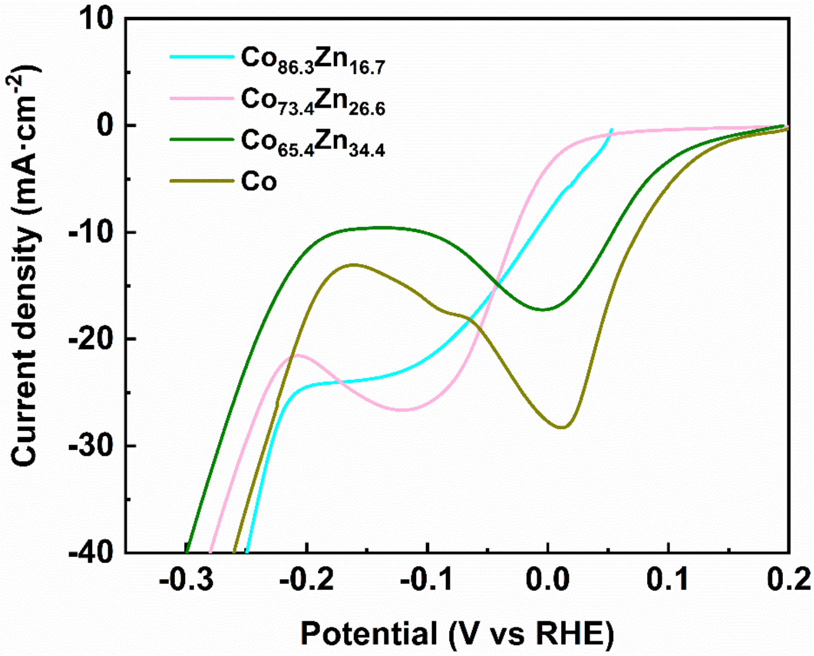

Figure 4.17 LSV curves of Co-Zn alloys with different atomic ratio.

4.8. Electrodeposition of Al in ethaline

Figure 4.18 Ethaline with 0.1M $AlCl_3$ (left) and 0.5 M $AlCl_3$ (right).

In addition to the electrodeposition of Zn in ethaline, preliminary investigations were performed for the electrodeposition of Al in ethaline. At this point, it is worth mentioning that only a few papers report on the electrodeposition of Al in reline (choline chloride/urea) [168]. There is no research about the electrodeposition of Al in ethaline after the bibliographic study. So, it is interesting to learn the possibility of the electrodeposition of Al in ethaline. Electrolytes were prepared using ethaline with 0.1 M $AlCl_3$ and 0.5 M $AlCl_3$. The addition of 0.1 M $AlCl_3$ does not cause any noticeable color change in ethaline (Figure 4.18.). However, by increasing the $AlCl_3$ concentration to 0.5 M, the solution changes to a milky white appearance, indicating the presence of fine crystals in suspension. Therefore, ethaline with 0.1M $AlCl_3$ was chosen as the electrolyte.

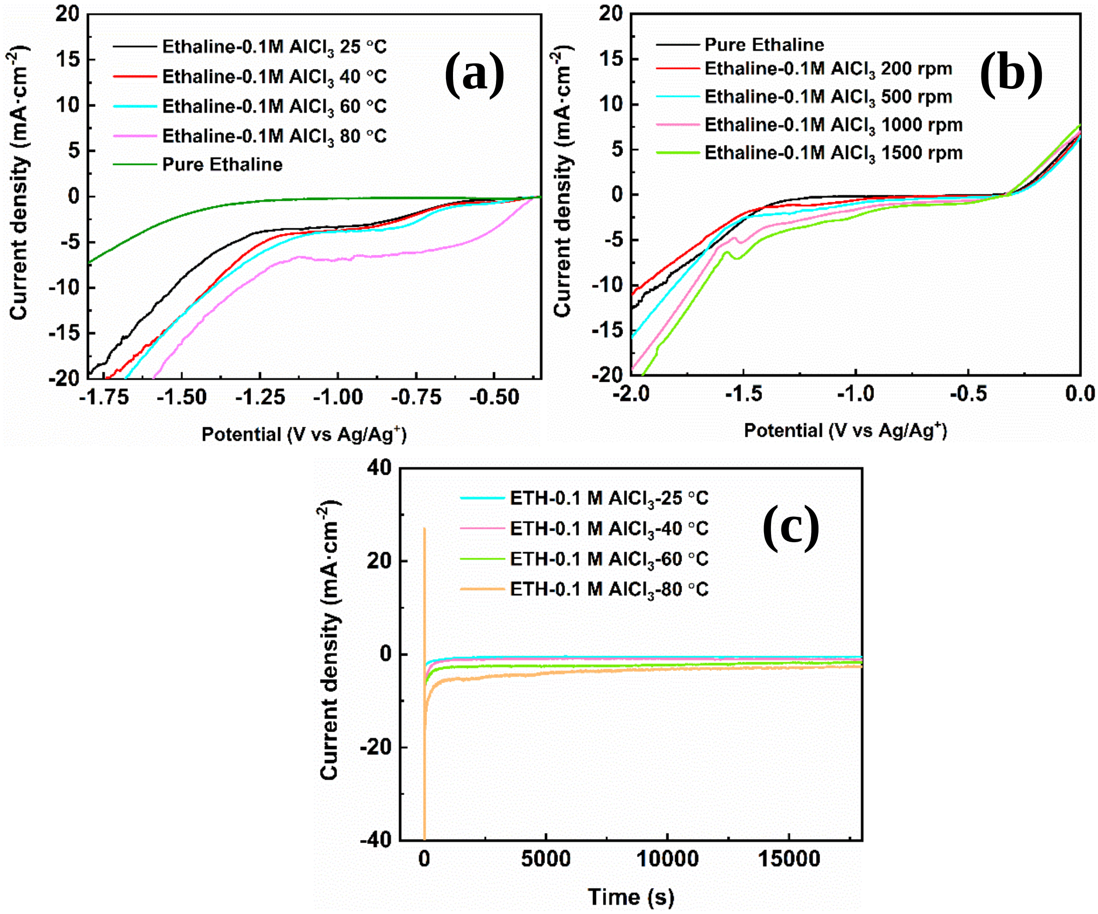

Figure 4.19 LSV curves of ethaline with 0.1 M $AlCl_3$ on Cu foam in different temperature (a), on Cu RDE with different rotation speed (b), current-time curves of different Al depositions.

To optimize the deposition efficiency, Cu foam was selected as working electrode for this study. As shown in Figure 4.19a, a significant increase in current density is observed on the Cu foam electrode when $AlCl_3$ is added to the ethaline electrolyte, and the magnitude of the increase is higher at elevated temperatures. To confirm that this reaction is attributed to the reduction of Al ions in the electrolyte, we performed experiments using a copper rotating disk electrode to explore the redox potential of aluminum on the copper surface. At 25 °C, the current density gradually increases with the rotation rate of the electrode, indicating that the reaction is indeed controlled by the diffusion of the Al^{3+} ions in the electrolyte (in this potential domain). Subsequently, electrodeposition experiments were performed with a potential of -1.2 V/Ag/Ag^+

at different temperatures, namely 25 °C, 40 °C, 60 °C, and 80 °C. Despite observing stable current densities during the deposition processes, no deposited aluminum was observed in the subsequent SEM and EDS analyses. An example of these results is presented in Figure 4.20, where the XRD patterns only exhibit the diffraction peaks corresponding to Cu, while no evidence of aluminum could have been detected.

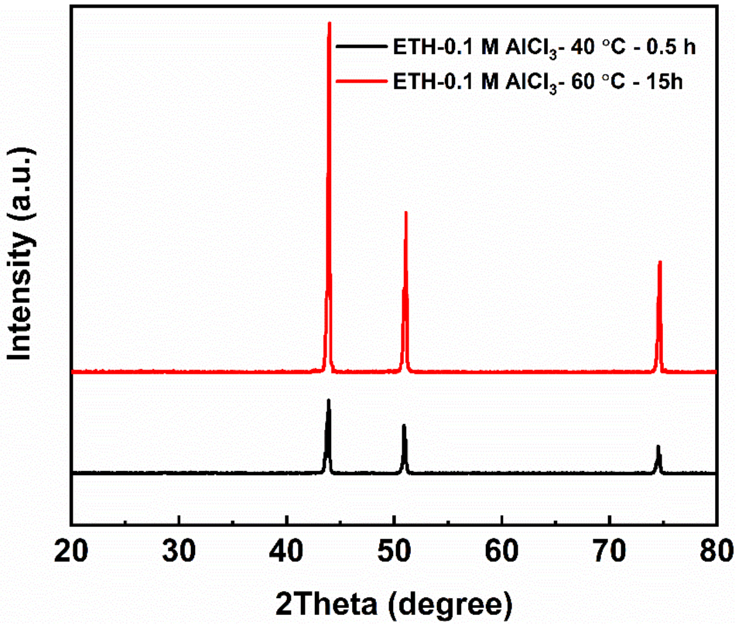

Figure 4.20 The XRD of samples after Al electrodepositions.

To investigate the feasibility of electrodeposition of aluminum on copper, we further increased the concentration of $AlCl_3$ to 0.5M and perform an electrodeposition for 5 hours. However, no aluminum deposit was obtained on the copper surface, as confirmed by SEM analysis and XRD results, which were consistent with the previous experiments. Based on these findings, it can be concluded that electrodeposition of aluminum on copper is not achievable in ethaline electrolyte. To pursue successful aluminum electrodeposition, alternative electrolytes or substrate materials should be explored, as they may offer more favorable conditions for the deposition process.

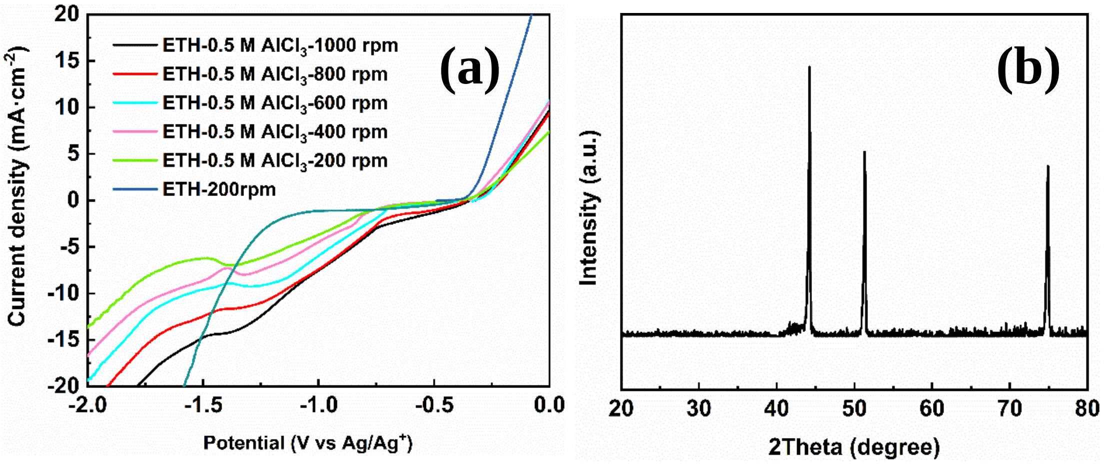

Figure 4.21 LSV curves of ethaline containing 0.5 M $AlCl_3$ on Cu RDE with different rotation rates and XRD diagram of the sample after a 5 h electrodeposition in this electrolyte.

4.9. Conclusion

This chapter focuses on the electrodeposition of pure metals and alloys on copper foam using a deep eutectic solvent (ethaline). The feasibility of this method has been successfully demonstrated, and it has been found that the electrocatalytic performance of Cu foam can be enhanced through nickel electrodeposition. Subsequently, the electrodeposition of zinc, nickel, cobalt, and their alloys on Cu foil in ethaline was investigated. It was shown that nearly pure zinc, nickel, and cobalt deposits can be electroplated using ethaline bath. Various electrolyte concentration ratios and electrodeposition parameters were explored to obtain dense and low-oxidized alloy films. The addition of zinc was found to improve the HER of Ni-based or Co-based alloys, but excessive zinc content negatively impacted the catalytic performance of the alloys. Therefore, it is crucial to identify suitable alloying ratios during the preparation of Ni-Zn or Co-Zn electrocatalytic materials. It should be noted that the Co-Zn alloy prepared in this works shown a relatively high oxygen content of approximately 20 at%, which posed challenges in evaluating their electrocatalytic performances. Additionally, the electrodeposition of aluminum in ethaline on copper substrates was found to be unfeasible, highlighting the need to explore alternative deep eutectic solvents or substitute deposition substrates. Overall, this study demonstrates the potential of DES, ethaline, as a promising approach for the electrodeposition of Ni-based materials, opening up new avenues for the synthesis of Ni/Co-based electrocatalysts. The successful incorporation of zinc in Ni-based alloys without significant degradation in electrocatalytic performance paves the way for subsequent studies on dealloying based on Zn-Ni alloys. However, the high oxygen content in Co-Zn alloys indicates their unsuitability for further dealloying investigations. This work paves also the way for the preparation of alloys of different compositions.

Chapter 5 Dealloying of nanoporous NiZn-based alloys and their HER properties

The fabrication of porous alloy electrodes is a highly effective strategy for enhancing electrocatalytic performance. Dealloying, a widely used technique, involves the selective dissolution of the less stable metal component, leaving behind empty pores in the remaining metal matrix. Zinc-based alloys have received particular attention as substrates for the preparation of porous alloys by chemical dealloying, due to the lower standard redox potential of zinc (-0.76 V/SHE, $Zn^{2+} + 2e^{-} \rightleftharpoons Zn^{0}$) compared with other elements such as nickel (-0.25 V/SHE, $Ni^{2+} + 2e^{-} \rightleftharpoons Ni^{0}$), cobalt (-0.28 V/SHE, $Co^{2+} + 2e^{-} \rightleftharpoons Co^{0}$), and copper (+0.34 V/SHE, $Cu^{2+} + 2e^{-} \rightleftharpoons Cu^{0}$) [169]. Moreover, the targeted element can also be selectively removed, by electrochemical dealloying, by applying a specific potential corresponding to its redox potential. In previous investigations, Zn was electrodeposited onto metal substrates such as Cu, forming a Zn-rich binary CuZn surface alloy, which was then selectively leached to create porous Cu and/or CuZn structures [170, 171]. In another work, ternary alloys were prepared onto stainless steel foils by electrodeposition in ethaline [172]. The use of Ethaline as electrolyte ensured high solubility and long-term stability of the metal halides, without the need for strong acids, bases, or ligands, which are usually required in aqueous electroplating baths. Subsequently, porous ZnCuNi alloys were prepared by selective electrochemical dealloying of Zn to enhance their activity towards nitrate reduction. Currently, the field of electrodeposition of ternary alloys in ethaline remains relatively limited, and, as such, the exploration of alternative methods to manipulate alloy composition should be considered.

In Chapter 4, we showed that incorporating a minor quantity of zinc does not reduce the electrocatalytic efficiency of the hydrogen evolution reaction on nickel; rather, it enhances the overall performance. In this chapter, we will discuss a way with a two-step electrodeposition method for the preparation and the dealloying of Zn-Ni-Cu-Co alloys. Co will be first electrodeposited on the surface of Cu foil. Cu-Co alloys can be obtained after a subsequent heat treatment. Then, Zn-Ni alloys are electrodeposited on the surface of Cu-Co alloys in ethaline. The second heat treatment generates Zn-Ni-Cu-Co alloys. Then, the preparations of porous alloys by dealloying of different ZnNi-based alloys are discussed. Their HER properties are presented at the end. In addition, the co-electrodeposition of three elements, Ni, Zn, Co, is also tested and discussed in this chapter. The electrodeposition steps are shown in Figure 5.1.

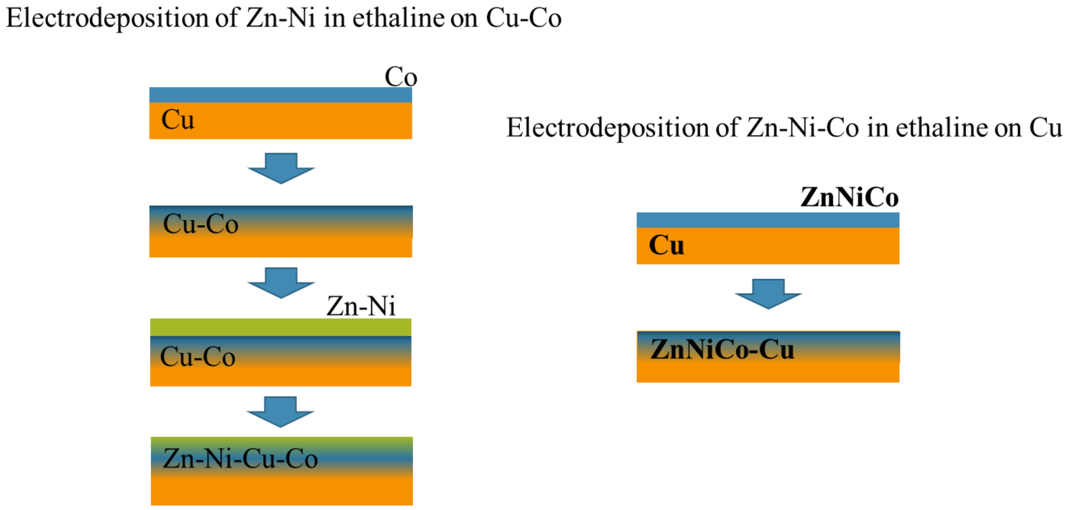

Figure 5.1 Electrodeposition scheme for various alloys in this chapter.

Heat treatment is applied to increase coating stability and cause Cu to diffuse to the surface, forming the Cu-based alloy. Furthermore, we have found it is not easy to obtain nanoporous structures if the dealloying is carried out without heat treatment. Therefore, heat treatment is applied after deposition. A three-electrode cell was used for the electrochemical dealloying. The prepared alloys were used as working electrode, a platinum grid was used as counter electrode, the Hg/HgO electrode was used as reference electrodes, respectively.

5.1. Preparation of porous Zn-Ni-Co-Cu alloys by electrodeposition/dealloying

As a first step, the possibility of the two-step electrodeposition for alloy preparation was investigated. Cobalt was electrodeposited on Cu foil for 30 min at a potential of -1.05 V/Ag/Ag$^+$, following the LSV curves in Figure 5.2a. It can be seen that 6.84×10^{-5} mol of cobalt were obtained on Cu foil by calculation from the results described in Figure 5.2b. Then, the as-deposited sample was subjected to a controlled heat treatment inside a tube furnace. Prior to heating, a continuous flow of argon gas was introduced for 2 hours to establish an inert atmosphere. The temperature inside the tubular oven was then raised from room temperature to 400 °C at a heating rate of 3 °C/min, and maintained at this temperature for 10 minutes to allow homogenous transformation. The sample was then gradually cooled to room temperature in the furnace, while maintaining the argon gas flow to prevent any exposure to atmospheric air throughout the process.

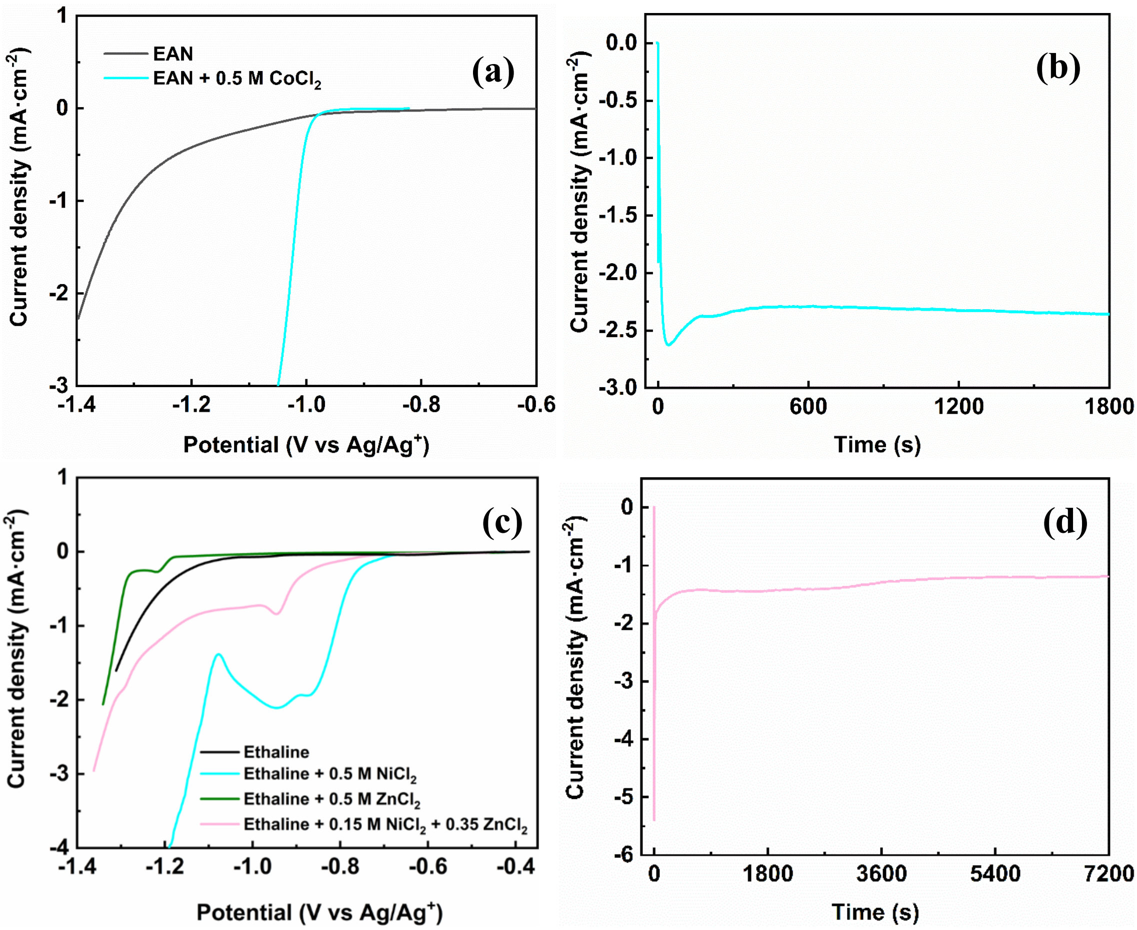

Figure 5.2 a) Linear sweep voltammetry (LSV) curves of 0.5 M $CoCl_2$ in EAN on Cu foil at 60 ºC in glove box. b) The current-time curve obtained during 30 min for Co electrodeposition. c) LSV curves of ethaline with $NiCl_2$/$ZnCl_2$ on Co-Cu foil at 40 ℃. d) The current-time curves obtained during 2 h of Zn-Ni electrodeposition on Co-Cu.

The electrochemical behavior of Co-Cu alloy samples deposited in different ethaline solutions is shown in Figure 5.2c. As for the pure Cu foil, the Ni^{2+} reduction reaction is observed within the ethaline electrochemical window on the Co-Cu alloy. Furthermore, the Zn^{2+} reduction reaction of occurs in the potential range between -1.2 V/Ag/Ag^+ and -1.28 V/Ag/Ag^+, slightly exceeding the limits of the ethaline electrochemical window. Zinc electrodeposition on the copper surface, although occurring outside the electrochemical window concomitantly with the ethaline or water reduction reaction of ethaline or water, offers thermodynamic advantages [170].

Although being accompanied by the hydrogen evolution reaction, it can still lead to the formation of deposits after a prolonged period of electrodeposition. For ethaline with 0.15 M $NiCl_2$ + 0.35 $ZnCl_2$, the two peaks at -0.92 V/Ag/Ag^+ and -1.28 V/Ag/Ag^+ correspond to the reduction of Ni^{2+} and Zn^{2+}, respectively. To illustrate the Zn-Ni deposition process, the Co-Cu alloy was electrodeposited at -1.3 V/Ag/Ag^+ for 2 hours in ethaline with 0.15 M $NiCl_2$ + 0.35 $ZnCl_2$, as shown in the LSV curve in Figure 5.2c. The corresponding current-time curve for this Zn-Ni deposition is depicted in Figure 5.2d. After 2 hours of electrodeposition, we can obtain 1.11×10^{-4} mol of Zn-Ni alloy on Co-Cu. After the previous steps, the electrodeposited sample underwent further heat treatment, with the same parameters as the Co-Cu heat treatment. The result is a Zn-Ni-Co-Cu alloy.

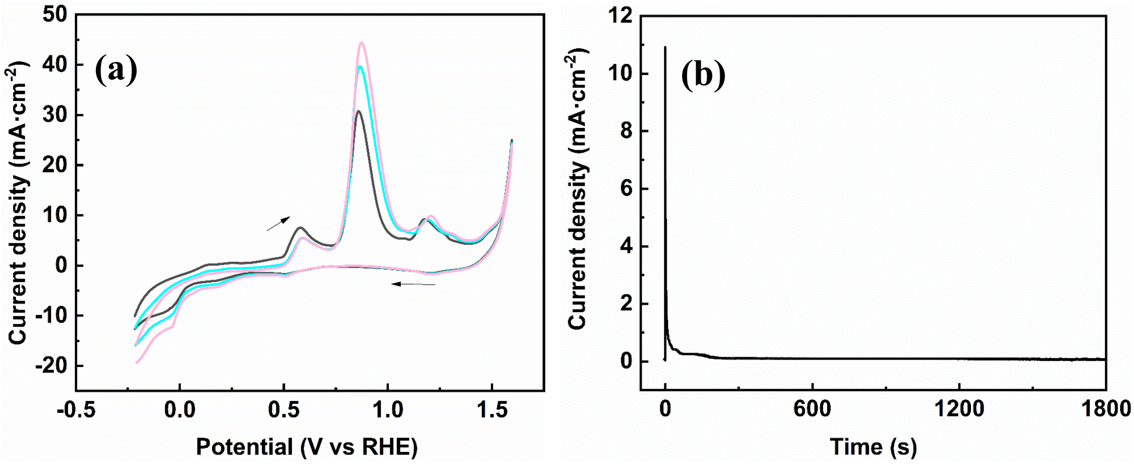

Figure 5.3 a) The CV curves of Zn-Ni on Co-Cu in 1 M KOH at 25 °C. b) The current-time curve during the electrochemical dealloying in 1 M KOH at 25 °C.

The CV curve for Zn-Ni-Co-Cu alloy immersed in a 1 M KOH solution is presented in Figure 5.3a, showing distinct oxidation peaks. For the electrochemical dealloying process, we selected the first peak observed during the anodic scan, representing an electrochemical dealloying potential of 0.67 V/RHE. The initial experiment involved electrochemical dealloying in a 1 M KOH solution at 25°C for durations of 0.5, 1, and 2 hours. The current-time curve during the 0.5 h electrodeposition process is shown in Figure 5.3b. Initially, the current density increases rapidly, due to the formation of a charged electric double layer on the material surface. Subsequently, after approximately 200 seconds, the current density gradually decreases and stabilizes at around 100 μA·cm^{-2}. This behavior is attributed to the reduction of dealloyed elements on the surface and the deceleration of element diffusion to the material surface.

5.2. Characterization of Zn-Ni-Co-Cu alloys

XRD patterns of the samples obtained after various steps are shown in Figure 5.4. In general, the limited amount of alloy deposition on the surface and the diffusion of copper, originating from the substrate, during the heat treatment result in the X-ray diffraction pattern displaying predominantly prominent Cu diffraction peaks, as illustrated in Figure 5.4a. After magnification and calibration, it becomes clear that the cobalt deposit does not produce detectable XRD signals on the surface. However, after the first heat treatment, CoO diffraction peaks appear due to the Co oxidation in the presence of trace of oxygen during the thermal process. Subsequent Zn-Ni electrodeposition leads to the covering of the surface with new deposits, and only small Zn diffraction peaks are observable, with no apparent diffraction peaks of other substances.

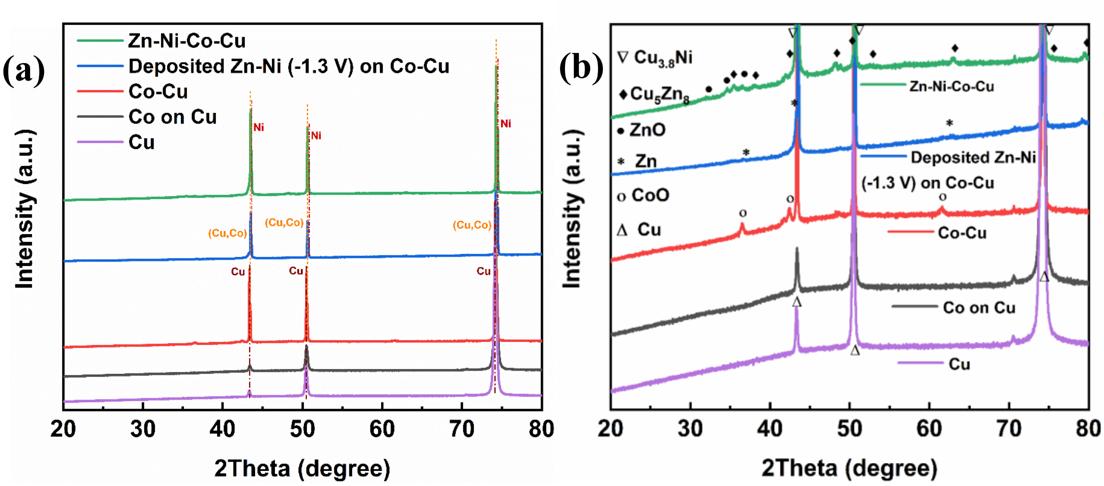

Figure 5.4 (a) XRD patterns of deposition materials before and after different heat treatment steps, and their magnifications (b).

Following the second heat treatment, clear evidence of the formation of other intermetallic compounds is observed, mainly Cu_5Zn_8 and $Cu_{3.8}Ni$, resulting from the diffusion of copper and the combination of other elements. Additionally, a small amount of ZnO is also present, arising from the minor oxidation of Zn during the heat treatment. Therefore, it can be seen that after heat treatment, the alloy composition becomes more complex, and the different intermetallic compounds have different dealloying potentials. The morphology should be studied in more details to compare the morphological characteristics before and after dealloying.

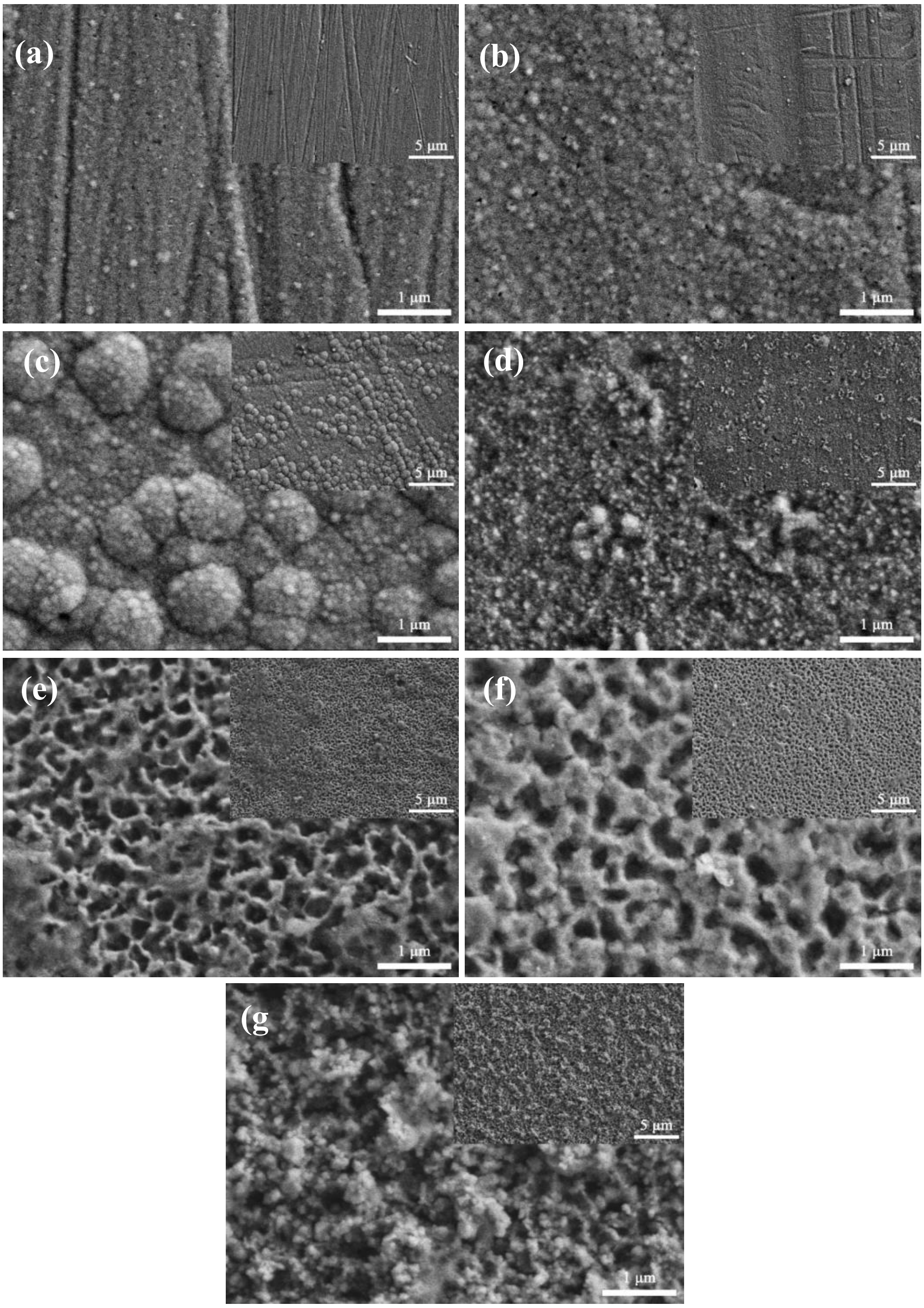

Figure 5.5 The morphologies of deposited Co on Cu before (a) and after heat treatment (b); the deposited Zn-Ni on Co-Cu alloy before (c) and after heat treatment (d); the dealloyed Zn-Ni-Co-Cu alloys for different treatment times: 0.5 h (e), 1 h (f) and 2 h (g).

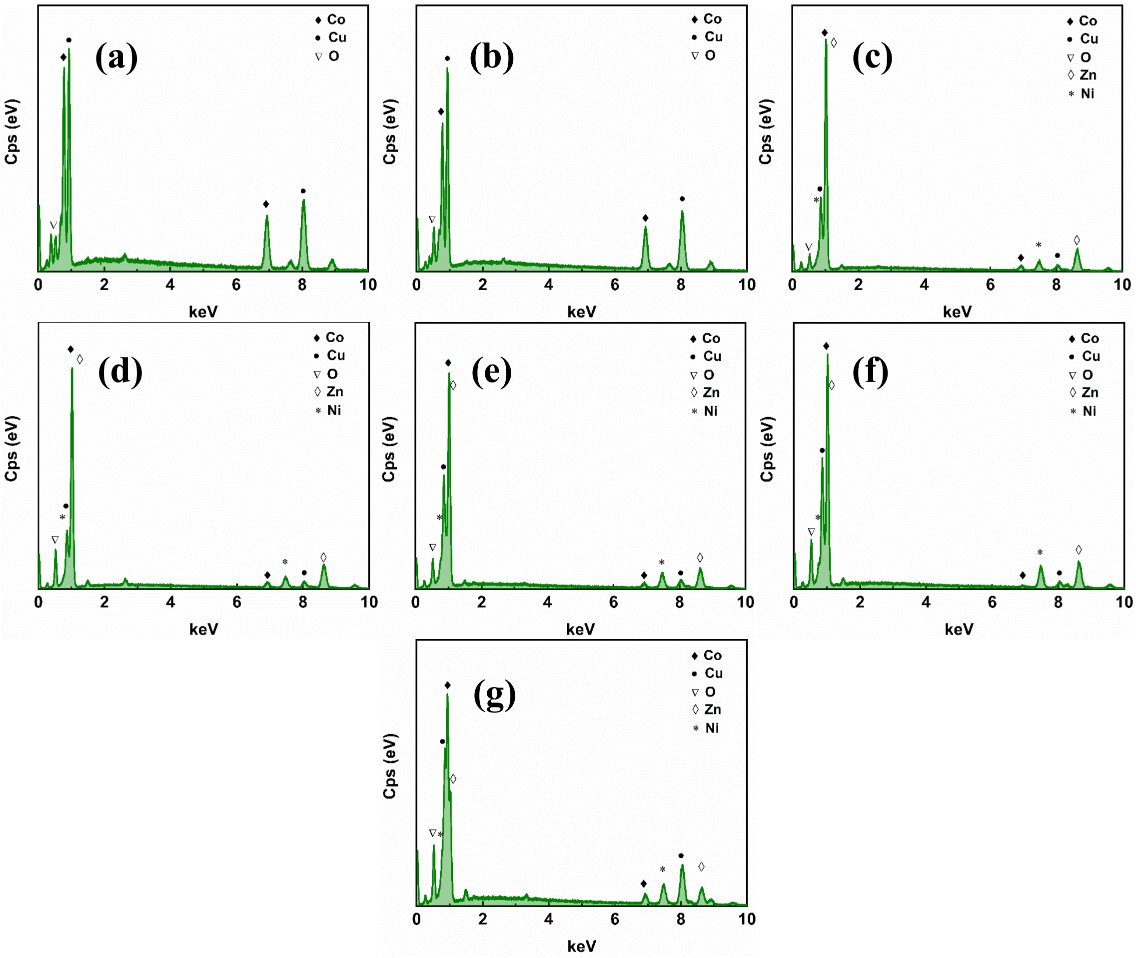

Figure 5.6 EDS curves of different deposited alloys before and after heat treatment steps and dealloying. a) The deposited Co on Cu; b) The deposited Co on Cu after the heat treatment; c) The deposited Zn-Ni on Co-Cu alloy; d) The deposited Zn-Ni on Co-Cu alloy after the heat treatment. The dealloyed Zn-Ni-Co-Cu alloys for different treatment times: 0.5 h (e), 1 h (f) and 2 h (g).

The morphologies of the different deposits before and after heat treatment, dealloying, are examined by SEM (Figure 5.5). The cobalt deposited in EAN exhibits a flat surface with growth following the grooves formed during the polishing process, similar to the cobalt deposits studied in Chapter 3. After 10 minutes of heat treatment, the surface morphology undergoes slight changes, revealing a granular appearance attributed to grain growth. The subsequently deposited Zn-Ni alloy surface appears non-uniform with scattered secondary particle morphologies. However, after 10 minutes of heat treatment, these morphologies disappear, and the surface is transformed into a composition of uniform fine grains and particles. It can be inferred that Zn will be dissolved first due to the potential difference, and this process will form the holes on the surface. When Zn is dissolved, the other elements containd in the grains of the Zn-based solid solution are also dissolved. As a result, the Cu/Co/Ni content will also decrease in different ranges. In this thesis, SEM characterization showed that the pore sizes after dealloying are less than 800 nm, and most of them are between 100 nm and 200 nm. Hence these alloys can be called nanoporous alloys.

In 1 M KOH, electrochemical dealloying at 0.67 V/RHE significantly alters the surface morphology of the alloy. Figure 5.5e shows that after 0.5 hours of dealloying, coherent pores with a diameter of approximately 300 nm corrode on the alloy surface. Increasing the dealloying treatment time to 1 hour significantly reduces the pore porosity. Although the pores become discontinuous compared to the 0.5-hour dealloying treatment, they maintain a diameter of 300 nm. Extending the dealloying time to 2 hours results in the disappearance of the porous surface structure, giving rise to the formation of fine grain, as with the Zn-Ni-Co-Cu alloy after heat treatment. It is plausible that an excessively prolonged dealloying time will disrupt the surface pore structure.

Table 5.1 Compositions of different samples before and after heat and dealloying treatments.

Solutions	Parameters	Heat treatment	Dealloying	Zn (at%)	Ni (at%)	Co (at%)	Cu (at%)	O (at%)
EAN + 0.5 M $CoCl_2$	-1.05 V, 60 °C, 30 min	×	×	-	-	38.0	51.5	10.5
		√	×	-	-	32.9	51.0	16.0
Ethaline + 0.35 M $ZnCl_2$ + 0.15 M $NiCl_2$	-1.3 V, 40 °C, 120 min	×	×	63.6	14.6	5.3	5.7	10.7
		√	×	51.8	14.1	5.0	6.0	23.1
			1 M KOH, 0.67 V 0.5 h	51.9	16.8	4.7	7.9	18.7
			1 M KOH, 0.67 V, 1 h	48.2	22.5	1.1	6.3	21.8
			1 M KOH, 0.67 V, 2 h	37.6	24.5	4.9	11.3	21.8

In this chapter, EDS is employed as a fundamental and crucial characterization method to investigate elemental changes before and after dealloying. The EDS spectrum presented in Figure 5.6 shows characteristic Cu peaks in all samples, and the oxygen content varies according to the different preparation methods. The corresponding element contents are given in Table 5.1. After heat treatment, cobalt deposited in EAN shows a significant increase in copper and a decrease in cobalt. This phenomenon can be attributed to copper diffusion during heat treatment, resulting in an increase in oxygen content from 10.5 at% to 16.0 at% due to oxide formation, which is consistent with XRD results indicating the presence of oxides. In the Zn-Ni alloy deposited in ethaline, zinc is the dominant element, accounting for 63.6 at%. After heat treatment, the oxygen content rises remarkably from 10.7 at% to 23.1 at%, which is again attributed to oxide formation, corresponding to the ZnO phase detected by XRD. Moreover, after heat treatment, the contents of Zn, Ni, and Co in the alloy elements decrease, while that of Cu increases, confirming the diffusion of Cu from the inside to the outside. The formation of other copper-containing compounds is also verified by XRD analysis. The alloy composition is summarized in Table 5.2. Notably, at the same electrochemical dealloying potential and temperature, the Zn content decreases significantly with increasing dealloying time, from 67.3 at% to 63.8 at%, and 61.6%, corresponding to dealloyed Zn-Ni-Co-Cu alloy for 0.5 h, 1 h, and 2 h, respectively. Conversely, the Ni content increases correspondingly with time.

Table 5.2 Compositions of different dealloyed alloys.

Solutions	Dealloying	Donated
Ethaline + 0.35 M $ZnCl_2$ + 0.15 M $NiCl_2$	Original	$Zn_{67.3}Ni_{18.3}Cu_{7.8}Co_{6.6}$
	1 M KOH, 0.67 V 0.5 h	$Zn_{63.8}Ni_{20.7}Cu_{9.7}Co_{5.8}$
	1 M KOH, 0.67 V, 1 h	$Zn_{61.6}Ni_{28.8}Cu_{8.1}Co_{1.5}$
	1 M KOH, 0.67 V, 2 h	$Zn_{48.1}Ni_{31.3}Cu_{14.5}Co_{6.1}$

5.3. Electrocatalytic properties of nanoporous Ni-alloys in HER

The electrocatalytic properties of porous Zn-Ni-Co-Cu alloys were investigated in 1 M KOH aqueous solution using linear sweep voltammetry (LSV) and cyclic voltammetry (CV), as illustrated in Figure 5.7 and Table 5.3. Electrocatalytic measurements followed the same procedure as for the electrocatalytic analysis of FTO glasses. Various nanoporous alloys were selected to assess their performance in the electrocatalytic hydrogen evolution reaction (HER).

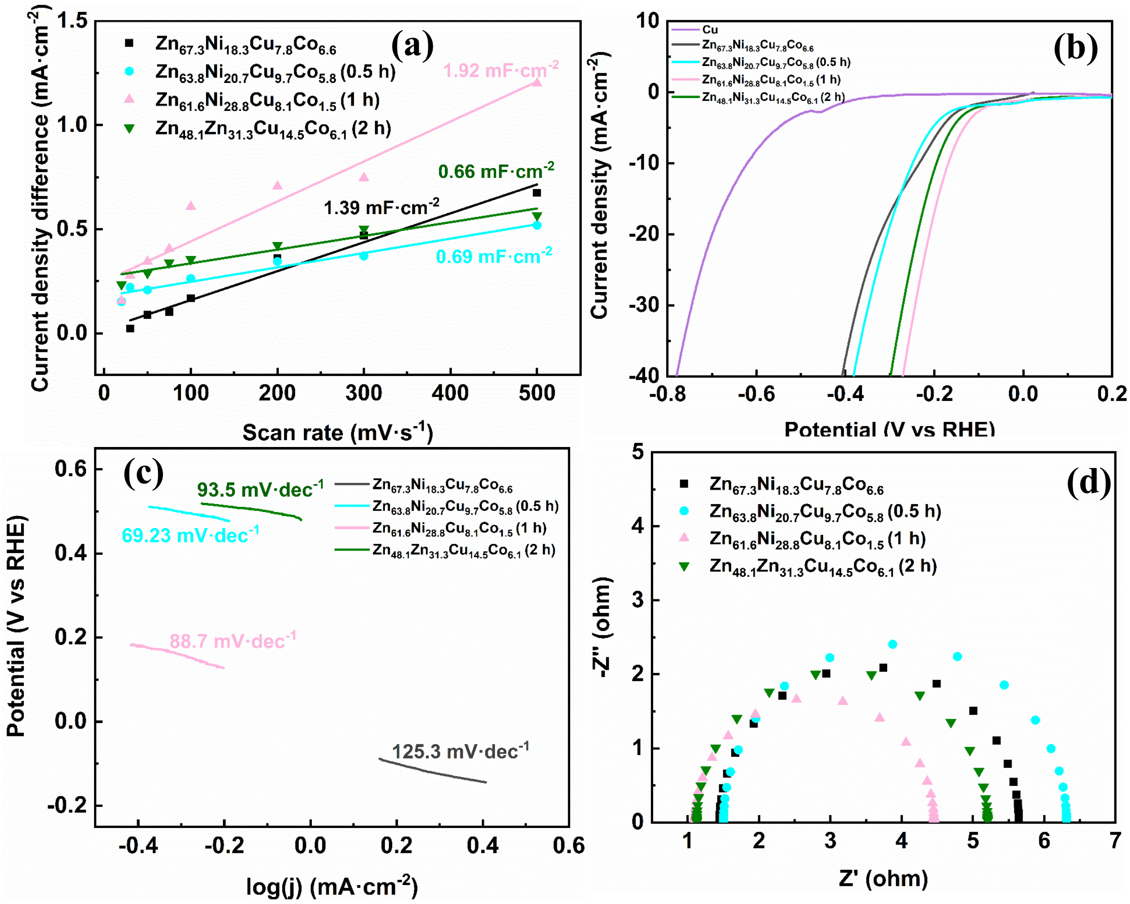

Figure 5.7 Electrocatalytic properties of nanoporous Zn-Ni-Co-Cu alloys towards the HER : a) Interfacial capacitance of different nanoporous alloys, b) LSV curves at a scan rate of 10 mV·s^{-1}, c) Tafel slopes, d) EIS curves.

The effective electrochemical surface area (ECSA) was determined by evaluating the interfacial capacitance (C^{σ}) from CV at various scan rates, as shown in Figure 5.7a. The $Zn_{67.3}Ni_{18.3}Cu_{7.8}Co_{6.6}$ alloy before dealloying exhibited an interfacial capacitance of 1.39 mF·cm^{-2}. Among the nanoporous alloys, only $Zn_{61.6}Ni_{28.8}Cu_{8.1}Co_{1.5}$ produced by dealloying for 1 hour showed a higher C^{σ} value of 1.92 mF·cm^{-2}. The presence of oxide capacitance adds complexity to the ECSA calculation, as discussed in Chapter 3.

Figure 5.7b illustrates the electrocatalytic performance of the nanoporous alloys, showing that all alloys have lower HER potentials than pure Cu. Compared to the untreated $Zn_{67.3}Ni_{18.3}Cu_{7.8}Co_{6.6}$ alloy, the HER potential decreased from -0.23 V/RHE to -0.16 V/RHE and -0.19 V/RHE after electrochemical dealloying for 1 hour and 2 hours, respectively, indicating that appropriate dealloying can enhance HER performance. The effect of the porous structure on the Tafel slope is also evident, as shown in Figure 5.7c. After dealloying, the Tafel slopes decreased from 125.3 mV·dec^{-1} to 69.2 mV·dec^{-1}, 88.7 mV·dec^{-1}, and 93.5 mV·dec^{-1}, corresponding to dealloying at 0.5 hours, 1 hour, and 2 hours, respectively, meaning that the porous structure significantly improves the reaction rate.

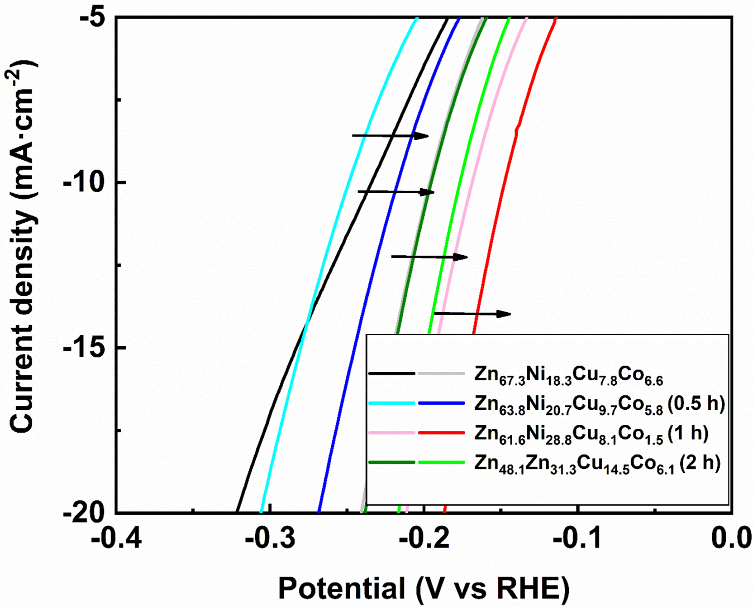

Figure 5.8 LSV curves of nanoporous Zn-Ni-Co-Cu alloys after 10 cycles of catalytic reaction.

Table 5.3 Properties of nanoporous Zn-Ni-Co-Cu alloys towards the HER.

	$Zn_{67.3}Ni_{18.3}Cu_{7.8}Co_{6.6}$	$Zn_{63.8}Ni_{20.7}Cu_{9.7}Co_{5.8}$	$Zn_{61.6}Ni_{28.8}Cu_{8.1}Co_{1.5}$	$Zn_{48.1}Ni_{31.3}Cu_{14.5}Co_{6.1}$
C^{σ} (mF·cm^{-2})	1.39	0.69	1.92	0.66
OCP (V/RHE)	0.42	0.35	0.33	0.32
Onset potential (V/RHE)	-0.05	-0.04	-0.04	0.01
HER potential (V/RHE)	-0.23	-0.25	-0.16	-0.19
Tafel slope (mV·dec^{-1})	125.3	69.2	88.7	93.5
HER potential after 10 cycles (V/RHE)	-0.2	-0.22	-0.15	-0.17
EIS (ohm)	4.2	4.83	3.36	4.08

The impedance spectrum shown in Figure 5.7d after fitting reveals that suitable electrochemical dealloying effectively reduces the electron transfer resistance value, such as $Zn_{61.6}Ni_{28.8}Cu_{8.1}Co_{1.5}$, which is 3.4 ohms, lower than that of the original alloy, $Zn_{67.3}Ni_{18.3}Cu_{7.8}Co_{6.6}$, which is 4.2 ohms. The corresponding LSV curves obtained after the cyclic experiments are shown in Figure 5.8. After 10 cycles, all alloys exhibited lower overpotential values, with $Zn_{61.6}Ni_{28.8}Cu_{8.1}Co_{1.5}$ reaching an HER potential of -0.15 V/RHE. This is attributed to the dissolution of the surface oxide film during the HER process, exposing the alloy to the liquid and allowing it to actively participate in the reaction.

Consequently, preliminary experiments with multi-step electrodeposition and electrochemical dealloying have successfully demonstrated the preparation of quaternary alloys by two electrodeposition steps followed by heat treatment. In addition, nanoporous alloys with a well-defined pore structure have been successfully obtained by electrochemical dealloying. Appropriate dealloying methods have significantly improved the performance of the electrocatalytic hydrogen evolution reaction (HER), notably by reducing overpotential and increasing the reaction rate, while maintaining good stability. Therefore, further exploration of various dealloying conditions to modify the alloy composition and morphology is promising for the control and optimization of catalytic performance.

5.4. Preparation of nanoporous Zn-Ni-Co-Cu alloys in different conditions

It can be seen that dealloying of Zn-Ni-Co-Cu alloy can be achieved in the KOH solution. And further tuning the HER performance requires different dealloying parameters application. In this part, we first electrodeposited cobalt for one hour and then deposited the Zn-Ni-Co-Cu alloy. After the electrodeposition, we tried different dealloying treatment in different ways.

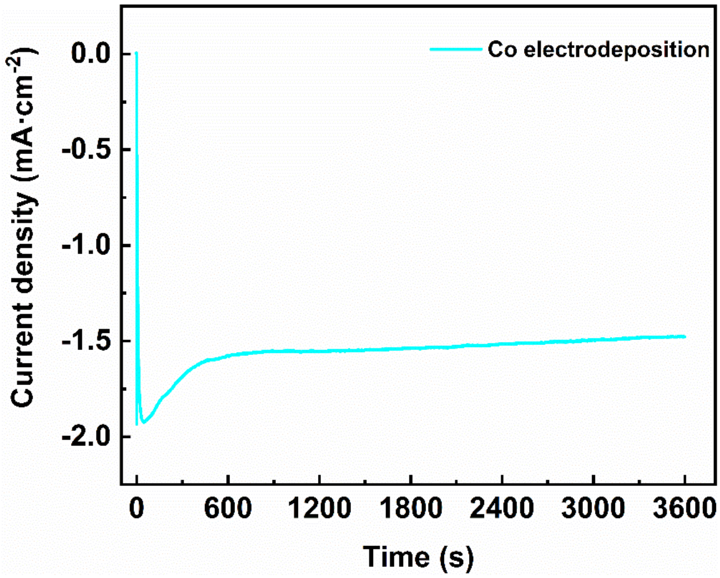

Figure 5.9 The current-time curve obtained for 1 h of Co electrodeposition in EAN.

Using the current-time curve shown in Figure 5.9, the total amount of electrons transferred during one hour of Co electrodeposition from 0.5 M solution of $CoCl_2$ in EAN was calculated to be 21.93 C. This corresponds to a deposit of 1.14×10^{-4} mol of cobalt. The deposited cobalt was then further heat-treated in a tube furnace. The temperature was raised to 400 °C and maintained for 30 minutes, resulting in the formation of a Co-Cu alloy.

After the electrodeposition and heat treatment of Co-Cu alloys, we moved the alloys to the ethaline solutions for the second step electrodeposition of Zn-Ni alloy at 40 °C, which is the same temperature of Ni-Zn electrodeposition in Chapter 4. The electrochemical behavior of Co-Cu alloy samples deposited for 1 h in ethaline containing 0.35 M $ZnCl_2$ + 0.15 M $NiCl_2$ is shown in Figure 5.10a. Similar to the previous Zn-Ni deposition on the Co-Cu substrate deposited for 0.5 h, the surface of the Co-Cu alloy exhibits the reduction reaction of Ni^{2+} in the electrochemical window of ethaline. Furthermore, the reduction reaction of Zn^{2+} occurs in the potential range between -1.25 and -1.31 V/Ag/Ag^+, slightly exceeding the limits of the ethaline electrochemical window. Subsequently, the same potential of -1.3 V/ Ag/Ag^+ was applied during the Zn-Ni deposition process, which lasted 2 hours. The corresponding current-time curve for this Zn-Ni deposition is presented in Figure 5.10b. By conducting a 2-hour electrodeposition process, a total electron transfer of 25.53 C was obtained, resulting in the deposition of 1.32×10^{-4} mol of Zn-Ni alloy on the Co-Cu substrate. Following the previous steps, the deposited sample underwent further heat treatment, using the same parameters as for the heat treatment of the Co-Cu alloy. The is a Zn-Ni-Co-Cu alloy.

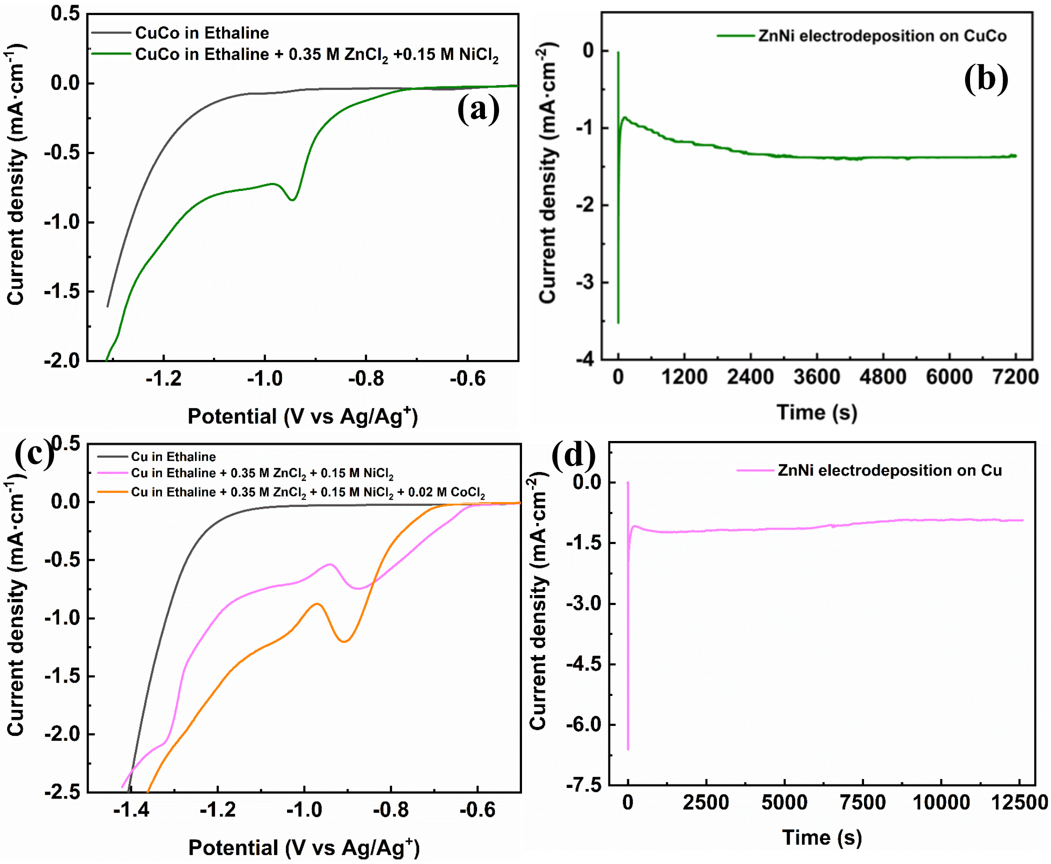

Figure 5.10 a) Linear sweep voltammetry curves of 0.35 M $ZnCl_2$ +0.15 M $NiCl_2$ in ethaline on Co-Cu substrate (obtained by 1h electrodeposition) at 40 °C. b) The current-time curve obtained during 2 h Zn-Ni electrodeposition on Co-Cu at 40 °C. c) Linear sweep voltammetry curves of ethaline with 0.35 M $ZnCl_2$ +0.15 M $NiCl_2$, 0.35 M $ZnCl_2$ +0.15 M $NiCl_2$ + 0.02 M $CoCl_2$ on Cu foil at 40 °C.

Furthermore, to assess the impact of cobalt addition on the electrocatalytic performance of HER in the first step, Zn-Ni electrodeposition was carried out directly on a copper substrate, followed by heat treatment to obtain a Zn-Ni-Cu alloy. The electrochemical behavior on copper in ethaline is demonstrated by the LSV curve in Figure 5.10c. As in the previous study, the electrodeposition of Zn-Ni on the copper substrate must be performed effectively at a potential of -1.3V/Ag/Ag^+. Moreover, in an attempt to achieve co-deposition of all three elements, a small amount of 0.02 M $CoCl_2$ was added to ethaline solution containing 0.35 M $ZnCl_2$ + 0.15 M $NiCl_2$, which will be discussed in more detail in the final stage of this study. Figure 5.10d illustrates that after 3.5 hours of electrodeposition, 3.19×10^{-4} mol of Zn-Ni alloy can be obtained, with a charge transfer of 61.69 C. After a second heat treatment step at 400 °C for half an hour, the Zn-Ni-Cu alloy is successfully obtained by element diffusion.

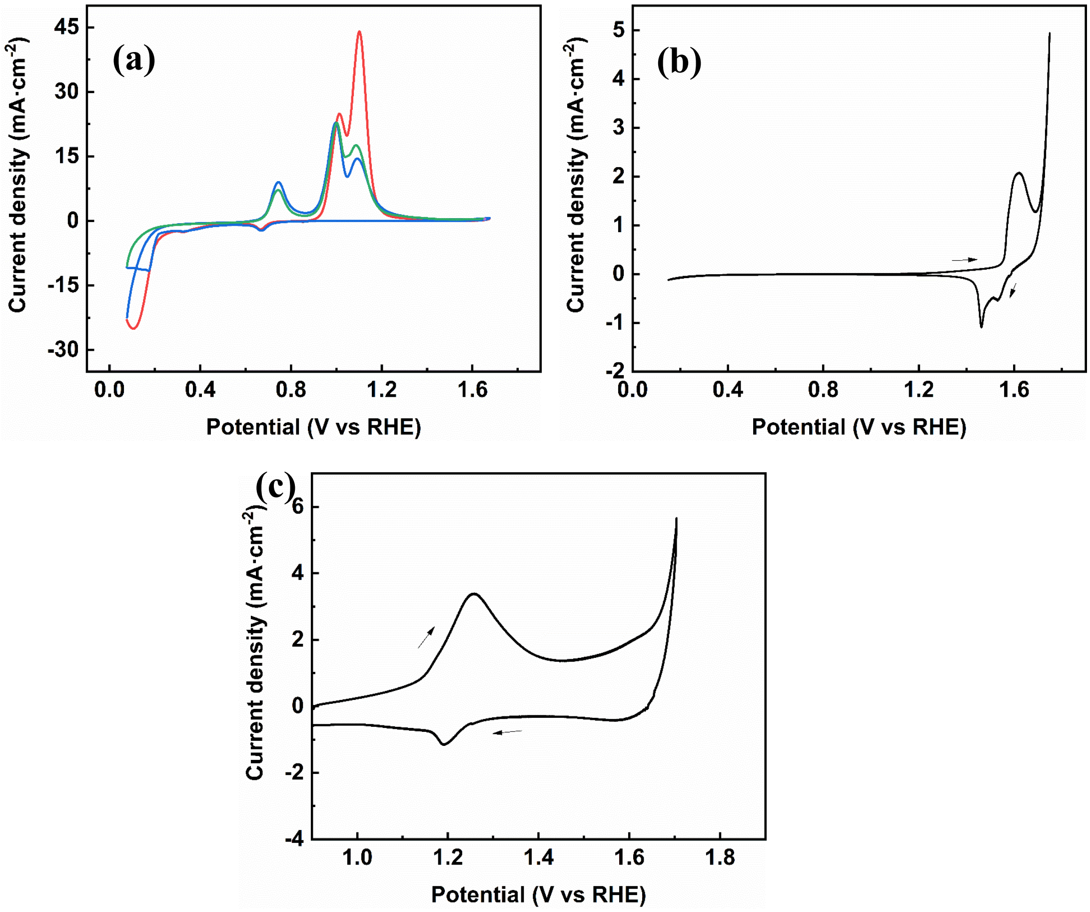

Figure 5.11. CV curves of Cu foil (a), Ni wire (b) and Co wire (c) in 1 M KOH at 40 °C.

The CV curve of the alloy (Figure 5.3a) exhibits several oxidation peaks, indicating the presence of selected elements that need to be removed. However, the reaction state of each element cannot be obtained from the CV curve of a single alloy. To do this, it is necessary to measure the oxidation potentials of the different elements in the alloy and select a more appropriate oxidation potential for the electrochemical dealloying process. The CV curve on Cu foil in 1 M KOH (Figure 5.11a) reveals distinct oxidation peaks at 0.75 V/RHE, 1.0 V/RHE, and 1.16 V/RHE, indicating that the oxidation potential range for Cu extends from 0.65 to 1.2 V/RHE. This observation is consistent with the results of previous research regarding the oxidation behavior of copper [173]. The CV curve for nickel is shown in Figure 5.11b. An oxidation peak is observed at 1.62 V/RHE, which would correspond to the transformation of Ni into Ni^{2+} and $Ni(OH)_2/NiOOH$ [174, 175]. The two peaks seen in the cathodic scan may correspond to the reduction reaction of Ni^{2+}. The CV curve of cobalt is shown in Figure 5.11c. During the anodic scan, an oxidation peak is observed in the potential range from 1.2 to 1.35 V/RHE, indicating the occurrence of the oxidation reaction of cobalt species. Similarly, in the cathodic scan, a reduction peak is evident, corresponding to the reduction reaction of cobalt species. The electrochemical behavior of zinc in 1M KOH is tricky to measure directly, due to its rapid and spontaneous dissolution in this alkaline solution. However, based on information from previous studies, it can be deduced that the reduction potential of zinc is lower than that of copper in an alkaline environment [176, 177].

The CV curves of the Zn-Ni-Co-Cu alloy were analyzed based on the CV curves of the individual metals in order to understand the different observed peaks. As shown in Figure 5.12a, the CV curve for the Zn-Ni-Co-Cu alloy exhibits several distinct peaks. At 0.26 V/RHE, a small peak can be attributed to the zinc exfoliation. This is followed by broad peaks at 0.75 V/RHE and between 0.95 and 1.24 V/RHE, corresponding to copper oxidation. Two peaks at 1.35 and 1.5 V/RHE can be attributed to nickel oxidation. Earlier studies, including our work described in Chapter 3 (Figure 3.4b), have shown that nickel reduction peaks can be attributed to multiple processes, such as Ni to Ni^{+}, and Ni^{+} to Ni^{2+}, and may involve the reduction of nickel to NiOOH or $Ni(OH)_2$, followed by further oxidation [170]. Cobalt, which sits beneath the Zn-Ni layer, has a relatively low overall content and is easily overshadowed by other peaks, making it difficult to highlight in the CV of the alloy. Furthermore, after the first scan, the current values corresponding to the reduction peaks of copper and nickel increase significantly. This is mainly due to the exfoliation of the surface oxide layer and the dissolution of zinc after the first redox scan. More copper, cobalt, and nickel are present inside the deposited layer, which is confirmed by subsequent EDS analysis, revealing a gradient distribution of the elements beneath the surface, which will be discussed in more detail in the following section. In addition, the irreversibility of α-$Ni(OH)_2$ to β-$Ni(OH)_2$ leads to its accumulation on the surface after the initial cycle, contributing to the increase in current during further oxidation of $Ni(OH)_2$/NiOOH[171]. A phenomenon similar to that of Zn-Ni-Co-Cu can also be found in the CV curves of Zn-Ni-Cu alloys in Figure 5.12b, with peaks at 0.76 V/RHE, 1 V/RHE and 1.16

V/RHE corresponding to the reduction potential of Cu, while the peaks at 1.25 and 1.51 V/RHE testify to the reduction of Ni.

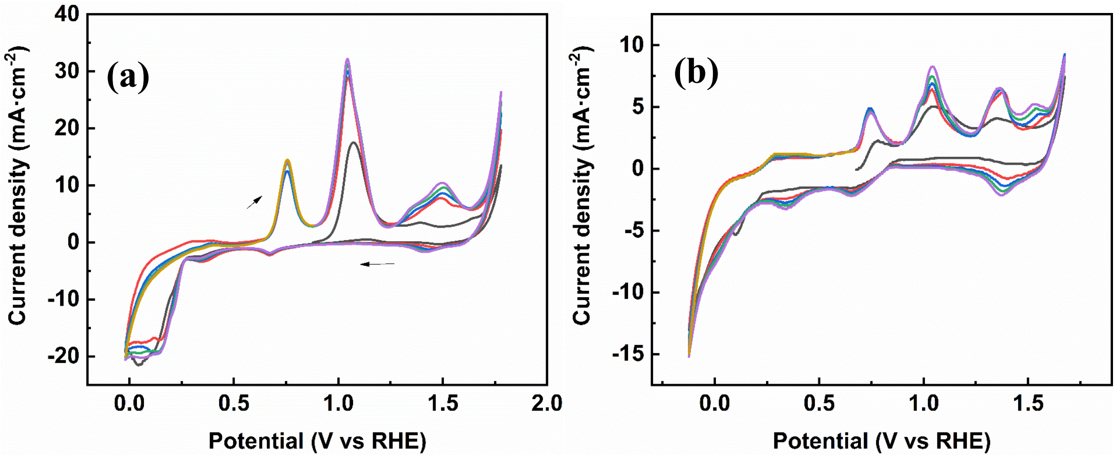

Figure 5.12 CV curves of Zn-Ni-Co-Cu alloy (a) and Zn-Ni-Cu (b) after the heat treatment in 1 M KOH at 40 ºC.

5.5. Characterization of nanoporous Zn-Ni-Co-Cu alloys

The XRD patterns are shown in Figure 5.13. By increasing the deposition time to 1 hour, the intensity of the characteristic cobalt peak shows no significant change, resulting in only the characteristic copper peak being visible in the XRD pattern of Co deposited before heat treatment. After heat treatment, the same CoO peaks observed in Figure 5.4 become evident, indicating slight oxidation of Co during the heat treatment process. In addition, peaks corresponding to $CuCoN_{0.6}$ are observed at 42°, 49°, and 72°. As mentioned in Chapter 3, the electrodeposition of Co in the electrolyte (EAN) is accompanied by a minor amount of residual nitrogen from the electrolyte, leading to the formation of this new phase by diffusion during the subsequent heat treatment process. After ZnNi deposition, the XRD pattern shows similar characteristics to those mentioned in the previous section, with only discreet diffraction peaks of Zn and Ni visible, and Cu originating from the matrix. However, after heat treatment, the XRD pattern reveals the appearance of complex phases. Apart from a small amount of unoxidized Zn, it is clear that the diffraction peaks arise mainly from the diffusion of Cu to form new solid solutions or intermetallic compounds, such as $Cu_{3.8}Ni$ and Cu_5Zn_8. In addition, a small amount of ZnO is present, indicating the oxidation of Zn during the heat treatment process.

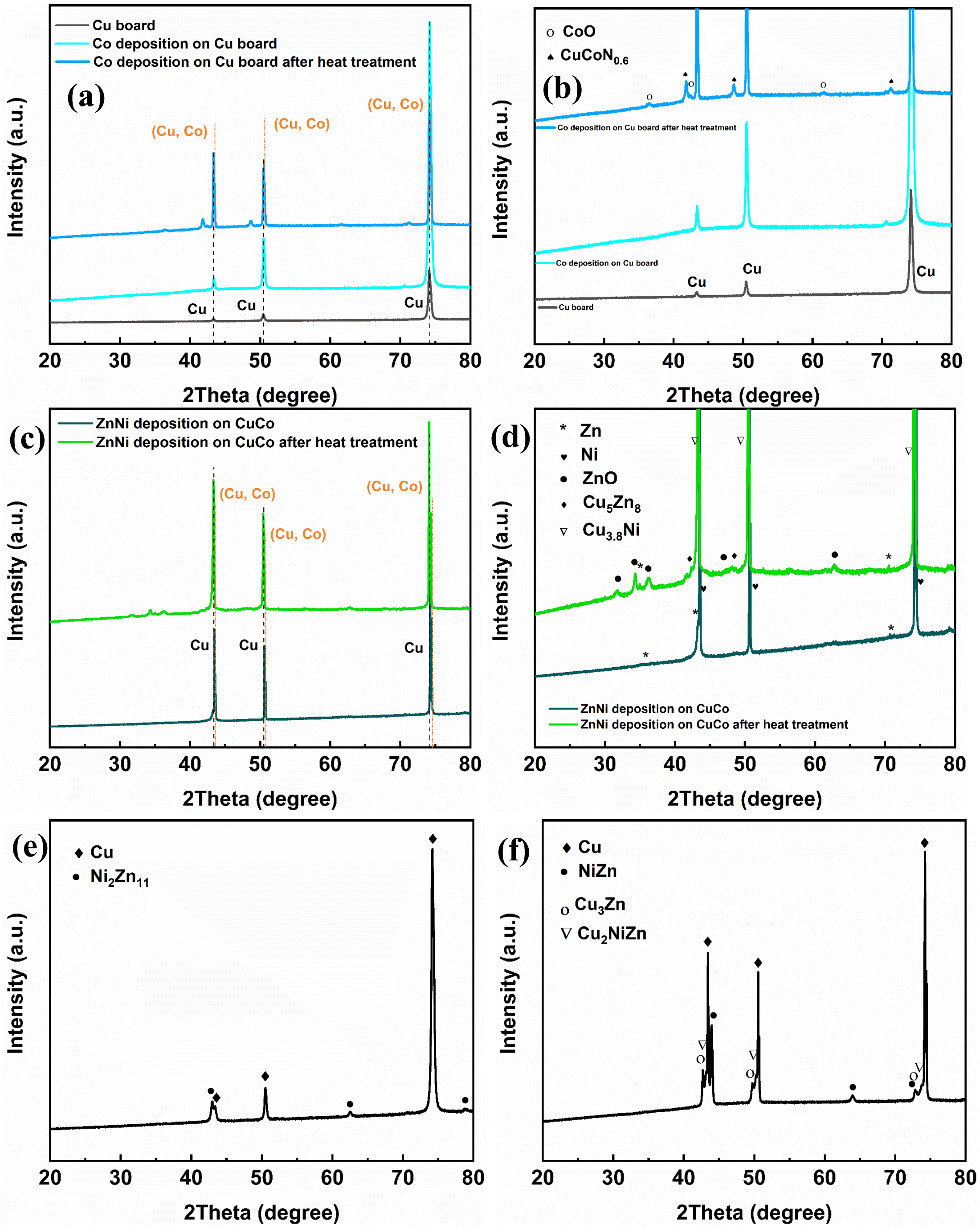

Figure 5.13 XRD patterns of (a, b) 1 h deposited Co on Cu before and after heat treatment periods, (c,d) deposited Zn-Ni on Cu-Co alloys before and after heat treatment periods, and(e) deposited Zn-Ni on Cu before and (f) after heat treatment.

We then characterized the deposited Zn-Ni alloy, as shown in Figure 5.13e. Besides the presence of Cu in the matrix, the diffraction peaks of Ni_2Zn_{11} are also observed, indicating the successful electrodeposition of the Zn-Ni alloy rather than individual Zn or Ni. After the alloy has been thermally treated at 400 °C for half an hour, various intermetallic compounds such as NiZn, Cu_3Zn, and Cu_2NiZn are formed due to the element diffusion. It is noteworthy that the formation of these intermetallic compounds can lead to changes in the intrinsic electrode potential, suggesting that the potential difference between the phases may have various effects on subsequent dealloying processes [130].

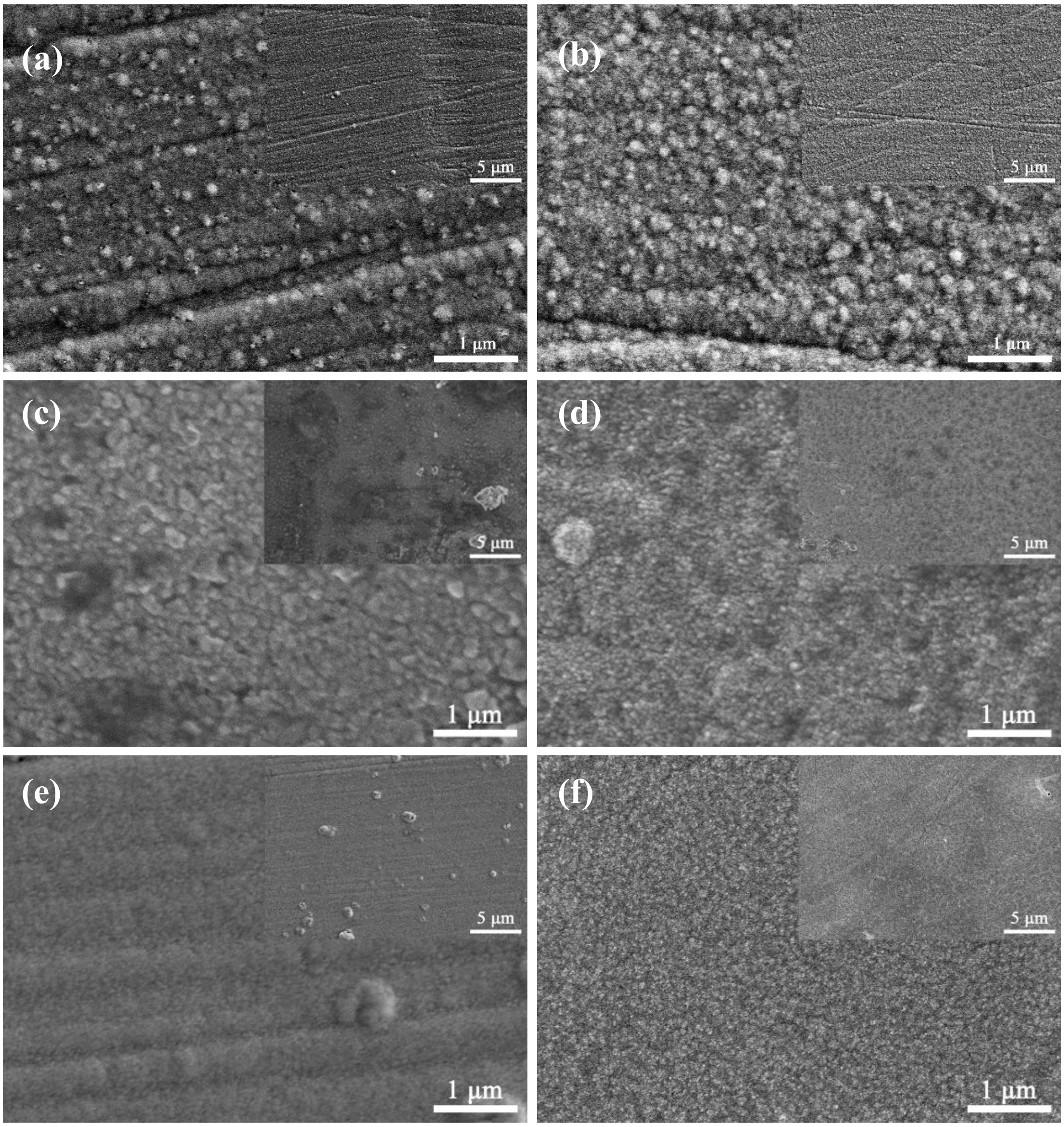

Figure 5.14 SEM images of (a) 1 h deposited Co on Cu before and (b) after heat treatment, (c) deposited Zn-Ni on Cu-Co alloys before and (d) after heat treatment, (e) deposited Zn-Ni on Cu before and (f) after heat treatment.

SEM analysis of Co electrodeposited for 1 hour reveals a surface morphology characterized by visible grains, as shown in Figure 5.14a. After the sample has been heat treated for 30 minutes, more visible and compact grain structures appear. The 2-hour Zn-Ni electrodeposition, shown in Figure 5.14c, also exhibits a similar grain morphology, suggesting that the deposition and growth process continues along the Co-Cu alloy after heat treatment, leading to the formation of a more compact structure after the second heat treatment. Similarly, the Zn-Ni electrodeposited on Cu also displays a similar phenomenon before and after heat treatment. As illustrated in Figure 5.14f, the surface structure shows clear grain separation, contrasting with the flat surface observed before heat treatment.

Table 5.4 The elements of different alloys before and after heat treatment.

	Parameters	Heat treatment	Zn (at%)	Ni (at%)	Co (at%)	Cu (at%)	O (at%)
EAN + 0.5 M $CoCl_2$	-1.05 V, 60 °C, 60 min	×	-	-	61.7	25.8	12.5
		√	-	-	50.6	35.5	13.8
Ethaline + 0.35 M $ZnCl_2$ + 0.15 M $NiCl_2$ on Co-Cu	-1.3 V, 40 °C, 120 min	×	68.1	10.0	8.1	3.6	10.3
		√	55.0	9.9	4.0	8.7	22.4
Ethaline + 0.35 M $ZnCl_2$ + 0.15 M $NiCl_2$ on Cu	-1.3 V, 40 °C, 210 min	×	68.0	16.4	-	1.7	13.9
		√	46.0	6.7	-	20.1	27.2

The EDS spectra presented in Figure 5.15 reveal distinct signals for Cu in all samples, with varying oxygen content. The corresponding element contents are summarized in Table 5.4. Comparing the results of 0.5 h cobalt electrodeposition, it is evident that a greater amount of Co is obtained on Cu, increasing significantly from 38.0 to 61.7 at% after a 1 h Co electrodeposition. Following the heat treatment, the Co content decreases to 50.6 at%, while the Cu content increases from 25.8 to 35.5 at%, which can be attributed to the diffusion of copper during the heat treatment. The oxygen content increases from 12.5 to 13.8 at%, leading to the formation of cobalt oxides, as confirmed by XRD analysis. In the case of the Zn-Ni alloy deposited in ethaline, zinc dominates with a content of 68.1 at%. After heat treatment, the oxygen content increases significantly from 10.3 to 22.4 at%, again due to the formation of oxides, corresponding to the ZnO phase detected in the XRD results. Moreover, after heat treatment, the content of Zn, Ni, and Co in the alloy elements decreases, while that of Cu increases, confirming the diffusion of Cu from the substrate to the alloy layer.

In addition, the electrodeposition of the Zn-Ni alloy on the Cu foil for 3.5 hours yielded 68.0 at% Zn and 16.4 at% Ni. After heat treatment, Cu composition also shows a significant increase, from 1.7 to 20.1 at%. Although the cobalt content in the Zn-Ni-Co-Cu alloy is not evident after heat treatment, it can still be used for the HER property comparison with the Zn-Ni-Cu alloy in the subsequent experimental conclusions due to the obvious different Cobalt content.

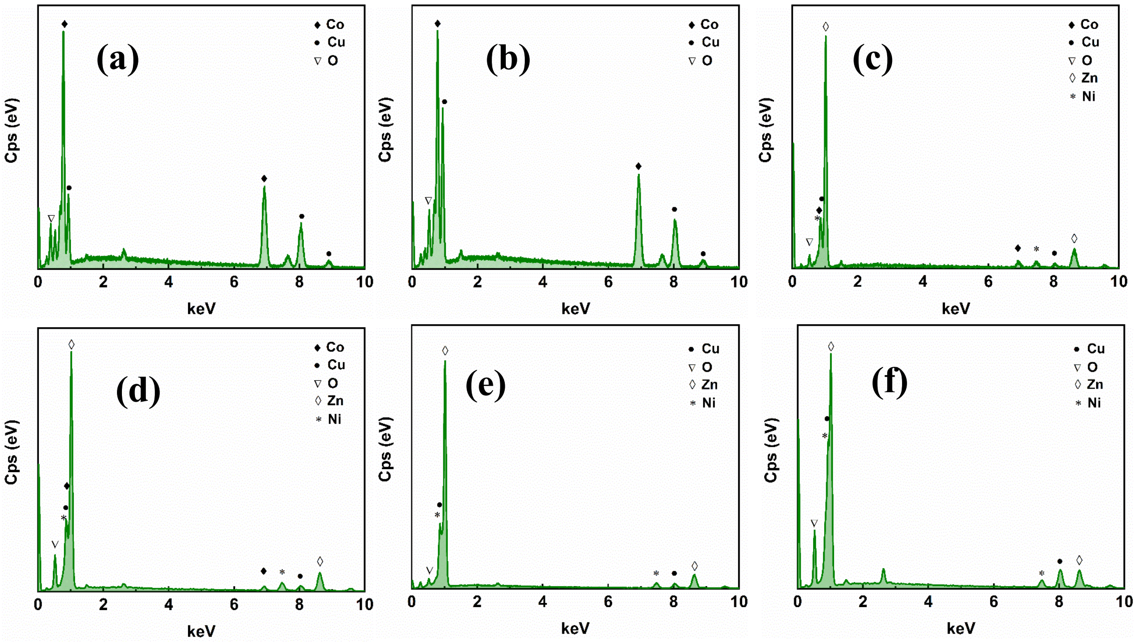

Figure 5.15 EDS curves of different deposited alloys: Co deposited on Cu before (a) and after the heat treatment (b); Zn-Ni deposited on Co-Cu before (c) and after the heat treatment (d); Zn-Ni deposited on Cu before (e) and after the heat treatment (f).

As mentioned above, although the distribution of elements after heat treatment is relatively more uniform than before, it is difficult to determine the element distribution of the deposited film based on surface elements alone. A more detailed distribution can be obtained by line scanning with EDS, as shown in Figure 5.16. Due to the ductility of copper, some copper may be incorporated into the deposit during the preparation of the SEM sample. However, on the whole, the individual elements can still be distinguished. After electrodeposition, it is evident that the Co is clearly separated from the substrate, and at a depth of 1.4 μm below the starting position of the measurement, there is no Co signal, replaced by a large amount of copper substrate. After heat treatment, due to the fixed angle of the sample, we measured the lateral and top surfaces, simultaneously. We observed a higher Cu content in the fractured part of the deposit, as well as at the contact surface between the deposit and the Cu substrate. This suggests that Co and Cu diffused into the each other during the heat treatment process. The higher copper content compared to Co can be attributed to the inclusion of copper from the substrate during sample preparation, and to the range of the electron beam that resulted in some of the Cu coming from other areas to be included in the analysis. The electrodeposition of Zn-Ni alloy on the Co-Cu alloy led to a higher concentration of Zn at a distance of 15 μm from the test point, while Cu was almost absent at this location, indicating good separation. After the heat treatment, the topography (Figure 5.16d) revealed the presence of two distinct thin films on the top surface of the sample. Analyzing the element distribution at the double film level, it can be observed that the Zn distribution is almost uniform, ranging from 1.0 to 1.7 μm from the test starting point. Simultaneously, Ni content is low, but its distribution position remains similar to that of Zn, also showing uniformity. Cu distribution, on the other hand, is progressive, with the highest Cu content observed further away from the alloy surface. As for Co, it is mainly concentrated in the second film (Co-Cu substrate) and the Cu substrate, a small amount of Co signal can still be detected when scanning the surface. In fact, based on the analysis of the element distribution and morphology of the final Zn-Ni-Co-Cu alloy obtained, it can be deduced that after heat treatment, Ni and Zn are uniformly distributed in the two deposit layers, while Co has less content in the first layer of deposits (Zn-Ni deposits), mainly concentrated in the second layer (Co-Cu), and diffuses into the Cu base with gradually decreased content. The distribution of Cu gradually decreases as it diffuses from the Cu base to the upper layer. The non-uniform distribution of some alloying elements observed in the present study suggests that further optimization of the heat treatment conditions may be required to achieve a more uniform distribution. However, it is crucial to strike a balance between improving distribution and preventing potential issues such as grain growth and the formation of new phases that could render the alloy fragile and unstable during the hydrogen evolution reaction. In addition, this distribution pattern suggests that, through appropriate dealloying, the inner Cu can become the main structure of the material, leading to a distinct element distribution and morphology. Therefore, the remainder of this research will be based on this prepared Zn-Ni-Co-Cu alloy.

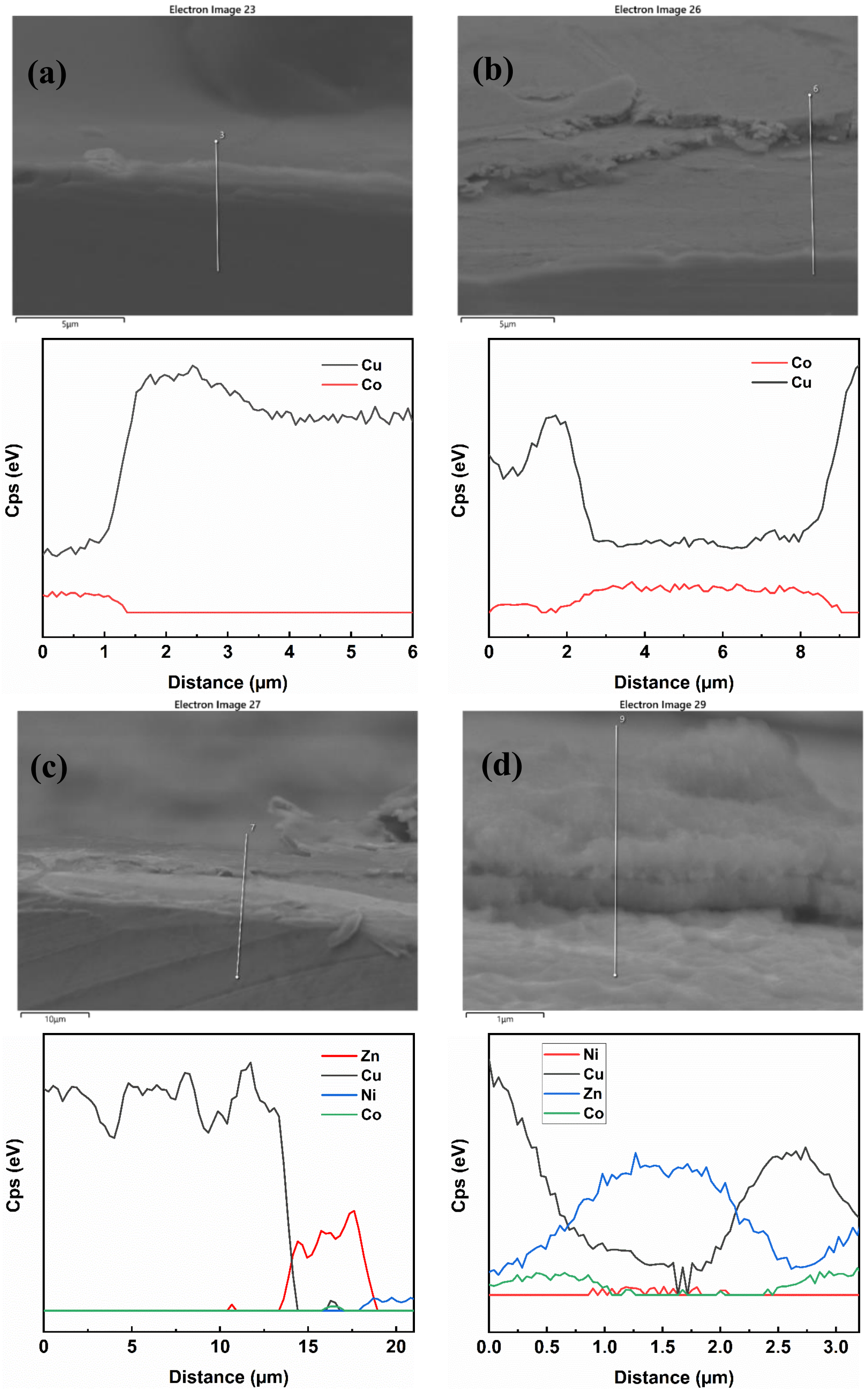

Figure 5.16 SEM and EDS line scan curves of different deposited alloys: Co deposited on Cu before (a) and after the heat treatment (b); Zn-Ni deposited on Co-Cu before (c) and after the heat treatment (d).

Based on the Zn-Ni-Co-Cu alloys prepared, different dealloying conditions were applied. The parameters are shown in Table 5.5. Alloys were treated by chemical dealloying in EAN + 0.01 M CH_3COOH, 1 M KOH and 0.01 M HNO_3, respectively. The electrochemical dealloying was applied in 1 M KOH with 1.09 V/RHE at different time, following the CV curves in Figure 5.12, corresponding to Cu oxidation. Dealloying procedures were carefully carried out under an argon flow to minimize sample oxidation. SEM topographic images of the chemical dealloying process in EAN + 0.01 M CH_3COOH are shown in Figure 5.17a and b. After 3 minutes of treatment, the alloy surface shows an irregular morphology, and after 5 minutes of treatment, a distinct pore structure emerges, evenly distributed all over the alloy surface. The complete pore diameter ranges from approximately 100 to 400 nm. For alloys chemically dealloyed in 1 M KOH, Figure 5.17c and d show the results after a half-hour treatment, where grooves are etched on the surface, together with dense and uniform pores with a diameter of 100 nm. On the other hand, one hour of dealloying results in a flat surface with numerous cracks, suggesting that an excessively prolonged dealloying time leads to the destruction of the surface features. The morphology after electrochemical dealloying in KOH is shown in Figure 5.17e and f. Remarkably, application of the potential for just 10 minutes results in the formation of dense and uniform nanopores, averaging around 100 nm size, on the surface. Comparing the samples after a 10-minute or a 30-minute electrochemical dealloying, it is evident that the longer treatment leads to an increase in pore size, which eventually connect with each other to form cracks and grooves. In addition, a chemical dealloying in HNO_3 resulted in a similar porous structure. The cross-section of the HNO_3-treated sample is displayed in Figure 5.17h, demonstrating that the porous structure caused by dealloying passes through the entire alloy film and is not limited to the sample surface. These observations illustrate that the dealloying process can generate nanoporous structures with controllable pore size and distribution.

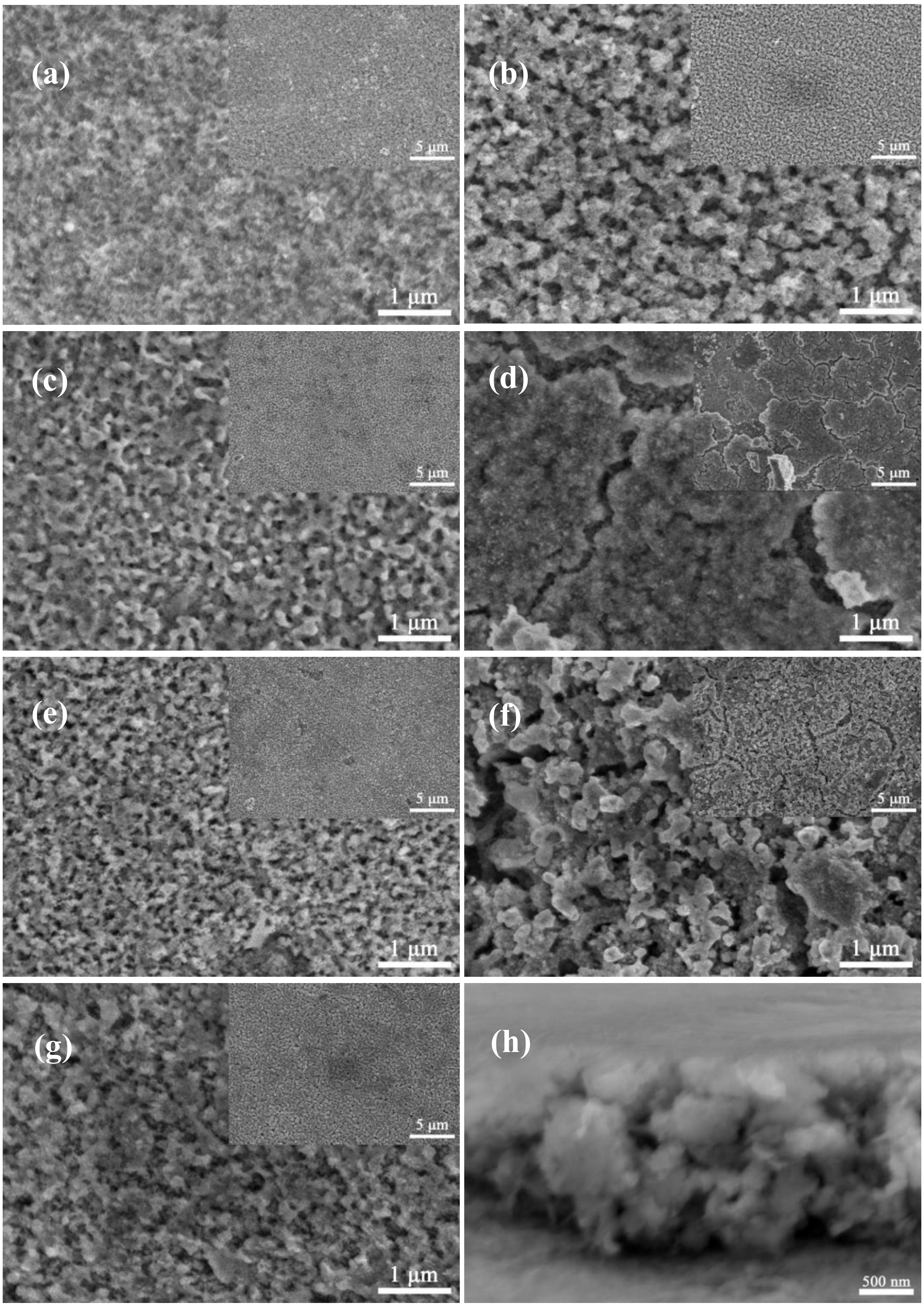

Figure 5.17 SEM of Zn-Ni-Co-Cu alloys treated in EAN + 0.01 CH_3COOH for 3 min (a) and 5 min (b); in 1 M KOH for 30 min (c) and 60 min (d) and electrochemical dealloying at 1.09 V/RHE for 10 min (e) and 30 min (f); in 0.01 M HNO_3 for 30 min (g) and (h).

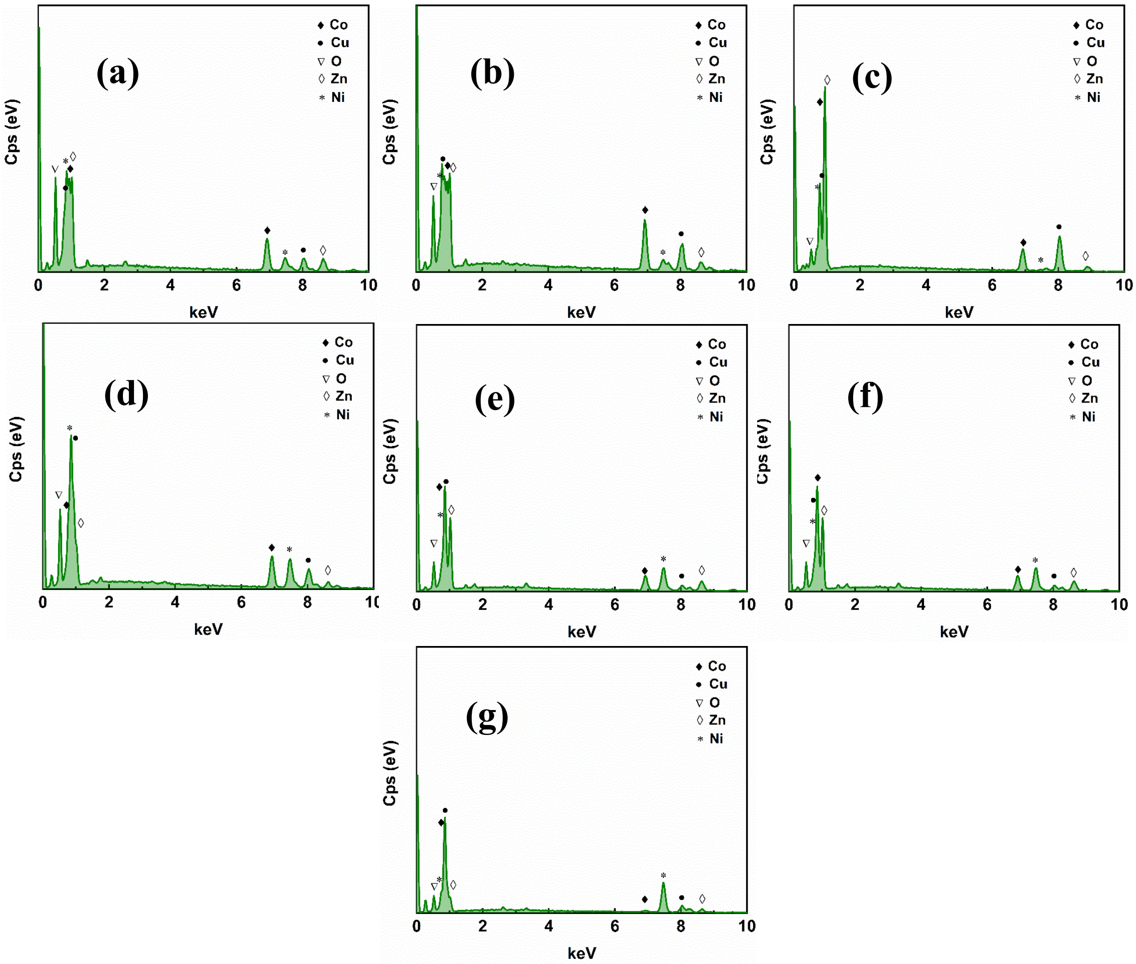

Figure 5.18 EDS of Zn-Ni-Co-Cu alloys treated in EAN + 0.01 CH_3COOH for 3 min (a) and 5 min (b); in 1 M KOH for 30 min (c) and 60 min (d) and electrochemical dealloying at 1.09 V/RHE for 10 min (e) and 30 min (f); in 0.01 M HNO_3 for 30 min (g).

The composition of the elements in the nanoporous alloy after dealloying is shown in Figure 5.18 and summarized in Table 5.5. Observation of the results clearly shows that, whatever the dealloying method, chemical or electrochemical, the proportion of Zn in the alloy decreased significantly after dealloying. In particular, after a half-hour dealloying in HNO_3, the surface shows no presence of Zn, reducing the Zn content to 10.5 at% after dealloying at a potential of 1.09 V for 10 minutes. This indicates that Zn in the alloy can be effectively stripped at this potential. Meanwhile, the nickel content of most samples increased significantly. As for the copper content, the initial content was 8.7 at%, and in most cases, the copper content increased after dealloying. At a dealloying potential of 1.09 V/Ag/Ag^+, Cu will theoretically be stripped. However, the distribution of Cu exhibits a gradient from the top layer surface (Zn-Ni deposits) to the interior, according to line scan EDS analysis. As a result, there are more Cu exposed after the electrochemical dealloying in KOH solution, reaching 15.8 at% and 22.2 at%, respectively (shown in Table 5.5).

Table 5.5 The elements of Zn-Ni-Co-Cu alloys after dealloying.

Solution	Conditions	Zn (at%)	Ni (at%)	Co (at%)	Cu (at%)	O (at%)	Donated
original	-	55.0	9.9	4.0	8.7	22.5	$Zn_{70.9}Ni_{12.7}Cu_{11.2}Co_{5.2}$
EAN + 0.01 M CH_3COOH	3 min	21.2	9.7	19	18.5	31.6	$Cu_{39.9}Zn_{31.9}Ni_{15.7}Co_{12.4}$
	5 min	22.3	7.0	28.4	18.3	24.0	$Co_{37.4}Zn_{29.3}Cu_{24.1}Ni_{9.2}$
1 M KOH	30 min	61.1	13.7	7.5	4.7	13.0	$Zn_{70.3}Ni_{15.7}Co_{8.6}Cu_{5.4}$
	60 min	29.9	30.5	15.5	7.2	17.0	$Ni_{36.7}Zn_{36.0}Co_{18.7}Cu_{8.6}$
	1.09 V, 10 min	10.5	57.2	2.0	15.8	14.6	$Ni_{66.9}Cu_{18.5}Zn_{12.3}Co_{2.3}$
	1.09 V, 30 min	11.2	22.0	18.7	22.2	25.9	$Zn_{44.3}Ni_{31.4}Cu_{13.0}Co_{11.3}$
0.01 M HNO_3	30 min	0	1.6	24.2	62.4	11.8	$Cu_{70.7}Co_{27.4}Ni_{1.9}$

In summary, chemical dealloying in EAN + 0.01 M CH_3COOH mainly reduces the Zn content to 21.2 at% and 22.3 at%, for 3 and 5 min, respectively. Ni content decreased slightly, while Co and Cu increased significantly, indicating that the elements diffused from the substrate to the surface when exposed to the solution. The slight increase in O content suggests that replacing water with EAN cannot effectively reduce the oxidation during dealloying. After 30 minutes of chemical dealloying in 1 M KOH, the alloying element content of did not change significantly, but the oxygen content decreased substantially from 22.5 to 13.0 at%, implying that the main surface oxide was removed during this treatment. Extending the chemical dealloying to 60 minutes resulted in a considerable decrease in Zn content, with Ni becoming the main element. Electrochemical dealloying exhibited a similar trend, with longer durations leading to a reduction in Ni content from 57.2 to 22.0 at%, while the relative content of Co and Cu increased. In the case of 0.01 M HNO_3, almost all of the Zn was exfoliated, making Cu the main alloying element.

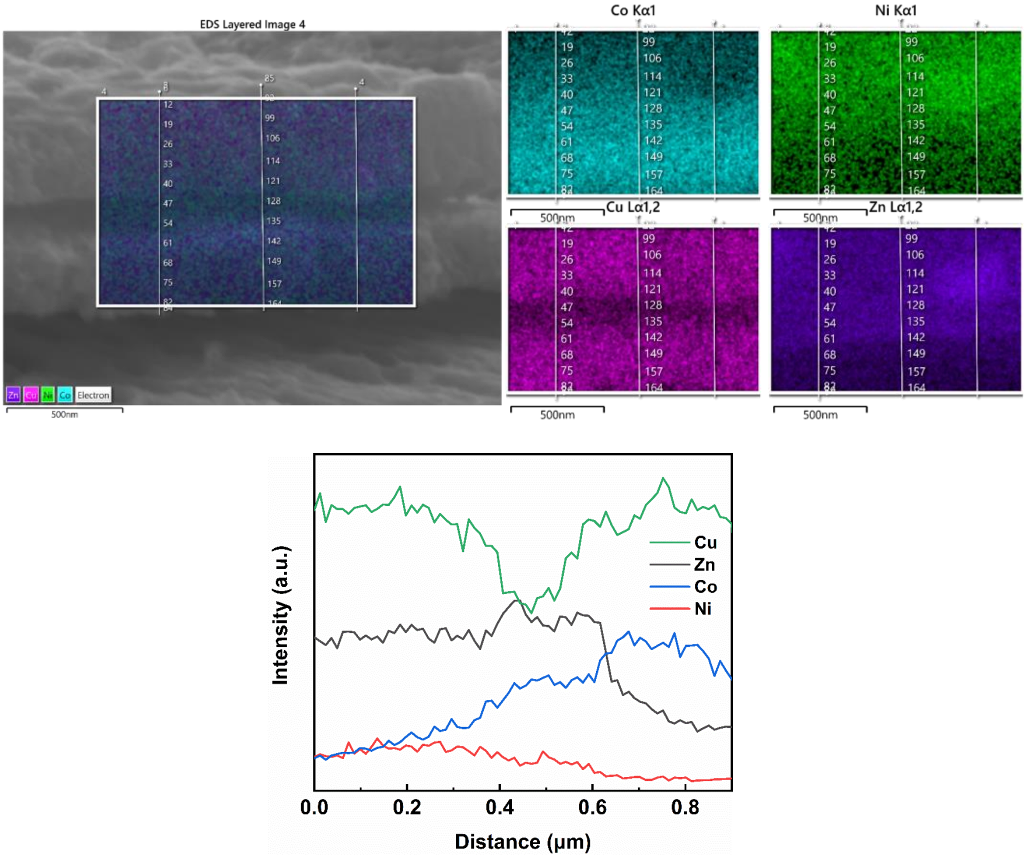

Figure 5.19 The EDS line scan of $Cu_{39.9}Zn_{31.9}Ni_{15.7}Co_{12.4}$.

Table 5.6 The elements of $Cu_{39.9}Zn_{31.9}Ni_{15.7}Co_{12.4}$ in EDS line scan.

Point	Cu (at%)	Zn (at%)	Co (at%)	Ni (at%)
Mapping	39.9	31.9	12.4	15.7
1	43.9	30.9	11.2	14.0
2	44.3	32.2	10.5	13.0
3	41.9	32.3	12.3	13.4
4	40.4	25.8	18.1	15.7
5	39.1	27.8	20.6	12.5
6	28.2	35.9	29.2	6.6
7	29.2	32.7	31.7	6.4
8	36.9	26.1	32.2	4.8
9	48.7	10.5	40.7	0
10	54.5	9.6	35.9	0

EDS line scans of $Cu_{39.9}Zn_{31.9}Ni_{15.7}Co_{12.4}$ obtained by dealloying in EAN + 0.01 M CH_3COOH for 3 minutes are presented in Figure 5.19. The mapping shows the distribution of elements after dealloying. It can be seen that Cu has diffused into the top layer, and its distribution becomes more uniform after dealloying, which can be attributed to atomic reorganization following the dealloying process [178]. To analyze this gradient distribution, points were taken regularly along the linear scan path, and their data are listed in Table 5.6. The data clearly show that Co content increases progressively from the surface inwards, from 11.2 to 35.9 at%. Conversely, Zn and Ni show a progressive decrease from the surface inwards, indicating that their distribution is uneven after heat treatment and dealloying.

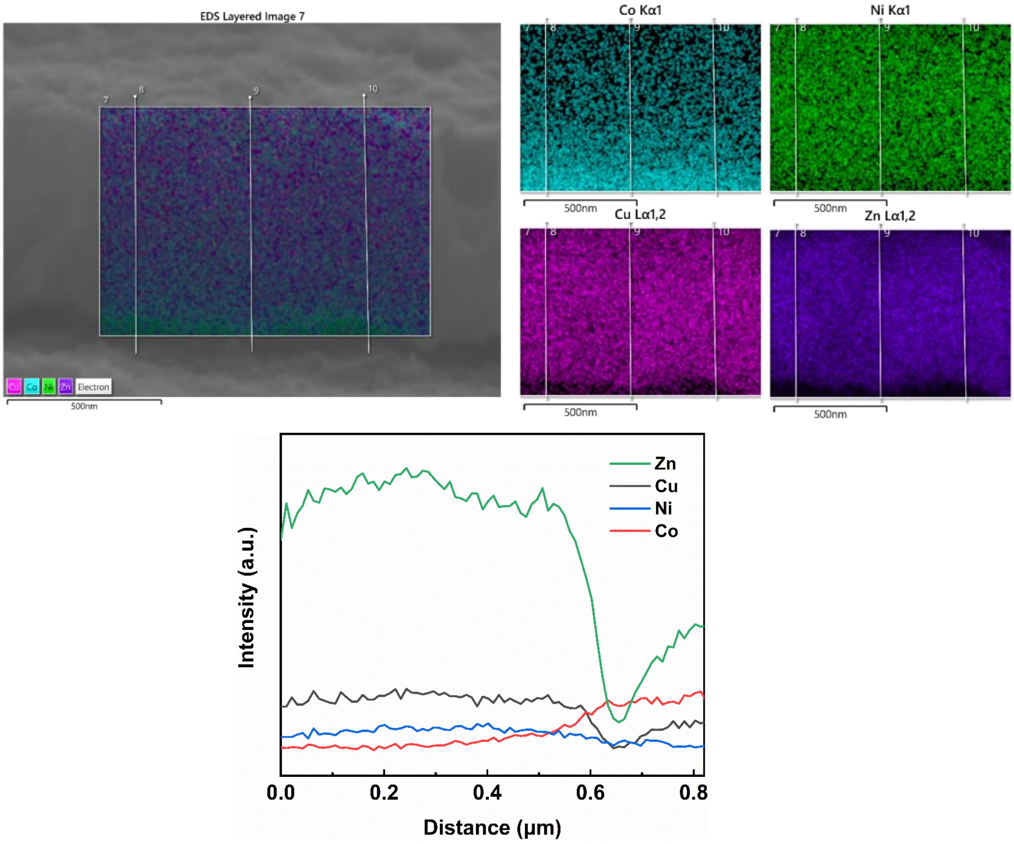

Figure 5.20 EDS line scan of $Zn_{44.3}Ni_{31.4}Cu_{13.0}Co_{11.3}$.

The $Zn_{44.3}Ni_{31.4}Cu_{13.0}Co_{11.3}$ sample electrochemically dealloyed in 1 M KOH at 1.09 V/RHE for 30 minutes exhibits a gradient distribution of elements, which is evident in Figure 5.20 and Table 5.7. Both the global mapping data and the point data from the line scan reveal a relatively uniform distribution of Cu and a continuous decrease in Ni from the surface to the deeper layers. However, Zn content shows an interesting pattern, increasing slightly from the surface and then decreasing towards the interior. Specifically, it increases from 65.1 at% at the surface, reaches 71.5 at% at some depth, and then decreases to 48.4 at% in the deeper layers. These observations validate the effective removal of Zn from the surface during the dealloying process and the Zn diffusion from the first layer to the interior after heat treatment.

Table 5.7 The elements of $Zn_{44.3}Ni_{31.4}Cu_{13.0}Co_{11.3}$ in EDS line scan.

Point	Cu (at%)	Zn (at%)	Co (at%)	Ni (at%)
Mapping	13	44.3	11.3	31.4
1	10.8	65.1	4.1	20.0
2	11.6	69.5	3.1	15.8
3	10.2	71.5	0	18.3
4	10.3	68.3	3.7	17.7
5	7.8	70.2	4.7	17.3
6	9.8	67	6.3	16.8
7	9.7	67.7	7	15.6
8	10.2	61.7	14.9	13.3
9	10	45.7	34.7	9.6
10	8.8	48.3	38	4.9

The morphology of the Zn-Ni-Cu alloy after dealloying is shown in Figure 5.21. When the alloy is chemically dealloyed in EAN + 0.01 M CH_3COOH for 3 minutes, the surface exhibits uneven pits, but no visible pores are observed. When the dealloying time is increased to 5 minutes, smaller but denser pores with an average size of about 200 nm can be observed. However, it is clear that these pores are not deep and do not penetrate through the alloy. On the other hand, the alloy surface obtained by chemical dealloying in 1 M KOH for 30 minutes exhibits a very typical morphology of dealloyed nanoporous copper [179]. There are no dense pores on the surface when the applied potential is 1.04 V/RHE and the sample is dealloyed for 10 minutes, but the porous morphology similar to that obtained by chemical dealloying for longer time becomes visible after increasing the dealloying time to 30 minutes. Although the time was extended to 60 minutes, the surface of Zn-Ni-Cu alloy dealloyed chemically with HNO_3 was not damaged. The surface contains a significant number of nanopores even after 30 minutes of chemical dealloying, but some flat areas remain. However, the flat areas decreased and denser porous structures appeared when the time was extended to 60 minutes. We believe that long-duration dealloying is favorable to the generation of a denser porous structure, but will also destroy that structure if extended excessively.

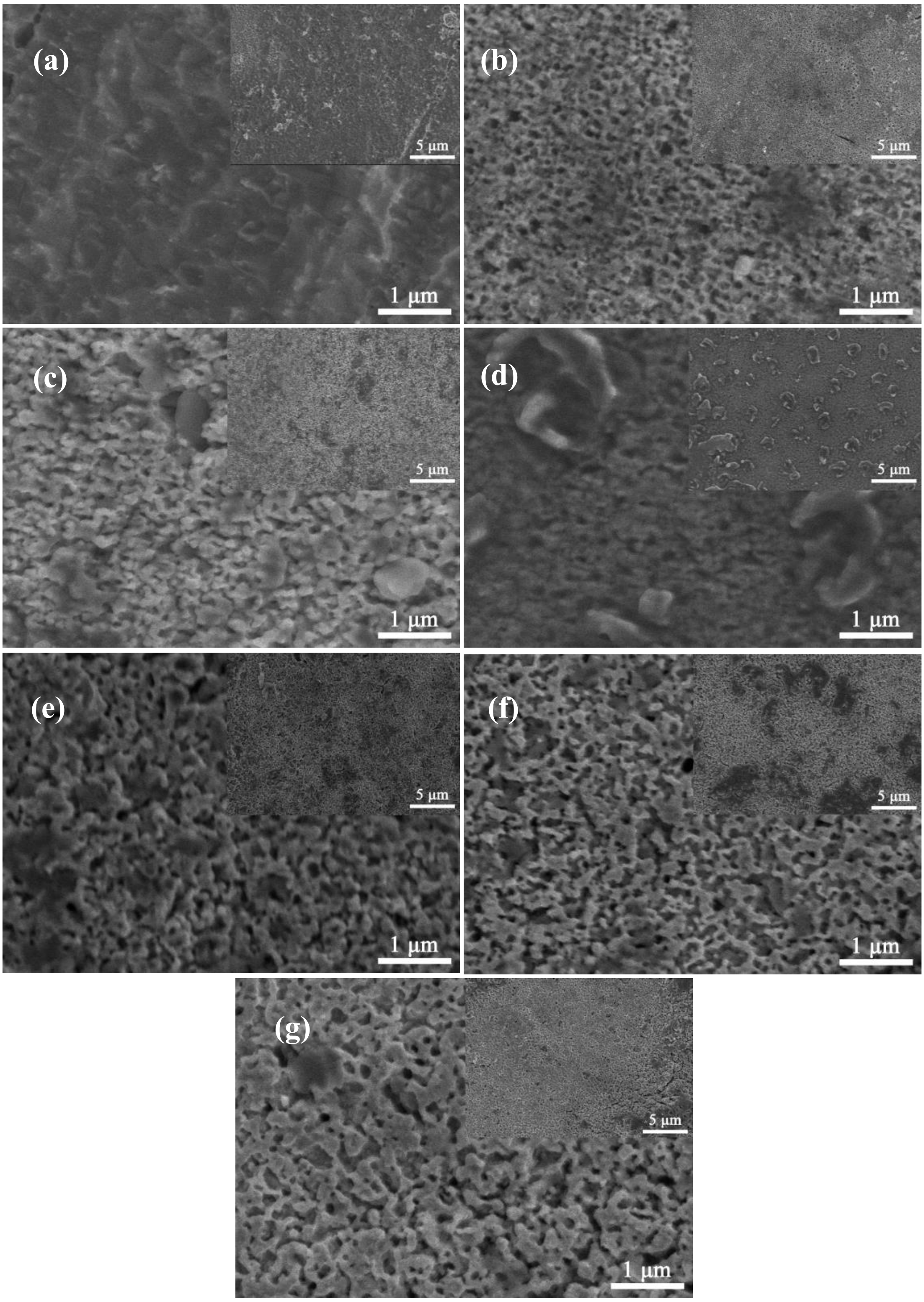

Figure 5.21 SEM of Zn-Ni-Cu alloys treated in EAN + 0.01 CH_3COOH for 3 min (a) and 5 min (b); in 1 M KOH for 30 min (c) and electrochemical dealloying at 1.04 V/RHE for 10 min (d) and 30 min (e); in 0.01 M HNO_3 for 30 min (f) and 60 min (g).

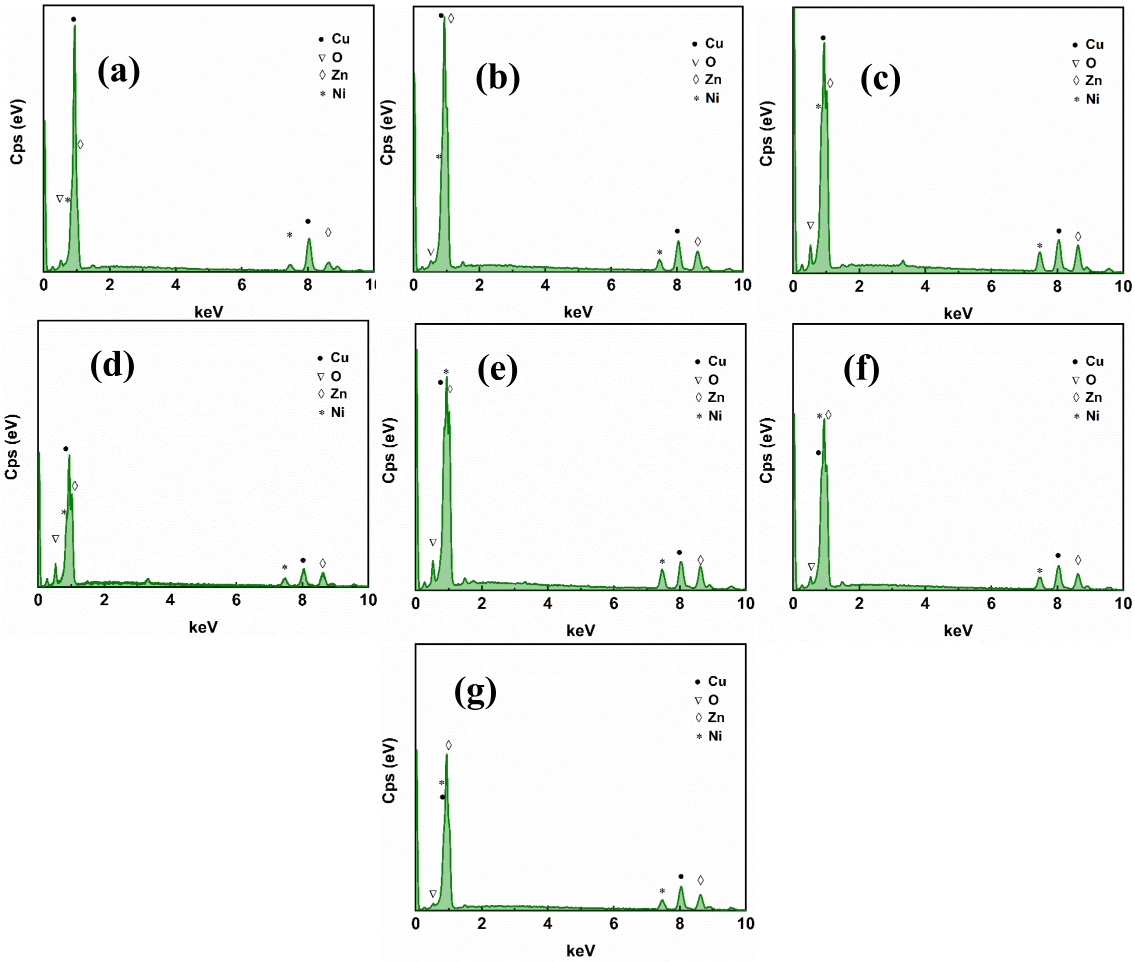

Figure 5.22 EDS of Zn-Ni-Cu alloys treated in EAN + 0.01 CH_3COOH for 3 min (a) and 5 min (b); in 1 M KOH for 30 min (c) and electrochemical dealloying at 1.04 V/RHE for 10 min (d) and 30 min (e); in 0.01 M HNO_3 for 30 min (f) and 60 min (g).

The element composition in the nanoporous Zn-Ni-Cu alloy after dealloying is illustrated in Figure 5.22 and summarized in Table 5.8. Various dealloying methods have demonstrated their ability to decrease the relative abundance of Zn, leading to its preferential removal. In the ternary alloy system, it is clear that Cu emerges as the main constituent, providing the fundamental structural support after dealloying. Prolonged exposure to chemical dealloying in an acidic solution (60 min) substantially reduces the relative Zn content, resulting in Cu-based compositions, illustrated by $Cu_{59.6}Zn_{31.0}Ni_{9.4}$ and $Cu_{44.2}Zn_{40.2}Ni_{15.6}$. Furthermore, our investigations in Chapter 3 revealed that the introduction of Co complicates the oxidation behavior of the alloy. When comparing Zn-Ni-Cu with Zn-Ni-Co-Cu, the oxygen content after dealloying decreased significantly from the initial 27.2 at%. This observation indicates that dealloying Zn-Ni-Cu alloy is more efficient at facilitating exfoliation of the oxide layer without the interference of Co.

Table 5.8 The elements of different Zn-Ni-Cu alloys after dealloying.

Solution	Conditions	Cu (at%)	Zn (at%)	Ni (at%)	O (at%)	Donated
original		20.1	46.0	6.7	27.2	$Zn_{63.2}Cu_{27.6}Ni_{9.2}$
EAN + 0.01 M CH_3COOH	3 min	41.5	44.7	11.3	2.5	$Zn_{45.8}Cu_{42.6}Ni_{11.6}$
	5 min	59.6	31.0	9.4	0	$Cu_{59.6}Zn_{31.0}Ni_{9.4}$
1 M KOH	30 min	33.5	40.8	16.2	9.5	$Zn_{45.1}Cu_{37.0}Ni_{17.9}$
	1.04 V, 10 min	33.7	38.5	12	15.8	$Zn_{45.7}Cu_{40.0}Ni_{14.3}$
	1.04 V, 30 min	32.0	40.8	16.5	10.7	$Zn_{45.7}Cu_{35.8}Ni_{18.5}$
0.01 M HNO_3	30 min	36.7	42.0	15.6	5.7	$Zn_{44.5}Cu_{38.9}Ni_{16.5}$
	60 min	43.2	39.3	15.2	2.3	$Cu_{44.2}Zn_{40.2}Ni_{15.6}$

5.6. Electrocatalytic properties of nanoporous Zn-Ni-Co-Cu/Zn-Ni-Cu alloys in HER

The effective electrochemical surface area (ECSA) of nanoporous alloys was determined by evaluating the interfacial capacitance (C^{σ}) at various scan rates, as shown in Figure 5.23a. The post-dealloying C^{σ} value is notably higher than that of the original alloy, $Zn_{70.9}Ni_{12.7}Cu_{11.2}Co_{5.2}$ (0.23 $mF \cdot cm^{-2}$), with a maximum value reaching 0.84 $mF \cdot cm^{-2}$, corresponding to $Ni_{36.7}Zn_{36.0}Co_{18.7}Cu_{8.6}$. Although the presence of oxides can influence the results, analysis of Table 5.5 indicates that the degree of oxidation is relatively similar among the samples, suggesting that this factor can be disregarded. Hence, the observed numerical increase in ECSA after dealloying can be attributed to the generation of a nanoporous structure.

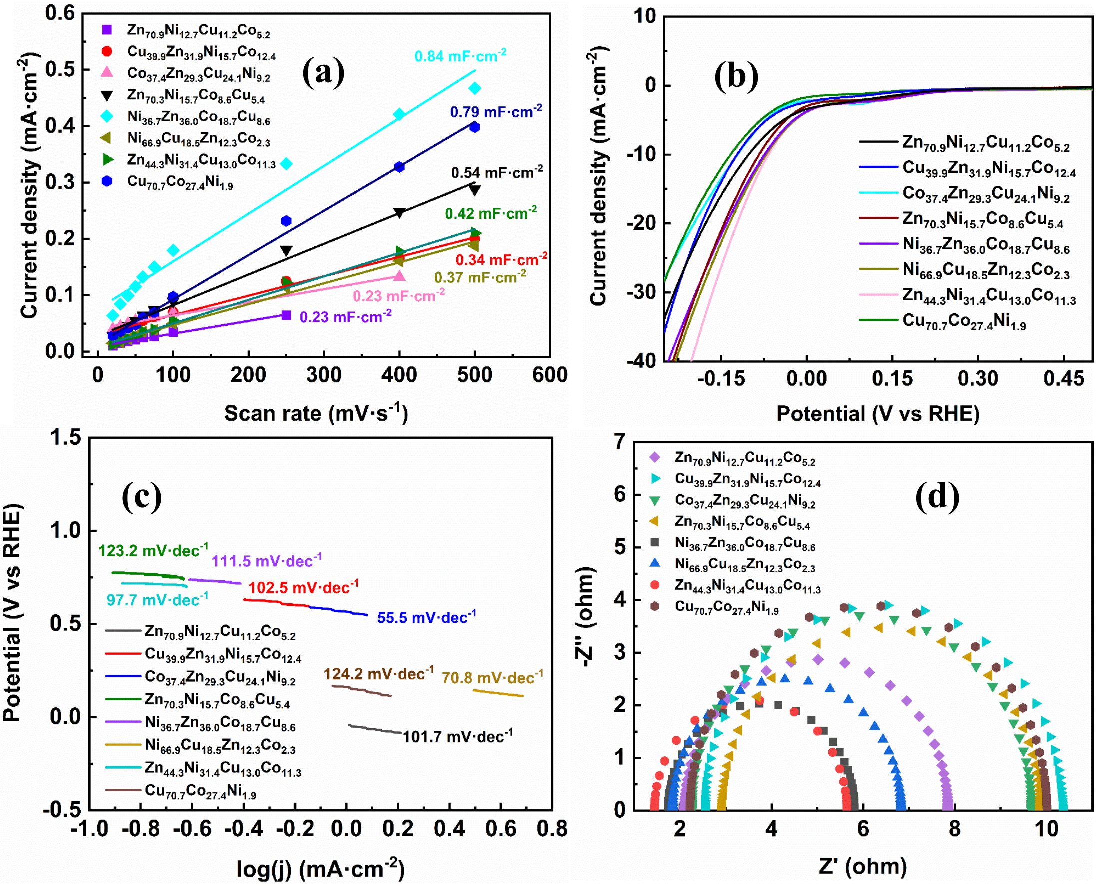

Figure 5.23 Electrocatalytic properties of the materials towards the HER for nanoporous Zn-Ni-Co-Cu alloys: C^{σ} (a), LSV curves (b), Tafel slopes (c) and EIS curves (d).

Figure 5.23b presents the electrocatalytic performance of the nanoporous alloy, revealing distinct characteristics. The nanoporous material obtained by chemical dealloying or electrochemical methods exhibits higher overpotentials for HER compared to the pristine alloy in acidic solution. Notably, specific compositions, such as $Zn_{70.3}Ni_{15.7}Co_{8.6}Cu_{5.4}$, $Ni_{36.7}Zn_{36.0}Co_{18.7}Cu_{8.6}$, $Ni_{66.9}Cu_{18.5}Zn_{12.3}Co_{2.3}$, and $Zn_{44.3}Ni_{31.4}Cu_{13.0}Co_{11.3}$, prepared in KOH solution, displayed remarkably low HER potential values of -0.084 V/RHE, -0.074 V/RHE, -0.071 V/RHE, and -0.067 V/RHE, respectively. These results indicate the higher HER performance potential of the nanoporous alloy. Although a sample prepared by dealloying in EAN + 0.01 M CH_3COOH, corresponding to the composition $Co_{37.4}Zn_{29.3}Cu_{24.1}Ni_{9.2}$, did not show an ideal overpotential value, it exhibited a lower Tafel slope of 55.5 mV·dec^{-1}. In addition, the alloy with a composition of $Ni_{66.9}Cu_{18.5}Zn_{12.3}Co_{2.3}$ also showed a lower Tafel slope of 70.8 mV·dec^{-1}. The distribution of main elements on the surface of these two nanoporous alloys, mainly Co and Ni, contributes to their enhanced electrocatalytic performance, compared with the surface filled by Zn.

The impedance spectra presented in Figure 5.23d, following fitting analysis, demonstrate that appropriate electrochemical dealloying significantly reduces the surface electron transfer resistance. Particularly, compositions like $Ni_{36.7}Zn_{36.0}Co_{18.7}Cu_{8.6}$ and $Ni_{66.9}Cu_{18.5}Zn_{12.3}Co_{2.3}$ exhibit lower surface electron transfer resistance values of 2.0 ohms and 2.5 ohms, respectively, compared to the original alloy, $Zn_{67.3}Ni1_{8.3}Cu_{7.8}Co_{6.6}$, which has an electron transfer resistance of 2.9 ohms. These results indicate the beneficial effect of suitable electrochemical dealloying in enhancing the electron transfer kinetics at the surface of the nanoporous alloy, potentially leading to improved electrocatalytic performance.

Table 5.9 Properties of nanoporous Zn-Ni-Co-Cu alloys towards the HER.

	C^{σ} ($mF\cdot cm^{-2}$)	OCP (V/RHE)	Onset potential (V/RHE)	HER potential (V/RHE)	Tafel slope ($mV\cdot dec^{-1}$)	EIS (ohm)
$Zn_{70.9}Ni_{12.7}Cu_{11.2}Co_{5.2}$	0.23	0.60	0.191	-0.102	101.7	2.89
$Cu_{39.9}Zn_{31.9}Ni_{15.7}Co_{12.4}$	0.34	0.54	0.136	-0.122	102.5	3.91
$Co_{37.4}Zn_{29.3}Cu_{24.1}Ni_{9.2}$	0.23	0.61	0.173	-0.121	55.5	3.67
$Zn_{70.3}Ni_{15.7}Co_{8.6}Cu_{5.4}$	0.54	0.62	0.204	-0.084	123.2	3.45
$Ni_{36.7}Zn_{36.0}Co_{18.7}Cu_{8.6}$	0.84	0.61	0.221	-0.074	111.5	2.03
$Ni_{66.9}Cu_{18.5}Zn_{12.3}Co_{2.3}$	0.37	0.59	0.199	-0.071	70.8	2.50
$Zn_{44.3}Ni_{31.4}Cu_{13.0}Co_{11.3}$	0.42	0.63	0.230	-0.067	97.7	2.10
$Cu_{70.7}Co_{27.4}Ni_{1.9}$	0.79	0.53	0.118	-0.133	124.2	3.88

The electrochemical properties of Zn-Ni-Cu nanoporous alloys after appropriate dealloying exhibit intriguing features, shown in Figure 5.24 and Table 5.9. The C^{σ} value is notably enhanced from 0.23 to 0.41 $mF\cdot cm^{-2}$ after dealloying, corresponding to the composition $Zn_{45.7}Cu_{35.8}Ni_{18.5}$, achieved at a potential of 1.04 V/RHE in 1 M KOH for 30 minutes of dealloying. Similarly, for the chemically dealloyed nanoporous $Cu_{59.6}Zn_{31.0}Ni_{9.4}$ alloy in EAN + 0.01 M CH_3COOH for 5 minutes, the C^{σ} value reaches 0.37 $mF\cdot cm^{-2}$. However, in contrast to the initial expectations, only $Cu_{59.6}Zn_{31.0}Ni_{9.4}$ among all the nanoporous alloys demonstrated a lower HER potential compared to the original alloy $Zn_{63.2}Cu_{27.6}Ni_{9.2}$, while the other nanoporous alloys exhibited increased HER potential values. Notably, only specific nanoporous alloys with Cu or Ni as the main element constituents can exhibit higher overpotential properties. When compared with pure Ni, Co, and Cu, only some nanoporous alloys have better HER potential properties ($Zn_{45.7}Cu_{35.8}Ni_{18.5}$, $Zn_{45.1}Cu_{37.0}Ni_{17.9}$, $Zn_{63.2}Cu_{27.6}Ni_{9.2}$, $Cu_{59.6}Zn_{31.0}Ni_{9.4}$). These results highlight the possibility of improving electrocatalytic performance through the appropriate composition of the nanoporous alloys.

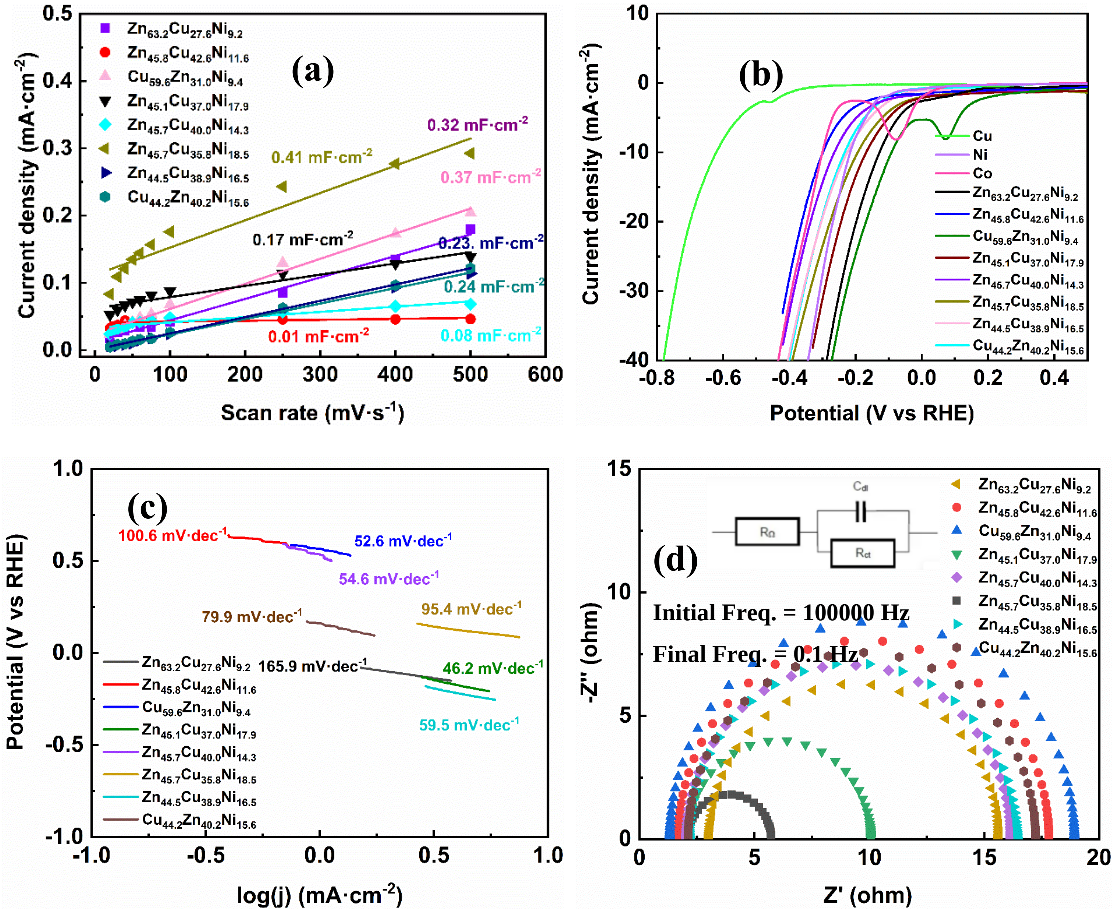

Figure 5.24 Electrocatalytic properties of the materials towards the HER for nanoporous Zn-Ni-Cu alloys: C^{σ} (a), LSV curves (b), Tafel slopes (c) and EIS curves (d).

Although the overpotential values did not always reach the ideal levels, the nanoporous alloys prepared by dealloying consistently exhibited lower Tafel slopes compared to the original alloy. The reduced Tafel slope suggests a higher reaction rate, indicating an improvement of electrocatalytic performance. Tafel slope values decreased from 165.9 to below 100 mV·dec^{-1}, with the lowest value being 46.2 mV·dec^{-1} observed for the $Zn_{45.1}Cu_{37.0}Ni_{17.9}$ alloy. The $Zn_{45.8}Cu_{42.6}Ni_{11.6}$ alloy, chemically dealloyed in EAN + 0.01 M CH_3COOH for 3 minutes, displayed a slightly higher Tafel slope value of 100.6 mV·dec^{-1}. This observation could be attributed to the absence of nanoporosity formation in relation to its surface morphology, illustrated in Figure 5.21a, resulting in an effect on the electrocatalytic behavior. The EIS curves are fitted through the circuit, shown in Figure 5.24d, where R_{Ω} is the solution resistance, C_{dl} is the double layer capacitance, R_{ct} is the charge-transfer resistance.

Table 5.10 Properties of nanoporous Zn-Ni-Cu alloys towards the HER.

	C^{σ} (mF·cm^{-2})	OCP (V/RHE)	Onset potential (V/RHE)	HER potential (V/RHE)	Tafel slope (mV·dec^{-1})	EIS (ohm)
$Zn_{63.2}Cu_{27.6}Ni_{9.2}$	0.23	0.66	0.159	-0.129	165.9	6.40
$Zn_{45.8}Cu_{42.6}Ni_{11.6}$	0.01	0.67	0.215	-0.299	100.6	7.90
$Cu_{59.6}Zn_{31.0}Ni_{9.4}$	0.37	0.64	0.376	-0.094	52.6	8.81
$Zn_{45.1}Cu_{37.0}Ni_{17.9}$	0.17	0.63	0.493	-0.169	46.2	3.93
$Zn_{45.7}Cu_{40.0}Ni_{14.3}$	0.08	0.67	0.311	-0.265	54.6	7.05
$Zn_{45.7}Cu_{35.8}Ni_{18.5}$	0.41	0.65	0.449	-0.195	95.4	1.77
$Zn_{44.5}Cu_{38.9}Ni_{16.5}$	0.32	0.68	0.095	-0.225	59.5	7.16
$Cu_{44.2}Zn_{40.2}Ni_{15.6}$	0.24	0.66	-0.041	-0.235	79.9	7.47

After conducting a thorough comparison, it becomes evident that the electrocatalytic performance of the nanoporous Zn-Ni-Co-Cu alloy surpasses that of the nanoporous Zn-Ni-Cu alloy. The addition of Co between Zn-Ni alloy and the Cu substrate to form Co-added nanoporous alloys is found to be crucial to improve the performance of hydrogen evolution reaction (HER). The incorporation of Co ensures that the alloy retains its advantageous properties, even after undergoing element recombination or changes in surface morphology, leading to an overall improvement in the HER performance.

5.7. Co-electrodeposition of Zn, Ni and Co on Cu foil and their dealloying

As we discussed in previous chapters, there has been a little research about the co-electrodeposition of three elements in ethaline on Cu, especially for Zn, Ni and Co. Here, we studied the electrodeposition of these three elements in ethaline with 0.35 M $ZnCl_2$ + 0.15 M $NiCl_2$ + 0.02 M $CoCl_2$ and their dealloying. Using Figure 5.10c, we chose a potential for the electrodeposition as -1.3 V/Ag/Ag^+, for 3.5 h. The chronoamperometry curve is shown in Figure 5.25. During the electrodeposition, the electron charge amount is 73.1 C, and 3.8×10^{-4} mol of Zn-Ni-Co based deposit is obtained. Afterwards, the alloy is treated in the same way as the last described heat treatment, for 30 min at 400 °C.

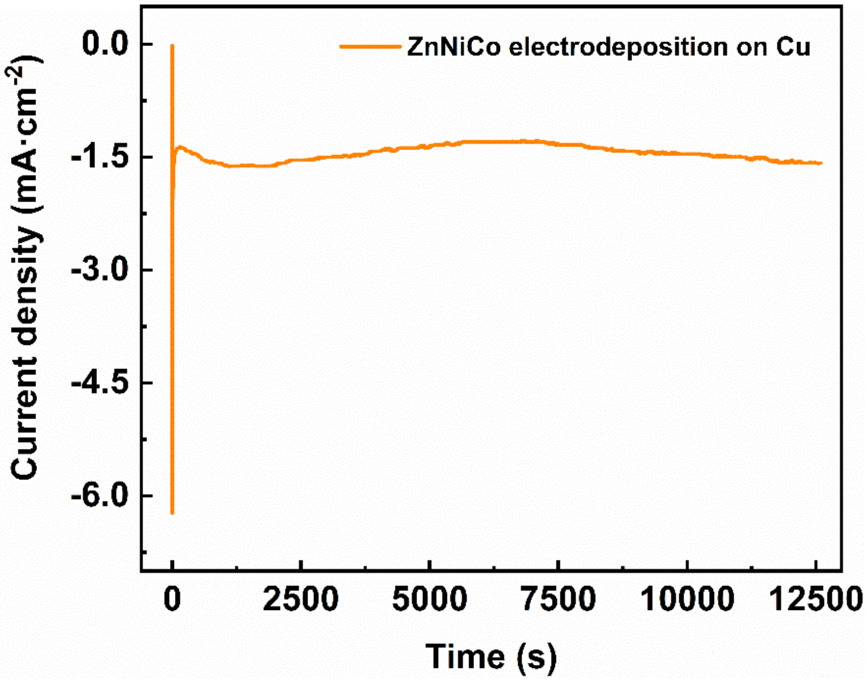

Figure 5.25 The current-time curve during the electrodeposition of Zn, Ni and Co.

The CV curves of deposited Zn-Ni-Co alloy on Cu foil before and after heat treatment were plotted in Figure 5.26. The CV curve of the Zn-Ni-Co on Cu foil before heat treatment exhibits a strong peak at 0.25 V/RHE, which can be attributed to the exfoliation of zinc in the first scan cycle [176, 177]. The peak at 1.31 V/RHE can be pointed as the oxidation of cobalt by the analyze of Figure 5.11c. It can be seen that the peak of zinc and cobalt oxidation reduces after the first scan cycle and the peaks at 0.76 V/RHE, 1 V/RHE obviously increase corresponding to the oxidation of copper. Combining the results with the previous line scan analysis in Figures 5.16, 5.19, 5.20, it is interesting to note that the element distribution in the thickness of the electrodeposit alloy is a gradual distribution. Therefore, it can be considered that due to the high content of Zn and Co detaching from the surface after the initial scanning, the internal Cu is exposed. After heat treatment of the alloy, only two peaks can be observed at 0.75 V/RHE, and between 1.0 to 1.2 V/RHE, corresponding to the oxidation of Cu, and a peak at 1.62 V/RHE, corresponding to the oxidation of Ni. Therefore, we chose two potentials, 0.76 and 1.04 V/RHE, for the electrochemical dealloying, which does not reach the exfoliation of Ni and Co.

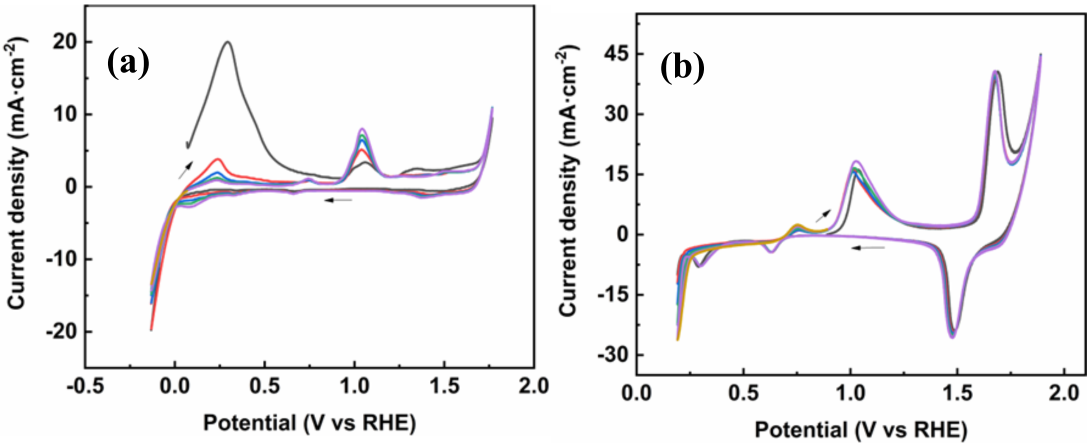

Figure 5.26 CV curves of deposited Zn-Ni-Co on Cu foil before (a) and after heat treatment (b).

5.8. Characterization of co-electrodeposited Zn-Ni-Co on Cu

The XRD patterns of Zn-Ni-Co alloy on Cu foil before and after heat treatment are shown in Figure 5.27. The results are similar to those of the previous Zn-Ni electrodeposit. It can be seen that the diffraction peak of Zn-Ni-Co obtained by electrodeposition cannot be clearly observed. It can be masked by the strong Cu peak around 44°. And after the heat treatment at 400 °C, new intermetallic compounds were exhibited (Figure 5.27b). As shown, ZnO is generated due to slight oxidation, while Cu_5Zn_8 and $CuCoN_{0.6}$ are new phases formed by diffusion, similar to the Zn-Ni-Co-Cu alloys in Figure 5.13.

SEM analysis of the Zn-Ni-Co electrodeposited during 3.5 hours reveals a surface morphology characterized by visible grains (Figures 5.28a, b). It can be seen that there is no significant difference in the surface morphology of the alloy before and after heat treatment, all are covered by dense grains. The EDS spectra presented in Figures 5.28c, d, also reveal distinct signals for

Cu in all samples, with various oxygen content. After heat treatment, the content of Zn and Ni decreased, especially Ni, from 20.7 to 3.2 at%, while the cobalt content remained basically unchanged. This may be due to the fact that the proportion of cobalt content is not high and uniform, so it cannot reflect significant differences. After heat treatment, the content of Cu significantly increased from 3.8 to 37.8 at% due to the diffusion of Cu. The data of elements contents are shown in Table 5.11.

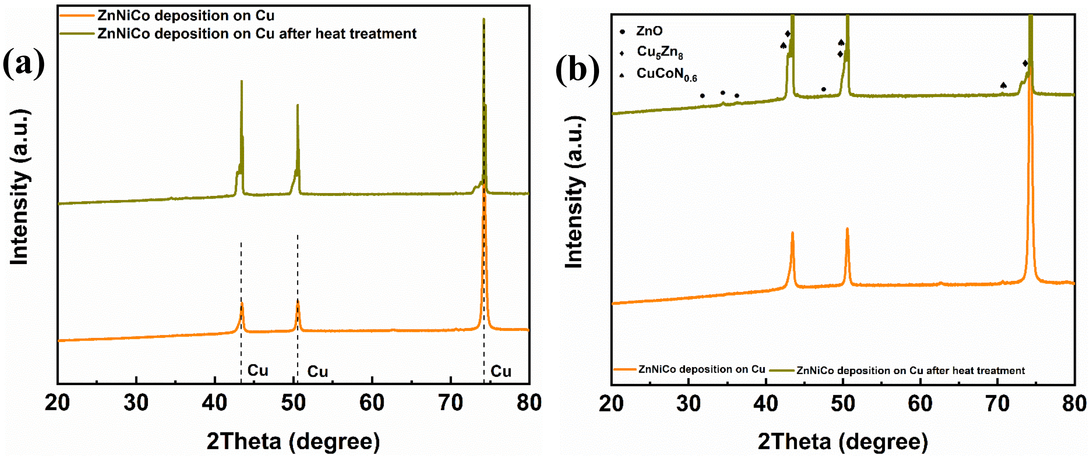

Figure 5.27 XRD patterns of deposited Zn-Ni-Co on Cu foil before (a) and after heat treatment (b).

Based on the prepared Zn-Ni-Co on Cu alloys, different dealloying conditions were applied. The parameters are shown in Table 5.12. The alloys were treated by a chemical dealloying in a 1 M KOH and 0.01 M HNO3, respectively. The electrochemical dealloying was applied in 1 M KOH at 0.76 V/RHE, and 1.04 V/RHE for 30 minutes, according to the CV curves in Figure 5.12, corresponding to the two oxidation peaks of Cu, respectively. The SEM topography images of the chemical dealloying process in 1 M KOH are presented in Figure 5.29a. After soaking in 1 M KOH for 30 minutes, the porous structure as shown in Figure 5.29a can be obtained, but its surface is also covered with a layer of non-dense octahedron crystals, and EDS cannot accurately confirm its composition.

The morphology after electrochemical dealloying in KOH is presented in Figures 5.29b and c. Remarkably, applying the potential of 0.76 V/RHE for only 30 minutes results in the formation of non-dense nanopores, on the surface. But there are no more octahedron crystals after electrochemical dealloying compared to the sample obtained after chemical dealloying. By extending the dealloying time to 30 minutes, the surface pore structure disappears. Similarly, increasing the potential to 1.04 V/RHE will also make the surface smoother. Additionally, an attempt was made to perform chemical dealloying in HNO3, which also yielded a similar pore structure (5.29e, f).

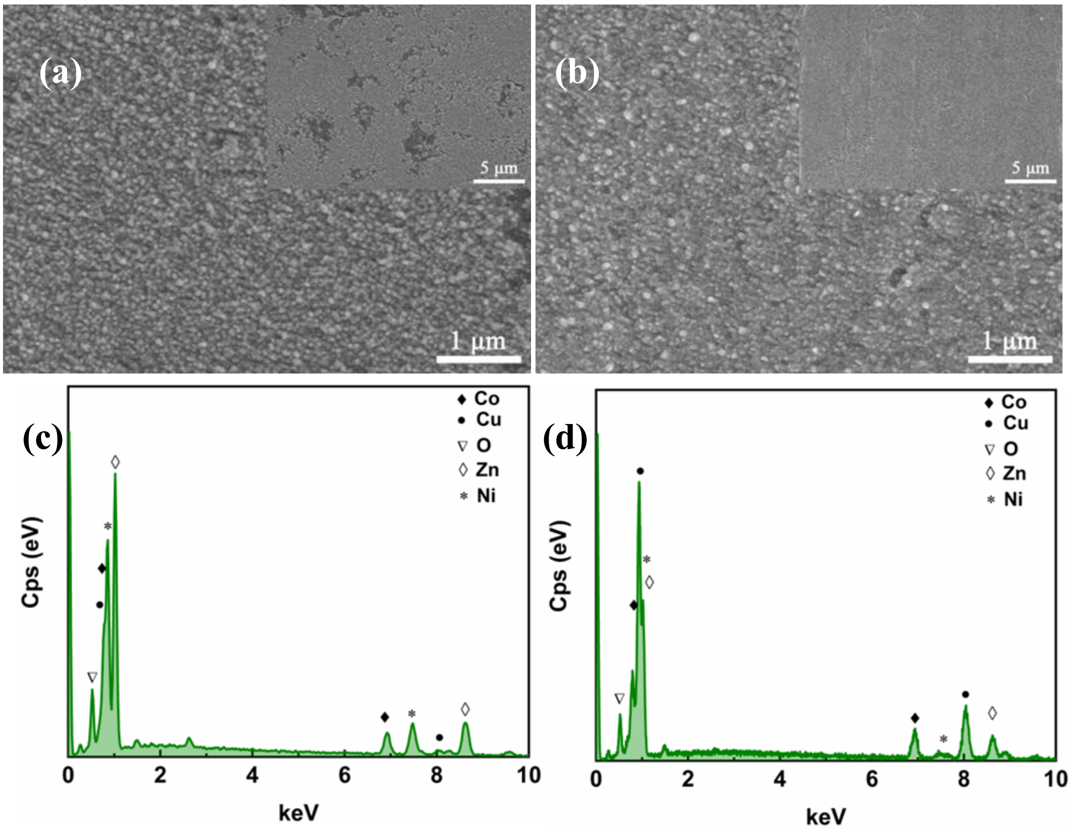

Figure 5.28 SEM and EDS of 3.5 h deposited Zn-Ni-Co on Cu foil before (a, c) and after heat treatment (b, d).

Table 5.11 Element distribution of Zn-Ni-Cu alloy on Cu foil before and after heat treatment.

Solution	Parameters	Heat treatment	Zn (at%)	Ni (at%)	Co (at%)	Cu (at%)	O (at%)
Ethaline + 0.35 M $ZnCl_2$ + 0.15 M $NiCl_2$ + 0.02 M $CoCl_2$	-1.3 V, 40 ℃, 210 min	×	45.1	20.7	11.3	3.8	19
		√	31.7	3.2	14.1	37.8	13.1

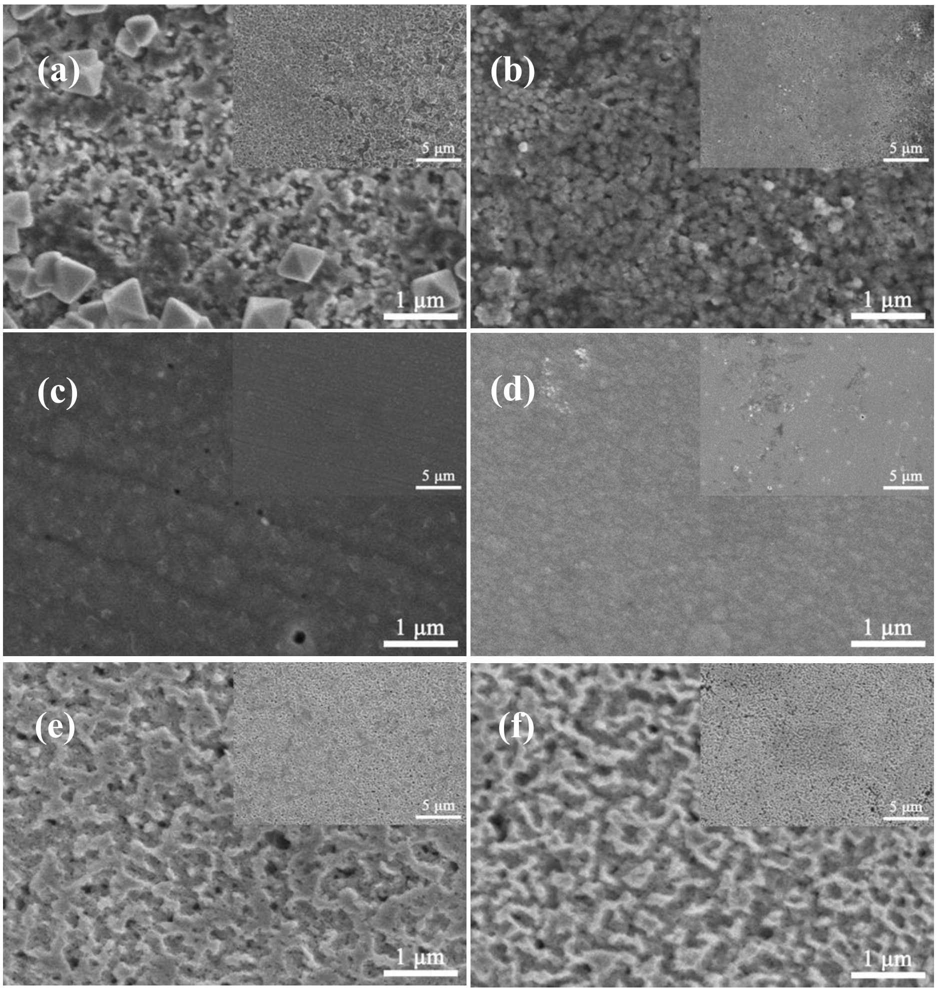

Figure 5.29 SEM of dealloyed Zn-Ni-Co on Cu foil in different conditions: 1 M KOH, 30 min (a); 1M KOH, 3 min (b) and 30 min (c), with 0.76 V/RHE; d) 1M KOH, 30 min, with 1.04 V/RHE; 0.01M HNO_3, 30 min (e) and 60 min (f).

The composition of alloying elements on the nanoporous Zn-Ni-Cu alloy after dealloying is illustrated in Figure 5.30 and summarized in Table 5.11. Various dealloying methods have demonstrated the capacity to diminish the relative abundance of Zn, leading to its preferential removal. In the ternary alloy system, it is clear that Cu emerges as the main constituent, providing the fundamental structural support post dealloying. Prolonged exposure to chemical dealloying in an alkaline or an acidic solution (60 min) substantially reduces the relative Zn content, resulting in Cu-based compositions, illustrated by $Cu_{68.9}Zn_{14.6}Co_{10.7}Ni_{5.8}$, $Cu_{69.5}Zn_{23.0}Ni_{5.0}Co_{2.5}$ and $Cu_{63.9}Zn_{29.1}Ni_{3.7}Co_{3.3}$. In electrochemical dealloying, under the dealloying potential of Cu, it is difficult to maintain the Cu based alloy structure. It can be seen that increasing the time or potential will reduce the Cu content of alloys.

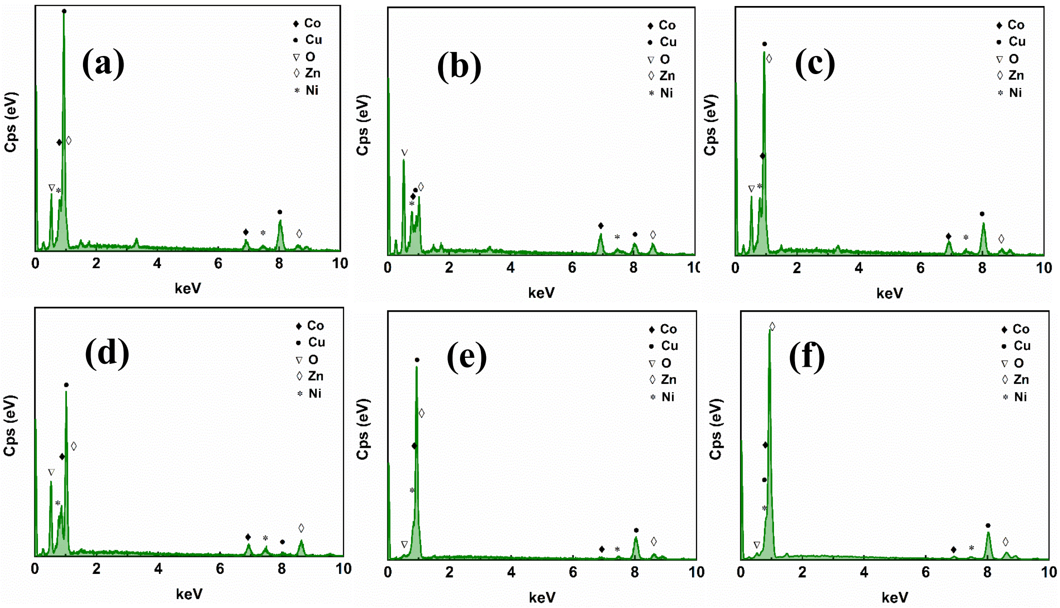

Figure 5.30 EDS of dealloyed Zn-Ni-Co on Cu foil in different conditions: a) 1 M KOH, 30 min; b) 1M KOH, 3 min, at 0.76 V/RHE; c) 1M KOH, 30 min, at 0.76 V/RHE; d) 1M KOH, 30 min, at 1.04 V/RHE; 0.01M HNO_3, 30 min (e) and 60 min (f).

Table 5.12 Elements contents in Zn-Ni-Cu alloy on Cu foil after dealloying.

Solution	Conditions	Zn (at%)	Ni (at%)	Co (at%)	Cu (at%)	O (at%)	Donated
original	-	31.7	3.2	14.1	37.8	13.1	$Cu_{43.6}Zn_{36.5}Co_{16.2}Ni_{3.7}$
1 M KOH	30 min	17.9	5	17	11.7	48.4	$Cu_{68.9}Zn_{14.6}Co_{10.7}Ni_{5.8}$
	0.76 V/RHE, 3 min	37.1	7.2	9.5	3.1	43	$Cu_{67.4}Co_{15.1}Zn_{11.8}Ni_{5.7}$
	0.76 V/RHE, 30 min	22.4	4.9	2.4	67.7	2.6	$Zn_{34.7}Co_{32.9}Cu_{22.7}Ni_{9.7}$
	1.04 V/RHE, 30 min	28.2	3.6	3.2	61.9	3.2	$Zn_{65.2}Co_{16.7}Ni_{12.7}Cu_{5.4}$
0.01 M HNO_3	30 min	10.5	4.2	7.7	49.7	27.9	$Cu_{69.5}Zn_{23.0}Ni_{5.0}Co_{2.5}$
	60 min	8.5	4.1	10.9	48.5	28	$Cu_{63.9}Zn_{29.1}Ni_{3.7}Co_{3.3}$

5.9. Electrocatalysis properties of co-deposited Zn-Ni-Co on Cu in HER

Co-deposited Zn-Ni-Co alloys with porous structures exhibit significantly higher C^{σ} values, which are 0.53 $mF \cdot cm^{-2}$ and 0.83 $mF \cdot cm^{-2}$, corresponding to $Cu_{69.5}Zn_{23.0}Ni_{5.0}Co_{2.5}$ and

$Cu_{63.9}Zn_{29.1}Ni_{3.7}Co_{3.3}$, respectively, higher than 0.40 mF·cm^{-2}, C^{σ} value of the initial alloy $Cu_{43.6}Zn_{36.5}Co_{16.2}Ni_{3.7}$. It means that dealloying in HNO_3 can effectively increase the surface-active area of the alloys and provide more potentials in the property improvement.

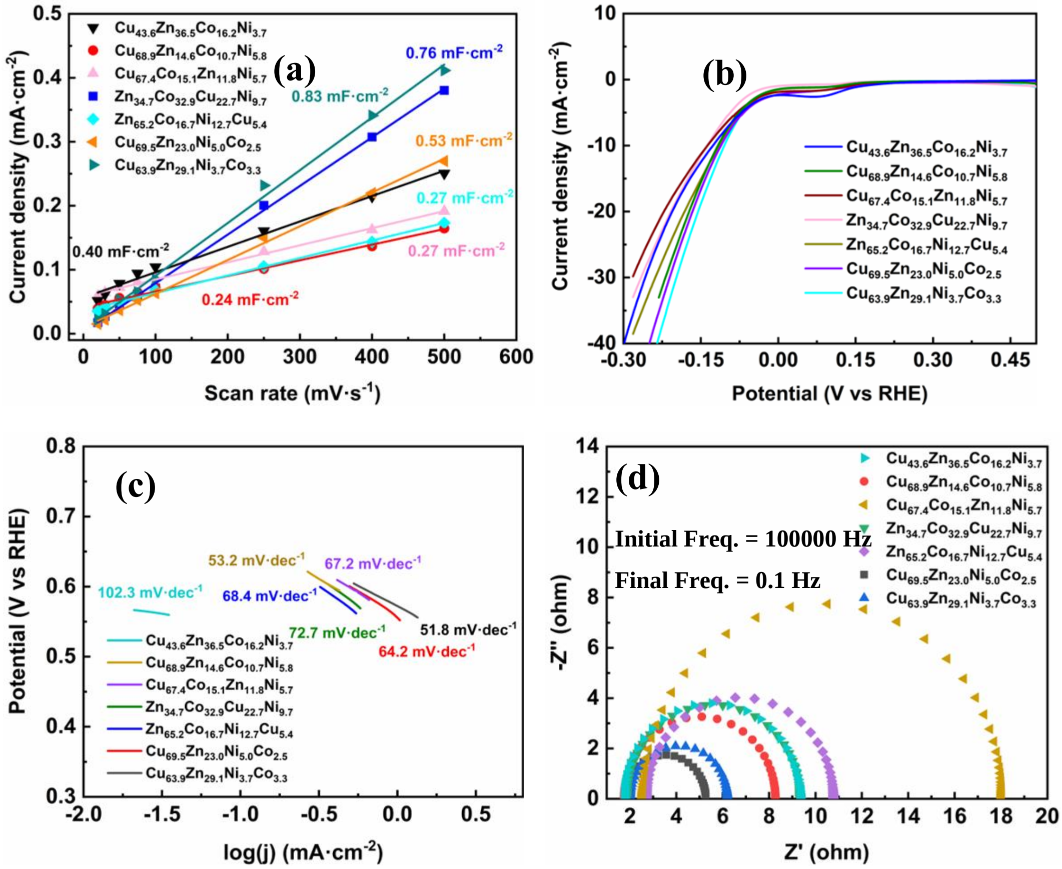

Figure 5.31 Electrocatalytic properties of the materials towards the HER for nanoporous co-deposited Zn-Ni-Co alloys: C^{σ} (a), LSV curves (b), Tafel slopes (c) and EIS curves (d).

It can be seen that the nanoporous structure caused by dealloying can also effectively reduce the HER potential value of the alloys, especially for the samples treated in HNO_3. Their HER potential can be reduced to -0.111 V/RHE and -0.105 V/RHE, which are significantly lower than -0.130 V/RHE. Moreover, all the dealloyed samples have lower Tafel slope values, which can reach 51.8 mV·dec^{-1} at the lowest, prepared by soaking in HNO_3 for 60 minutes ($Cu_{63.9}Zn_{29.1}Ni_{3.7}Co_{3.3}$).

Although the dealloying can further improve the HER performance of the prepared co-deposited Zn-Ni-Co alloy, its overall performance, especially for HER potential is worse compared to the alloys prepared by two-step electrodeposition discussed earlier. At present, there is no relevant comparative literature, and the mechanism for explaining this difference still requires further research.

Table 5.13 Properties of nanoporous co-deposited Zn-Ni-Cu alloys towards the HER.

Sample	C^{σ} (mF·cm^{-2})	OCP (V/RHE)	Onset potential (V/RHE)	HER potential (V/RHE)	Tafel slope (mV·dec^{-1})	EIS (ohm)
$Cu_{43.6}Zn_{36.5}Co_{16.2}Ni_{3.7}$	0.40	0.58	0.153	-0.130	102.3	3.79
$Cu_{68.9}Zn_{14.6}Co_{10.7}Ni_{5.8}$	0.24	0.57	0.104	-0.126	53.2	3.29
$Cu_{67.4}Co_{15.1}Zn_{11.8}Ni_{5.7}$	0.27	0.54	0.134	-0.137	67.2	7.75
$Zn_{34.7}Co_{32.9}Cu_{22.7}Ni_{9.7}$	0.76	0.66	-0.005	-0.137	72.7	3.78
$Zn_{65.2}Co_{16.7}Ni_{12.7}Cu_{5.4}$	0.27	0.57	0.117	-0.115	68.4	4.02
$Cu_{69.5}Zn_{23.0}Ni_{5.0}Co_{2.5}$	0.53	0.60	0.168	-0.111	64.2	1.63
$Cu_{63.9}Zn_{29.1}Ni_{3.7}Co_{3.3}$	0.83	0.58	0.111	-0.105	51.8	2.02

5.10. Conclusions

In this work, the electrodeposition and dealloying of Zn-Ni on Co-Cu, Zn-Ni on Cu, Zn-Ni-Co on Cu in different ethaline solutions, and their properties in HER electrocatalysis were studied. Nanoporous alloys show interesting features in morphology, element distribution and properties in HER. Different dealloying conditions were studied by changing the solution (KOH, HNO_3, CH_3COOH in EAN) in order to change the morphology and element distribution of the nanoporous alloys. As shown, Zn is the easiest element to remove from the alloy, it then leaves vacant locations that lead to the formation of pores. We hypothesized that the observed nanoporous structure is made possible by the diffusion of Cu. Thus, we prepared nanoporous Zn-Ni-Co-Cu alloys using a two-step deposition method, heat treatment and dealloying. Compared to nanoporous Zn-Ni-Cu alloys without Co, its HER performance is significantly improved, and its potential can reach -0.067 V/RHE at the lowest. Performance improvement requires a combination of specific surface area and element distribution of the alloys.

In addition, we have succeeded in preparing, for the first time in ethaline to our knowledge, Zn-Ni-Co alloys on Cu foil by co-electrodeposition. Similarly, dealloying can improve the element distribution and form nanoporous structures, thereby improving the overall HER electrocatalytic performance of the alloys. This study demonstrates the possibility of electrodepositing ternary alloys (Zn, Ni, Co) in ethaline, paves a new way for the preparation of Zn-Ni-Co-Cu electrocatalysts by co-electrodeposition followed by heat treatment, and provides an interesting avenue for tuning alloy composition by electrodeposition.

Conclusions and perspectives

The development of hydrogen energy is full of hope for the future. Therefore, it is necessary to develop new hydrogen production methods by different methods. In the above discussion, the electrodeposition of Ni/Co in ionic liquids or deep eutectic solvents for the preparation of electrocatalysis and further dealloying surface treatment have brought some new insights in the development of catalyst materials for hydrogen evolution.

In Chapters 1 and 2, we provide a more detailed bibliographic aspects and background to this research. We have comprehensively presented the experimental details, including methods for characterizing and measuring various materials and their respective properties. Our presentation includes an in-depth exploration of the existing landscape of hydrogen energy and the hydrogen evolution reaction, with discussions on its mechanisms and measurement techniques. Furthermore, we provide an overview of the use of alloys in the context of the hydrogen evolution reaction, and elucidate the process of electrodeposition of alloys in ionic liquids.

In Chapter 3, we conducted an extensive investigation into the electrodeposition process of Ni, Co, and various Ni-Co alloy compositions on FTO glasses and Cu foils, using EAN as a protic ionic liquid. The physicochemical properties of different EAN-based electrolytes were measured and discussed. Our work has resulted in the successful synthesis, described for the first time in EAN to our knowledge, of pure amorphous cobalt, nanocrystalline nickel, and nanocrystalline/amorphous Ni-Co alloy structures by electrodeposition on FTO glass under oxygen-free conditions. The phases were studied and confirmed by XRD and TEM, respectively. The morphologies of the various coatings were measured by SEM. Most samples have a smooth surface. We investigated the impact of cobalt addition on the HER performance of Ni-based alloys, examining both FTO glasses and copper foils as substrates. It should be noted that the amorphous state of the alloy exhibits a lower HER potential and a faster reaction rate compared to crystalline alloys with similar atomic ratios. Alloys deposited on Cu foil are more stable than those on FTO glass.

In addition, we mainly discussed the electrodeposition of Ni in the deep eutectic solvent ethaline in Chapter 4, and found that the electrocatalytic performance of copper foam can be enhanced by nickel electrodeposition. Almost pure deposits of Zinc, Nickel and Cobalt can be obtained by electrodeposition in ethaline with different parameters. It has also been found that the addition of zinc can improve the electrocatalytic hydrogen evolution reaction of nickel-based alloys, but excessive zinc content will have a negative impact on the catalytic performance. Therefore, it is essential to determine the appropriate alloy ratio during the preparation process of Ni-Zn electrocatalytic materials. In addition, the electrodeposition of Aluminum in ethaline has been attempted in this chapter. Unfortunately, the efficiency of Al deposition is not high and it cannot be obtained in large quantities.

In Chapter 5, we focused on the electrodeposition, dealloying processes, and electrocatalytic performance for the hydrogen evolution reaction (HER) of Zn-Ni/Co-Cu, Zn-Ni/Cu, and Zn-Ni-Co/Cu, using various ethaline. It is noteworthy that nanoporous alloys exhibit intriguing characteristics in terms of their morphological attributes, elemental distribution, and performance in HER. By modifying the dealloying solution and associated parameters, to control both the morphology and the distribution of elements in these nanoporous alloys could be controlled. Zn was found to be more easily removed, paving the way for the formation of pores and nanoporous structures with Cu serving as framework in regions previously occupied by Zn. We prepared nanoporous Zn-Ni-Co-Cu alloys using one-step and two-step electrodeposition techniques, followed by heat treatment and dealloying. Zn-Ni-Co alloys were first electrodeposited on Cu foils, and further heat treatment yielded Zn-Ni-Co-Cu alloys in one-step electrodeposition. For two-step electrodeposition, the Co coating was deposited on Cu foil and the Zn-Ni alloys were deposited on Co-Cu alloys, respectively. After heat treatment, we also obtain Zn-Ni-Co-Cu alloys. Compared with Co-free nanoporous Zn-Ni-Cu alloys, the HER performance of the Zn-Ni-Co-Cu variant has improved considerably. To achieve this improved performance, the specific surface area of the alloy and the distribution of elements in the material must be carefully optimized. In addition, the Zn content remains high in all nanoporous alloys. In order to achieve better HER properties, it is necessary to further investigate different dealloying parameters to reduce the Zn content.

Based on these results, we believe that more element combinations in alloy electrodeposition should be investigated, such as Ni-Al, Co-Mg, due to their potential differences. Nanoporous alloys can be prepared using these different combinations. New nanoporous alloys can then be obtained by selective dealloying for electrocatalysis or other catalytic applications.

Finally, large-scale electrodeposition will be necessary. In the following research, based on the findings of this thesis, large-scale electrodeposition of nickel-based alloys in ionic liquids can be attempted. This will be the most important step towards industrialization in this study, and it also corresponds to the aim of this work, providing new directions for the development of electrocatalysts that can be used in industry.

Annexes

1. Chemicals and materials

Ethylamine ($CH_3CH_2NH_2$, 70 wt.% in water, Acros Organics), nitric acid (HNO_3, 68 wt.% in water, AnalaR NORMAPUR), potassium chloride (KCl, 99%, Acros Organics), choline chloride (ChCl, Acros Organics, purity ⩾ 99%), ethylene glycol (EG, VWR Chemical, purity ⩾ 99%), DL-Menthol (Sigma Aldrich, purity ⩾ 95%), ethanolamine (Sigma Aldrich, purity ⩾ 98%), acetic acid (Sigma Aldrich, purity ⩾ 99.7%), potassium hydroxide (KOH, 86%, Fisher Scientific), Zinc chloride ($ZnCl_2$, 98% purity, Sigma-Aldrich), cobalt chloride ($CoCl_2$, 98% purity, Sigma-Aldrich) and nickel chloride ($NiCl_2$, 98%, Sigma-Aldrich) were used as received.

Fluorine-doped Tin Oxide glasses (FTO glass) were purchased from Solems (80 nm thickness, 1.5 cm × 0.5 cm × 0.1 cm). Cu foil (purity 99.9%, 0.2 mm thickness) and Cu foam (purity 99.9%, 1 mm thickness) were purchased from Qiaona, China. Nickel wire (purity > 99%, Φ 1 mm) was purchased from Chempur (Germany), cobalt wire (> 99.99%, Φ 1 mm) and zinc wire (> 99.99%, Φ 0.3 mm) was purchased from Chengshuo (China), and silver wire (99.99%) was from Mateck (Germany).

2. Additional tables

Table 0.1 Physicochemical properties of solutions used in this work.

Concentration	Temperature (°C)	Density ($g\cdot cm^{-3}$)	Viscosity (mPa·s)	Conductivity ($mS\cdot cm^{-1}$)	pH	Water content (ppm)
Pure EAN	25	1.21040	36.4	21.8	5.6	56
	40	1.20119	22.7	24.9	5.2	
	60	1.18930	13.7	29.0	4.4	
	80	1.17779	9.2	32.7	4.1	
0.5 M $NiCl_2$	25	1.25004	55.0	15.6	4.1	851
	40	1.24016	31.8	18.9	3.3	
	60	1.22733	17.8	23.2	2.4	

	80	1.21484	12.5	28.	2.2	
0.5 M $CoCl_2$	25	1.24308	37.2	21.74	4.1	775
	40	1.23326	22.9	25.8	3.9	
	60	1.22081	13.7	28.3	3.3	
	80	1.20871	10.0	33.1	2.8	
0.25 M $NiCl_2$ + 0.25 M $CoCl_2$	25	1.24233	69.2	19.6	4.2	1034
	40	1.23263	41.5	20.2	3.5	
	60	1.22001	24.2.	25.6	3.0	
	80	1.20785	17.13	30.91	2.7	
0.375 M $CoCl_2$ +0.125 M $NiCl_2$	25	1.24544	48.40	16.93	4.0	780
	40	1.23577	29.09	19.47	3.3	
	60	1.22338	16.93	23.84	2.9	
	80	1.21138	12.13	27.10	2.2	

Table 0.2 Assignation of the Raman vibration of the EAN spectrum.

Band (cm^{-1})	Bonding
420	The bending motions of C-C
718	The bending of NO_3^-
873	C-N stretching motions
960	C-C stretching motions
1044	The symmetric stretching of NO_3^-
1200	CH_n groups rocking motions
1330	CH_n scissoring motions
1450	CH_2/CH_3 bending motions
1610	$-NH_3$ scissoring/rocking motions.

Table 0.3 Exchanged charge and amount of material electroplated for Ni and Co in EAN.

	Potential (V/Ag/Ag^+)	Time (h)	Temperature (°C)	Electron charge (C)	Electrodeposition quantity (mol)
0.5 M $NiCl_2$	-1.25	2	60	19.67	1.02×10^{-4}
0.5 M $CoCl_2$	-1.3	2	60	9.98	5.17×10^{-5}
0.25 M $CoCl_2$ + 0.25 M $NiCl_2$	-1.1	2	60	5.59	2.90×10^{-5}
	-1.2	2	60	10.13	5.25×10^{-5}
	-1.3	2	60	11.51	5.96×10^{-5}
	-1.3	1	60	7.55	3.91×10^{-5}
	-1.3	2	80	15.84	8.21×10^{-5}
0.375 M $CoCl_2$ +0.125 M $NiCl_2$	-1.2	2	60	6.97	3.61×10^{-5}
	-1.3	2	60	11.99	6.21×10^{-5}

Table 0.4 XPS binding energy of different compounds [151-154].

	Ni	Co	NiO /$Ni(OH)_2$	CoO /$Co(OH)_2$	Co-Ni	$(NO_3)^-$	SnO
Ni 2p3/2 (eV)	852.8	-	855.5, 855.6	-	852.7	-	-
Co 2p3/2 (eV)	-	778.2	-	780.5, 780.6	778.5	-	-
O 1s (eV)	-	-	528.9/532.3	529.1/532.5	-	-	530.9, 531.0
N 1s (eV)	-	-	-	-	-	406.7	-

Table 0.5 Physicochemical properties of solutions used in this chapter.

Concentration	Temperature (°C)	Density (g·cm^{-3})	Viscosity (mPa·s)	Conductivity (mS·cm^{-1})	pH
Ethaline	25	1.116403	43.68	7.97	4.18
	40	1.107858	24.92	9.77	4.02
	60	1.096607	13.63	15.32	3.8
	80	1.085478	9.152	21.34	3.65
0.5 M $NiCl_2$	25	1.162129	110.9	4.02	5.35
	40	1.153427	55.52	6.77	5.15
	60	1.141552	25.67	10.35	5.05
	80	1.128869	13.39	13.6	4.75
0.5 M $CoCl_2$	25	1.147278	39.17	8.6	-
	40	1.138522	22.47	12.44	-
	60	1.126946	12.45	16.57	-
	80	1.115439	7.934	22.89	-
0.5 M $ZnCl_2$	25	1.150352	36.05	8.33	7.76
	40	1.141558	20.68	11.93	7.45
	60	1.129912	11.52	16.56	7.02
	80	1.118317	7.881	23.3	6.67
0.5 M $NiCl_2$ + 0.25 M $ZnCl_2$	25	1.181785	89.50	4.43	5.52
	40	1.173079	45.95	6.97	5.42
	60	1.161475	22.36	10.96	5.22
	80	1.149488	12.36	14.26	5.00
0.5 M $NiCl_2$ + 0.5 M $ZnCl_2$	25	1.192525	110.3	8.43	5.87
	40	1.183686	55.24	11.97	5.77
	60	1.171884	26.07	13.86	5.57
	80	1.159665	15.35	17.25	5.46
0.2 M $NiCl_2$ + 0.4 M $ZnCl_2$	25	1.160655	77.93	6.43	5.2
	40	1.151918	41.08	9.33	5.13
	60	1.140268	20.58	13.56	4.97
	80	1.128280	11.61	17.13	4.89
0.15 M $NiCl_2$ + 0.35 M $ZnCl_2$	25	1.167740	64.61	8.12	5.68
	40	1.159040	35.08	11.54	5.49
	60	1.147544	18.26	13.67	5.4
	80	1.135996	10.85	17.34	5.29
0.15 M $NiCl_2$ + 0.35 M $ZnCl_2$ + 0.02 M $CoCl_2$	25	1.164253	64.61	8.23	5.58
	40	1.155532	35.08	11.57	5.53
	60	1.144026	18.26	13.88	5.38
	80	1.132529	10.85	17.56	5.29
0.2 M $CoCl_2$ + 0.4 M $ZnCl_2$	25	1.156264	37.96	8.3	7.75
	40	1.147407	25.92	11.12	7.66
	60	1.135733	14.02	13.38	7.58
	80	1.124168	8.766	17.8	7.45
0.15 M $CoCl_2$ + 0.35 M $ZnCl_2$	25	1.149151	38.89	8.7	7.54
	40	1.140343	22.25	11.54	7.41
	60	1.128701	12.34	14.89	7.2
	80	1.117138	7.608	18.22	7.14
0.4 M $CoCl_2$ + 0.4 M $ZnCl_2$	25	1.155204	36.86	8.6	7.85
	40	1.146375	24.43	13.4	7.41
	60	1.134727	14.82	16.79	7.28
	80	1.123191	7.966	19.22	7.15

List of figures

List of tables

Reference list

1. Nady, H.; Negem, M., Electroplated Zn–Ni nanocrystalline alloys as an efficient electrocatalyst cathode for the generation of hydrogen fuel in acid medium. *International Journal of Hydrogen Energy* **2018,** *43* (10), 4942-4950.

2. Feng, H.; Yu, J.; Tang, L.; Wang, J.; Dong, H.; Ni, T.; Tang, J.; Tang, W.; Zhu, X.; Liang, C., Improved hydrogen evolution activity of layered double hydroxide by optimizing the electronic structure. *Applied Catalysis B: Environmental* **2021,** *297*, 120478.

3. Jiao, S.; Fu, X.; Wang, S.; Zhao, Y., Perfecting electrocatalysts via imperfections: towards the large-scale deployment of water electrolysis technology. *Energy & Environmental Science* **2021,** *14* (4), 1722-1770.

4. Liu, T.; Asiri, A. M.; Sun, X., Electrodeposited Co-doped NiSe2 nanoparticles film: a good electrocatalyst for efficient water splitting. *Nanoscale* **2016,** *8* (7), 3911-3915.

5. He, J.; Zu, L.; Liu, X.; Zhang, L.; Duan, B., Porous NiCu alloy cathode with oriented pore structure for hydrogen evolution reaction by freeze casting. *Journal of Porous Materials* **2019,** *26* (5), 1533-1539.

6. de Kleijne, K.; de Coninck, H.; van Zelm, R.; Huijbregts, M. A. J.; Hanssen, S. V., The many greenhouse gas footprints of green hydrogen. *Sustainable Energy & Fuels* **2022,** *6* (19), 4383-4387.

7. Busch, P.; Kendall, A.; Lipman, T., A systematic review of life cycle greenhouse gas intensity values for hydrogen production pathways. *Renewable and Sustainable Energy Reviews* **2023,** *184*, 113588.

8. Yan, Y.; Xia, B. Y.; Zhao, B.; Wang, X., A review on noble-metal-free bifunctional heterogeneous catalysts for overall electrochemical water splitting. *Journal of Materials Chemistry A* **2016,** *4* (45), 17587-17603.

9. Zou, X.; Zhang, Y., Noble metal-free hydrogen evolution catalysts for water splitting. *Chemical Society Reviews* **2015,** *44* (15), 5148-5180.

10. Guo, Y.; Park, T.; Yi, J. W.; Henzie, J.; Kim, J.; Wang, Z.; Jiang, B.; Bando, Y.; Sugahara, Y.; Tang, J.; Yamauchi, Y., Nanoarchitectonics for Transition-Metal-Sulfide-Based

Electrocatalysts for Water Splitting. *Advanced Materials* **2019,** *31* (17), 1807134.

11. Sapountzi, F. M.; Gracia, J. M.; Weststrate, C. J.; Fredriksson, H. O. A.; Niemantsverdriet, J. W., Electrocatalysts for the generation of hydrogen, oxygen and synthesis gas. *Progress in Energy and Combustion Science* **2017,** *58*, 1-35.

12. Morfopoulou, C. I.; Andreopoulou, A. K.; Daletou, M. K.; Neophytides, S. G.; Kallitsis, J. K. J. J. o. M. C. A., Cross-linked high temperature polymer electrolytes through oxadiazole bond formation and their applications in HT PEM fuel cells. *Journal of Materials Chemistry A* **2013,** *1* (5), 1613-1622.

13. Papadimitriou, K. D.; Geormezi, M.; Neophytides, S. G.; Kallitsis, J. K., Covalent cross-linking in phosphoric acid of pyridine based aromatic polyethers bearing side double bonds for use in high temperature polymer electrolyte membrane fuelcells. *Journal of membrane science* **2013,** *433*, 1-9.

14. Qu, Y.; Pan, H.; Kwok, C. T.; Wang, Z., A first-principles study on the hydrogen evolution reaction of VS 2 nanoribbons. *Physical Chemistry Chemical Physics* **2015,** *17* (38), 24820-24825.

15. Yang, X.-F.; Wang, A.; Qiao, B.; Li, J.; Liu, J.; Zhang, T., Single-Atom Catalysts: A New Frontier in Heterogeneous Catalysis. *Accounts of Chemical Research* **2013,** *46* (8), 1740-1748.

16. Zare, M.; Saleheen, M. S.; Singh, N.; Uline, M. J.; Faheem, M.; Heyden, A., Liquid-Phase Effects on Adsorption Processes in Heterogeneous Catalysis. *JACS Au* **2022,** *2* (9), 2119-2134.

17. Bhunia, K.; Chandra, M.; Kumar Sharma, S.; Pradhan, D.; Kim, S.-J., A critical review on transition metal phosphide based catalyst for electrochemical hydrogen evolution reaction: Gibbs free energy, composition, stability, and true identity of active site. *Coordination Chemistry Reviews* **2023,** *478*, 214956.

18. Greeley, J.; Jaramillo, T. F.; Bonde, J.; Chorkendorff, I.; Nørskov, J. K., Computational high-throughput screening of electrocatalytic materials for hydrogen evolution. *Nature Materials* **2006,** *5* (11), 909-913.

19. Zhao, M.; Abe, K.; Yamaura, S.-i.; Yamamoto, Y.; Asao, N., Fabrication of Pd–Ni–P

Metallic Glass Nanoparticles and Their Application as Highly Durable Catalysts in Methanol Electro-oxidation. *Chemistry of Materials* **2014,** *26* (2), 1056-1061.

20. Wang, J.; Xu, F.; Jin, H.; Chen, Y.; Wang, Y., Non-Noble Metal-based Carbon Composites in Hydrogen Evolution Reaction: Fundamentals to Applications. *Advanced Materials* **2017,** *29* (14), 1605838.

21. Seeber, R.; Zanardi, C.; Inzelt, G., Links between electrochemical thermodynamics and kinetics. *ChemTexts* **2015,** *1* (4), 18.

22. Lazanas, A. C.; Prodromidis, M. I., Electrochemical Impedance Spectroscopy─A Tutorial. *ACS Measurement Science Au* **2023,** *3* (3), 162-193.

23. Mann, R. F.; Amphlett, J. C.; Peppley, B. A.; Thurgood, C. P., Application of Butler–Volmer equations in the modelling of activation polarization for PEM fuel cells. *Journal of Power Sources* **2006,** *161* (2), 775-781.

24. Zeng, K.; Zhang, D., Recent progress in alkaline water electrolysis for hydrogen production and applications. *Progress in Energy and Combustion Science* **2010,** *36* (3), 307-326.

25. Gao, M.-R.; Liang, J.-X.; Zheng, Y.-R.; Xu, Y.-F.; Jiang, J.; Gao, Q.; Li, J.; Yu, S.-H., An efficient molybdenum disulfide/cobalt diselenide hybrid catalyst for electrochemical hydrogen generation. *Nature Communications* **2015,** *6* (1), 5982.

26. McCrory, C. C. L.; Jung, S.; Peters, J. C.; Jaramillo, T. F., Benchmarking Heterogeneous Electrocatalysts for the Oxygen Evolution Reaction. *Journal of the American Chemical Society* **2013,** *135* (45), 16977-16987.

27. Watzele, S.; Bandarenka, A. S., Quick Determination of Electroactive Surface Area of Some Oxide Electrode Materials. *Electroanalysis* **2016,** *28* (10), 2394-2399.

28. Luo, H.; Lei, H.; Yuan, Y.; Liang, Y.; Qiu, Y.; Zhu, Z.; Wang, Z. Engineering Ternary Copper-Cobalt Sulfide Nanosheets as High-performance Electrocatalysts toward Oxygen Evolution Reaction. *Catalysts* **2019,** 9(5):459.

29. Kempler, P. A.; Nielander, A. C., Reliable reporting of Faradaic efficiencies for electrocatalysis research. *Nature Communications* **2023,** *14* (1), 1158.

30. Zhang, L.; Roling, L. T.; Wang, X.; Vara, M.; Chi, M.; Liu, J.; Choi, S.-I.; Park, J.;

Herron, J. A.; Xie, Z.; Mavrikakis, M.; Xia, Y., Platinum-based nanocages with subnanometer-thick walls and well-defined, controllable facets. *Science* **2015,** *349* (6246), 412-416.

31. Li, Z.; Ge, R.; Su, J.; Chen, L., Recent Progress in Low Pt Content Electrocatalysts for Hydrogen Evolution Reaction. *Advanced Materials Interfaces* **2020,** *7* (14), 2000396.

32. Zhang, L.; Han, L.; Liu, H.; Liu, X.; Luo, J., Potential-Cycling Synthesis of Single Platinum Atoms for Efficient Hydrogen Evolution in Neutral Media. *Angewandte Chemie International Edition* **2017,** *56* (44), 13694-13698.

33. Tavakkoli, M.; Holmberg, N.; Kronberg, R.; Jiang, H.; Sainio, J.; Kauppinen, E. I.; Kallio, T.; Laasonen, K., Electrochemical Activation of Single-Walled Carbon Nanotubes with Pseudo-Atomic-Scale Platinum for the Hydrogen Evolution Reaction. *ACS Catalysis* **2017,** *7* (5), 3121-3130.

34. Tang, T.; Ding, L.; Yao, Z.-C.; Pan, H.-R.; Hu, J.-S.; Wan, L.-J., Synergistic Electrocatalysts for Alkaline Hydrogen Oxidation and Evolution Reactions. *Advanced Functional Materials* **2022,** *32* (2), 2107479.

35. Wei, Y.-C.; Liu, C.-W.; Lee, H.-W.; Chung, S.-R.; Lee, S.-L.; Chan, T.-S.; Lee, J.-F.; Wang, K.-W., Synergistic effect of Co alloying and surface oxidation on oxygen reduction reaction performance for the Pd electrocatalysts. *International Journal of Hydrogen Energy* **2011,** *36* (6), 3789-3802.

36. Singh, A. K.; Xu, Q., Synergistic Catalysis over Bimetallic Alloy Nanoparticles. *ChemCatChem* **2013,** *5* (3), 652-676.

37. Du, M.; Li, X.; Pang, H.; Xu, Q., Alloy electrocatalysts. *EnergyChem* **2023,** *5* (2), 100083.

38. Jiao, S.; Fu, X.; Huang, H., Descriptors for the Evaluation of Electrocatalytic Reactions: d-Band Theory and Beyond. *Advanced Functional Materials* **2022,** *32* (4), 2107651.

39. Hu, J.; Al-Salihy, A.; Zhang, B.; Li, S.; Xu, P. Mastering the D-Band Center of Iron-Series Metal-Based Electrocatalysts for Enhanced Electrocatalytic Water Splitting. *International Journal of Molecular Sciences* **2022,** 23, 15405.

40. Wang, J.; Xin, S.; Xiao, Y.; Zhang, Z.; Li, Z.; Zhang, W.; Li, C.; Bao, R.; Peng, J.; Yi, J.; Chou, S., Manipulating the Water Dissociation Electrocatalytic Sites of Bimetallic

Nickel-Based Alloys for Highly Efficient Alkaline Hydrogen Evolution. *Angewandte Chemie International Edition* **2022,** *61* (30), e202202518.

41. Du, X. X.; He, Y.; Wang, X. X.; Wang, J. N., Fine-grained and fully ordered intermetallic PtFe catalysts with largely enhanced catalytic activity and durability. *Energy & Environmental Science* **2016,** *9* (8), 2623-2632.

42. Yang, T.; Zhu, H.; Wan, M.; Dong, L.; Zhang, M.; Du, M., Highly efficient and durable PtCo alloy nanoparticles encapsulated in carbon nanofibers for electrochemical hydrogen generation. *Chemical Communications* **2016,** *52* (5), 990-993.

43. Oh, A.; Sa, Y. J.; Hwang, H.; Baik, H.; Kim, J.; Kim, B.; Joo, S. H.; Lee, K., Rational design of Pt–Ni–Co ternary alloy nanoframe crystals as highly efficient catalysts toward the alkaline hydrogen evolution reaction. *Nanoscale* **2016,** *8* (36), 16379-16386.

44. Zalineeva, A.; Baranton, S.; Coutanceau, C.; Jerkiewicz, G., Octahedral palladium nanoparticles as excellent hosts for electrochemically adsorbed and absorbed hydrogen. *Science Advances* **2017,** *3* (2), e1600542.

45. Zhu, J.; Hu, L.; Zhao, P.; Lee, L. Y. S.; Wong, K.-Y., Recent advances in electrocatalytic hydrogen evolution using nanoparticles. *Chemical reviews* **2019,** *120* (2), 851-918.

46. Zhang, J.; Zhang, Q.; Feng, X., Support and Interface Effects in Water-Splitting Electrocatalysts. *Advanced Materials* **2019,** *31* (31), 1808167.

47. Song, J.; Wei, C.; Huang, Z.-F.; Liu, C.; Zeng, L.; Wang, X.; Xu, Z. J., A review on fundamentals for designing oxygen evolution electrocatalysts. *Chemical Society Reviews* **2020,** *49* (7), 2196-2214.

48. Hinnemann, B.; Moses, P. G.; Bonde, J.; Jørgensen, K. P.; Nielsen, J. H.; Horch, S.; Chorkendorff, I.; Nørskov, J. K., Biomimetic hydrogen evolution: MoS2 nanoparticles as catalyst for hydrogen evolution. *Journal of the American Chemical Society* **2005,** *127* (15), 5308-9.

49. Bonde, J.; Moses, P. G.; Jaramillo, T. F.; Nørskov, J. K.; Chorkendorff, I., Hydrogen evolution on nano-particulate transition metal sulfides. *Faraday Discussions* **2009,** *140* (0), 219-231.

50. Walter, C.; Menezes, P. W.; Driess, M., Perspective on intermetallics towards efficient electrocatalytic water-splitting. *Chemical Science* **2021,** *12* (25), 8603-8631.

51. Furukawa, S.; Komatsu, T., Intermetallic Compounds: Promising Inorganic Materials for Well-Structured and Electronically Modified Reaction Environments for Efficient Catalysis. *ACS Catalysis* **2017,** *7* (1), 735-765.

52. Norskov, J. K.; Bligaard, T.; Logadottir, A.; Kitchin, J. R.; Chen, J. G.; Pandelov, S.; Norskov, J. K., Trends in the exchange current for hydrogen evolution. *J. Electrochem. Soc.* **2005,** *152* (3), J23-J26.

53. Hinnemann, B.; Moses, P. G.; Bonde, J.; Jørgensen, K. P.; Nielsen, J. H.; Horch, S.; Chorkendorff, I.; Nørskov, J. K., Biomimetic Hydrogen Evolution: MoS2 Nanoparticles as Catalyst for Hydrogen Evolution. *Journal of the American Chemical Society* **2005,** *127* (15), 5308-5309.

54. Gong, M.; Wang, D.-Y.; Chen, C.-C.; Hwang, B.-J.; Dai, H., A mini review on nickel-based electrocatalysts for alkaline hydrogen evolution reaction. *Nano Research* **2016,** *9* (1), 28-46.

55. Karimzadeh, A.; Aliofkhazraei, M.; Walsh, F. C., A review of electrodeposited Ni-Co alloy and composite coatings: Microstructure, properties and applications. *Surf. Coat. Technol.* **2019,** *372*, 463-498.

56. Cui, X.; Chen, M.; Xiong, R.; Sun, J.; Liu, X.; Geng, B., Ultrastable and efficient H2 production via membrane-free hybrid water electrolysis over a bifunctional catalyst of hierarchical Mo–Ni alloy nanoparticles. *J. Mater. Chem. A* **2019,** *7* (27), 16501-16507.

57. Chen, L.; Yang, S.; Qian, K.; Wei, W.; Sun, C.; Xie, J., In situ growth of N-doped carbon coated CoNi alloy with graphene decoration for enhanced HER performance. *Journal of Energy Chemistry* **2019,** *29*, 129-135.

58. Im, S. W.; Ahn, H.; Seo, D. H.; Park, S.; Choi, S.; Ryu, W.; Kim, K.; Park, E. S.; Nam, K. T., A scalable Al–Ni alloy powder catalyst prepared by metallurgical microstructure control. *J. Mater. Chem. A* **2020,** *8* (22), 11133-11140.

59. Laszczyńska, A.; Szczygieł, I., Electrocatalytic activity for the hydrogen evolution of the electrodeposited Co–Ni–Mo, Co–Ni and Co–Mo alloy coatings. *International Journal of*

Hydrogen Energy **2020,** *45* (1), 508-520.

60. Skibińska, K.; Kutyła, D.; Kula, A.; Gajewska, M.; Marzec, M. M.; Żabiński, P., Hydrogen evolution reaction (HER) activity of conical Co–Fe alloy structures and their application as a sensitive and rapid sensor for H2O2 detection. *Archives of Civil and Mechanical Engineering* **2022,** *22* (2), 76.

61. Sequeira, C. A. C.; Santos, D. M. F.; Brito, P. S. D., Electrocatalytic activity of simple and modified Fe–P electrodeposits for hydrogen evolution from alkaline media. *Energy* **2011,** *36* (2), 847-853.

62. Patil, R. B.; Mantri, A.; House, S. D.; Yang, J. C.; McKone, J. R., Enhancing the Performance of Ni-Mo Alkaline Hydrogen Evolution Electrocatalysts with Carbon Supports. *ACS Applied Energy Materials* **2019,** *2* (4), 2524-2533.

63. González-Buch, C.; Herraiz-Cardona, I.; Ortega, E.; García-Antón, J.; Pérez-Herranz, V., Synthesis and characterization of macroporous Ni, Co and Ni–Co electrocatalytic deposits for hydrogen evolution reaction in alkaline media. *International Journal of Hydrogen Energy* **2013,** *38* (25), 10157-10169.

64. Zhang, X.; Li, Y.; Guo, Y.; Hu, A.; Li, M.; Hang, T.; Ling, H., 3D hierarchical nanostructured Ni–Co alloy electrodes on porous nickel for hydrogen evolution reaction. *International Journal of Hydrogen Energy* **2019,** *44* (57), 29946-29955.

65. Lotfi, N.; Shahrabi, T.; Yaghoubinezhad, Y.; Darband, G. B., Surface modification of Ni foam by the dendrite Ni-Cu electrode for hydrogen evolution reaction in an alkaline solution. *Journal of Electroanalytical Chemistry* **2019,** *848*, 113350.

66. Herraiz-Cardona, I.; Ortega, E.; Pérez-Herranz, V., Impedance study of hydrogen evolution on Ni/Zn and Ni–Co/Zn stainless steel based electrodeposits. *Electrochimica Acta* **2011,** *56* (3), 1308-1315.

67. Shetty, S.; Hegde, A. C., A Study on Composition Dependent Electrocatalytic Behaviour of Electrodeposited Ni-Mo Alloy. *Nano Hybrids and Composites* **2017,** pp 113-120.

68. Xie, S. H.; Xie, Y. L.; Kruzic, J. J.; Gu, K. M.; Yang, H. P.; Deng, Y. M.; Zeng, X. R., The Pivotal Role of Boron in Improving the Azo Dye Degradation of Glassy Fe-based Catalysts. *Chemcatchem* **2020,** *12* (3), 750-761.

69. Jia, Z.; Zhao, Y.; Wang, Q.; Lyu, F.; Tian, X.; Liang, S. X.; Zhang, L. C.; Luan, J.; Wang, Q.; Sun, L.; Yang, T.; Shen, B., Nanoscale Heterogeneities of Non-Noble Iron-Based Metallic Glasses toward Efficient Water Oxidation at Industrial-Level Current Densities. *ACS Appl Mater Interfaces* **2022,** *14* (8), 10288-10297.

70. Zhai, Y.; Ren, X.; Yan, J.; Liu, S., High Density and Unit Activity Integrated in Amorphous Catalysts for Electrochemical Water Splitting. *Small Structures* **2021,** *2* (4), 24.

71. Wang, W. H., Dynamic relaxations and relaxation-property relationships in metallic glasses. *Prog. Mater Sci.* **2019,** *106*, 100561.

72. Nomoto, K.; Ceguerra, A. V.; Gammer, C.; Li, B.; Bilal, H.; Hohenwarter, A.; Gludovatz, B.; Eckert, J.; Ringer, S. P.; Kruzic, J. J., Medium-range order dictates local hardness in bulk metallic glasses. *Materials Today* **2021,** *44*, 48-57.

73. Han, Q.; Cui, S.; Pu, N.; Chen, J.; Liu, K.; Wei, X., A study on pulse plating amorphous Ni–Mo alloy coating used as HER cathode in alkaline medium. *International Journal of Hydrogen Energy* **2010,** *35* (11), 5194-5201.

74. Bachvarov, V.; Lefterova, E.; Rashkov, R., Electrodeposited NiFeCo and NiFeCoP alloy cathodes for hydrogen evolution reaction in alkaline medium. *International Journal of Hydrogen Energy* **2016,** *41* (30), 12762-12771.

75. Ullal, Y.; Hegde, A. C., Electrodeposition and electro-catalytic study of nanocrystalline Ni–Fe alloy. *International Journal of Hydrogen Energy* **2014,** *39* (20), 10485-10492.

76. Li, Y.; Zhang, X.; Hu, A.; Li, M., Morphological variation of electrodeposited nanostructured Ni-Co alloy electrodes and their property for hydrogen evolution reaction. *International Journal of Hydrogen Energy* **2018,** *43* (49), 22012-22020.

77. Negem, M.; Nady, H.; Dunnill, C. W., Nanocrystalline Ni–Cu Electroplated Alloys Cathodes for Hydrogen Generation in Phosphate-Buffered Neutral Electrolytes. *Journal of Bio- and Tribo-Corrosion* **2020,** *6* (4).

78. Xie, J.; Xie, Y., Structural Engineering of Electrocatalysts for the Hydrogen Evolution Reaction: Order or Disorder? *ChemCatChem* **2015,** *7* (17), 2568-2580.

79. Rosalbino, F.; Macciò, D.; Saccone, A.; Scavino, G., Study of Co–W crystalline alloys as hydrogen electrodes in alkaline water electrolysis. *International Journal of Hydrogen Energy*

2014, *39* (24), 12448-12456.

80. Ramesh, L.; Sheshadri, B. S.; Mayanna, S. M., Electrolytic preparation and characterization of Ni–Fe–Mo alloys: cathode materials for alkaline water electrolysis. *International Journal of Energy Research* **1999,** *23* (10), 919-924.

81. Chu, F.; Wu, K.; Meng, Y.; Edalati, K.; Lin, H.-J., Effect of high-pressure torsion on the hydrogen evolution performances of a melt-spun amorphous Fe73.5Si13.5B9Cu1Nb3 alloy. *International Journal of Hydrogen Energy* **2021,** *46* (49), 25029-25038.

82. McKone, J. R.; Sadtler, B. F.; Werlang, C. A.; Lewis, N. S.; Gray, H. B., Ni–Mo Nanopowders for Efficient Electrochemical Hydrogen Evolution. *ACS Catalysis* **2013,** *3* (2), 166-169.

83. Chen, J.; Ling, Y.; Qu, D.; Huang, L.; Li, J.; Tang, P.; He, A.; Jin, X.; Zhou, Y.; Xu, M.; Du, J.; Han, Z.; Xu, Q., Enhanced electrocatalysis of NiMnIn Heusler alloy films for hydrogen evolution reaction by magnetic field. *J. Alloys Compd.* **2021,** *877*.

84. Bayatsarmadi, B.; Zheng, Y.; Russo, V.; Ge, L.; Casari, C. S.; Qiao, S. Z., Highly active nickel-cobalt/nanocarbon thin films as efficient water splitting electrodes. *Nanoscale* **2016,** *8* (43), 18507-18515.

85. Gutić, S. J.; Jovanović, A. Z.; Dobrota, A. S.; Metarapi, D.; Rafailović, L. D.; Pašti, I. A.; Mentus, S. V., Simple routes for the improvement of hydrogen evolution activity of Ni-Mo catalysts: From sol-gel derived powder catalysts to graphene supported co-electrodeposits. *International Journal of Hydrogen Energy* **2018,** *43* (35), 16846-16858.

86. Solmaz, R.; Döner, A.; Kardaş, G., Preparation, characterization and application of alkaline leached CuNiZn ternary coatings for long-term electrolysis in alkaline solution. *International Journal of Hydrogen Energy* **2010,** *35* (19), 10045-10049.

87. Ahn, S. H.; Hwang, S. J.; Yoo, S. J.; Choi, I.; Kim, H.-J.; Jang, J. H.; Nam, S. W.; Lim, T.-H.; Lim, T.; Kim, S.-K.; Kim, J. J., Electrodeposited Ni dendrites with high activity and durability for hydrogen evolution reaction in alkaline water electrolysis. *J. Mater. Chem.* **2012,** *22* (30).

88. Wang, J.; Shao, H.; Ren, S.; Hu, A.; Li, M., Fabrication of porous Ni-Co catalytic electrode with high performance in hydrogen evolution reaction. *Appl. Surf. Sci.* **2021,** *539*.

89. He, X.; Sun, Z.; Zou, Q.; Yang, J.; Wu, L., Codeposition of Nanocrystalline Co-Ni Catalyst Based on 1-ethyl-3-methylimidazolium Bisulfate and Ethylene Glycol System for Hydrogen Evolution Reaction. *J. Electrochem. Soc.* **2019,** *166* (16), D908-D915.

90. He, X.; Hu, Z.; Zou, Q.; Yang, J.; Guo, R.; Wu, L., Co-deposition of Co-Ni alloy catalysts from an ethylene glycol system for the hydrogen evolution reaction. *RSC Adv* **2023,** *13* (13), 8901-8914.

91. Barati Darband, G.; Aliofkhazraei, M.; Rouhaghdam, A. S., Facile electrodeposition of ternary Ni-Fe-Co alloy nanostructure as a binder free, cost-effective and durable electrocatalyst for high-performance overall water splitting. *J. Colloid Interface Sci.* **2019,** *547*, 407-420.

92. Mundotiya, B. M.; Ullah, W., Morphology controlled synthesis of the nanostructured gold by electrodeposition techniques. In *Novel Metal Electrodeposition and the Recent Application*, IntechOpen London, UK: **2018**.

93. Zhou, H.; Peng, C.; Jiao, S.; Zeng, W.; Chen, J.; Kuang, Y., Electrodeposition of nanoscaled nickel in a reverse microemulsion. *Electrochem. Commun.* **2006,** *8* (7), 1142-1146.

94. Darband, G. B.; Aliofkhazraei, M.; Rouhaghdam, A. S.; Kiani, M. A., Three-dimensional Ni-Co alloy hierarchical nanostructure as efficient non-noble-metal electrocatalyst for hydrogen evolution reaction. *Appl. Surf. Sci.* **2019,** *465*, 846-862.

95. Ganci, F.; Cusumano, V.; Livreri, P.; Aiello, G.; Sunseri, C.; Inguanta, R., Nanostructured Ni–Co alloy electrodes for both hydrogen and oxygen evolution reaction in alkaline electrolyzer. *Int. J. Hydrogen Energy* **2021,** *46* (16), 10082-10092.

96. Maurya, A.; Suman, S.; Bhardwaj, A.; Mohapatra, L.; Kushwaha, A. K., Substrate Dependent Electrodeposition of Ni–Co Alloy for Efficient Hydrogen Evolution Reaction. *Electrocatalysis* **2022,** *14* (1), 68-77.

97. Emel'yanenko, V. N.; Boeck, G.; Verevkin, S. P.; Ludwig, R., Volatile Times for the Very First Ionic Liquid: Understanding the Vapor Pressures and Enthalpies of Vaporization of Ethylammonium Nitrate. *Chemistry – A European Journal* **2014,** *20* (37), 11640-11645.

98. Walden, P., Molecular weights and electrical conductivity of several fused salts. *Bull. Acad. Imper. Sci.(St. Petersburg)* **1914,** *1800.*

99. Wilkes, J. S.; Zaworotko, M. J., Air and water stable 1-ethyl-3-methylimidazolium based ionic liquids. *Journal of the Chemical Society, Chemical Communications* **1992,** (13), 965-967.

100. Bao, W.; Wang, Z.; Li, Y., Synthesis of Chiral Ionic Liquids from Natural Amino Acids. *The Journal of Organic Chemistry* **2003,** *68* (2), 591-593.

101. Hirao, M.; Ito, K.; Ohno, H., Preparation and polymerization of new organic molten salts; N-alkylimidazolium salt derivatives. *Electrochimica Acta* **2000,** *45* (8-9), 1291-1294.

102. Silva, W.; Zanatta, M.; Ferreira, A. S.; Corvo, M. C.; Cabrita, E. J. Revisiting Ionic Liquid Structure-Property Relationship: A Critical Analysis, *International Journal of Molecular Sciences* **2020**, 21(20), 7745.

103. Ghandi, K., A review of ionic liquids, their limits and applications. *Green and sustainable chemistry* **2014,** *2014*.

104. Introduction: Ionic Liquids. *Chemical Reviews* **2017,** *117* (10), 6633-6635.

105. Kaur, G.; Kumar, H.; Singla, M., Diverse applications of ionic liquids: A comprehensive review. *Journal of Molecular Liquids* **2022,** *351*, 118556.

106. Tang, J.; Azumi, K., Improvement of Al coating adhesive strength on the AZ91D magnesium alloy electrodeposited from ionic liquid. *Surface and Coatings Technology* **2012,** *208*, 1-6.

107. Zhang, Q.; Wang, Q.; Zhang, S.; Lu, X., Effect of nicotinamide on electrodeposition of Al from aluminium chloride (AlCl3)-1-butyl-3-methylimidazolium chloride ([Bmim]Cl) ionic liquids. *Journal of Solid State Electrochemistry* **2014,** *18* (1), 257-267.

108. Deng, M.-J.; Lin, P.-C.; Chang, J.-K.; Chen, J.-M.; Lu, K.-T., Electrochemistry of Zn(II)/Zn on Mg alloy from the N-butyl-N-methylpyrrolidinium dicyanamide ionic liquid. *Electrochimica Acta* **2011,** *56* (17), 6071-6077.

109. Zhang, Q.; Wang, Q.; Zhang, S.; Lu, X.; Zhang, X., Electrodeposition in Ionic Liquids. *ChemPhysChem* **2016,** *17* (3), 335-351.

110. Bakkar, A.; Neubert, V., Electrodeposition onto magnesium in air and water stable ionic liquids: From corrosion to successful plating. *Electrochemistry Communications* **2007,** *9* (9), 2428-2435.

111. Abbott, A. P.; McKenzie, K. J., Application of ionic liquids to the electrodeposition of metals. *Phys. Chem. Chem. Phys.* **2006,** *8* (37), 4265-79.

112. Susan, A. B. H.; Saha, S.; Ahmed, S.; Begum, F.; Rahman, M. M.; Mollah, M. Y. A., Electrodeposition of cobalt from a hydrophilic ionic liquid at ambient condition. *Materials Research Innovations* **2012,** *16* (5), 345-349.

113. Zhu, Y.-L.; Katayama, Y.; Miura, T., Electrochemical Preparation of Nickel and Iron Nanoparticles in a Hydrophobic Ionic Liquid. *Electrochemical and Solid-State Letters* **2011,** *14* (12), D110.

114. Suryanto, B. H. R.; Gunawan, C. A.; Lu, X.; Zhao, C., Tuning the electrodeposition parameters of silver to yield micro/nano structures from room temperature protic ionic liquids. *Electrochimica Acta* **2012,** *81*, 98-105.

115. Liu, Z.; El Abedin, S. Z.; Endres, F., Dissolution of zinc oxide in a protic ionic liquid with the 1-methylimidazolium cation and electrodeposition of zinc from ZnO/ionic liquid and ZnO/ionic liquid–water mixtures. *Electrochemistry Communications* **2015,** *58*, 46-50.

116. Meenatchi, B.; Renuga, V.; Manikandan, A., Electrodeposition of Nickel on Glassy Carbon Electrode from Protic Ionic Liquids with Imidazolium Cation. *Journal of Inorganic and Organometallic Polymers and Materials* **2016,** *26* (2), 423-430.

117. Saranya, D.; Velayutham, D.; Suryanarayanan, V., Electrodeposition of Ni–Cu alloys from a protic ionic liquid medium-voltammetric and surface morphologic studies. *Journal of Electroanalytical Chemistry* **2014,** *734*, 70-78.

118. Dan, Z.; Qin, F.; Sugawara, Y.; Muto, I.; Hara, N., Fabrication of nanoporous copper by dealloying amorphous binary Ti–Cu alloys in hydrofluoric acid solutions. *Intermetallics* **2012,** *29*, 14-20.

119. Zhang, C.; Sun, J.; Xu, J.; Wang, X.; Ji, H.; Zhao, C.; Zhang, Z., Formation and microstructure of nanoporous silver by dealloying rapidly solidified Zn–Ag alloys. *Electrochimica Acta* **2012,** *63*, 302-311.

120. Li, R.; Liu, X. J.; Wang, H.; Zhou, D. Q.; Wu, Y.; Lu, Z. P., Formation mechanism and characterization of nanoporous silver with tunable porosity and promising capacitive performance by chemical dealloying of glassy precursor. *Acta Materialia* **2016,** *105*, 367-377.

121. Lu, Q.; Hutchings, G. S.; Yu, W.; Zhou, Y.; Forest, R. V.; Tao, R.; Rosen, J.; Yonemoto, B. T.; Cao, Z.; Zheng, H.; Xiao, J. Q.; Jiao, F.; Chen, J. G., Highly porous non-precious bimetallic electrocatalysts for efficient hydrogen evolution. *Nature Communications* **2015,** *6* (1), 6567.

122. Tan, Y.; Wang, H.; Liu, P.; Cheng, C.; Zhu, F.; Hirata, A.; Chen, M., 3D Nanoporous Metal Phosphides toward High-Efficiency Electrochemical Hydrogen Production. *Advanced Materials* **2016,** *28* (15), 2951-2955.

123. Wang, D.; Yu, Y.; Zhu, J.; Liu, S.; Muller, D. A.; Abruña, H. D., Morphology and Activity Tuning of Cu3Pt/C Ordered Intermetallic Nanoparticles by Selective Electrochemical Dealloying. *Nano Letters* **2015,** *15* (2), 1343-1348.

124. Asnavandi, M.; Zhao, C., Hydrogen Bubble-Assisted Electrodeposition of Metal Nanoparticles from Protic Ionic Liquids for Electrocatalysis. *ACS Sustainable Chemistry & Engineering* **2017,** *5* (1), 85-89.

125. Wu, L.; Hofmann, J. P., Comparing the Intrinsic HER Activity of Transition Metal Dichalcogenides: Pitfalls and Suggestions. *ACS Energy Letters* **2021,** *6* (7), 2619-2625.

126. Suryanto, B. H. R.; Lu, X.; Chan, H. M.; Zhao, C., Controlled electrodeposition of cobalt oxides from protic ionic liquids for electrocatalytic water oxidation. *RSC Advances* **2013,** *3* (43).

127. Chaabene, N.; Ngo, K.; Turmine, M.; Vivier, V., New hydrophobic deep eutectic solvent for electrochemical applications. *Journal of Molecular Liquids* **2020,** *319*, 114198.

128. Mischler, S.; Munoz, A. I., Tribocorrosion. In *Encyclopedia of Interfacial Chemistry*, Wandelt, K., Ed. Elsevier: Oxford, **2018**; pp 504-514.

129. Kurzweil, P., Electrochemical terminology: Cell nomenclature. In *Reference Module in Chemistry, Molecular Sciences and Chemical Engineering*, Elsevier: **2023**.

130. Xie, S.; Xie, Y.; Kruzic, J. J.; Gu, K.; Yang, H.; Deng, Y.; Zeng, X., The Pivotal Role of Boron in Improving the Azo Dye Degradation of Glassy Fe-based Catalysts. *ChemCatChem* **2020,** *12* (3), 750-761.

131. Elgrishi, N.; Rountree, K. J.; McCarthy, B. D.; Rountree, E. S.; Eisenhart, T. T.; Dempsey, J. L., A Practical Beginner's Guide to Cyclic Voltammetry. *Journal of Chemical*

Education **2018,** *95* (2), 197-206.

132. Bontempelli, G.; Dossi, N.; Toniolo, R., Voltammetry | Polarography. In *Encyclopedia of Analytical Science (Third Edition)*, Worsfold, P.; Poole, C.; Townshend, A.; Miró, M., Eds. Academic Press: Oxford, **2019,** pp 218-229.

133. Guy, O. J.; Walker, K.-A. D., Chapter 4 - Graphene Functionalization for Biosensor Applications. In *Silicon Carbide Biotechnology (Second Edition)*, Saddow, S. E., Ed. Elsevier: **2016,** pp 85-141.

134. Le Pevelen, D. D., Small Molecule X-Ray Crystallography, Theory and Workflow. In *Encyclopedia of Spectroscopy and Spectrometry (Second Edition)*, Lindon, J. C., Ed. Academic Press: Oxford, **2010,** pp 2559-2576.

135. Zhou, W.; Apkarian, R.; Wang, Z. L.; Joy, D., Fundamentals of scanning electron microscopy (SEM). *Scanning Microscopy for Nanotechnology: Techniques and Applications* **2007**, 1-40.

136. Suryanto, B. H. R.; Lu, X.; Chan, H. M.; Zhao, C., Controlled electrodeposition of cobalt oxides from protic ionic liquids for electrocatalytic water oxidation. *RSC Advances* **2013,** *3* (43), 20936-20942.

137. Zhou, F.; Izgorodin, A.; Hocking, R. K.; Spiccia, L.; MacFarlane, D. R., Electrodeposited MnOx Films from Ionic Liquid for Electrocatalytic Water Oxidation. *Advanced Energy Materials* **2012,** *2* (8), 1013-1021.

138. Asnavandi, M.; Suryanto, B. H. R.; Zhao, C., Controlled electrodeposition of nanostructured Pd thin films from protic ionic liquids for electrocatalytic oxygen reduction reactions. *RSC Advances* **2015,** *5* (90), 74017-74023.

139. Gunawan, C. A.; Suryanto, B. H. R.; Zhao, C., Electrochemical Study of Copper in Room Temperature Protic Ionic Liquids Ethylammonium Nitrate and Triethylammonium Methylsulfonate. *Journal of The Electrochemical Society* **2012,** *159* (10), D611.

140. Khan, M.; Xiao, J.; Zhou, F.; Yablonskikh, M.; MacFarlane, D. R.; Spiccia, L.; Aziz, E. F., On the Origin of the Improvement of Electrodeposited MnOx Films in Water Oxidation Catalysis Induced by Heat Treatment. *ChemSusChem* **2015,** *8* (11), 1980-1985.

141. Kanzaki, R.; Uchida, K.; Hara, S.; Umebayashi, Y.; Ishiguro, S.-i.; Nomura, S., Acid–

Base Property of Ethylammonium Nitrate Ionic Liquid Directly Obtained Using Ion-selective Field Effect Transistor Electrode. *Chemistry Letters* **2007,** *36* (5), 684-685.

142. Pająk, M.; Hubkowska, K.; Czerwiński, A., Nitrate protic ionic liquids as electrolytes: Towards hydrogen sorption in Pd. *Electrochimica Acta* **2019,** *324*, 134851.

143. Gupta, A.; Srivastava, C., Nucleation and growth mechanism of tin electrodeposition on graphene oxide: A kinetic, thermodynamic and microscopic study. *J. Electroanal. Chem.* **2020,** *861*.

144. Feng, Z.; Wang, L.; Li, D.; Sun, Q.; Lu, P.; Xing, P.; An, M., Electrodeposition of Ni-Se in a chloride electrolyte: An insight of diffusion and nucleation mechanisms. *J. Electroanal. Chem.* **2019,** *847*.

145. Zhao, C.; MacFarlane, D. R.; Bond, A. M., Modified Thermodynamics in Ionic Liquids for Controlled Electrocrystallization of Nanocubes, Nanowires, and Crystalline Thin Films of Silver−Tetracyanoquinodimethane. *Journal of the American Chemical Society* **2009,** *131* (44), 16195-16205.

146. Scharifker, B.; Hills, G., Theoretical and experimental studies of multiple nucleation. *Electrochim. Acta* **1983,** *28* (7), 879-889.

147. Zhou, X.; Wang, Y.; Liu, X.; Liang, Z.; Jin, H. Electrodeposition Kinetics of Ni/Nano-Y2O3 Composite Coatings. *Metals* **2018,** 8(9), 669.

148. Yuan, Y.; Luo, G.; Li, N., New in situ description of electrodepositing multiple nucleation processes under galvanostatic stimuli. *RSC Advances* **2021,** *11* (50), 31526-31532.

149. Guo, C.; Fang, Y.; Wu, B.; Lan, S.; Peng, G.; Wang, X.-l.; Hahn, H.; Gleiter, H.; Feng, T., Ni-P nanoglass prepared by multi-phase pulsed electrodeposition. *Materials Research Letters* **2017,** *5* (5), 293-299.

150. García-Torres, J.; Gómez, E.; Vallés, E., Modulation of magnetic and structural properties of cobalt thin films by means of electrodeposition. *J. Appl. Electrochem.* **2009,** *39* (2), 233-240.

151. Biesinger, M. C.; Payne, B. P.; Lau, L. W. M.; Gerson, A.; Smart, R. S. C., X-ray photoelectron spectroscopic chemical state quantification of mixed nickel metal, oxide and hydroxide systems. *Surf. Interface Anal.* **2009,** *41* (4), 324-332.

152. Biesinger, M. C.; Payne, B. P.; Grosvenor, A. P.; Lau, L. W. M.; Gerson, A. R.; Smart, R. S. C., Resolving surface chemical states in XPS analysis of first row transition metals, oxides and hydroxides: Cr, Mn, Fe, Co and Ni. *Applied Surface Science* **2011,** *257* (7), 2717-2730.

153. Turner, N. H.; Single, A. M., Determination of peak positions and areas from wide-scan XPS spectra. *Surf. Interface Anal.* **1990,** *15* (3), 215-222.

154. Ansell, R. O.; Dickinson, T.; Povey, A. F.; Sherwood, P. M. A., Quantitative use of the angular variation technique in studies of tin by X-ray photoelectron spectroscopy. *Journal of Electron Spectroscopy and Related Phenomena* **1977,** *11* (3), 301-313.

155. Qian, H.; Li, K.; Mu, X.; Zou, J.; Xie, S.; Xiong, X.; Zeng, X., Nanoporous NiFeMoP alloy as a bifunctional catalyst for overall water splitting. *Int. J. Hydrogen Energy* **2020,** *45* (33), 16447-16457.

156. Gorospe, A. E. G. B.; Balela, M. D. L., Ni-Co nanocomposites deposited on carbon fiber paper as an electrocatalyst towards hydrogen evolution reaction. *Materials Today: Proceedings* **2020,** *22*, 255-261.

157. Sun, T.; Cao, J.; Dong, J.; Du, H.; Zhang, H.; Chen, J.; Xu, L., Ordered mesoporous Ni Co alloys for highly efficient electrocatalytic hydrogen evolution reaction. *Int. J. Hydrogen Energy* **2017,** *42* (10), 6637-6645.

158. Edgington, J.; Seitz, L. C., Advancing the Rigor and Reproducibility of Electrocatalyst Stability Benchmarking and Intrinsic Material Degradation Analysis for Water Oxidation. *ACS Catalysis* **2023,** *13* (5), 3379-3394.

159. Zhang, R.; Tang, C.; Kong, R.; Du, G.; Asiri, A. M.; Chen, L.; Sun, X., Al-Doped CoP nanoarray: a durable water-splitting electrocatalyst with superhigh activity. *Nanoscale* **2017,** *9* (14), 4793-4800.

160. Anand Raj, M.; Arumainathan, S., Comparative study of hydrogen evolution behavior of Nickel Cobalt and Nickel Cobalt Magnesium alloy film prepared by pulsed electrodeposition. *Vacuum* **2019,** *160*, 461-466.

161. Lado, J. L.; Wang, X.; Paz, E.; Carbó-Argibay, E.; Guldris, N.; Rodríguez-Abreu, C.; Liu, L.; Kovnir, K.; Kolen'ko, Y. V., Design and Synthesis of Highly Active Al–Ni–P Foam Electrode for Hydrogen Evolution Reaction. *ACS Catalysis* **2015,** *5* (11), 6503-6508.

162. Du, H.; Xia, L.; Zhu, S.; Qu, F.; Qu, F., Al-Doped Ni2P nanosheet array: a superior and durable electrocatalyst for alkaline hydrogen evolution. *Chemical Communications* **2018,** *54* (23), 2894-2897.

163. Danilov, F. I.; Protsenko, V. S.; Kityk, A. A.; Shaiderov, D. A.; Vasil'eva, E. A.; Kumar, U. P.; Kennady, C. J., Electrodeposition of Nanocrystalline Nickel Coatings from a Deep Eutectic Solvent with Water Addition. *Protection of Metals and Physical Chemistry of Surfaces* **2017,** *53* (6), 1131-1138.

164. Abbott, A. P.; El Ttaib, K.; Ryder, K. S.; Smith, E. L., Electrodeposition of nickel using eutectic based ionic liquids. *Transactions of the IMF* **2008,** *86* (4), 234-240.

165. Bernasconi, R.; Panzeri, G.; Firtin, G.; Kahyaoglu, B.; Nobili, L.; Magagnin, L., Electrodeposition of ZnNi Alloys from Choline Chloride/Ethylene Glycol Deep Eutectic Solvent and Pure Ethylene Glycol for Corrosion Protection. *The Journal of Physical Chemistry B* **2020,** *124* (47), 10739-10751.

166. Alesary, H. F.; Cihangir, S.; Ballantyne, A. D.; Harris, R. C.; Weston, D. P.; Abbott, A. P.; Ryder, K. S., Influence of additives on the electrodeposition of zinc from a deep eutectic solvent. *Electrochimica Acta* **2019,** *304*, 118-130.

167. Huang, J. H.; Kargl-Simard, C.; Oliazadeh, M.; Alfantazi, A. M., pH-Controlled precipitation of cobalt and molybdenum from industrial waste effluents of a cobalt electrodeposition process. *Hydrometallurgy* **2004,** *75* (1), 77-90.

168. Huynh, T.-C.; Dao, Q. P. D.; Truong, T.-N.; Doan, N.-G.; Ho, S.-L., Electrodeposition of aluminum on cathodes in ionic liquid based choline chloride/urea/AlCl3. *Environ. Pollut* **2014,** *3* (4), 59-69.

169. Milazzo, G.; Caroli, S.; Braun, R. D., Tables of Standard Electrode Potentials. *Journal of The Electrochemical Society* **1978,** *125* (6), 261C.

170. Zhang, Q. B.; Abbott, A. P.; Yang, C., Electrochemical fabrication of nanoporous copper films in choline chloride–urea deep eutectic solvent. *Physical Chemistry Chemical Physics* **2015,** *17* (22), 14702-14709.

171. Cai, J.; Xu, J.; Wang, J.; Zhang, L.; Zhou, H.; Zhong, Y.; Chen, D.; Fan, H.; Shao, H.; Zhang, J., Fabrication of three-dimensional nanoporous nickel films with tunable

nanoporosity and their excellent electrocatalytic activities for hydrogen evolution reaction. *International journal of hydrogen energy* **2013,** *38* (2), 934-941.

172. Lo, N.-C.; Sun, I. W.; Chen, P.-Y., Electrochemical preparation of porous ZnCuNi by electrodeposition in ethaline deep eutectic solvent followed by anodic or cathodic dealloying in alkaline aqueous solutions for higher nitrate reduction activity. *Journal of Electroanalytical Chemistry* **2021,** *890*, 115256.

173. Koh, S.; Strasser, P., Electrocatalysis on Bimetallic Surfaces: Modifying Catalytic Reactivity for Oxygen Reduction by Voltammetric Surface Dealloying. *Journal of the American Chemical Society* **2007,** *129* (42), 12624-12625.

174. Medway, S. L.; Lucas, C. A.; Kowal, A.; Nichols, R. J.; Johnson, D., In situ studies of the oxidation of nickel electrodes in alkaline solution. *Journal of Electroanalytical Chemistry* **2006,** *587* (1), 172-181.

175. Bing, L.; Huatang, Y.; Yunshi, Z.; Zuoxiang, Z.; Deying, S., Cyclic voltammetric studies of stabilized α-nickel hydroxide electrode. *Journal of power sources* **1999,** *79* (2), 277-280.

176. Wang, J. M.; Zhang, L.; Zhang, C.; Zhang, J. Q., Effects of bismuth ion and tetrabutylammonium bromide on the dendritic growth of zinc in alkaline zincate solutions. *Journal of Power Sources* **2001,** *102* (1), 139-143.

177. Ko, Y.; Park, S.-M., Zinc Oxidation in Dilute Alkaline Solutions Studied by Real-Time Electrochemical Impedance Spectroscopy. *The Journal of Physical Chemistry C* **2012,** *116* (13), 7260-7268.

178. Chuang, A.; Erlebacher, J. Challenges and Opportunities for Integrating Dealloying Methods into Additive Manufacturing. *Materials* **2020,** 13(17), 3706.

179. Ibrahim, S.; Dworzak, A.; Crespo, D.; Renner, F. U.; Dosche, C.; Oezaslan, M., Nanoporous Copper Ribbons Prepared by Chemical Dealloying of a Melt-Spun ZnCu Alloy. *The Journal of Physical Chemistry C* **2022,** *126* (1), 212-226.